

AD-A183 046

NAVY TACTICAL APPLICATIONS GUIDE VOLUME 6 PART 1

1/3

TROPICAL WEATHER ANALYSIS (U) BOWAN (WALTER A) CO PARK

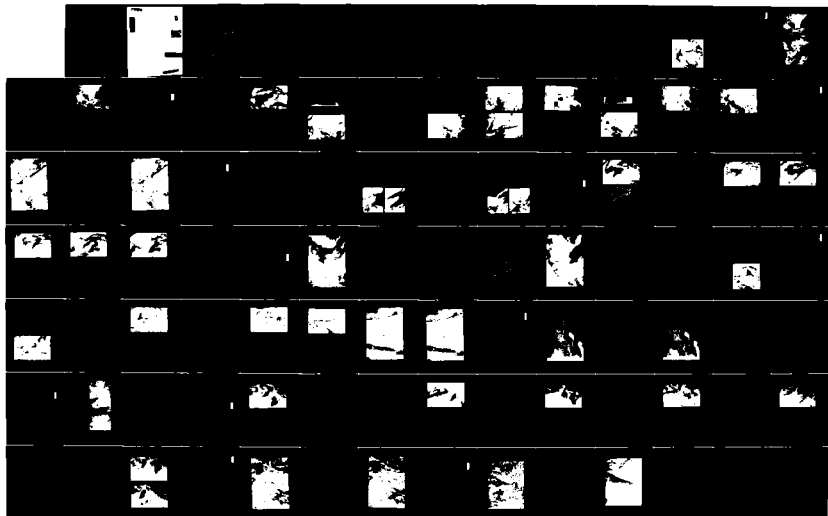
RIDGE IL R W FETT ET AL AUG 86 NEPRF-TR-86-02-U6-PI-2

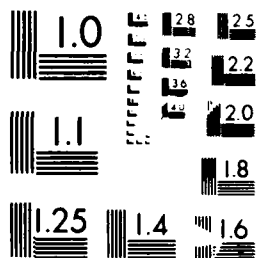
UNCLASSIFIED

NO0238-85-C-3398

F/G 4/2

NL





Resolution Test Chart
 (The numbers indicate the resolution in lines per inch.)

DTIC FILE COPY

AD-A183 046



ANALYSIS OF TROPICS GUIDE

VOLUME 6

TROPICS

ANALYSIS

APPLICATIONS

DTIC
SELECTED
JUL 29 1987
G4 D

DTIC COPY
Approved for public release
Distribution unlimited

2

3

NAVY TACTICAL APPLICATIONS GUIDE

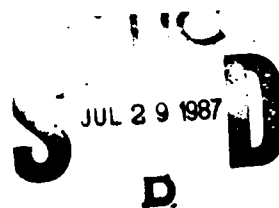
VOLUME 6

PART 1

TROPICS

WEATHER ANALYSIS AND FORECAST APPLICATIONS

METEOROLOGICAL
SATELLITE SYSTEMS



Prepared under the direction of

Robert W. Fett

Weather Analysis

and Forecast Department

Naval Environmental Prediction Research Facility

Scientific Coordinator

Walter A. Bohan

The Walter A. Bohan Company

1986



LIBRARY

THE WALTER A. BOHAN COMPANY

2026 OAKTON STREET, PARK RIDGE, ILLINOIS 60068
APPLIED RESEARCH IN SATELLITE METEOROLOGY AND OCEANOGRAPHY

List of Contributors

Robert W. Fett, Head

Tactical Applications Department
Naval Environmental Prediction Research Facility
Monterey, CA 93943

Walter A. Bohan, Certified Consulting Meteorologist

The Walter A. Bohan Company
Park Ridge, IL 60068

Robert H. Whritner, Manager

Scripps Satellite Oceanography Facility
La Jolla, CA 92093

S. A. Hsu, Professor

Coastal Studies Institute
Louisiana State University
Baton Rouge, LA 70803

Steven W. Lyons, Meteorologist

Pacific Missile Test Center
Point Mugu, CA 93042

Jay Rosenthal, Head

Geophysical Sciences Branch
Pacific Missile Test Center
Point Mugu, CA 93042



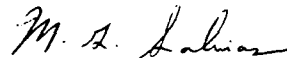
Accession For	
NTIS (CRA&I)	<input checked="" type="checkbox"/>
DIR TAB	<input type="checkbox"/>
Unpublished	<input type="checkbox"/>
Justified	
By	
Distribution /	
Availability Codes	
Dist	Availability Codes
A-1	

Foreword

The Navy Tactical Applications Guide (NTAG), Volume 6, is devoted to regional weather analysis and forecast applications of meteorological satellite imagery in the tropics. Part 1 deals with operationally significant phenomena and effects in the tropics, excluding tropical cyclones. Part 2, to be published at a later date, will focus on tropical cyclone genesis and evolution in areas around the globe.

The volume is organized into four regional areas: Tropical Atlantic Ocean, Tropical Eastern Pacific Ocean (EASTPAC), Tropical Western Pacific Ocean (WESTPAC), and Tropical Indian Ocean. In each section, synoptic-scale phenomena are discussed first, followed by mesoscale phenomena. A number of new analysis techniques, never before published, appear in this volume. The analysis techniques will be useful to Navy meteorologists aboard ships operating in coastal regions or in mid-ocean transit.

Navy meteorologists in the tropics may have the opportunity to occasionally document additional important phenomena. It is desired to update the NTAG series on a periodic basis. Forecasters are encouraged to submit their contributions to assist in this purpose.



M. G. SALINAS
Commander, U.S. Navy
Commanding Officer, NEPRF

Acknowledgments

This volume could not have been published without the devoted effort of the NEPRF Meteorological Laboratory personnel who obtained case study documentations and spent many hours on the computer terminal entering data for the analyses utilized in the studies. Directed by AGCM Shelton, the following personnel: AG1 Danielson, AG2 Davis, AG3 Haynes, and AG3 Livingston did an outstanding job in supporting the work effort required for this volume.

PHI Rutschky processed many of the original photos utilized in the volume. Correlative meteorological data were provided by the Fleet Numerical Oceanography Center, Monterey, CA, and the U.S. Naval Oceanographic Detachment, Asheville, NC.

Additional satellite imagery was supplied by the National Environmental Satellite Data and Information Service (NESDIS) of the National Oceanic and Atmospheric Administration (NOAA). METEO-SAT imagery was supplied by the European Space Agency (ESA).

The assistance of the staff of the Walter A. Bohan Company is again acknowledged. Lido A. Andreoni designed the format of the publication and layout of the case studies. Gregory E. Terhune edited and formatted the text and assisted in the preparation of case study graphics. The high quality of the reproduction of the satellite imagery used in the case studies and the excellent printing of the publication are due to the combined efforts of Peter M. Samorez and Michael E. Brock.

Contents

<i>List of Contributors</i>	iii
<i>Foreword</i>	v
<i>Introduction</i>	iv

Section 1

Tropical Atlantic Ocean

1A Introduction	1A-1
-----------------------	------

Case Studies

1B Synoptic-scale	1B-1
1C Mesoscale	1C-1

Section 2

Tropical Eastern Pacific Ocean

2A Introduction	2A-1
-----------------------	------

Case Studies

2B Synoptic-scale	2B-1
2C Mesoscale	2C-1

Section 3

Tropical Western Pacific Ocean

3A Introduction	3A-1
-----------------------	------

Case Studies

3B Synoptic-scale	3B-1
3C Mesoscale	3C-1

Section 4

Tropical Indian Ocean

4A Introduction	4A-1
-----------------------	------

Case Studies

4B Synoptic-scale	4B-1
4C Mesoscale	4C-1

Introduction

For the purposes of this volume, case studies are presented for the major tropical ocean basins and are limited to the region from 30° N to 30° S. Very often, extratropical patterns influence tropical weather events; in these cases the salient extratropical patterns are included.

In the major oceanic basins of the Atlantic, Pacific and Indian Oceans, routine surface and upper air observations continue to be limited mostly to land areas. Weather satellite data over the oceans are very important to the Navy meteorologist because they can often provide useful indicators of low-level and upper-level flow patterns. When this information is integrated with known tropical circulation models, atmospheric circulation patterns can be deduced in areas of limited routine meteorological data. This, however, can only be fully realized if the meteorologist is well trained in the methodology of satellite data processing, data analysis, interpretation, and use as a short-range forecast aid.

The material in this volume has been developed to demonstrate some of the more operationally significant uses of satellite data in each of the major tropical ocean basins of the world. Studies are categorized as either synoptic-scale or mesoscale depending upon the phenomenon in question. However, this distinction is somewhat arbitrary in that synoptic-scale analysis depends upon an understanding of mesoscale features as indicators of pressure and flow patterns in three dimensions. With more rapid satellite views of a region, the fourth dimension time becomes an additional factor which can provide an understanding of the evolution of a weather system or feature.

The meteorologist well-versed in the art of satellite data interpretation can very quickly become confident of his or her forecasts even in unfamiliar areas of the world. It is the purpose of this volume to assist in the development of such skills.

UNCLASSIFIED

UNCLASSIFIED

REPORT DOCUMENTATION PAGE				
1a REPORT SECURITY CLASSIFICATION UNCLASSIFIED		1b RESTRICTIVE MARKINGS		
2a SECURITY CLASSIFICATION AUTHORITY		3 DISTRIBUTION AVAILABILITY OF REPORT Approved for Public Release Distribution Unlimited		
2b DECLASSIFICATION/DOWNGRADING SCHEDULE				
4 PERFORMING ORGANIZATION REPORT NUMBER(S)		5 MONITORING ORGANIZATION REPORT NUMBER(S) TR86-02		
6a NAME OF PERFORMING ORGANIZATION The Walter A. Bohan Company	6b OFFICE SYMBOL (if applicable)	7a NAME OF MONITORING ORGANIZATION Naval Environmental Prediction Research Facility		
6c ADDRESS (City, State, and ZIP Code) 2026 Oakton Street Park Ridge, IL 60068		7b ADDRESS (City, State, and ZIP Code) Monterey, CA 93943-5006		
8a NAME OF FUNDING SPONSORING ORGANIZATION Office of Naval Research	8b OFFICE SYMBOL (if applicable) ONT	9 PROCUREMENT INSTRUMENT IDENTIFICATION NUMBER N00228-85-C-3398		
8c ADDRESS (City, State, and ZIP Code) Department of the Navy Washington, D.C. 20361 (Publication funded by Naval Oceanography Command, Bay St. Louis, MS 39529)		10 SOURCE OF FUNDING NUMBERS PROGRAM ELEMENT NO 62435 N OMN-1	TASK NO RM35682	WORK UNIT ACCESSION NO DN656759
11 TITLE (Include Security Classification) Navy Tactical Applications Guide, Volume 6, Part 1 Tropical Weather Analysis and Forecast Applications (Unclassified)				
12 PERSONAL AUTHOR(S) Fett, Robert W., and Walter A. Bohan				
13a TYPE OF REPORT FINAL	13b TIME COVERED FROM 9/13/85 TO 9/12/86	14 DATE OF REPORT (Year, Month, Day) 1986, August	15 PAGE COUNT 182	
16 SUPPLEMENTARY NOTATION See also companion publications TR77-03, TR77-04, TR80-07, TR83-01, TR83-02, TR83-03, and TR85-01, Navy Tactical Applications Guides				
17 COSATI CODES			18 SUBJECT TERMS (Continue on reverse if necessary and identify by block number)	
FIELD 04	GROUP 02	SUB-GROUP	Tropical Meteorology, Weather Satellites, Sunlight Barrier Effects, Fog, Severe Storms, Windflow Patterns, Nocturnal Jets, Squall Lines, Equatorial Trough, Oil Spills	
19 ABSTRACT (Continue on reverse if necessary and identify by block number)				
<p>Weather satellite case studies of synoptic and mesoscale weather effects in the tropics are described in each of the major ocean basins of the world. The material focuses on environmental effects of operational importance to ships at sea and in coastal regions. Each study comes to specific conclusions concerning the nature of the phenomenon and provides suggestions for further application in analysis and short-range forecasts.</p> <p>ADDENDUM. Change in Department Name</p> <p>From: Tactical Applications Department Naval Environmental Prediction Research Facility</p> <p>To: Weather Analysis and Forecast Department Naval Environmental Prediction Research Facility</p>				
20 DISTRIBUTION AVAILABILITY OF ABSTRACT <input checked="" type="checkbox"/> UNCLASSIFIED/UNLIMITED <input type="checkbox"/> SAME AS RPT <input type="checkbox"/> OTIC USERS		21 ABSTRACT SECURITY CLASSIFICATION UNCLASSIFIED		
22a NAME OF RESPONSIBLE INDIVIDUAL Mr. Robert W. Fett, contract monitor		22b TELEPHONE (Include Area Code) (408) 647-4728	22c OFFICE SYMBOL WU 62-9 and OMN-1	

DD FORM 1473, 84 MAR

83 APR edition may be used until exhausted
All other editions are obsolete

UNCLASSIFIED

UNCLASSIFIED

Section 1

Tropical Atlantic Ocean

1A Introduction

Tropical Atlantic Ocean	1A-1
-------------------------------	------

1B Synoptic-scale Case Studies

1 Cloud Pattern Changes in Cold Airflow over Warmer Oceanic Waters	1B-1
Deducing Shifts in Wind Direction from Changes in Cellular Cloud Patterns Subtropical Western North Atlantic Gulf of Mexico February 1979	1B-2
2 Effect of Coastal Ranges and Shallow Offshore Bathymetry on Rainfall Distribution	1B-5
A Tropical Coastal Region of Unusually Heavy Rainfall Nicaragua, Central America August 1976	1B-8

1C Mesoscale Case Studies

1 Deducing Wind Direction and Pressure Distribution from Sea Breeze-Generated Cloud Lines	1C-1
Enhanced Sea Breeze Cloud Line Formation Texas Gulf Coast July 1977	1C-2
2 Mesoscale Nocturnal Jets	1C-5
Mesoscale Nocturnal Jet Florida West Coast February 1977	1C-8
3 The "Enhanced-V" or "White Tornado" Squall Line Cloud Formation	1C-11
Severe Squall Line Development Gulf of Mexico Straits of Florida April 1980	1C-12
4 The "White Tornado" Cloud Pattern	1C-19
Severe Squall Line Development Gulf of Mexico Tampa Bay May 1980	1C-20

Tropical Atlantic Ocean

The tropical Atlantic Ocean is dominated by easterly flow positioned between high-pressure cells in the Northern and Southern Hemisphere. A convergence of northeasterly flow from the Northern Hemisphere with southeasterly flow from the Southern Hemisphere often produces a cloud band which can stretch unbroken from Africa to South America (IA-1a).

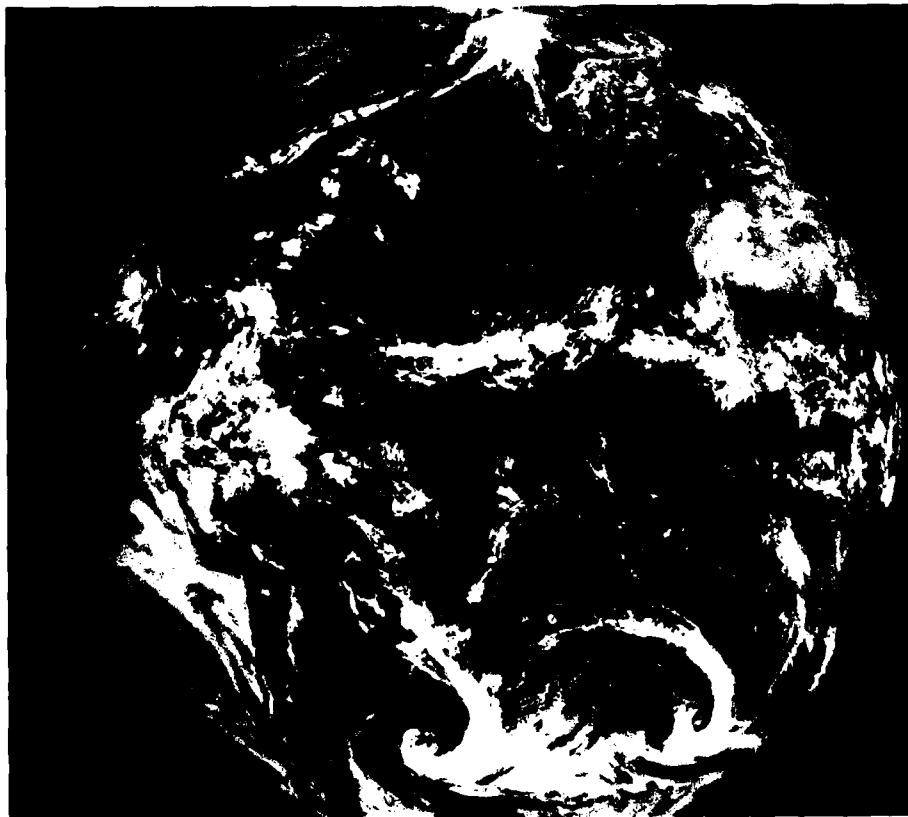
The band tends to lie closer to the equator during winter months and becomes centered near 9° N during the summer.

Perturbations (easterly waves) are observed in this easterly flow moving off Africa just north of the convergence cloud band, which, during summer months and early fall frequently develop to hurricane strength.

Island barrier effects and land and sea breeze effects are clearly evident in satellite imagery from the Canaries and Cape Verde Islands through the islands of the Caribbean.

Continental effects become more evident near North America as cold surges and frontal zones frequently sweep into tropical latitudes during the winter season. Squall lines form and severe weather with tornado activity are not uncommon. The weather satellite offers a unique tool for observing and forecasting the movement of such events.

IA-1a. SMS-1
Visible Image
1330 GMT
19 September 1974



IA-1

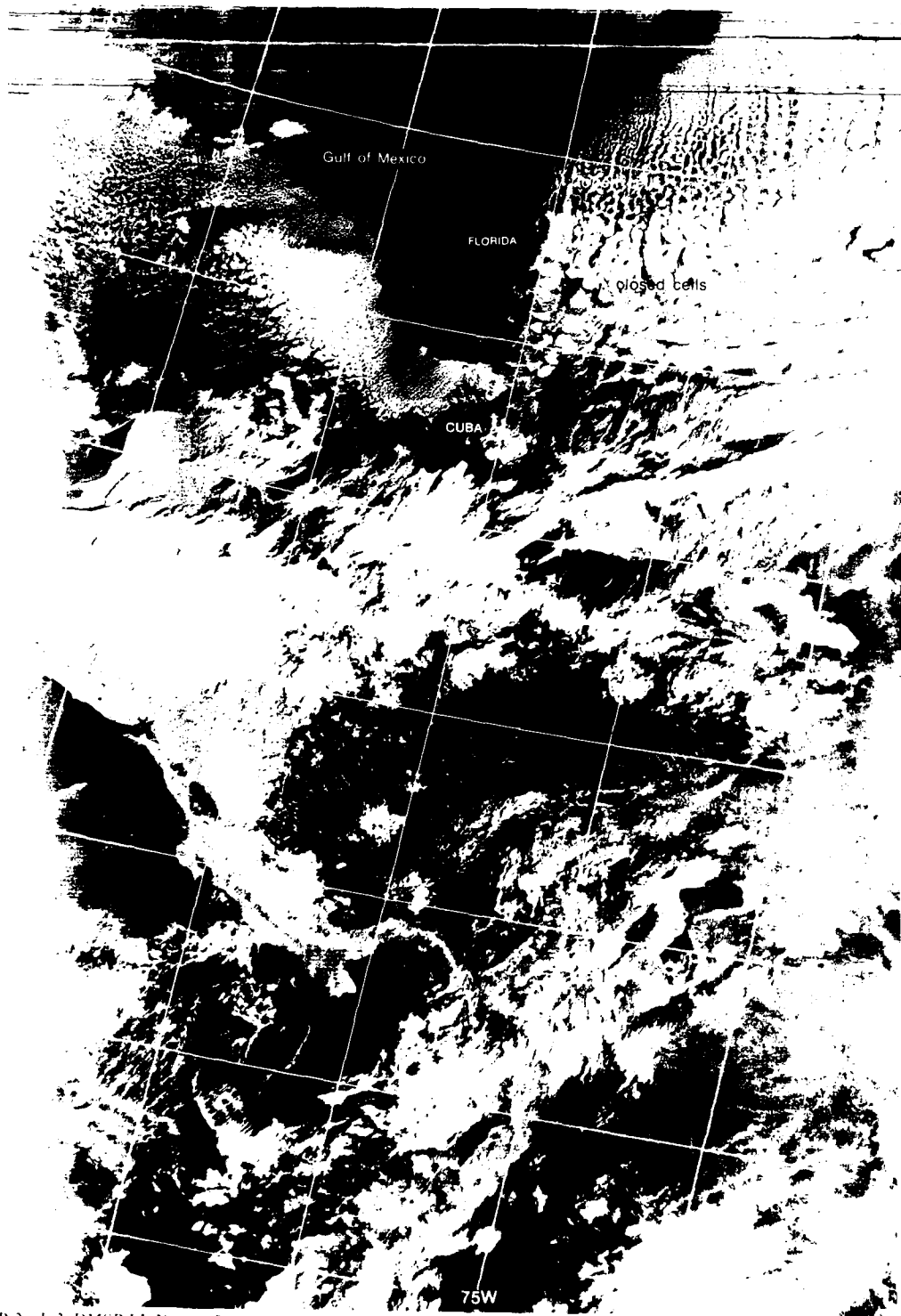
Case 1 Cloud Pattern Changes in Cold Airflow over Warmer Oceanic Waters

During winter months in the Northern Hemisphere cold surges from the eastern and southern shores of continents are frequently observed plunging southward into tropical latitudes. The large air-sea temperature differences under such circumstances lead to strong heat and moisture fluxes from the ocean, and low-level cloud forms develop rapidly in the offshore flow. Lines of cumulus generated under such conditions tend to be aligned with the low-level offshore wind.

As the cold surge advances seaward over the open water, low-level cellular cloud patterns (open cell closed cell) develop which reflect the curvature (vorticity) and changes in the curvature of the flow. Open cellular cloud patterns tend to develop in straight or cyclonically curved flow; closed cellular cloud patterns tend to develop in anticyclonically curved flow (see NTAG, Vol. 2, Sec. 1B).

The beginning of a closed cell cloud pattern on the upwind side is often abrupt, coinciding with a sudden pronounced change in curvature from cyclonic to anticyclonic, indicating a ridge line beyond which the flow continues to turn in an anticyclonic fashion. An abrupt beginning may also occur when the flow changes in a more subtle fashion from slightly cyclonic to slightly anticyclonic. This occurs along or near a line connecting inflection points in the flow.

Termination of the closed cell pattern on the downwind side may be similarly abrupt and coincide with a ridge line where flow transitions very rapidly downstream to cyclonic, or anticyclonic flow suddenly turns to cyclonic, forming a trough at the downwind edge of the cloud cell pattern.



1B-2a 1-2 DMSP LE Normal Enhancement 1331 GMT 10 February 1979

*Deducing Shifts in Wind Direction from Changes in Cellular Cloud Patterns
Subtropical Western North Atlantic Gulf of Mexico
February 1979*

10 February

The DMSP visible image at 1331 GMT (1B-2a) shows the typical cloud line formations associated with a cold surge into tropical latitudes off the U.S. east coast. Cloud formation is inhibited over the cold slope waters adjacent to the coast, but occurs rapidly as the cold surge moves over the warmer waters of the Gulf Stream (see NLAG, Vol. 2, Sec. 3A, Case 1).

Cloud elements within the lines became larger downstream, implying a deepening of the boundary layer and a lifting of the low-level inversion due to turbulent mixing effects produced by the strong flux of heat from the ocean into the air.

There is a very abrupt change in the cellular cloud pattern along a line extending from central Florida to the east-northeast. In this region the open-cellular pattern changes to a closed-cellular pattern. The closed-cellular pattern also terminates rather abruptly along a line nearly parallel to 25° N.

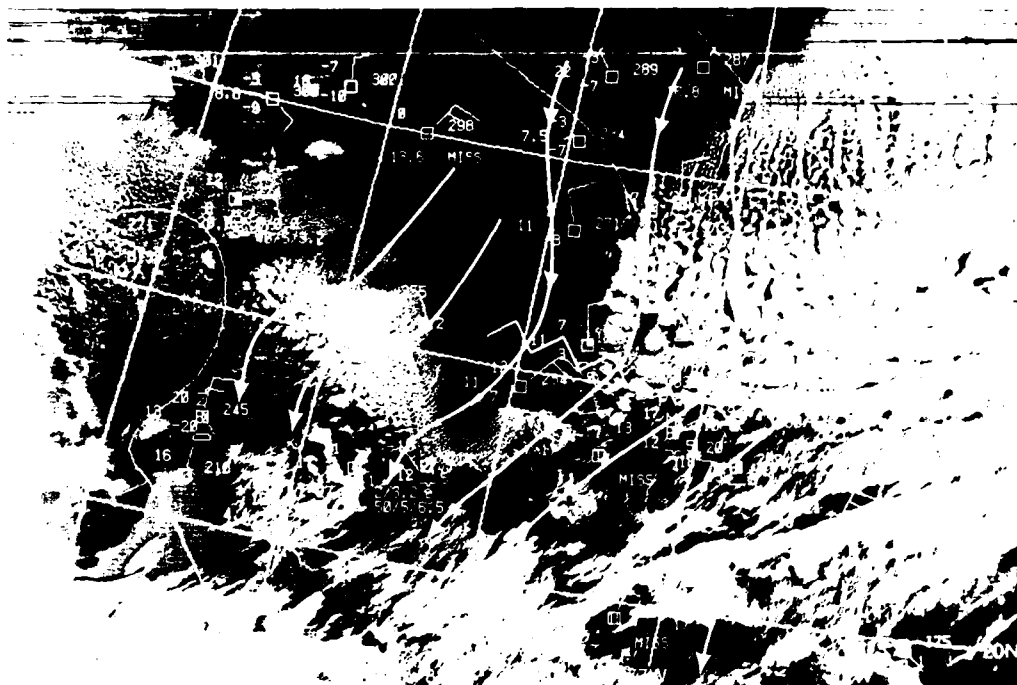
The NMC 850-mb analysis at 1200 GMT (1B-3b), about 1 1/2 hr before the time of the DMSP image, shows the pronounced cold air advection occurring along the east coast from Florida to north of Maine. Winds of 20 kt and higher are blowing perpendicular to isotherms in this region, identifying the synoptic situation as a cold surge event. The NMC surface analysis (1B-3c) shows below-freezing coastal temperatures from Florida to New York and below-zero temperatures northward.

A streamline analysis of surface wind reports, superimposed on the DMSP image (1B-3a), shows that the abrupt change in the cellular cloud pattern from open cells to closed cells east-northeast of central Florida coincides with the line connecting inflection points where the surface flow changes from cyclonic to anticyclonic. On the other hand, the abrupt termination of closed cells near 25° N coincides with a ridge line through that region and a change to more cyclonic flow downstream.

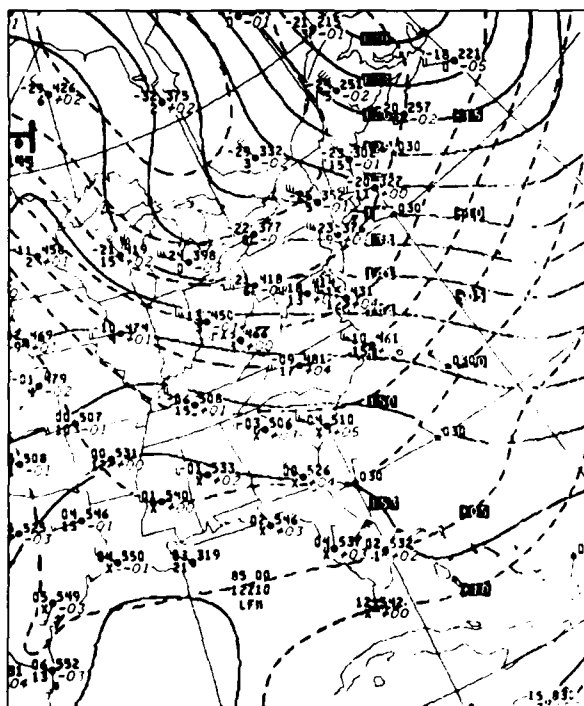
Note the similar, but more subtle effect occurring over the patch of stratocumulus in the Gulf of Mexico west of the southern tip of Florida. In this case, a ridge line is suggested at the upwind edge of the closed cell pattern, and a trough along the downwind edge.

Important Conclusions

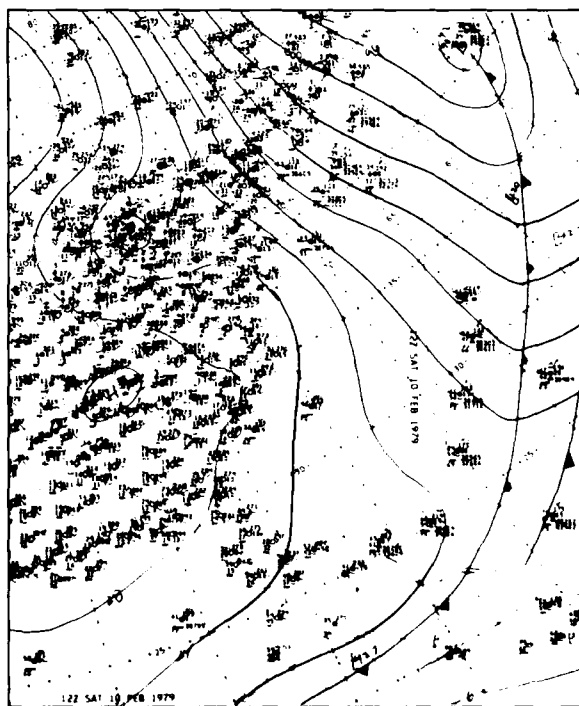
1. An abrupt change in cloud patterns from open-cell to closed-cell in a region of cold air advection over warmer, open oceanic regions indicates a change in the curvature of the flow from cyclonic to anticyclonic.
2. Troughs, ridges, lines, or lines connecting inflection points in the flow often define the upwind and/or downwind edge of the closed cell pattern.



1B-3a. F-2. DMSP LF Normal Enhancement. 1331 GMT 10 February 1979. Surface Wind Reports (1200 GMT) and Streamlines.



1B-3b. NMC 850-mb Analysis. 1200 GMT 10 February 1979.



1B-3c. NMC Surface Analysis. 1200 GMT 10 February 1979.

*Case 2 Effect of Coastal Ranges and Shallow
Offshore Bathymetry on Rainfall
Distribution*

Unusually heavy rainfall can be expected in tropical coastal regions under the following conditions: (1) a coast with a nearby mountain range that is exposed to a persistent trade wind regime, and (2) a broad, shallow sea area located offshore. One such area of heavy rainfall is located along the tropical Atlantic coast of Nicaragua, in Central America.

The Miskito Bank

The Miskito Bank (1B-7a) is a shallow water area with typical depths of only 30 m extending to well over 200 km offshore (Murray *et al.*, 1982). The absence of a continental slope can be seen in the more detailed map of the offshore bathymetry (1B-7b), which shows depths dropping off abruptly to several hundred meters. A profile across the West Florida Shelf, considered to be extremely low sloping by North American standards, is presented for comparison. The Miskito Bank is located in a region of persistent northeasterly trade winds.

The rainfall rate along contiguous Miskito Bank coastal watersheds is one of the highest in the world, exceeding 6 m (nearly 20 ft) per year along the southern end of the bank. In the Rio Escondido Basin (1B-7b), terminating at El Bluff, the rainfall rate (1B-7c) shows a maximum of 4.5 m year⁻¹ at the coast, dropping off linearly to 2 m year⁻¹ at the head of the basin, 250 km inland (United Nations, 1968).

Note that the coastal plain (1B-7c) extends 3-5 times further inland in the northern and central parts of the coast than at the southern end in Nicaragua. Long-term wind data indicate that the general large-scale direction of the trade wind does not change appreciably between Puerto Cabezas and El Bluff, although the wind speed is higher at Puerto Cabezas. Nevertheless, annual rainfall at the Nicaragua-Costa Rica border is more than twice that at the Nicaragua-Honduras border (Portig, 1965 and 1972). The blocking effect of the mountainous topography near the coast in the southern region is believed to be the dominating cause for the increased precipitation at that location.

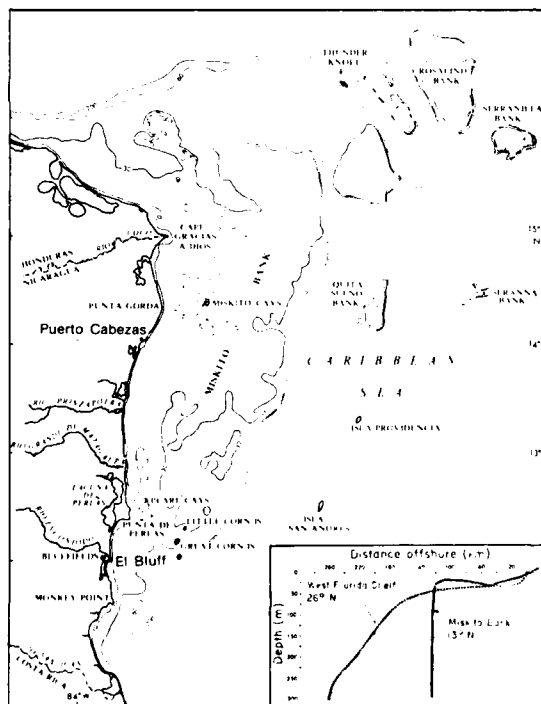
Another important cause for this unusually heavy rainfall is the atmospheric convective activity caused by intensive air-sea interaction on the broad and shallow coastal shelf. Regional rainfall data in Central America indicate that a similar, albeit much smaller, focus on unexplained intense rainfall off Colon, Panama (e.g., Portig, 1972), is also associated with a shallow bank offshore.

References

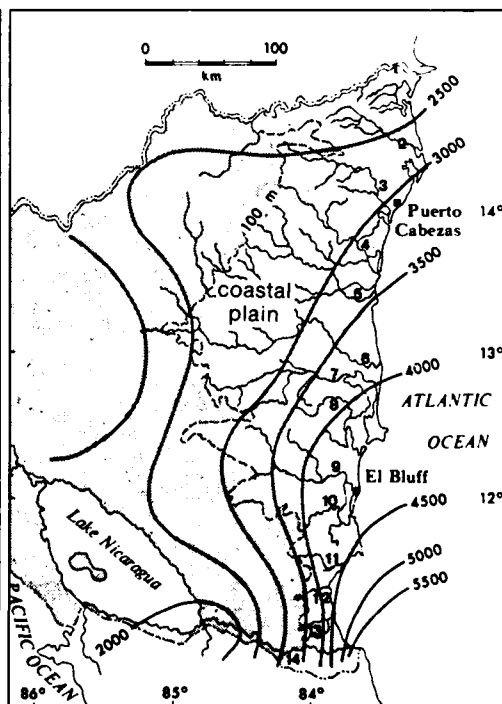
- Murray, S. P., A. Hsu, H. H. Roberts, E. H. Owens, and R. L. Crout, 1982: Physical processes and sedimentation on a broad, shallow bank. *Estuarine, Coastal and Shelf Science*, **14**, 135-157.
- Portig, W. H., 1965: Central American Rainfall. *Geographical Review*, **55**, 68-90.
- Portig, W. H., 1972: The climate of Central America. In *World Survey of Climatology*, Vol. 12, Elsevier, Amsterdam, pp. 405-478.
- United Nations, 1968: Atlantic port and highway study - Republic of Nicaragua. Vol. 7, Hydrographic Appendix. U.N. Development Programme Special Fund and International Bank for Reconstruction and Development.



1B-7a. Location Map of Miskito Bank.



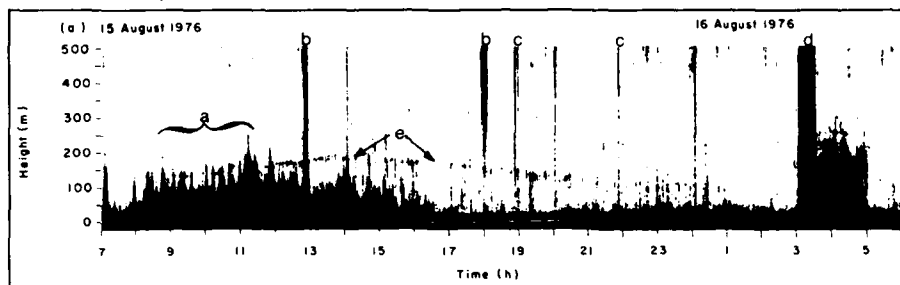
1B-7b. Schematic drawing of Miskito Bank off the east coast of Nicaragua. Inset: Comparative bathymetric cross-sections of the Miskito Bank and West Florida Shelf. (After Murray, *et al.*, 1982.)



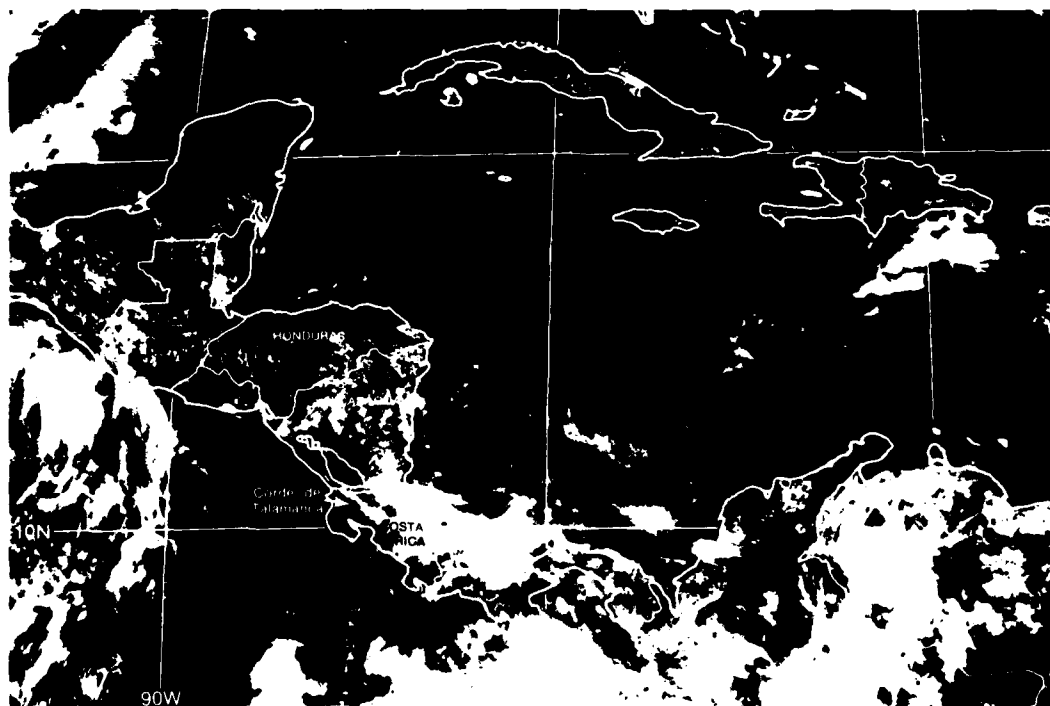
1B-7c. General Topography, major rivers used in sediment and water discharge calculations and annual rainfall (mm) for eastern Nicaragua. (After Murray, *et al.*, 1982.)

15-16 August 1976

- a - fair weather plumes
- b - rain showers
- c - spurious noise
- d - weak disturbances
- e - inversion layer



1B-8a. Acoustic soundings of the atmospheric boundary layer, El Bluff, Nicaragua.



1B-8b. GOES-E. Visible Image. 1700 GMT 15 August 1976.

*A Tropical Coastal Region of Unusually Heavy Rainfall
Nicaragua, Central America
August 1976*

15-16 August, Fair Weather Conditions

Acoustic radar (upward-looking) sounding data (1B-8a) acquired at El Bluff, Nicaragua (Hsu, 1978), show conditions typical of fair weather convective activity.

Reflections from temperature gradients and temperature discontinuities in the lower atmosphere are recorded as dark traces in the same manner as conventional echo sounder charts of the sea floor.

Fair-weather conditions are indicated by the "spiky" dark traces, i.e., the thermal roots of convective plumes, extending from the surface to various heights, depending upon how much warmer the sea surface is than the overlying air. An example of fair weather events is shown from approximately 0700 LST 15 August to 0300 LST 16 August.

During the night the shallow bank water cools faster than the deeper ocean because it has less capacity for heat storage. Typically, as night approaches, the plumes become smaller and weaker, both in dimension and intensity, as shown after 1700 LST 15 August.

In the GOES visible image at 1700 GMT (1100 LST) 15 August (1B-8b), local convective activity appears along the Nicaraguan coast, as suggested by the fair weather root convection depicted on this date by the acoustical sounder data. Note, however, that more intense convective activity is present over Costa Rica where moist, trade wind air is advected upward against the Cordillera de Talamanca (see also 1B-7a). An earlier DMSP view at 1229 GMT (0629 LST; 1B-9b) shows that the convection in this region was quite intense, although the coast of Nicaragua shows only widely scattered convective activity in this early morning view.

The FNOG surface analysis for 1800 GMT (1B-9a) shows a portion of the equatorial trough over Panama and northern South America, with 15 kt easterly trade winds blowing onshore into Nicaragua.

The GOES visible image at 1700 GMT (1100 LST) on 16 August (1B-10a), reveals wide-spread intense convection over the mountains of Costa Rica and southern Nicaragua. Scattered low-level convective activity continues to predominate over northern Nicaragua.

The large amount of cirrus covering the area is not apparent in the GOES visible image but is clearly depicted in the simultaneous infrared image (1B-10b). Note in particular the band of cirrus cloudiness over Guatemala and the Yucatan Peninsula, which is almost undetectable in the visible image (1B-10a). Such cirrus, when advected over a continental region, acts to impede the development of low-level convective activity.

DMSP visible image at 1216 GMT (1B-11a), a few hours earlier, shows that heavy convection over Costa Rica and southern Nicaragua was present earlier in the

day. This indicates that diurnal surface heating and strong upslope motion have combined to produce the intense convective activity observed.

The FNOG surface analysis for 1800 GMT 16 August (1B-11b) shows continued easterly trade wind flow into the Nicaragua region.

21-22 August, Disturbed Conditions

The GOES visible image at 1700 GMT (1100 LST) 21 August (1B-12b) reveals heavy convective cloudiness extending north to El Bluff. This relates well with the acoustic sounder data (1B-12a) showing shower activity associated with a weak disturbance passage from about 1300 to about 1800 LST on 21 August. The DMSP visible image at 1258 GMT (0658 LST; 1B-13a), shows an area of heavy convective activity approaching El Bluff while Puerto Cabezas is relatively in the clear.

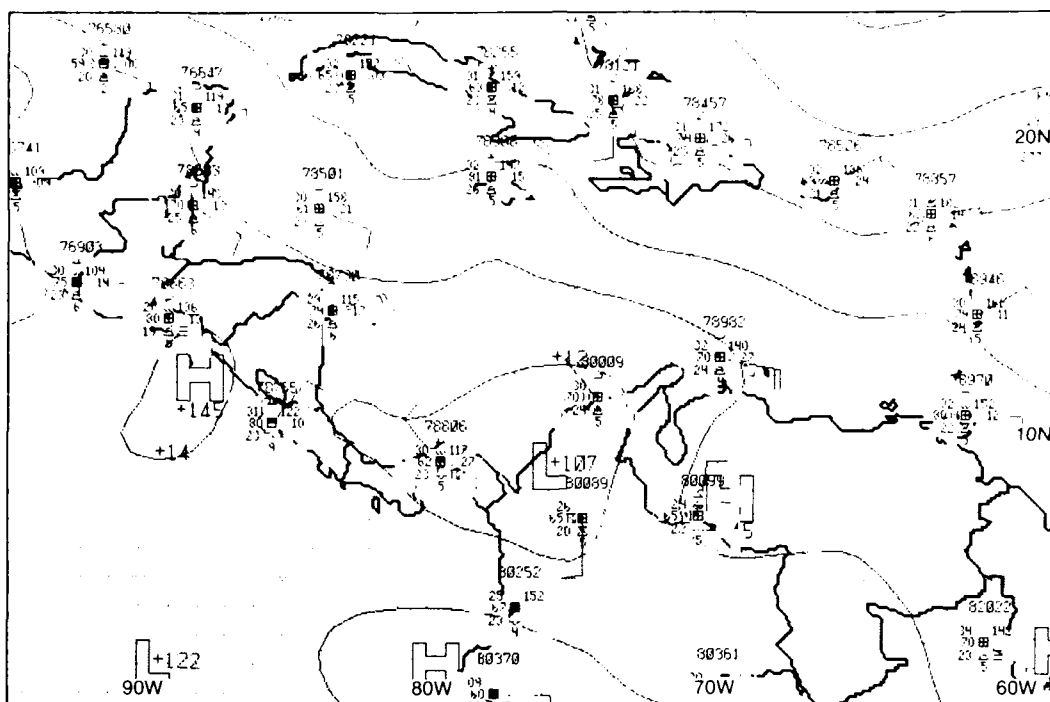
The FNOG surface analysis for 1800 GMT (1200 LST; 1B-13b) shows an extension of the equatorial trough low over Central America, bringing disturbed easterly trade wind flow into Nicaragua.

The tendency for heavy showers over El Bluff and Costa Rica while Puerto Cabezas remains relatively unaffected is evident in the GOES visible image on 22 August (1B-13c), which again shows large convective cells restricted to the southern region.

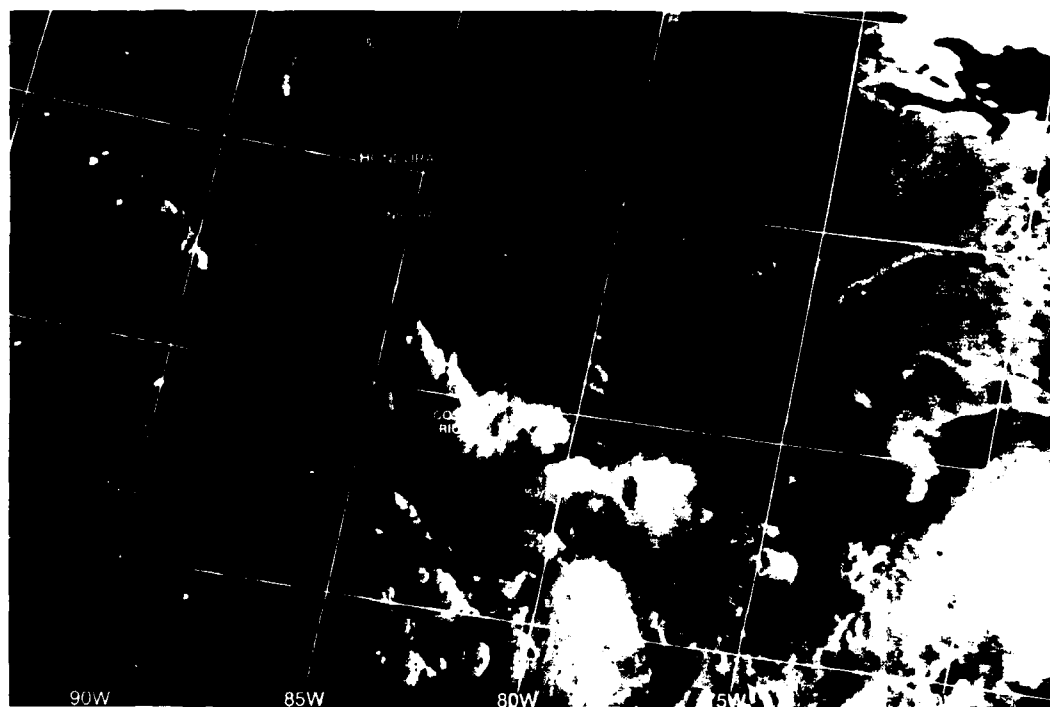
FNOG surface data for 1800 GMT (1B-13d) reveals a weakening of the equatorial trough low over Panama; however easterly trade flow continues across Nicaragua.

Important Conclusions

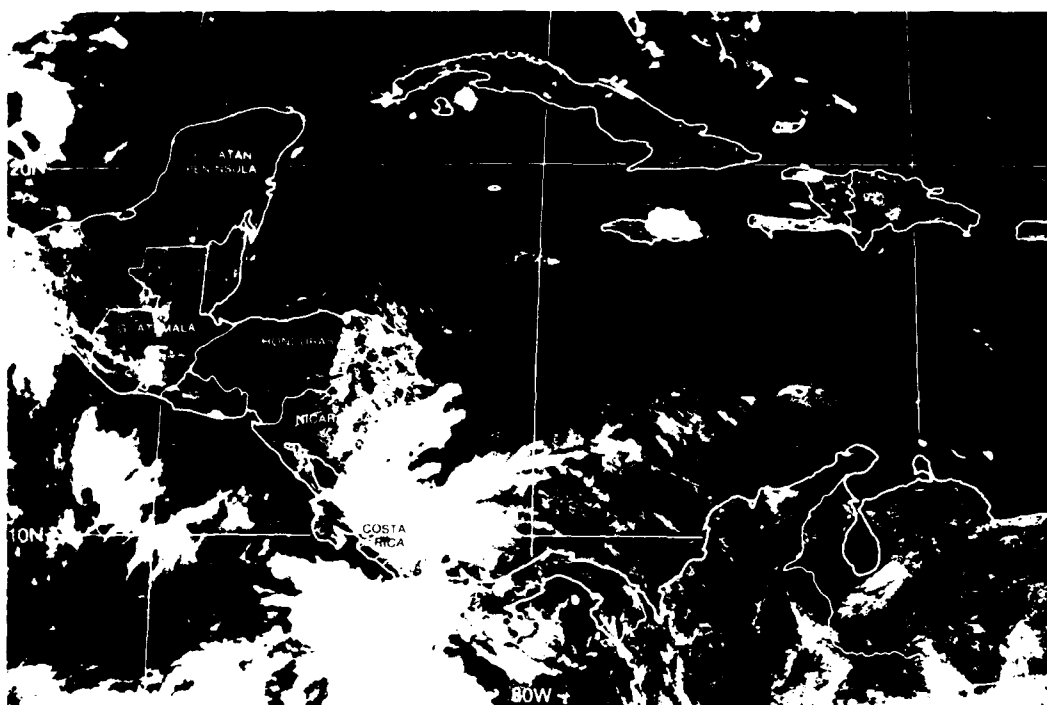
1. The exceedingly high rainfall along the coast bordering the southern half of the Miskito Bank is due to the enhanced convective activity produced in the warm, moist, easterly trade flow. The atmospheric boundary layer of the trades is rendered unstable by its transit across the elevated temperatures of the shallow bank waters, and the subsequent lifting of the unstable air along the mountainous terrain, which is much closer to the coast in the southern half of the Miskito Bank region. This results in deep convection and heavy rainfall.
2. Similar local effects can be anticipated in other coastal mountain regions having prevailing onshore flow crossing shallow coastal banks in tropical latitudes.
3. Satellite data are useful in determining preferential regions for convective development.



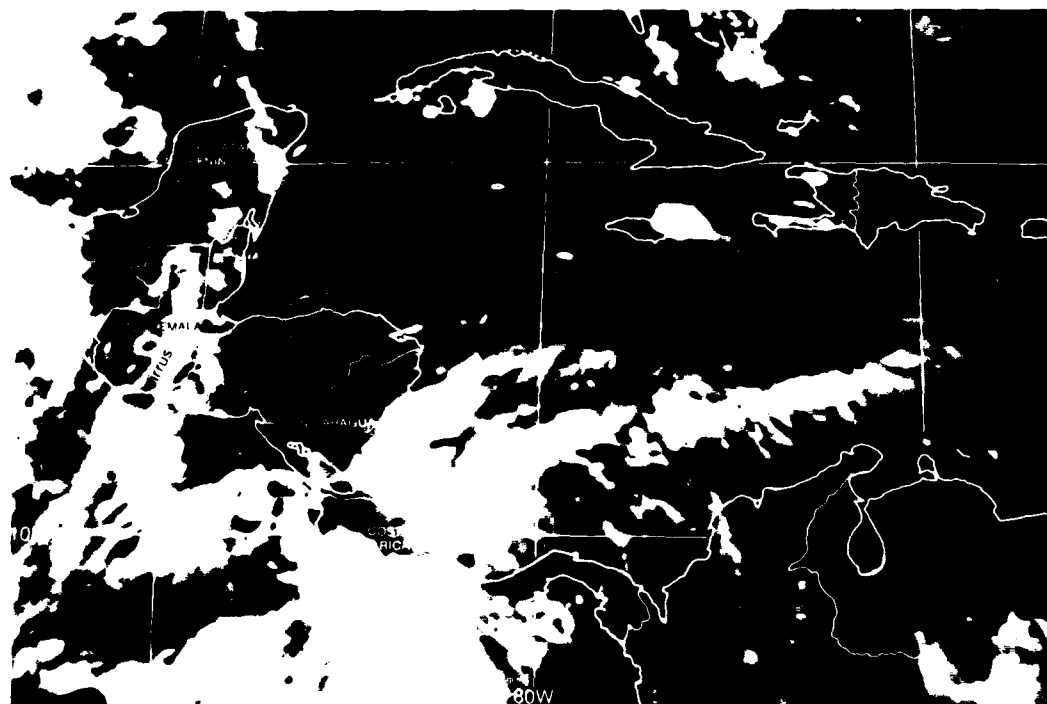
1B-9a. ENOP Surface Analysis. 1800 GMT 15 August 1976.



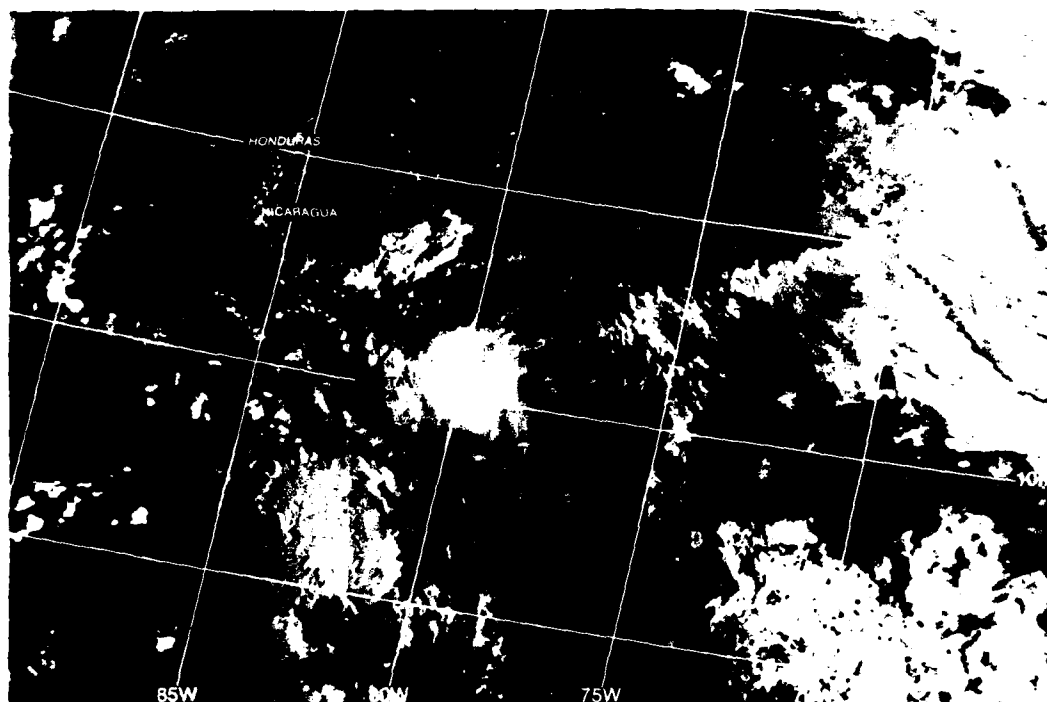
1B-9b. FTV-33. DMSP I.S. Low Enhancement 1229 GMT 15 August 1976.



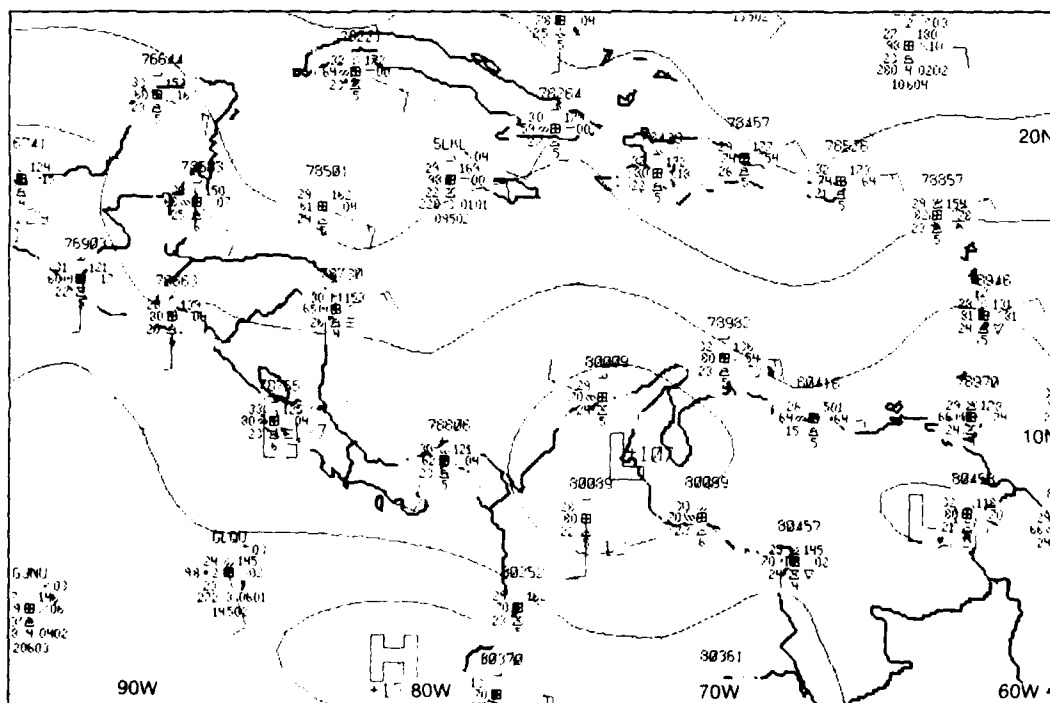
1B-10a. GOES-1. Visible Image. 1700 GMT 16 August 1976.



1B-10b. GOES-1. Infrared Image. 1700 GMT 16 August 1976.



1B-11a F1V-33 DMSP 1.5 Low Enhancement, 1216 GMT 16 August 1976.

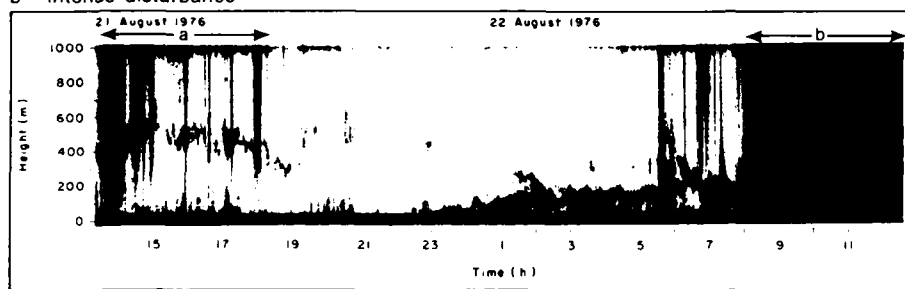


1B-11b ENOC Surface Analysis 1800 GMT 16 August 1976

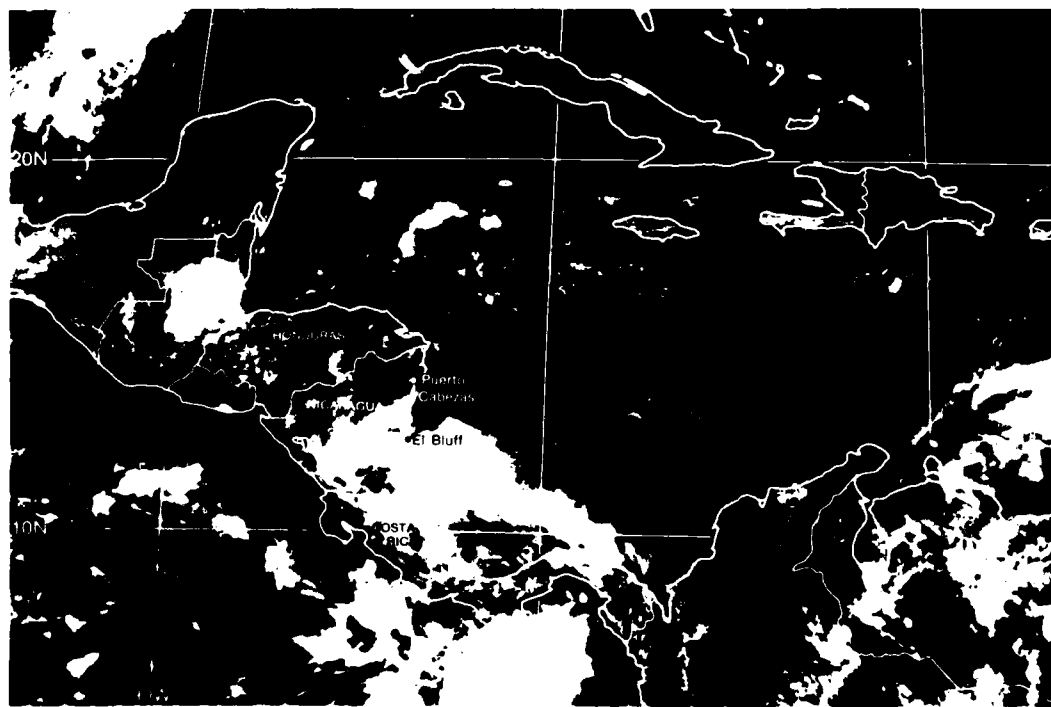
21-22 August 1976

a - weak disturbance

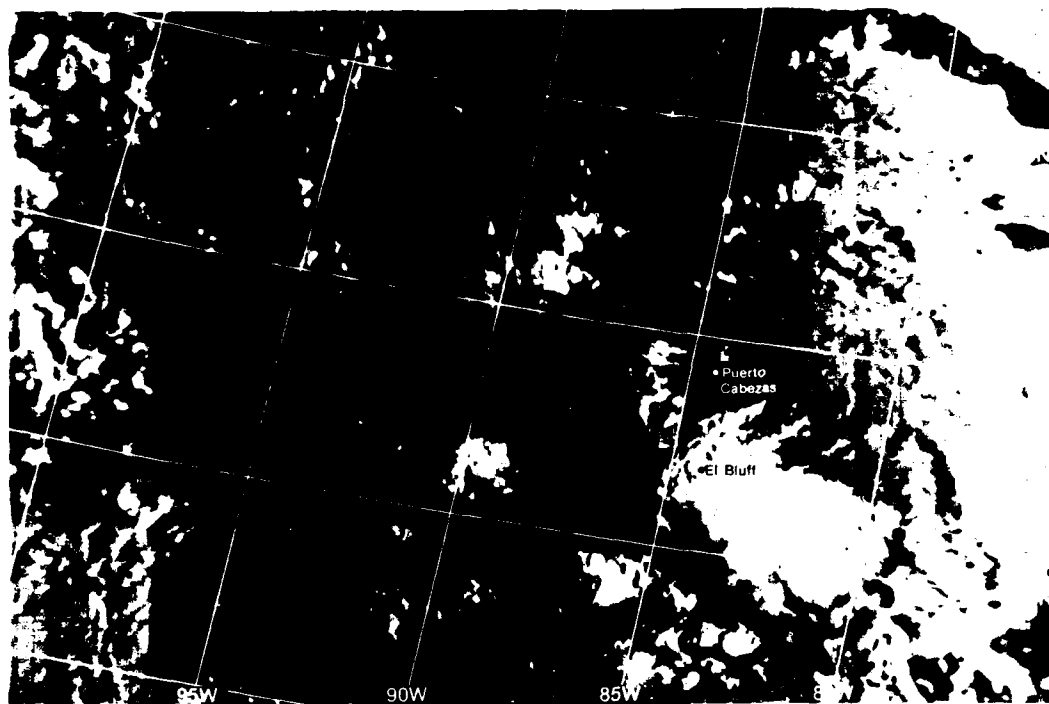
b - intense disturbance



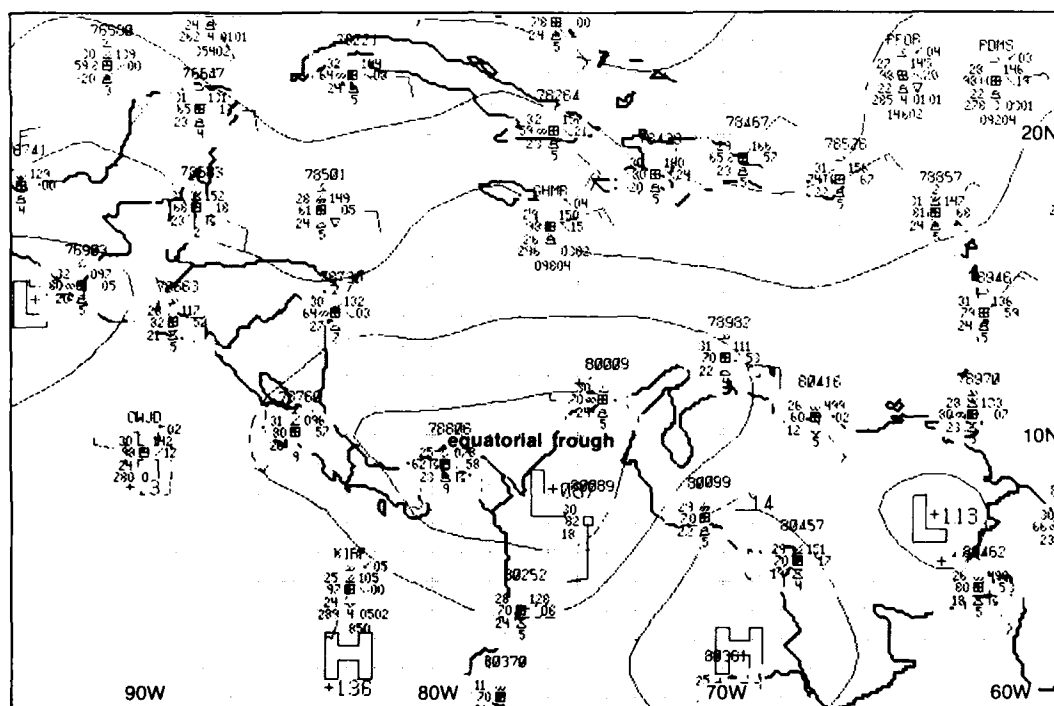
1B-12a. Acoustic soundings of the atmospheric boundary layer, El Bluff, Nicaragua.



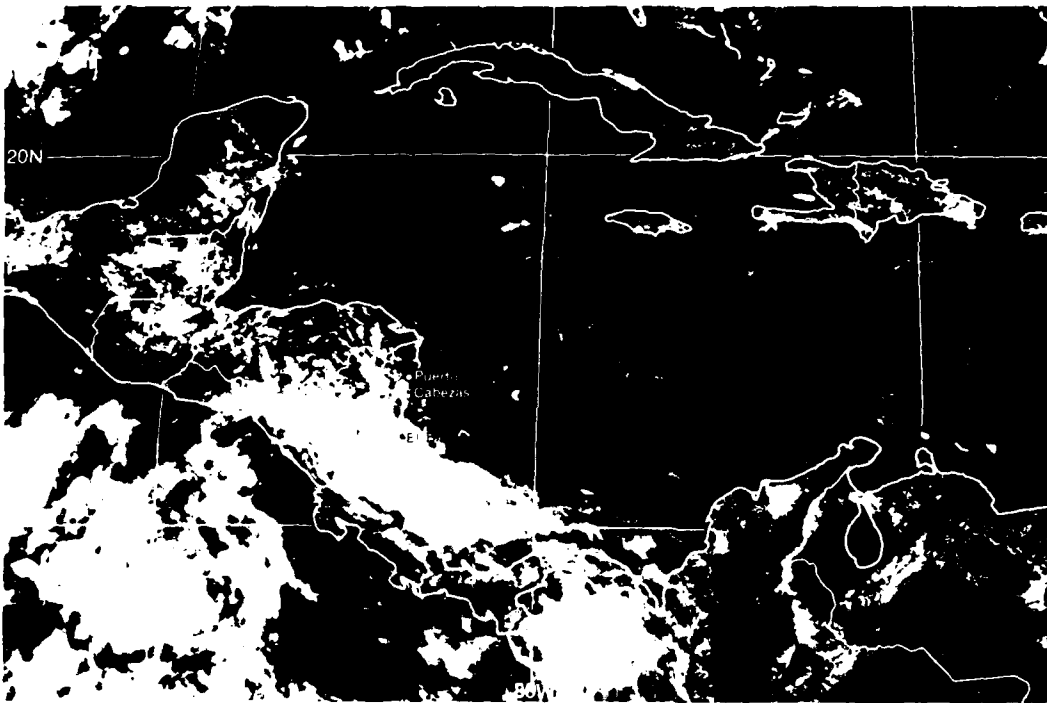
1B-12b GOES-F Visible Image. 1700 GMT 21 August 1976.



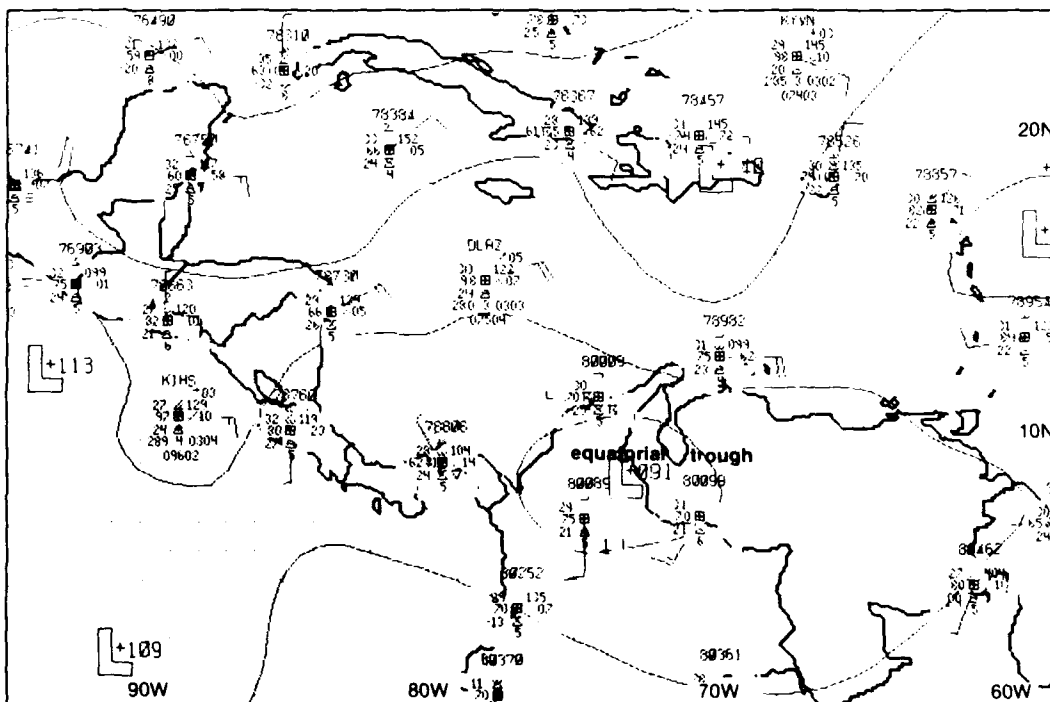
1B-13a FTV-33 DMSP L5 Low Enhancement. 1258 GMT 21 August 1976.



1B-13b FNOC Surface Analysis. 1800 GMT 21 August 1976.



1B-13c GOES-E Visible Image 1700 GMT 22 August 1976

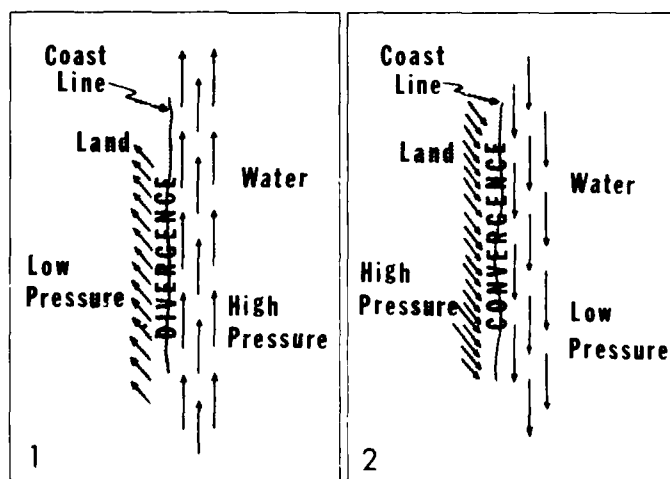


1B-13d FNOG Surface Analysis 1800 GMT 22 August 1976

Case 1 *Deducing Wind Direction and Pressure Distribution from Sea Breeze-Generated Cloud Lines*

In synoptic flow parallel to the coast of a land mass, wind speed will be strongest over the water and slowed by friction over land. In southerly flow parallel to a coastline (Northern Hemisphere), with high pressure to the east (over water) and low pressure to the west (over land), the reduced wind speed over the land will cause winds to be deflected toward the lower pressure (IC-1a-1). This will result in a local coastal divergence zone unfavorable for sea breeze cloud line development (Anderson *et al.*, 1966). With northerly flow parallel to the coastline and low pressure to the east and high pressure to the west, the slowed winds over the land are deflected toward low pressure, resulting in a coastal convergence zone favorable for enhanced sea breeze cloud line formation (IC-1a-2).

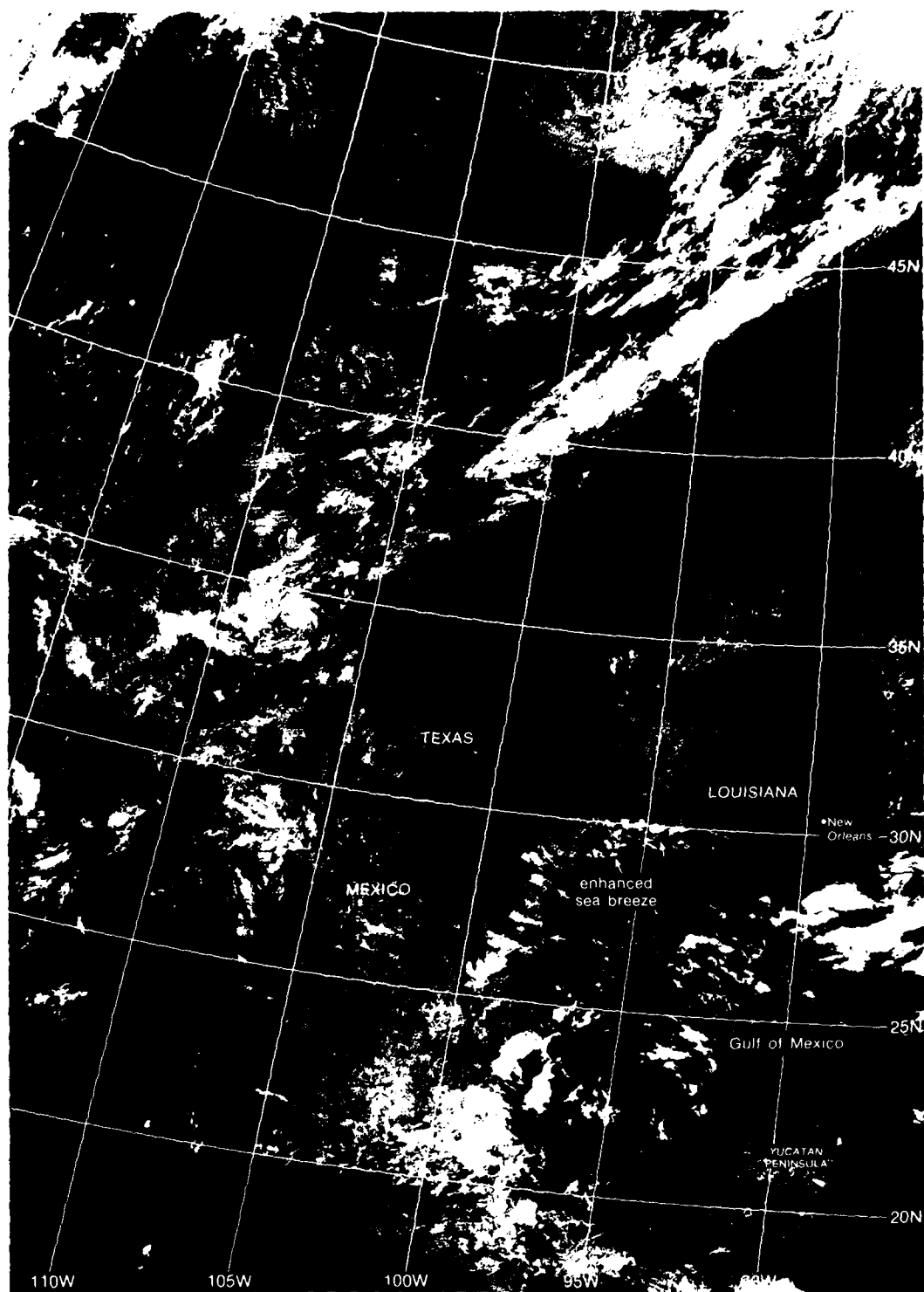
Satellite data can be utilized to detect enhanced sea breeze cloud line development and, according to the above discussion, wind direction and pressure distribution can be inferred.



IC-1a Schematic illustrating the effects of friction on low-level wind flow

Reference

Anderson, R. K., E. W. Ferguson, and V. J. Oliver. 1966. The Use of Satellite Pictures in Weather Analysis and Forecasting. World Meteorological Organization, Tech. Note No. 75, WMO-No. 190, TP 96, Secretariat of the WMO, Geneva Switzerland, pp. 166.



IC-2a F-1, DMSP LE Low Enhancement, 1747 GMT 14 July 1977.

*Enhanced Sea Breeze Cloud Line Formation
Texas Gulf Coast
July 1977*

14 July

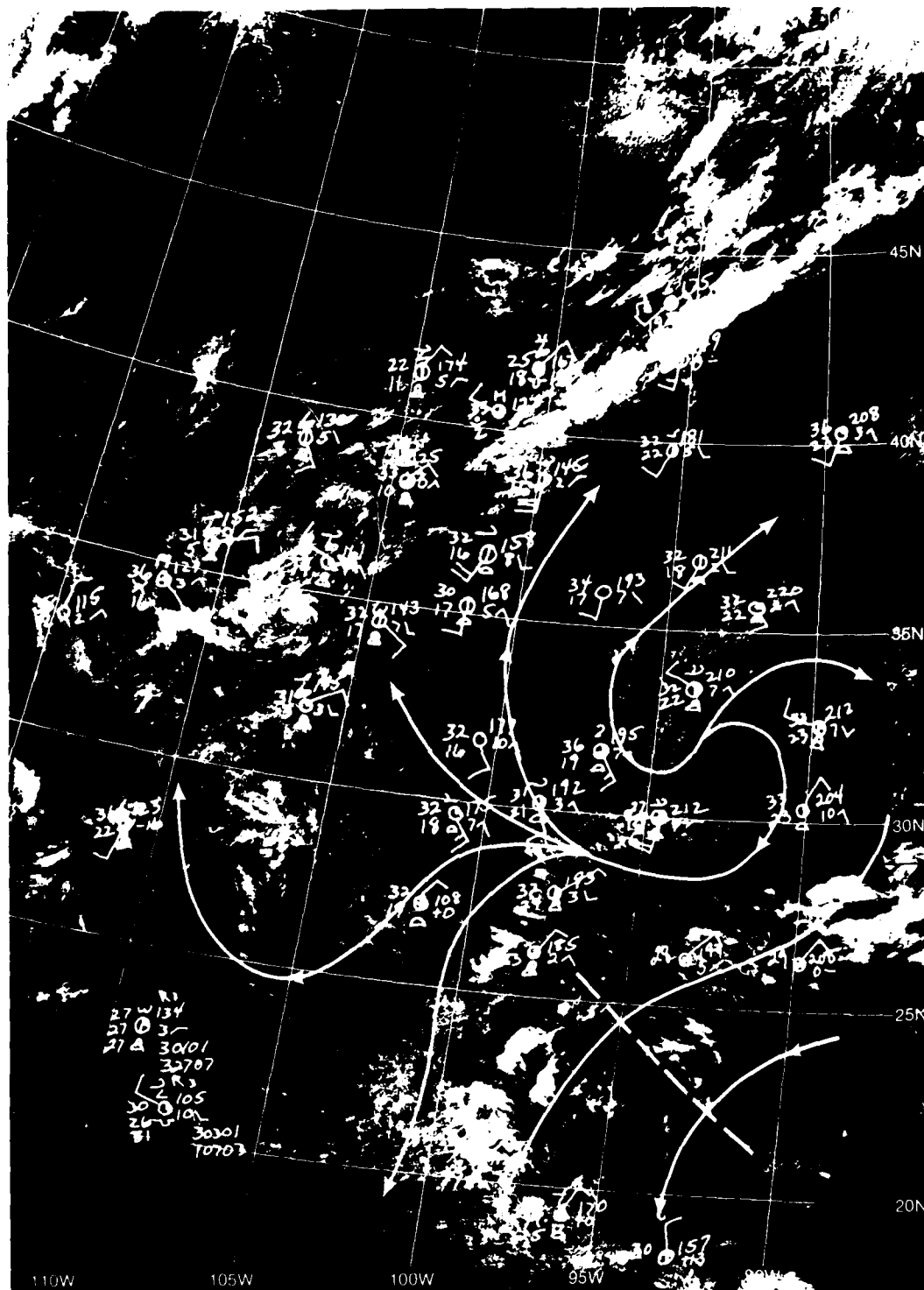
The mid-morning DMSP visible image at 1756 GMT (1156 LST, IC-2a) reveals an enhanced sea breeze cloud line stretching from western Louisiana southward along the Texas coast and along the east coast of Mexico.

Based on the concepts illustrated in the introduction (IC-1a) and the absence of surface reports, one would anticipate easterly flow over the water south of Louisiana, turning to northerly or northeasterly flow along the coast of Texas and Mexico. This would imply lower pressure over the gulf and higher pressure inland over Louisiana, Texas and Mexico.

The streamline analysis based on available surface reports, superimposed on the DMSP image (IC-3a), confirm the inferred flow pattern and pressure distribution. An anticyclonic center is located inland over Louisiana, and winds are turning anticyclonically over southern Texas and central Mexico. A low pressure trough is also analyzed over the western Gulf of Mexico.

Note that an enhanced convection sea breeze cloud line does not appear over the New Orleans region or over the northern coastline of the Yucatan Peninsula where wind flow is less favorable for enhanced coastline convergence.

IC 2 B



IC-3a. F-I DMSP LE Low Enhancement. 1747 GMT 14 July 1977. Surface Wind Reports (1800 GMT) and Streamlines.

Case 2 *Mesoscale Nocturnal Jets*

Along coastal land areas which are relatively flat, cool oceanic air brought in behind a sea breeze front may be subjected to further nighttime radiational cooling and form a distinct low-level cool pool, or mesohigh (Hsu, 1979). At the top of the mesohigh is a microscale inversion layer below which the winds are nearly calm. When there is a mesoscale inversion layer present at higher levels at the same time, conditions are favorable for the formation of a low-level mesoscale jet. The jet usually appears between 100 and 600 m (between the inversion layers) and extends from about 40–50 km onshore to a few kilometers offshore. It is most likely to occur when the prevailing geostrophic wind is less than 10–12 kt ($5\text{--}6\text{ m sec}^{-1}$) and blows from land to sea; the wind shear within the planetary boundary layer is less than 80° ; and air temperatures over nearby waters are at least 9°F (5°C) warmer than over land.

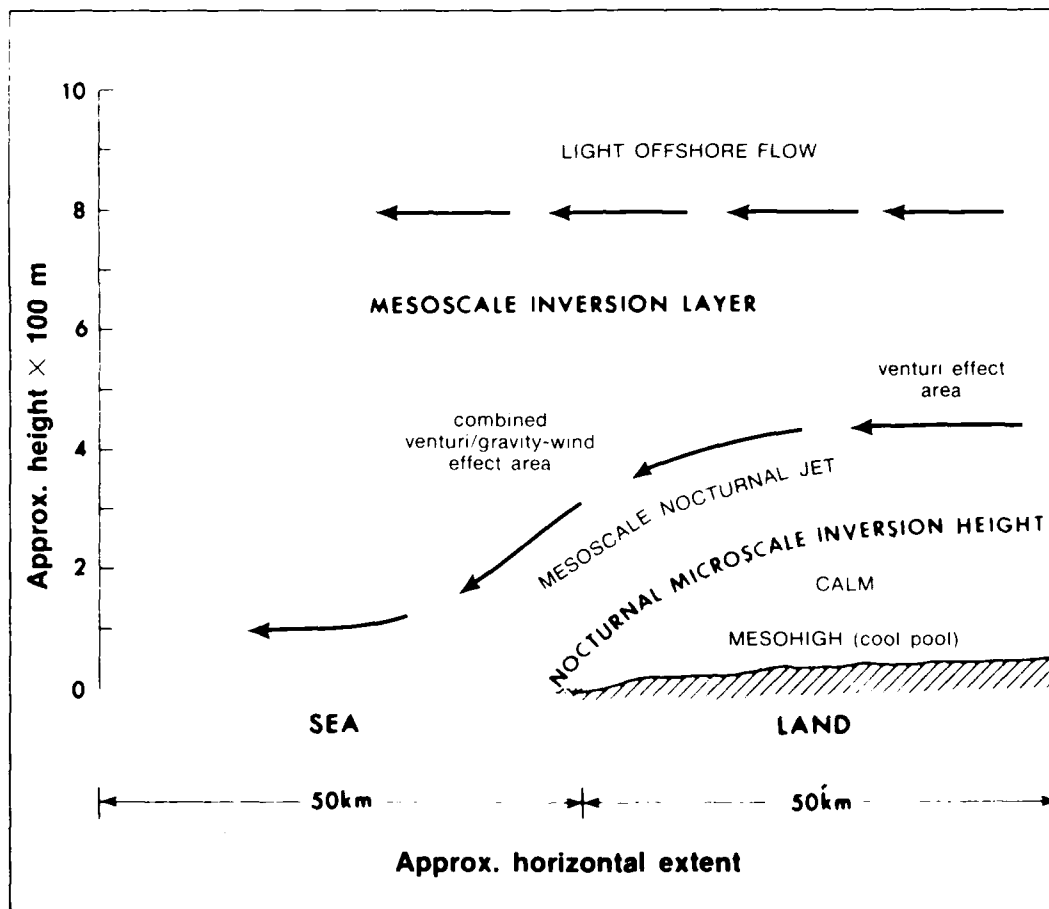
Reference

Hsu, S. A., 1979: Mesoscale nocturnal jetlike winds within the planetary boundary layer over a flat open coast. *Boundary Layer Meteorology*, **17**, 485–494.

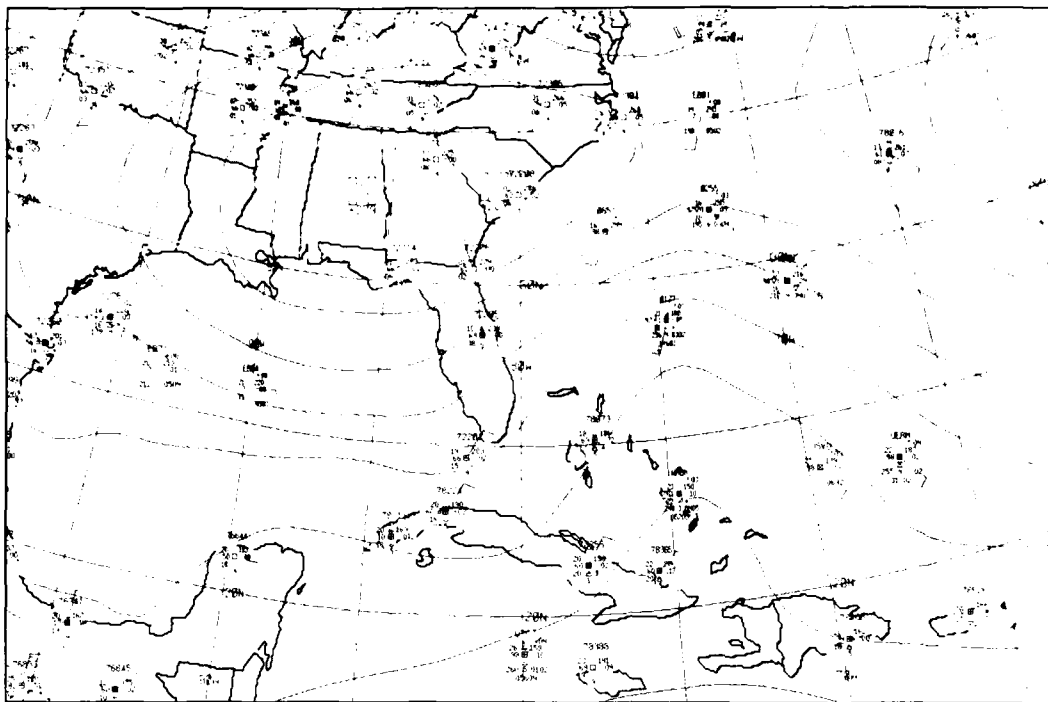
Coastal Mesoscale Nocturnal Jet Formation

The mechanism of formation of a coastal mesoscale jet system is a combination of Venturi and gravity wind effects (IC-6a). Venturi speedup of the air occurs first in the flow between the nocturnal microscale inversion over the mesohigh (cold pool) and the higher-level mesoscale inversion. This is followed by a further increase in wind speed as the air flows down the microscale inversion (gravity effect). As the air travels down the slope of the nocturnal microscale inversion, it is also accelerated by a land to sea pressure gradient due to lower pressure over the warmer water surface, which causes the higher offshore wind speeds observed in mesoscale nocturnal jets.

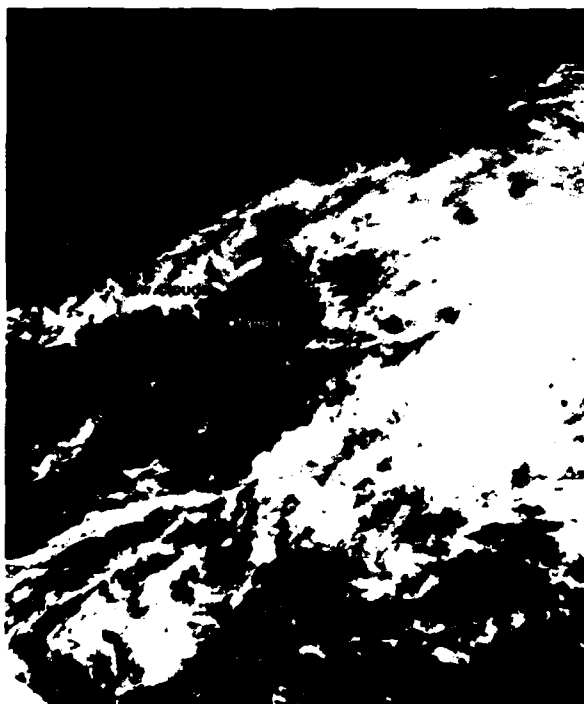
In February 1977, upper-air soundings were obtained on the west coast of Florida at Tarpon Springs, in an effort to detect a mesoscale nocturnal jet. The precursor conditions for jet formation were satisfied during two periods: 7-10 and 14 February (IC-7a). On these days, high pressure prevailed over the area, with light winds blowing from land to sea. Jetlike winds were observed during the night and early morning. Evidence of a diminished jet during the daytime is indicated by the soundings.



IC-6a. Coastal Mesoscale Nocturnal Jet



IC-8a. FNOG Surface Analysis. 0600 GMT 10 February 1977.



IC-8b. GOES-F. Visible Image. 1700 GMT 9 February 1977.



IC-8c. GOES-F. Infrared Image. 1700 GMT 9 February 1977

*Mesoscale Nocturnal Jet
Florida West Coast
February 1977*

9-10 February

The GOES visible image at 1700 GMT (1200 LST) 9 February (1C-8b) shows clear skies over central Florida and broken, lower-level cloudiness over the Tampa area. It is apparent in the corresponding GOES infrared image (1C-8c) that, off the west coast of Florida, gulf water temperatures in cloud-free areas are cooler (medium tones) than land temperatures (dark tones) over Florida in this midday pass. The narrow, light-tone band extending offshore (west of Tampa) is a layer of low clouds obscuring the coastal waters in this area. Mean offshore temperatures in the gulf adjacent to the west coast of Florida for February 1977 were about 68° F (Gulfstream, 1977) while daytime temperatures at Tampa reached as high as 74° F.

The FNOG surface analysis for 0600 GMT (0100 LST; 1C-8a) shows a cell of high pressure over the southeastern U.S. causing light offshore flow over the west coast of Florida. Hourly observations (not shown) at Tampa, at 0055 LST, indicate that the skies have cleared, with visibility 10 miles, temperature 48° F, dew point 36° F, and northeasterly winds from 040° at 10 kt.

A low-level jet was observed at Tarpon Springs, about 25 mi northwest of Tampa (1C-7a), at 0020 LST 9 February (0620 GMT 10 February). The local land-water temperature difference had reversed by this time. The land air temperature had dropped to 48° F - a full 20 deg colder than the adjacent coastal water region. This provided ideal conditions for the development of the mesoscale nocturnal jet. The GOES infrared image at this time (1C-9b) show land temperatures as cold as the adjacent sea, and reveals that the heavy cloud cover (bright tones; 1C-8c) over northern Florida has dissipated by the time of occurrence of the nocturnal mesoscale jet.

The regular Tampa radiosonde for 0000 GMT (1900 LST; 1C-9a), about 5 hours prior to the high resolution sounding (1C-7a), is of interest in that (1) no evidence of a low-level jet could be deduced from the sounding, even if it had been present at this earlier hour, due to poor vertical resolution of normal RAOBS in the boundary layer; and (2) verification of the mesoscale inversion (1C-7a) suggested near 1,400 m is confirmed by the sharp inversion shown at the 850-mb level (1,544 m; 1C-9a).

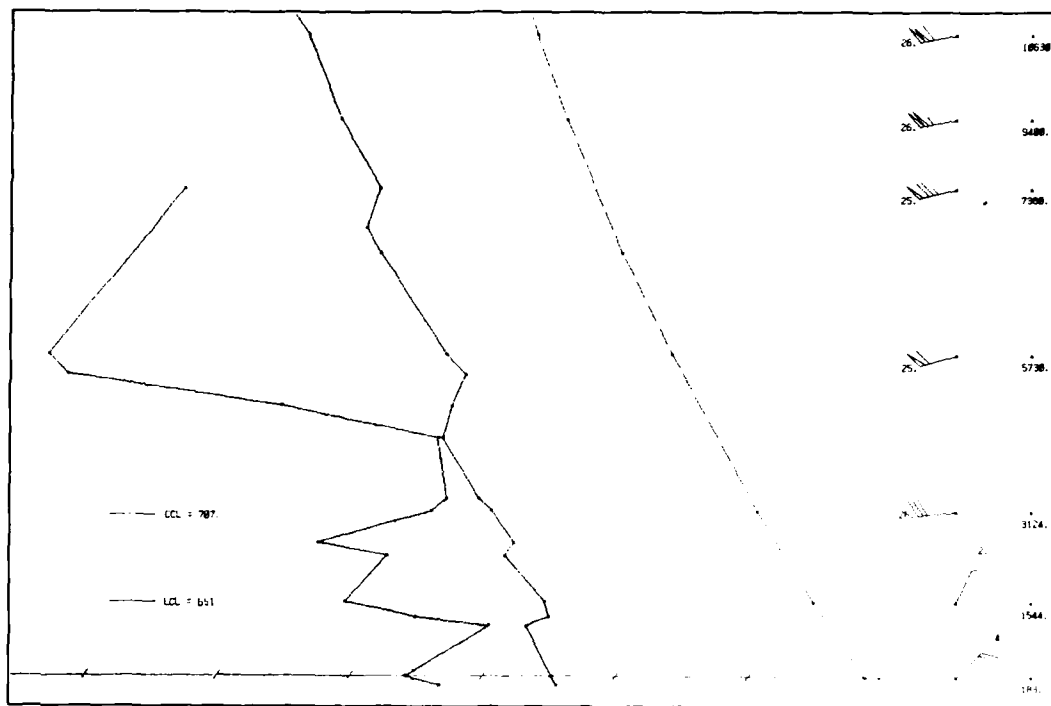
The GOES visible image at 1700 GMT (1200 LST; 1C-9c) provides additional evidence that cloud cover had dissipated over the Tarpon Springs-Tampa area during the previous night, confirming the 0100 LST 9 February Tampa observation of clear skies.

Important Conclusions

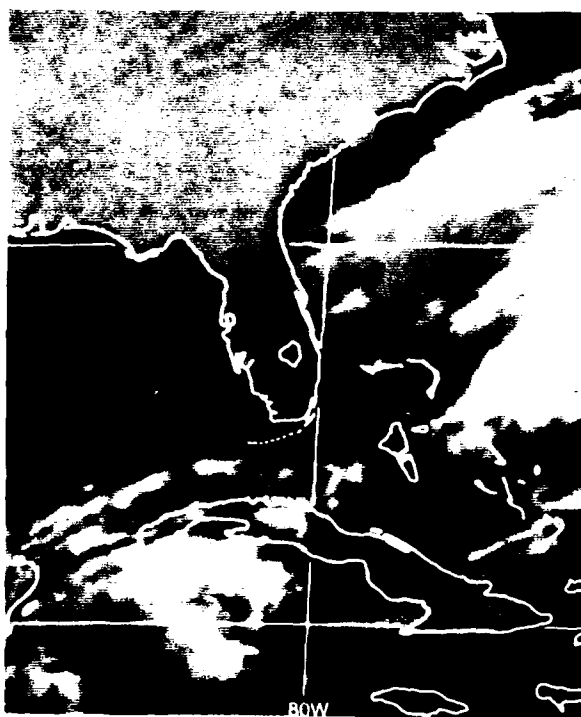
1. A low-level, mesoscale nocturnal jet development over a coast from land to sea, can be anticipated when:
 - a. High pressure exists north of a flat terrain west-coastal location.
 - b. Skies are clear at night.
 - c. Land temperature drops during the night to at least 9° F (5° C) lower than the adjacent coastal sea temperature.
 - d. Prevailing offshore wind is less than 10-12 kt (5-6 m sec⁻¹).
 - e. Little vertical wind shear is present in the boundary layer.
2. Under such conditions a low-level, nocturnal jet may appear at an altitude between 100 and 600 m. This is low enough to be an important factor in aircraft landing approaches toward the east since wind speeds may drop from a 30 to 40-kt headwind component to calm in only a few seconds during the landing operation.

Reference

Gulfstream, 1977. U.S. Dept. of Commerce, NOAA, NWS, Washington, D.C. Vol. III, No. 2 February 1977, pp. 7



IC-9a. RAOB. Tampa Bay, Florida. 0000 GMT 10 February 1977.



IC-9b. GOES-E. Infrared Image. 0600 GMT 10 February 1977.



IC-9c. GOES-E. Visible Image. 1700 GMT 10 February 1977.

Case 3 The "Enhanced-V" or "White Tornado" Squall Line Cloud Formation

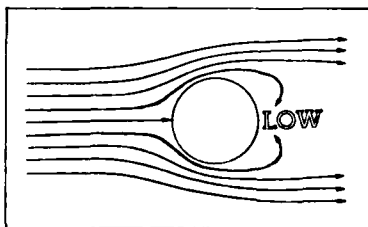
There is a distinctive type of squall line which in satellite visible and infrared imagery appears as a funnel or V-shaped cloud formation laid on its side. The cloud formation is composed of a series of thunderstorms or thunderstorm cells characterized by overshooting tops, many of which penetrate the tropopause. The V-shape occurs because strong upper-level winds are diverted around the strong updrafts which form the core of the thunderstorm cells much as horizontal flow would be forced around the sides of an upright cylinder (IC-11a). Brandli (1976) has named the satellite-observed cloud pattern equivalent (IC-11b) a "White Tornado."

Development of such a cloud formation may be particularly enhanced in regions where the polar and subtropical jet, after converging, suddenly diverge (IC-11c), producing a region of strong diffluence and divergence aloft, which encourages vigorous, deep convection.

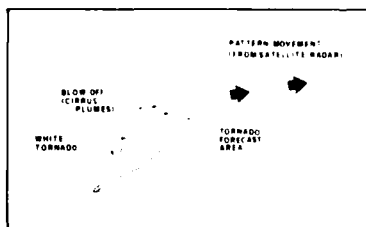
This type of cloud formation is frequently associated with tornadoes spawned from individual thunderstorms within the band. Even without tornado formation, the downbursts induced by the collapsing tops can give rise to surface winds of 60 kt and higher, which can persist for an extended time. An example of a navy ship encountering this type of squall line was documented in NTAG, Vol. 2, Sec. 2D, Case 1, during which the crew of USS *Mitscher* was forced to general quarters. In this instance, unforecast winds of 60 mph with heavy rain were encountered as the ship entered the cloud band south of Sicily on 16 October 1975.

References

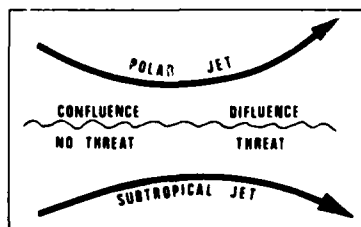
- Brandli, H. W., 1976: Satellite Meteorology. AWS-TR-76-264, Hq. Air Wea. Svc., Scott AFB, IL 62225, pp. 188.
- McCann, D. W., 1981: The Enhanced-V, A Satellite Observable Severe Storm Signature. NOAA Tech. Memo NWS NSSFC-4, Nat. Wea. Svc., Wash., D.C., pp. 31.



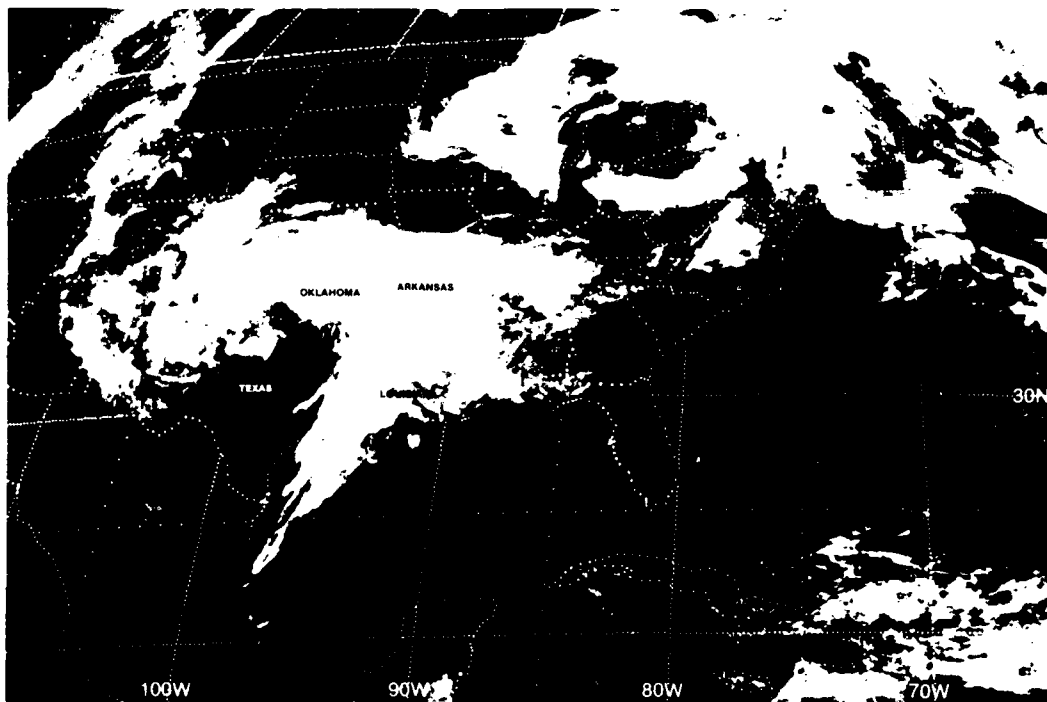
IC-11a. Flow Past a Cylinder
(After McCann, 1981.)



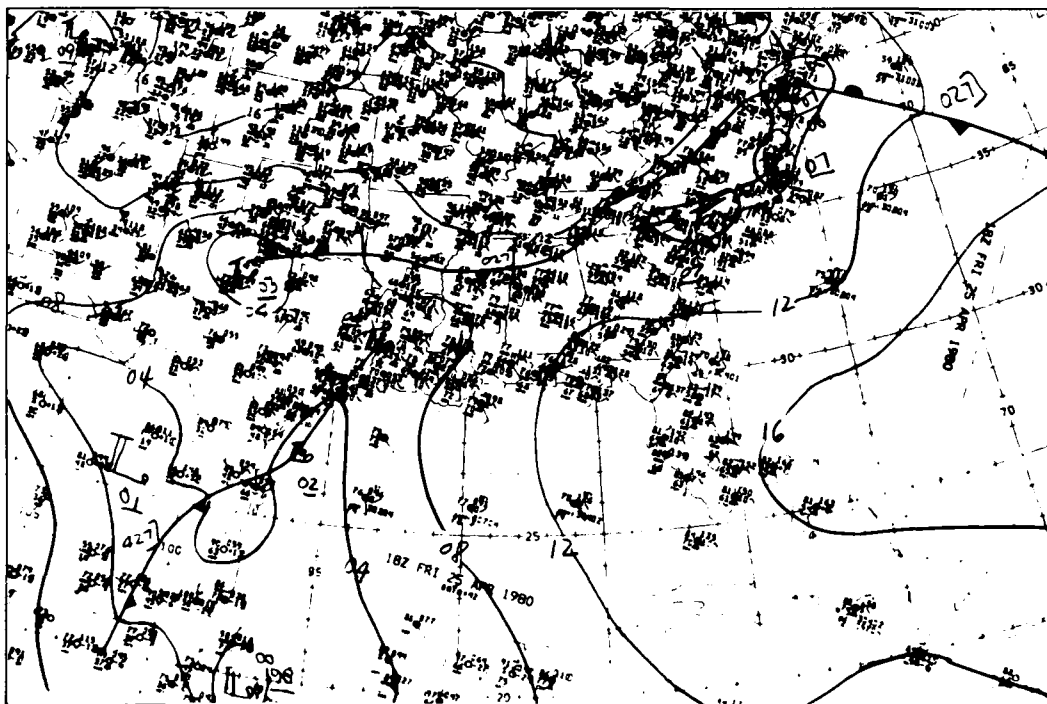
IC-11b. White Tornado Cloud Formation.
(After Brandli, 1976.)



IC-11c. Polar Subtropical Jet Confluence-Diffluence Pattern. (After Brandli, 1976.)



IC-12a GOES-1 Visible Image 1700 GMT 25 April 1980



IC-12b NMC Surface Analysis 1800 GMT 25 April 1980

Severe Squall Line Development Gulf of Mexico Straits of Florida April 1980

25 April

The GOES-E visible image at 1700 GMT (IC-12a) shows an area of tapered cloudiness along the extreme western portion of the Gulf of Mexico. The cloud formation crosses the coast along the border of Texas and Louisiana, extends into Arkansas, Oklahoma, and covers the northern portion of Texas.

The NMC surface analysis for 1800 GMT (IC-12b) depicts a cold front that parallels the back side of the tapered cloud formation, and then extends into eastern Texas western Louisiana. A warm front, associated with a low-pressure center near the Texas panhandle, is shown over the northern Texas-southern Oklahoma region.

The GOES-E infrared image for the same time (IC-13a) reveals that the most well-developed portion of cloudiness in this system is that immediately onshore of Texas, extending into Louisiana as a "white tornado" cloud formation.

The NMC 300-mb analysis (IC-13b) reveals the characteristic diffluent pattern aloft that encourages especially intense convection. Storm Data (1980) reported no damage from southern Texas, but in Louisiana, directly under the "white tornado," severe damage occurred as roof-tops, powerlines, and trees were downed.

26 April

The GOES-E visible image at 1700 GMT (IC-14a) again reveals the tapered cloud form of a "white tornado" which has apparently persisted from the previous day; drifting now into northern Florida, southern Alabama, and Georgia.

The NMC surface analysis for 1800 GMT (IC-14b) reveals a cold front (the eastward progression of the front previously over eastern Texas; IC-12b) now extending from the central Gulf of Mexico into northern Florida and northeastward. The GOES-E infrared image (IC-15a) shows very clearly the cold, tapered shape of the "white tornado" cloud pattern.

At 300-mb (IC-15b), the continued strong diffluence promoting the strong convection is clearly evident.

Storm Data (1980) reports indicate tornado activity in Georgia during the afternoon on this date.

NOAA - Office of Applied Meteorology

A major tropical cyclone threat exists for the Gulf of Mexico and Caribbean Sea. A tropical storm or hurricane could develop in the next few days.

NOAA - Office of Applied Meteorology

A tropical storm or hurricane could develop in the next few days. A major tropical cyclone threat exists for the Gulf of Mexico and Caribbean Sea.

27 April

On this day a great sea disaster occurred as an unknown number of refugees from Cuba were caught in a severe storm while attempting to reach the Florida Keys (Storm Data, 1980).

NOAA - Office of Applied Meteorology

Storm Data (1980) also reports a tornado that crossed Cudjoe Key, causing a great deal of property damage and some minor injuries.

NOAA - Office of Applied Meteorology

A tropical storm or hurricane could develop in the next few days. A major tropical cyclone threat exists for the Gulf of Mexico and Caribbean Sea.

The GOES-E visible image at 1700 GMT (IC-16a) reveals intense convection in the Straits of Florida and over the Florida Keys. The NMC surface analysis for 1800 GMT (IC-16b) places a cold front at the trailing edge of this intense convection. Thunderstorms are reported by all stations on a line from Havana to Miami (see FNOG surface analysis, IC-17c).

The NMC 300-mb analysis at 1200 GMT (IC-17b) again shows the appreciable upper-level diffluent flow over the convective area.

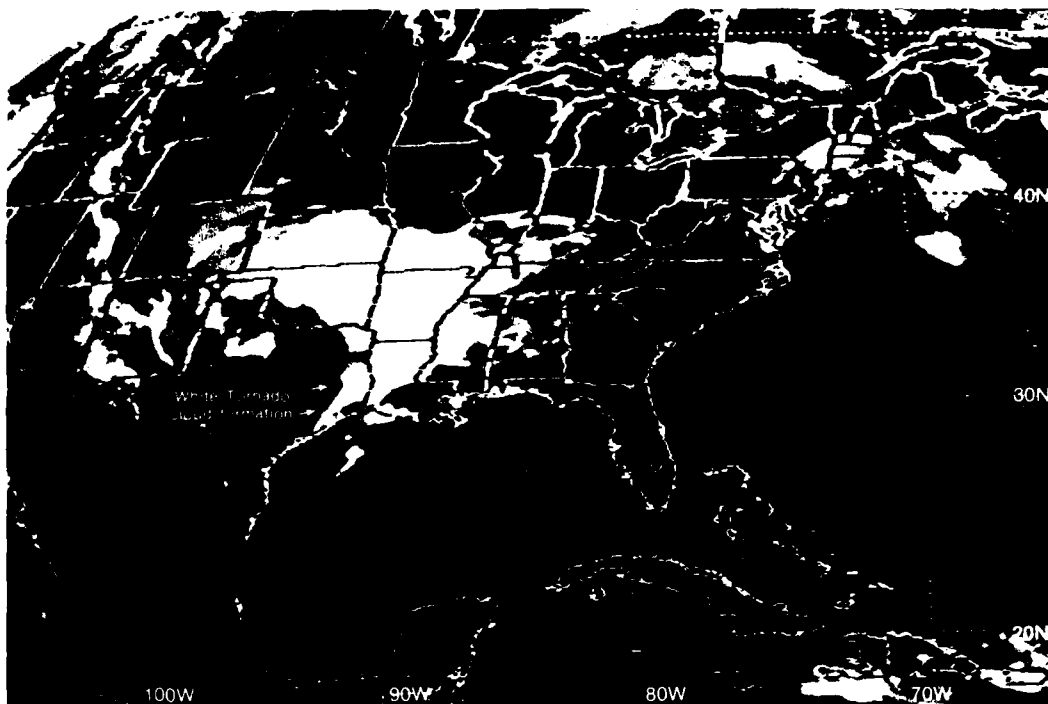
The GOES-E infrared image (IC-17a) shows extremely cold temperatures extending along the convective region from the western tip of Cuba in a broad plume covering almost all of Florida. The plume at this time does not have the classical tapered shape of the "white tornado." However, this feature as we have seen, has been tracked in its classical form for at least a two day period, and (e.g., USS *Mitscher*; NTAG, Vol. 2, Sec. 2D, Case 1) it is not unusual to see a variant of this form, as intense convection produces a high cloud shield that can assume a broader shape and become almost circular at times.

Important Conclusions

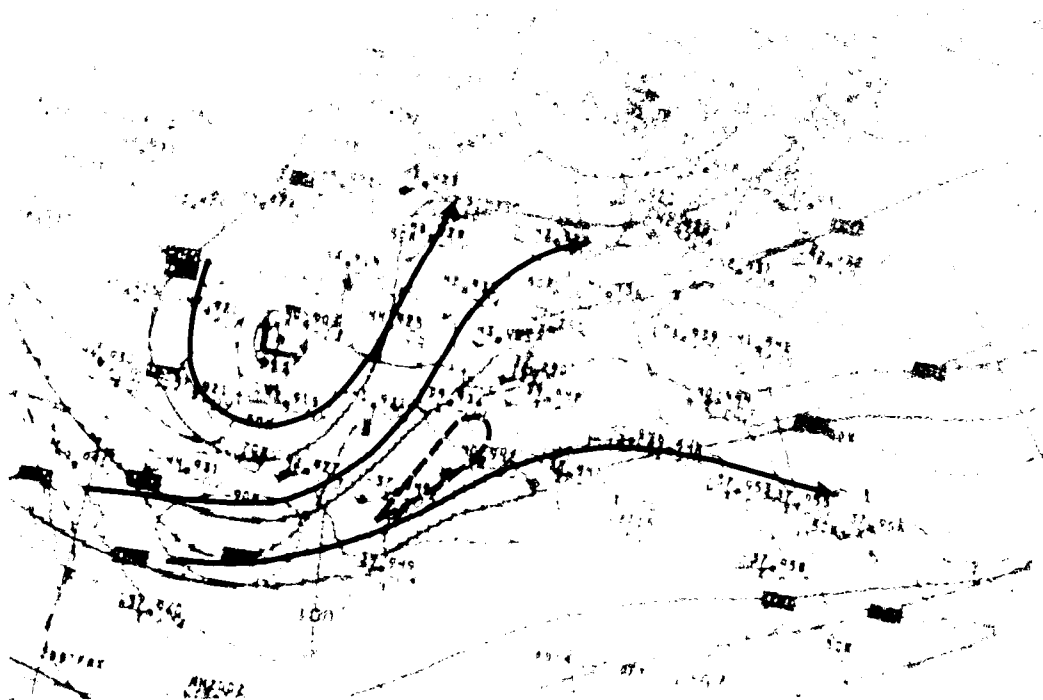
1. The "white tornado" cloud formation is a characteristic signature of an extremely severe squall line that often spawns tornadoes and gives rise to hurricane-force winds at the surface.
2. When an upper-level diffluent pattern is apparent over such a cloud formation, forecasters should be alerted for possible severe weather consequences.
3. The "white tornado" cloud formation can persist with its characteristic pattern for several days.

Reference

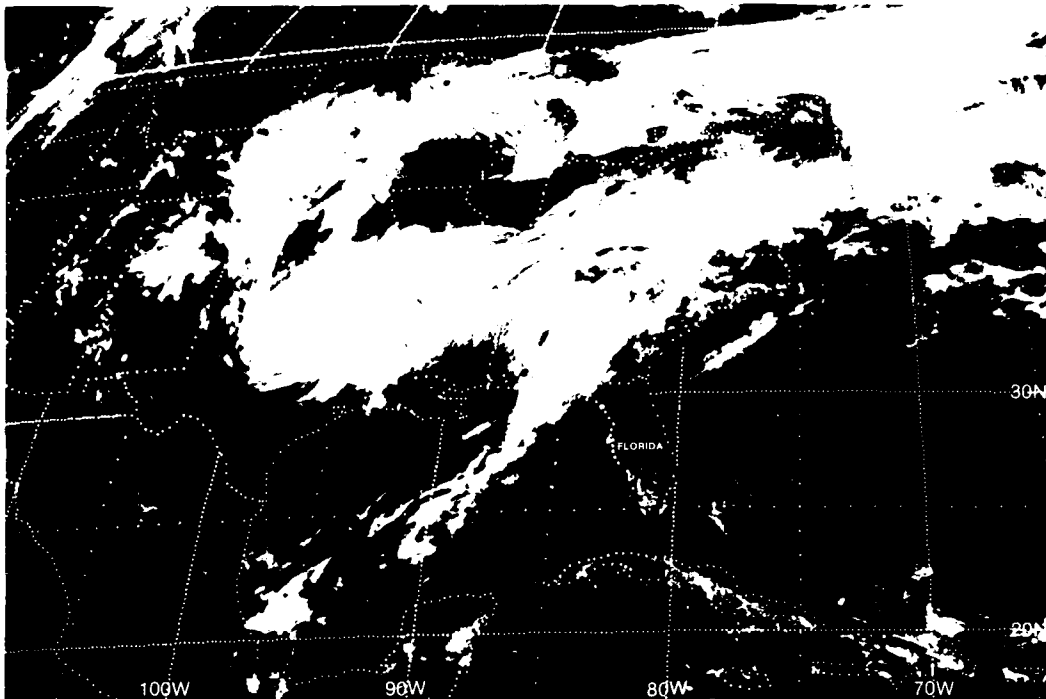
Storm Data, 1980. Dept. of Commerce, NOAA. FDIS. Nat. Clim. Ctr., Asheville, N.C., Vol. 22, No. 4, pp. 21.



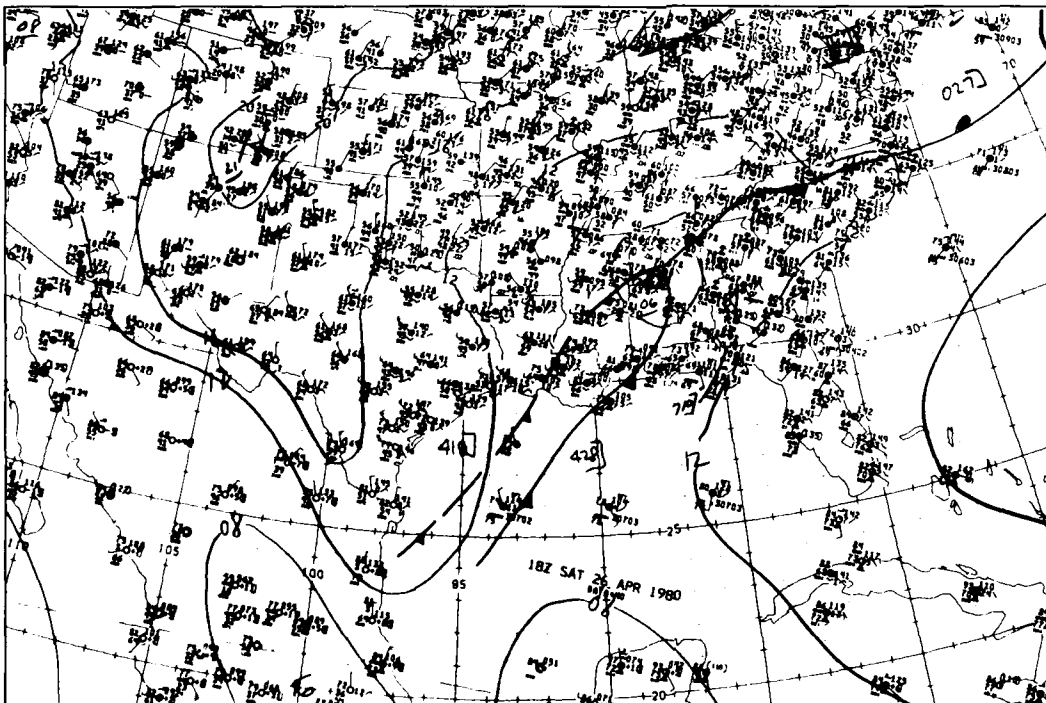
IC-13a GOES-E Infrared Image 1700 GMT 25 April 1980.



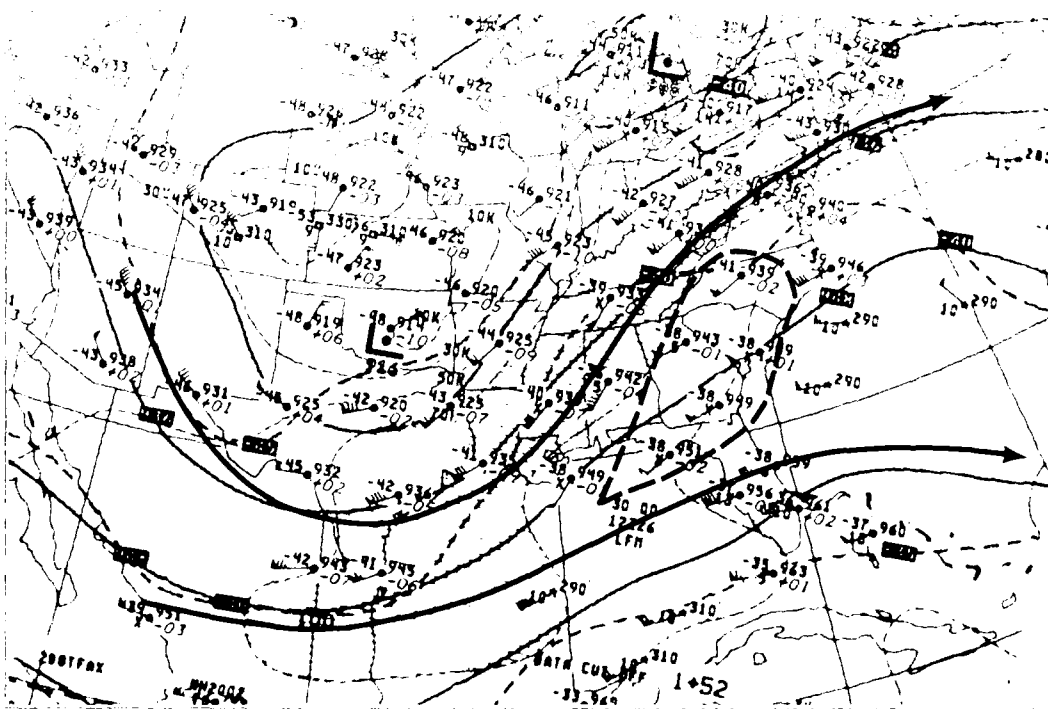
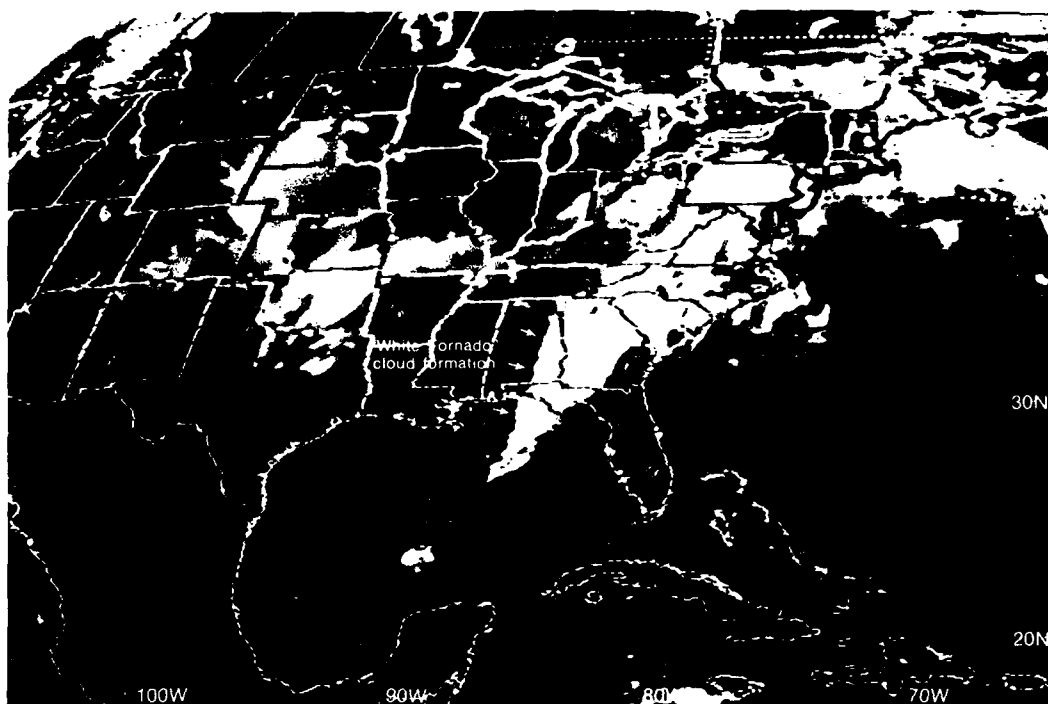
IC-13b NMC 300-mb Analysis and Streamlines 1200 GMT 25 April 1980

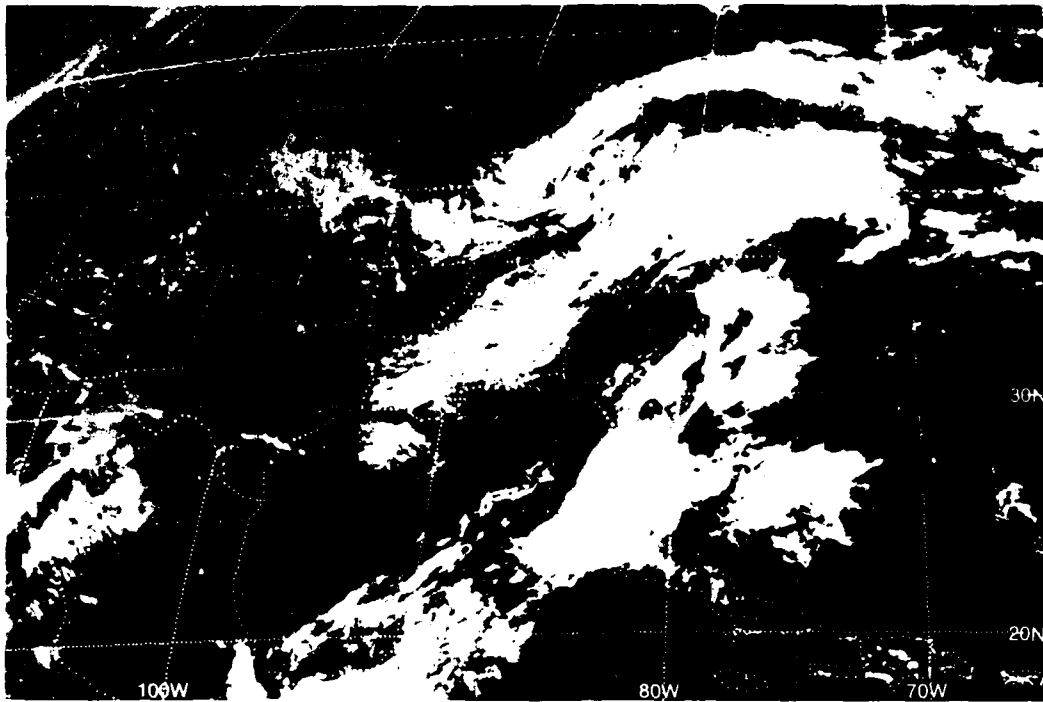


IC-14a. GOES-F. Visible Image. 1700 GMT 26 April 1980.

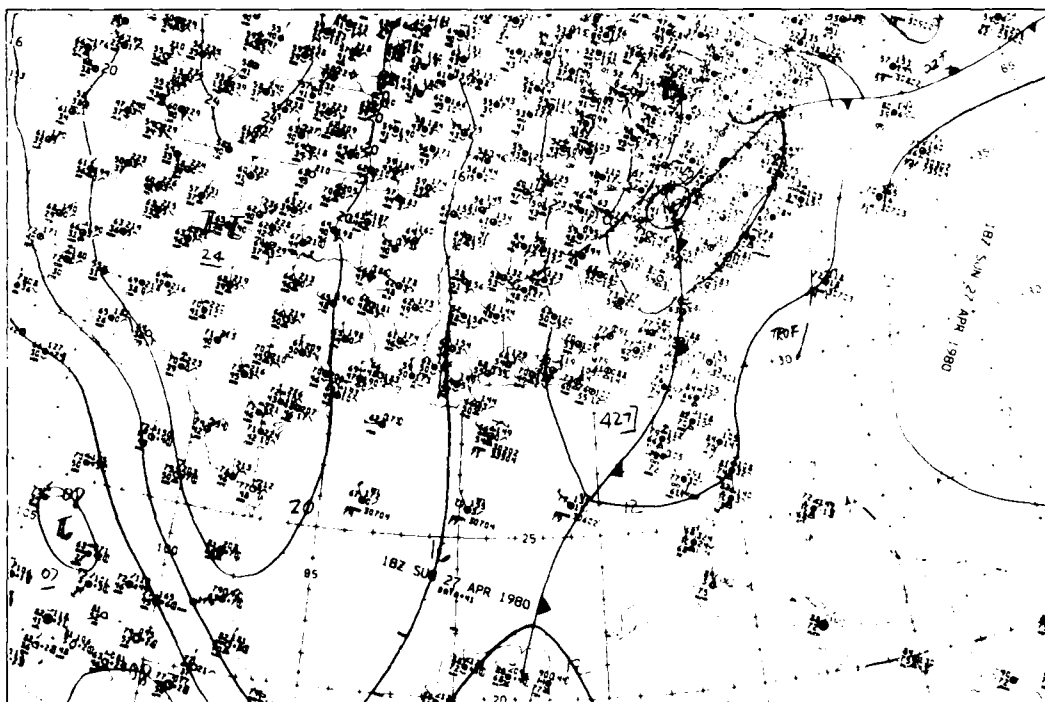


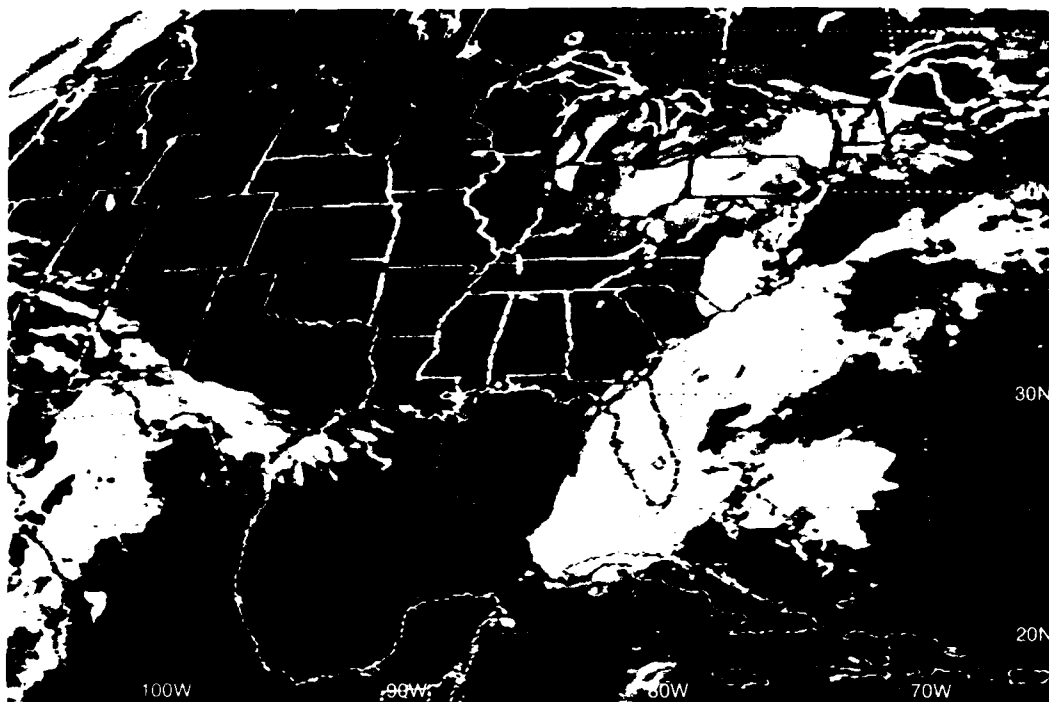
IC-14b. NMC Surface Analysis. 1800 GMT 26 April 1980





IC-16a GOES-E Visible Image 1700 GMT 27 Apr 1980

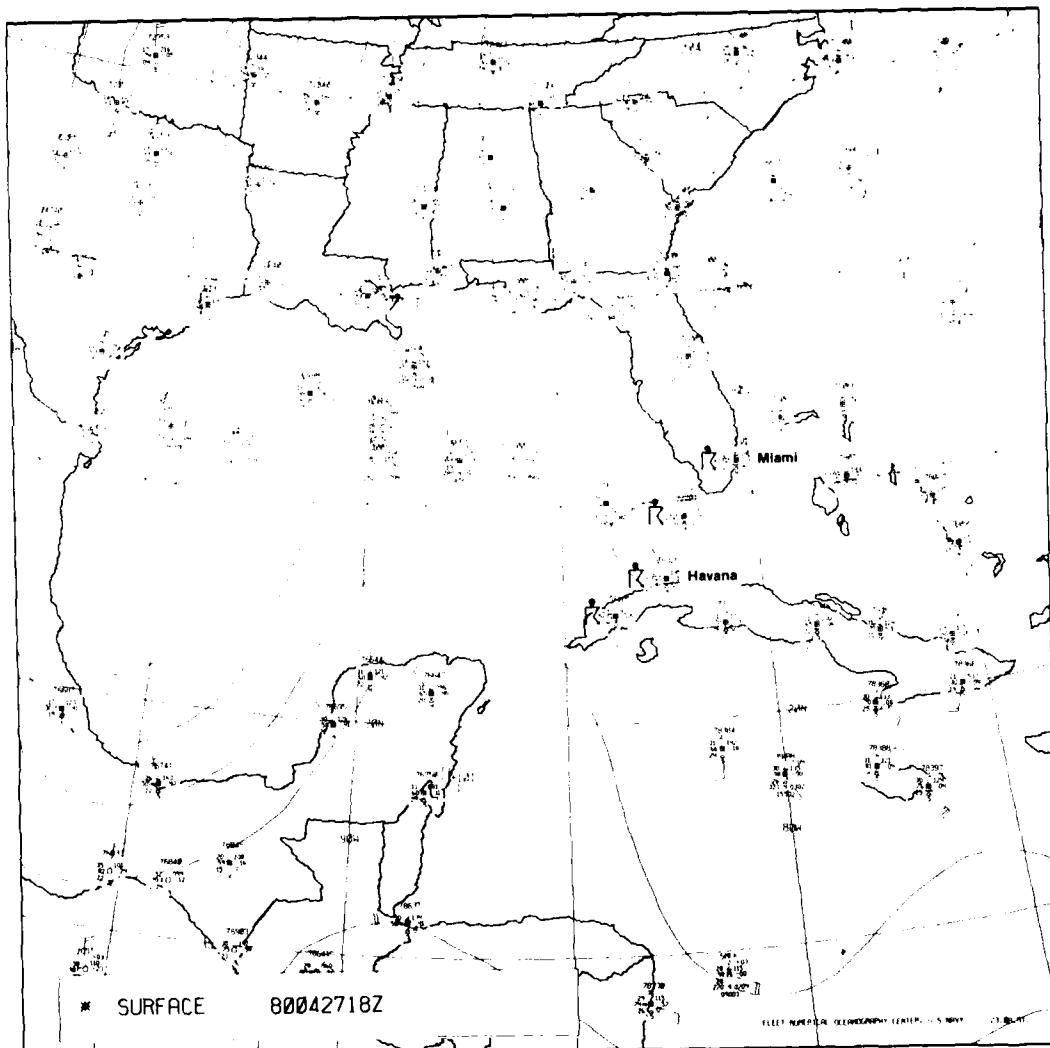




IC-17a GOES-I Infrared Image. 1700 GMT 27 April 1980.



IC-17b NMC 300-mb Analysis and Streamlines. 1200 GMT 27 April 1980.

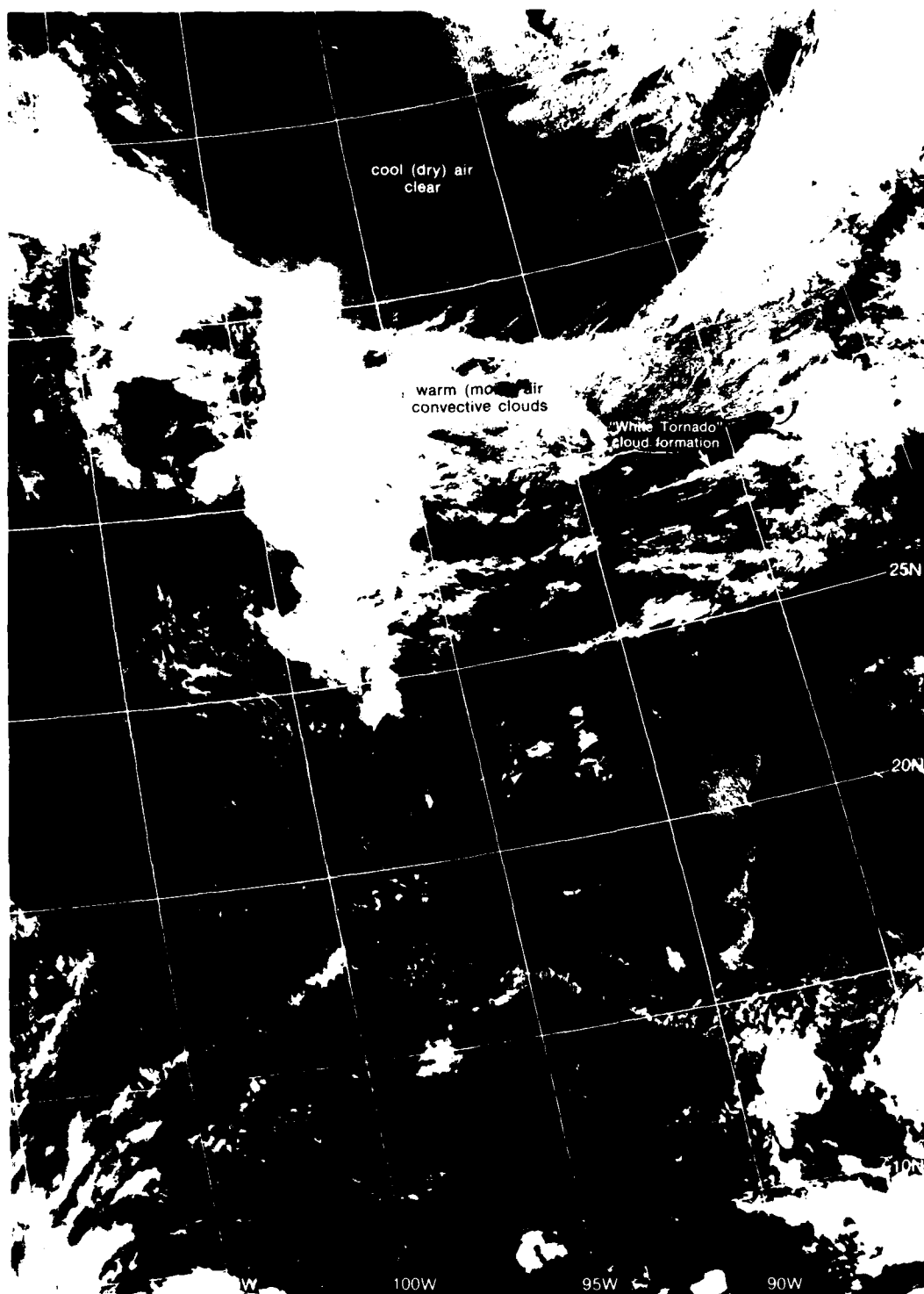


IC-17c. FNOG Surface Analysis. 1800 GMT 27 April 1980.

Case 4 The "White Tornado" Cloud Pattern

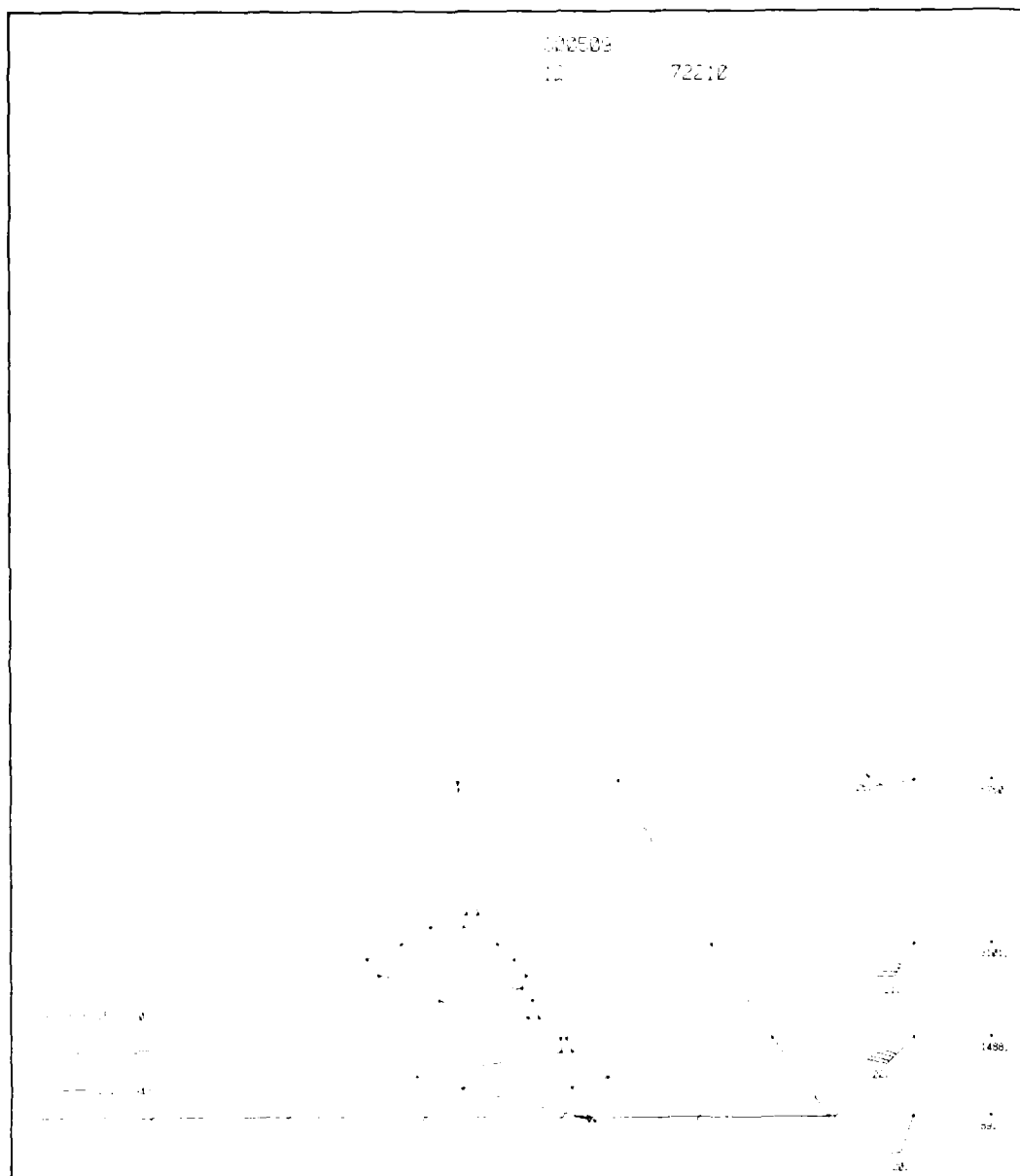
"White tornado" squall line formations are common in the tropics and have produced some disastrous results in Florida and the Caribbean. This is another example of a "white tornado" squall line development that was a contributing factor in the collapse of the Tampa Bay Sunshine Skyway Bridge, which resulted in a number of deaths.

IC Case 4

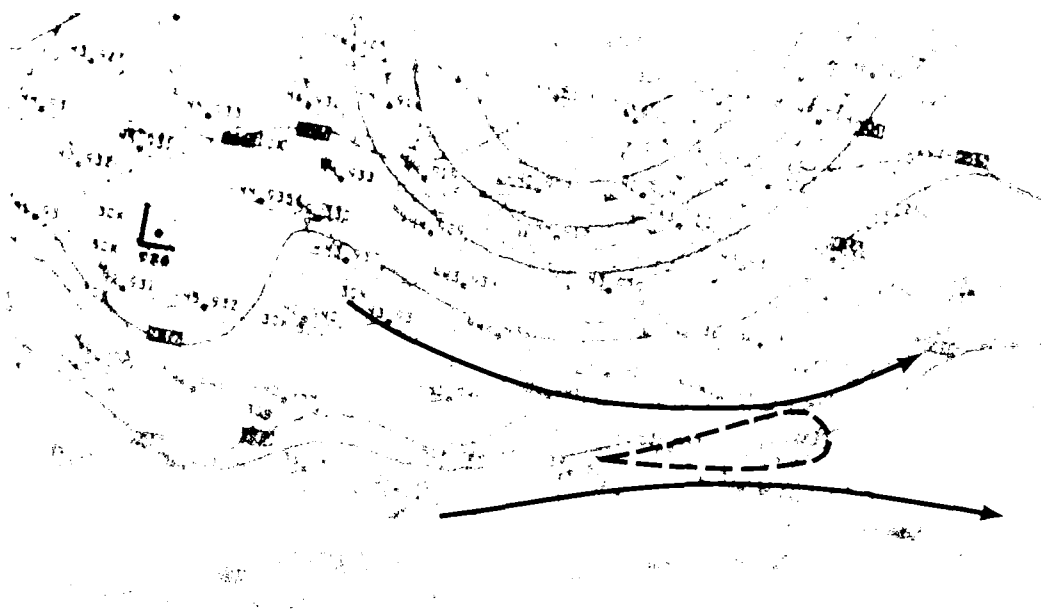


TC-20a 1-4 DMSP EE Low Enhancement 1644 GMT 8 May 1980

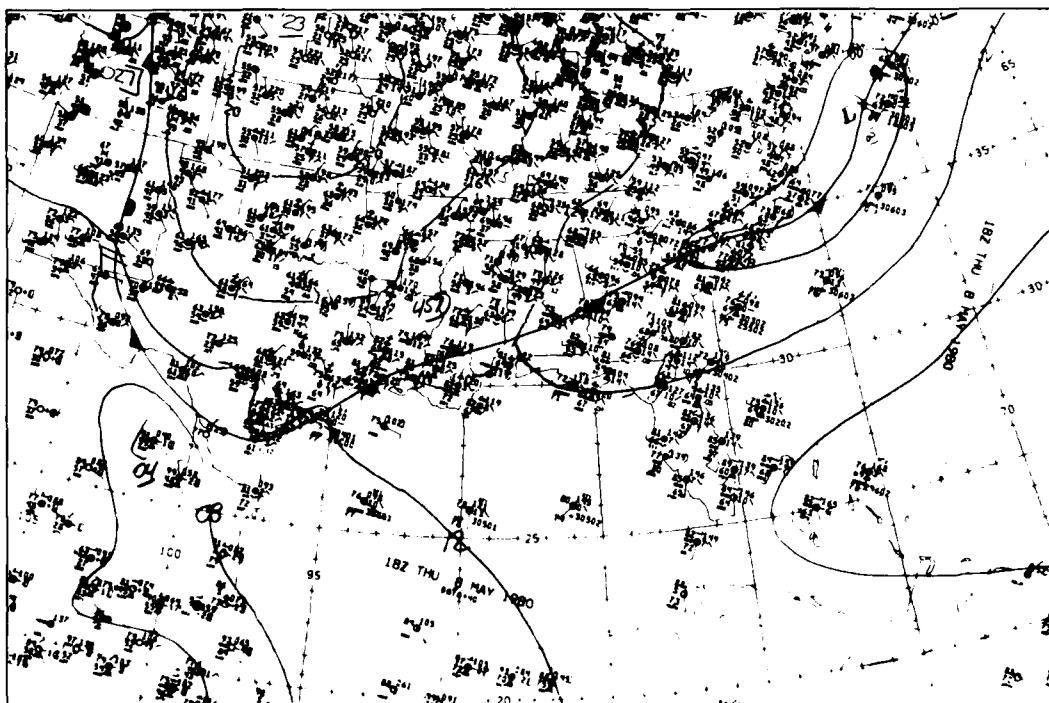
100-20



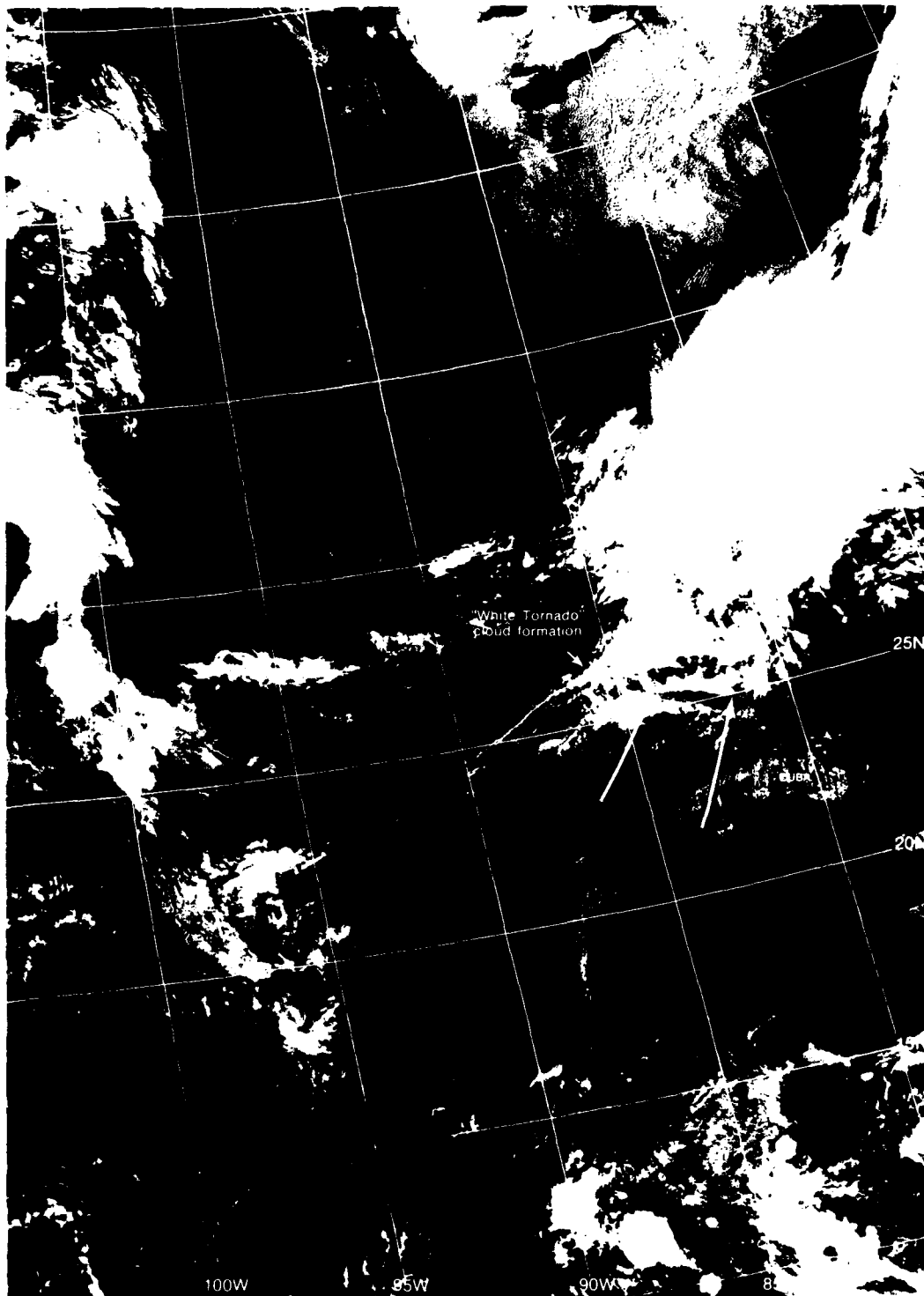
IC-21c RAOB Tampa Bay, Florida 1200 GMT 8 May 1980



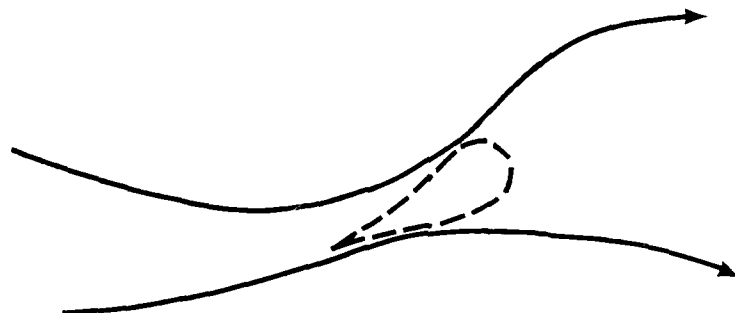
IC-21a. NMC 300-mb Analysis and Streamlines 1200 GMT 8 May 1980



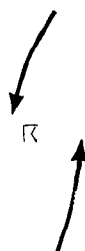
IC-21b. NMC Surface Analysis 1800 GMT 8 May 1980



IC-22a. F-4. DMSP LF Low Enhancement. 1624 GMT 9 May 1980.



IC-23a NMC 300-mb Analysis and Streamlines, 1200 GMT 9 May 1980



IC-23b NMC Surface Analysis, 1200 GMT 9 May 1980

Section 2

Tropical Eastern Pacific Ocean

2A Introduction

Tropical Eastern Pacific Ocean	2A-1
--------------------------------------	------

2B Synoptic-scale Case Studies

<i>1 The Central Pacific Near-Equatorial Convergence Zone</i>	<i>2B-1</i>
Location of the Equatorial Trough Using Sunlint Equatorial Central Pacific March 1979, July 1984, and December 1977	2B-4
<i>2 Identification of Planetary Boundary Layer Height Changes from Satellite Imagery</i>	<i>2B-9</i>
Ridge Line Passage Guadalupe Island, Mexico Tropical Eastern North Pacific April 1984	2B-10
<i>3 Use of Sunlint in Locating Ridge Lines in the Tropics</i>	<i>2B-15</i>
Location of a Ridge Line in Advance of a Cold Front Tropical Eastern North Pacific July 1979	2B-16
<i>4 Tropical Developments of Polar Origin</i>	<i>2B-19</i>
Induced Frontal Wave (Vorticity Comma) Cyclogenesis Tropical Eastern North Pacific January 1981	2B-20

2C Mesoscale Case Studies

<i>1 Use of Cloud Lines and Mesoscale Clear Regions as an Aid in Synoptic Analysis</i>	<i>2C-1</i>
Identification of an Easterly Wave Central Tropical North Pacific November 1977	2C-2
<i>2 Identification of Island-Produced Cloud Plumes</i>	<i>2C-5</i>
Deep Convection Cirrus Debris-- Mistaken as an Island-Produced Cloud Plume Hawaiian Islands June 1975	2C-6

Tropical Eastern Pacific Ocean

Like the Atlantic the tropical eastern Pacific Ocean is dominated by easterly flow between high pressure cells in the Northern and Southern Hemispheres. Convergence of flow from the two hemispheres similarly produces a cloud band near 5° – 10° N stretching westward from South America past Christmas Island across the Pacific.

Perturbations, similarly, form north of the convergence cloud band. However, the easterly wave form, typical in the Atlantic, is only rarely seen and, more commonly, the perturbation forms in a monsoonal trough with westerlies, rather than easterlies, south of the circulation and vorticity center.

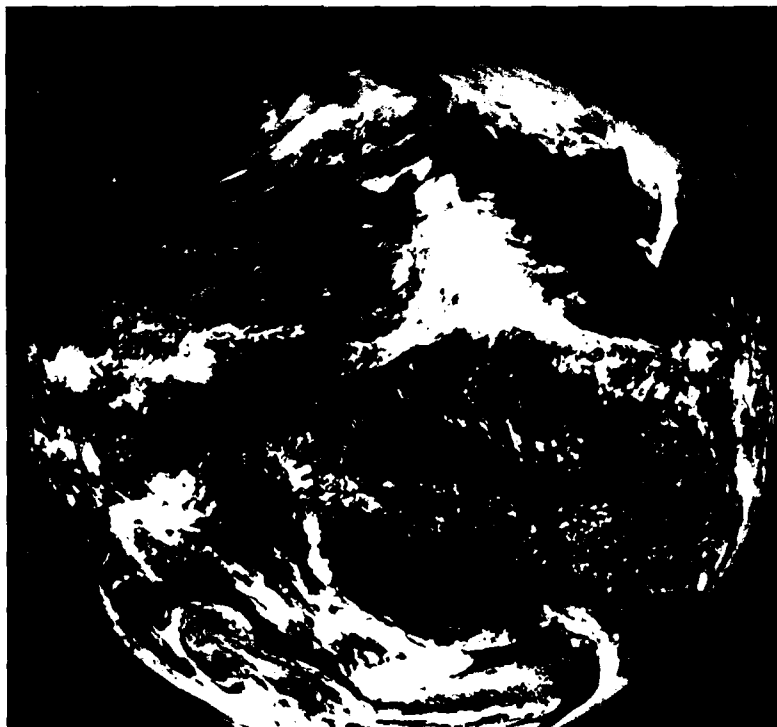
Interactions of midlatitude westerly troughs and the tropical convergence cloud band is more frequent in the Pacific and a major cause of intense storm development which brings significant and often unexpected heavy rain to the southwestern U.S. (2A-1a).

Upper-cold low development is also common, especially during winter in the eastern North Pacific. Such storms are often detectable in their early stages only through satellite observations showing a few cyclonic wisps of cirrus curving about an upper-level center.

In Hawaii, such storms (known as "Kona" storms), when fully developed, are a major source of the total annual precipitation received by the islands.

Through a careful analysis of high resolution and properly enhanced satellite imagery, the Navy meteorologist can be attuned to subtle but important changes affecting weather developments in this region.

2A-1a. GOES-W.
Visible Image.
2045 GMT
25 January 1978.



2A-1

Case 1 *The Central Pacific Near-Equatorial Convergence Zone*

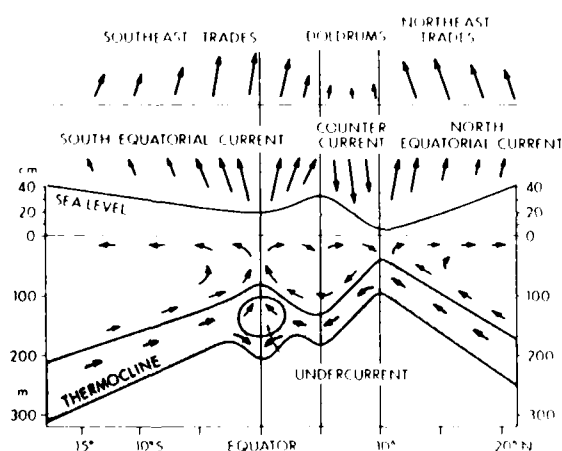
The central Pacific near-equatorial convergence zone (CZ) lies north of the equator throughout the year. On an average it moves between 4° N in spring (April) and 8° N in autumn (September). The movement is in response to variations in the strength of the northeast and southeast trade winds. These winds converge north of the equator forming the CZ axis.

The CZ overlies the North Equatorial Countercurrent which flows eastward counter to the northeast trades. Sea surface temperature (SST) is highest in this region, lying between a zone of equatorial upwelling and upwelling near 10° N (2B-1a).

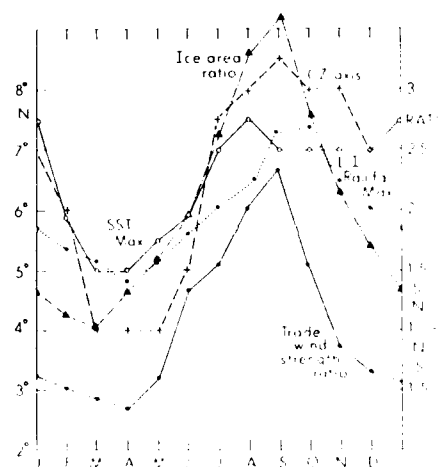
On an average the CZ in the North Pacific is found along 6° N. According to Flohn (1967 and 1971) this results from the Southern Hemisphere's greater tropospheric baroclinicity due to more extensive ice sheets.

Support for the idea that the central Pacific CZ stays north of the equator comes from the finding (Treshnikov, 1967; Walsh and Johnson, 1979) that the ratio of the areas of Arctic and Antarctic ice sheets and the CZ latitude vary in phase throughout the year (2B-1b). The figure also shows that the variation in latitude of the CZ is in phase with the variation in latitude of the SST maximum and the ratio of the strength of the northeast and southeast trades.

2B-1a Schematic meridional section showing location of Equatorial Countercurrent (After Ramage, 1981.)



2B-1b Latitudes of surface wind convergence zone axis; sea surface temperature maximum; trade wind strength ratio (North Pacific-South Pacific); and ice area ratio (Arctic-Antarctic). (After Ramage, 1981.)



2B-1

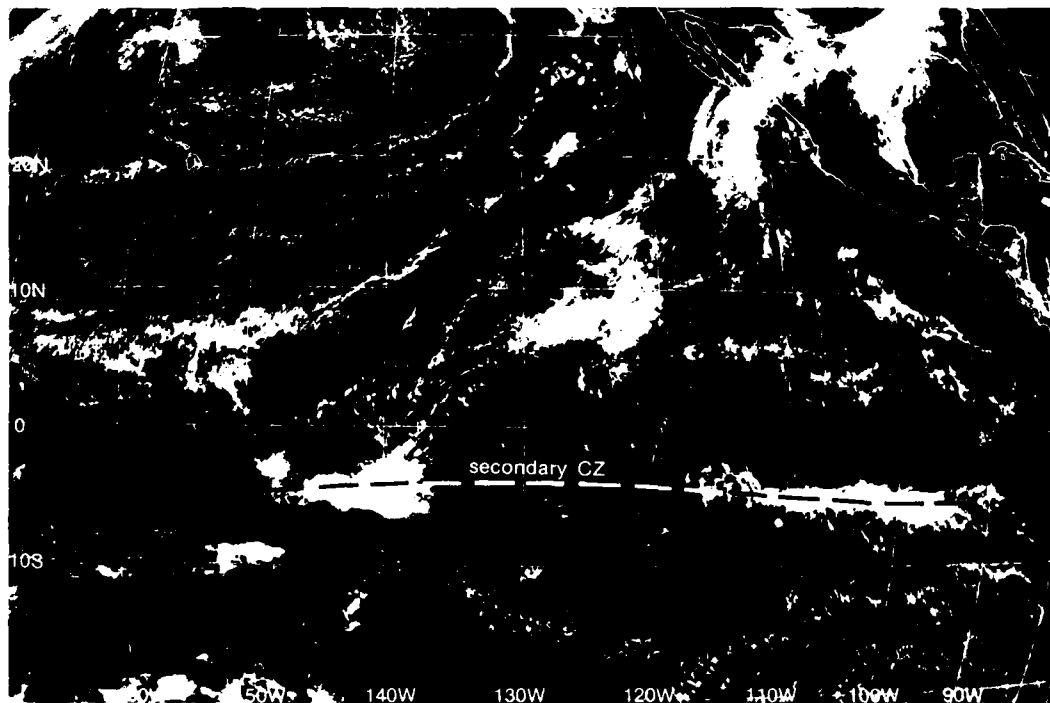
Although the North Pacific CZ never moves into the Southern Hemisphere, in March and April—when the North Pacific trades are relatively strongest and the Arctic ice sheet relatively largest—not only is the CZ closest to the equator but a secondary convergence zone frequently appears as a cloudiness maximum along about 5° S (Kornfield *et al.*, 1967; Sadler, 1968; and Sadler *et al.*, 1976). The GOES-E visible image (2B-2a) shows an example of a secondary convergence zone south of the equator over the eastern South Pacific on 10 March 1979.

Small pressure gradients, sparse data, and observational errors make it difficult to document details of the pressure field, the wind field, and CZ cloudiness on any given date. However, when climatological data showing seasonal extremes of equatorial trough location for January and July are compared to mean monthly cloudiness (derived from satellite data over a 10-year period; Sadler *et al.*, 1984) for these same months (2B-3a and 3b), a tendency is shown for the trough to lie south of the CZ cloudiness during January and north of the CZ cloudiness during July.

Satellite imagery can be used to test this hypothesis, through sunglint analysis (NTAG Vol. 1, Sec. 2). Trough axes, similar to ridge axes, are also axes of minimum wind speed. Hence, more intense sunglint should be detected from the location of the equatorial trough than further north or south, where wind speeds are stronger.

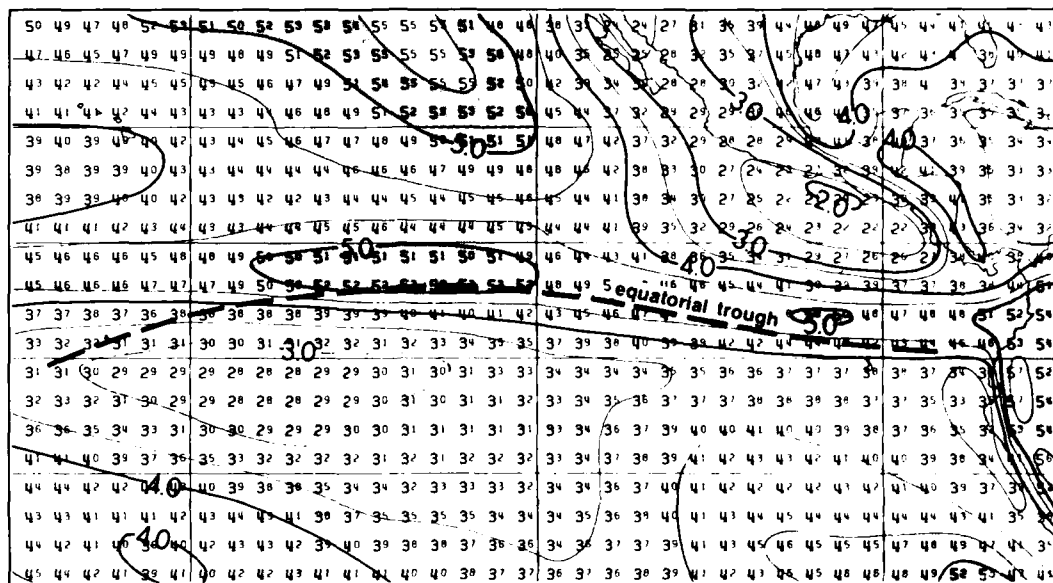
References

- Flohn, H., 1971: Tropical circulation patterns. *Bonner Meteorol. Abh.*, **15**, 1–55.
 Kornfield, J. A., A. F. Hasler, K. I. Hanson, and V. F. Suomi, 1967: Photographic cloud climatology from ESSA III and V and computer-produced mosaics. *Bull. Am. Meteorol. Soc.*, **48**, 878–883.
 Ramage, C. S., 1981: The central Pacific near-equatorial trough. *J. Geophys. Res.*, **86**, 6580–6598.

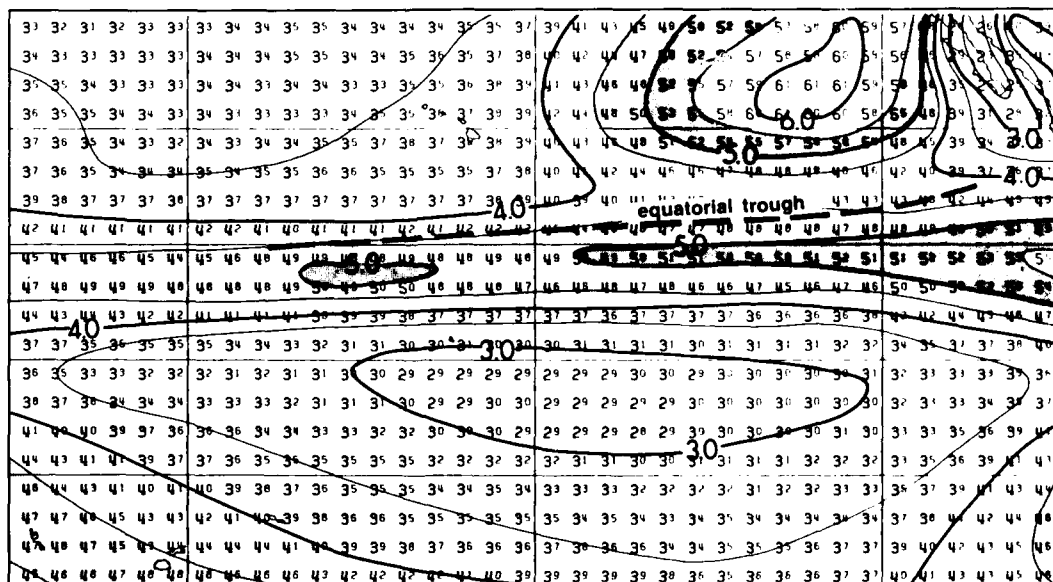


2B-2a. GOES-W Visible Image. 2045 GMT 10 March 1979.

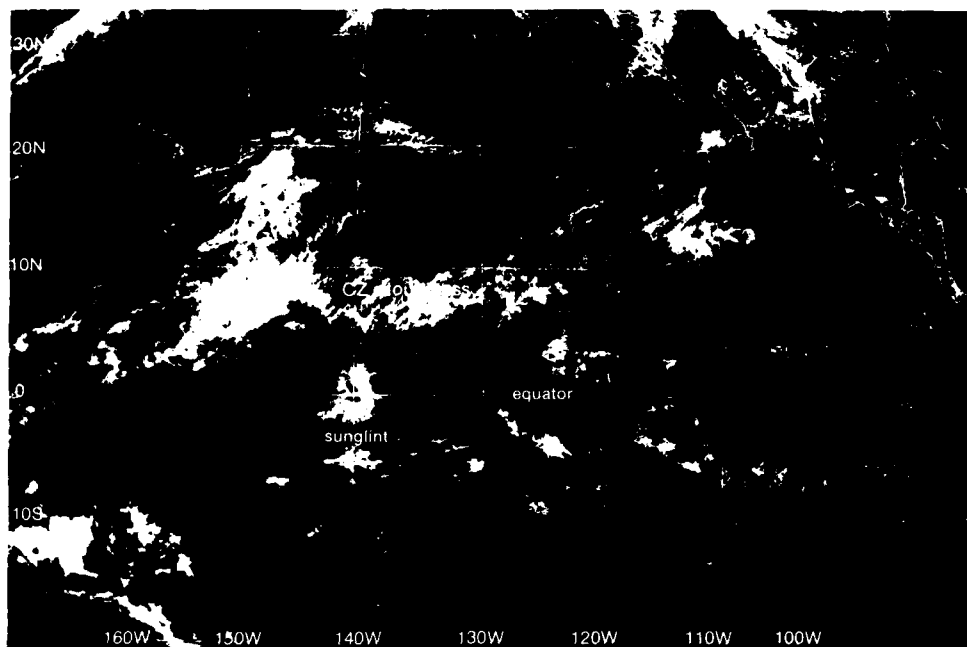
- Sadler, J. C., 1968: Average cloudiness in the tropics from satellite observations. *Int. Indian Ocean Exped. Meteorol. Monogr.*, Vol. 2, University Press of Hawaii, Honolulu.
- Sadler, J. C., L. Oda, and B. J. Kilonsky, 1976: Pacific ocean cloudiness from satellite observations. UHMET 76-01, Dept. of Meteorol. Univ. of Hawaii, Honolulu.
- Sadler, J. C., B. Kilonsky, L. Oda, and A. Hori, 1984: Mean cloudiness over the global tropics from satellite observations. NAVENVPRDRSH-AC Contractor Report CR 84-09, Naval Environmental Prediction Research Facility, Monterey, CA 93943, pp. 55.
- Treshnikov, A. F., 1967: The ice in the southern ocean. *Proc. Symp. Pacific-Antarctic Sci.*, Tokyo, 113-123.
- Walsh, J. E., and C. M. Johnson, 1974: An analysis of Arctic sea ice fluctuations. *J. Phys. Oceanogr.*, 9, 580-591.



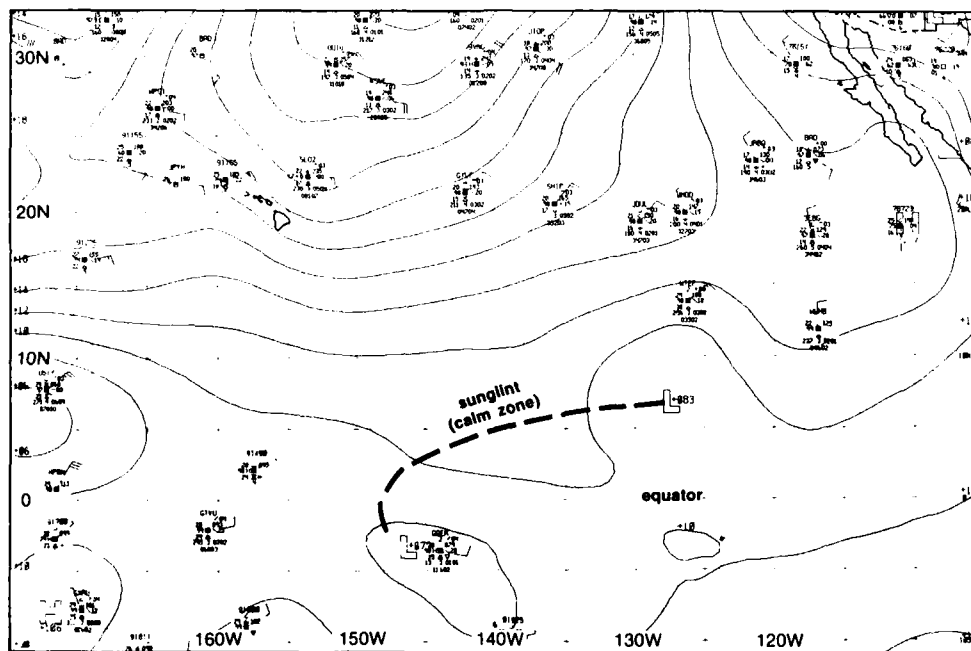
2B-3a. Mean monthly tropical cloudiness for January (dashed line: near-equatorial trough). (After Sadler, 1984.)



2B-3b. Mean monthly tropical cloudiness for July (dashed line: near-equatorial trough). (After Sadler, 1984.)



2B-4a. GOES-W. Visible Image. 2145 GMT 20 March 1979.



2B-4b. FNOG Surface Analysis and Wind Field. 0000 GMT 21 March 1979.

*Location of the Equatorial Trough Using Sunlight
Equatorial Central Pacific
March 1979, July 1984, and December 1977*

March 1979

The GOES-W visible image at 2145 GMT on 20 March (2B-4a) shows brilliant sunglint along the equator at 140° W. CZ cloudiness appears to the north between latitudes 5° and 10° N. An FNOC surface analysis and wind field, valid a little over 2 hr later (2B-4b), verifies lower pressures and a trough axis south of the CZ cloudiness.

July 1984

By way of contrast, the GOES-W visible image at 2045 GMT on 10 July (2B-5a) shows brilliant sunglint north of the CZ cloudiness, near 12° N, 134° W. The FNOC surface analysis and wind field about 2 hr later (2B-5b), verifies a trough axis north of the CZ cloudiness, with a low center of 1010.4 mb almost precisely overlying the sunglint position.

The change in the location of the trough axis (as the seasons change) from the south side to the north side of the CZ cloud areas creates more favorable conditions for increased cyclonic vorticity on the north side due to horizontal speed shear (strong northeast trades decreasing to near calm at the trough axis). For this reason cloud vortices develop more frequently during the summer period on the north side of CZ cloudiness. Conversely, cloud vortices are rarely observed along the CZ cloudiness edge (northern or southern) during winter months. Their development on the south side of the CZ, it may be argued, would tend to be inhibited by opposing forces of the southeast trades.

December 1977

The GOES-W visible image at 2045 GMT on 9 December (2B-6a) shows a "classical" CZ in the equatorial North Pacific. On this day a research aircraft traversed the region and CZ cloud bands were observed between 8° and 5° N. The bands extended from 135° to 175° W, beneath an overcast of middle and high clouds, bordered by uniform northeast and southeast trades.

Within the CZ moist updrafts coincided with convergence and rain. Downdrafts were dry and associated with divergence and no rain. There was a broad maximum in SST in the CZ. At 11° N very dry air was found above a moderate inversion at 2,600 m. Beneath, air was moist and contained strong easterly flow. At 0.5° S air was moist throughout the aircraft vertical sounding (to 3,200 m). Winds were weak, being southeasterly below 1,400 m and southwesterly above. Fanning Island (3.8° N, 159.3° W), just south of the CZ, recorded no rain and light variable winds on 9 December. D-values, adjusted for diurnal pressure variation, were applied to eight flights through the CZ from 13 to 22 December. The values were averaged and then the mean for the flight was subtracted. The data revealed falling pressure reaching minimum values in a broad trough near the equator south of CZ cloudiness. The FNOC surface analysis and wind field (2B-6b), valid shortly after the time of the GOES-W data, shows the location of the equatorial trough.

A DMSP visible image of the region (2B-7a) about 1 hr after the GOES-W image, provides a high resolution view between Hawaii and Christmas Island. The image indicates that Fanning Island (northwest of Christmas Island) is, indeed, south of the heavy convection associated with the CZ, but is obscured by cirrus or middle cloud elements.

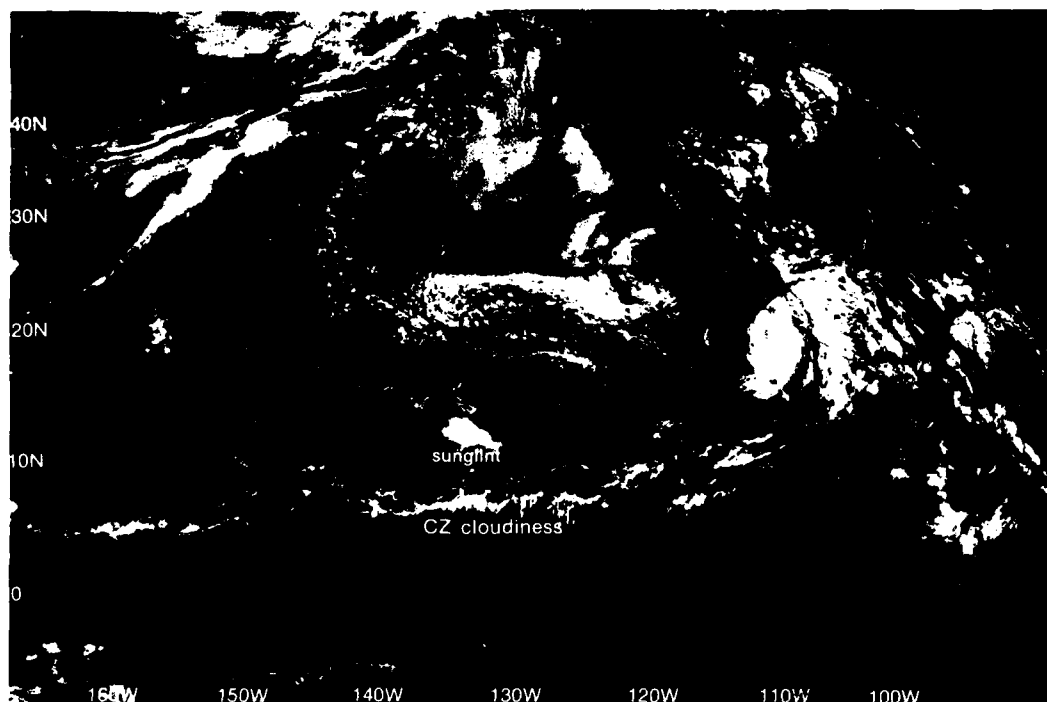
The streamline analysis (2B-7b) indicates northeasterly trades to the north of the CZ, while the report at Christmas Island, south of the CZ, reveals southeasterly flow at 15 kt. A streamline trough is apparent extending from near the Equator and 164° W southeastward toward a tropical cyclone in the Southern Hemisphere (F.C. Tessa; near 17° S, 137° W; 2B-6a).

The research aircraft flights demonstrated that the CZ somewhat resembles an orographic phenomenon. The lifting of boundary-layer air between the convergent trade wind flows is necessary but not sufficient for significant rain; middle and upper tropospheric effects are also important.

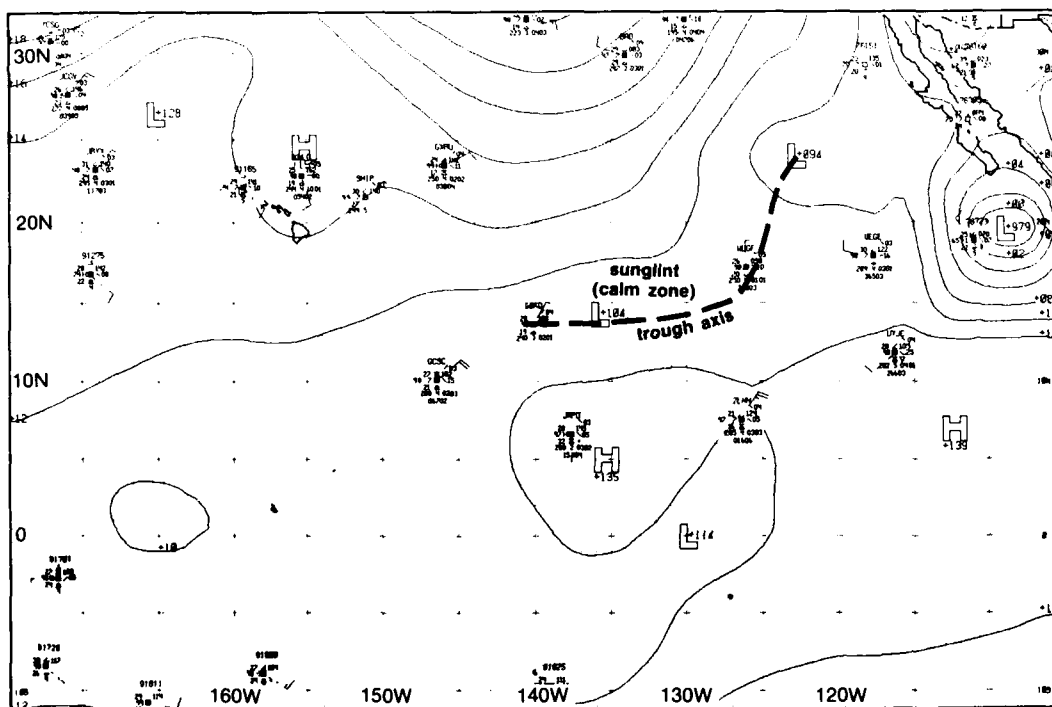
The most conservative property of the CZ is its latitude, which varies little from day to day. However, weather in the zone fluctuates greatly. If satellite pictures are used to classify CZ intensity as weak, moderate, or strong, then at a particular longitude the same category persists from one day to the next less than one third of the time, while simultaneous intensities at points 10 deg longitude apart are apparently unrelated.

Important Conclusions

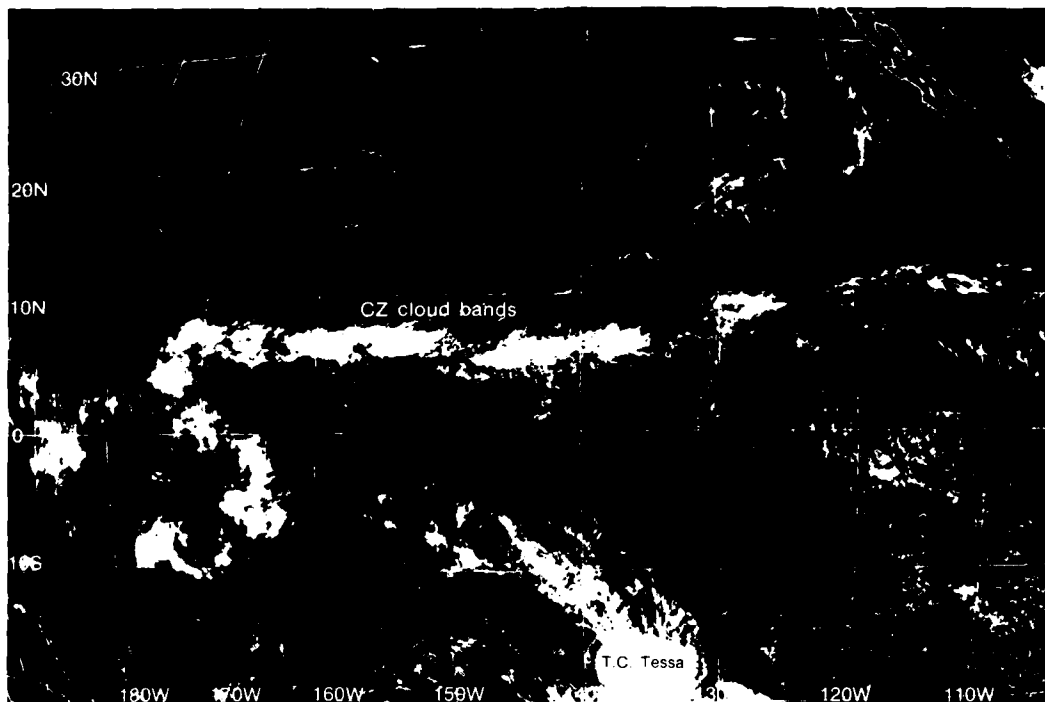
1. The equatorial trough is generally located north of the CZ during the Northern Hemisphere summer and south of the CZ during Northern Hemisphere winter.
2. Sunlight data from polar orbiting and geostationary satellites can be very helpful in locating the latitudinal position of the equatorial trough.



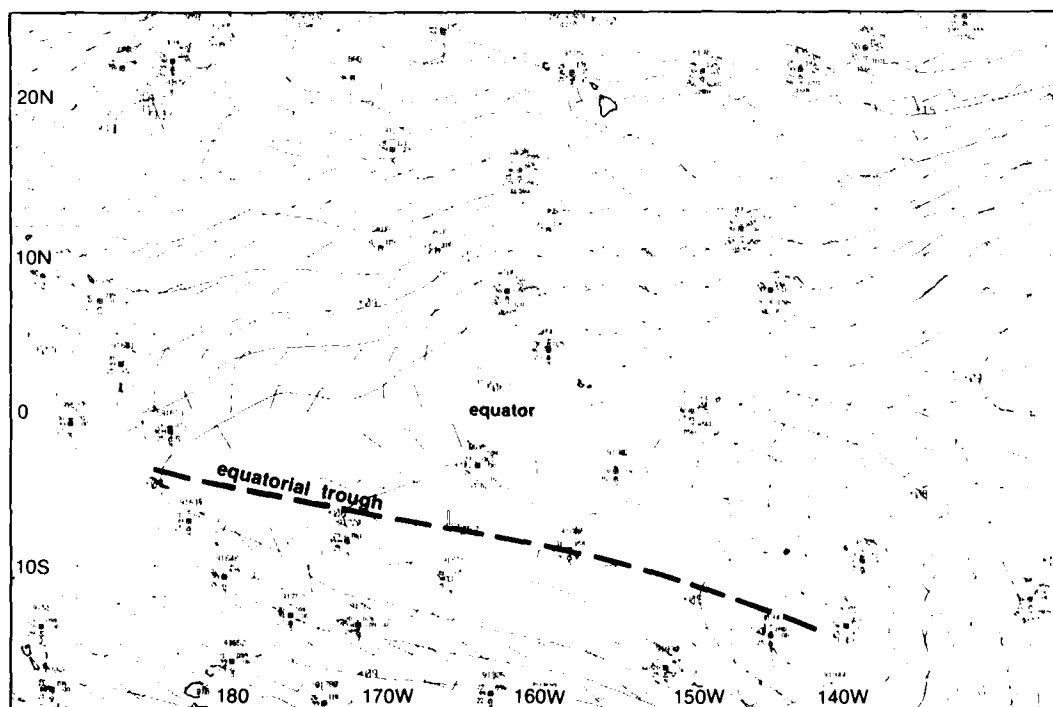
2B-5a. GOES-W. Visible Image. 2045 GMT 10 July 1984.



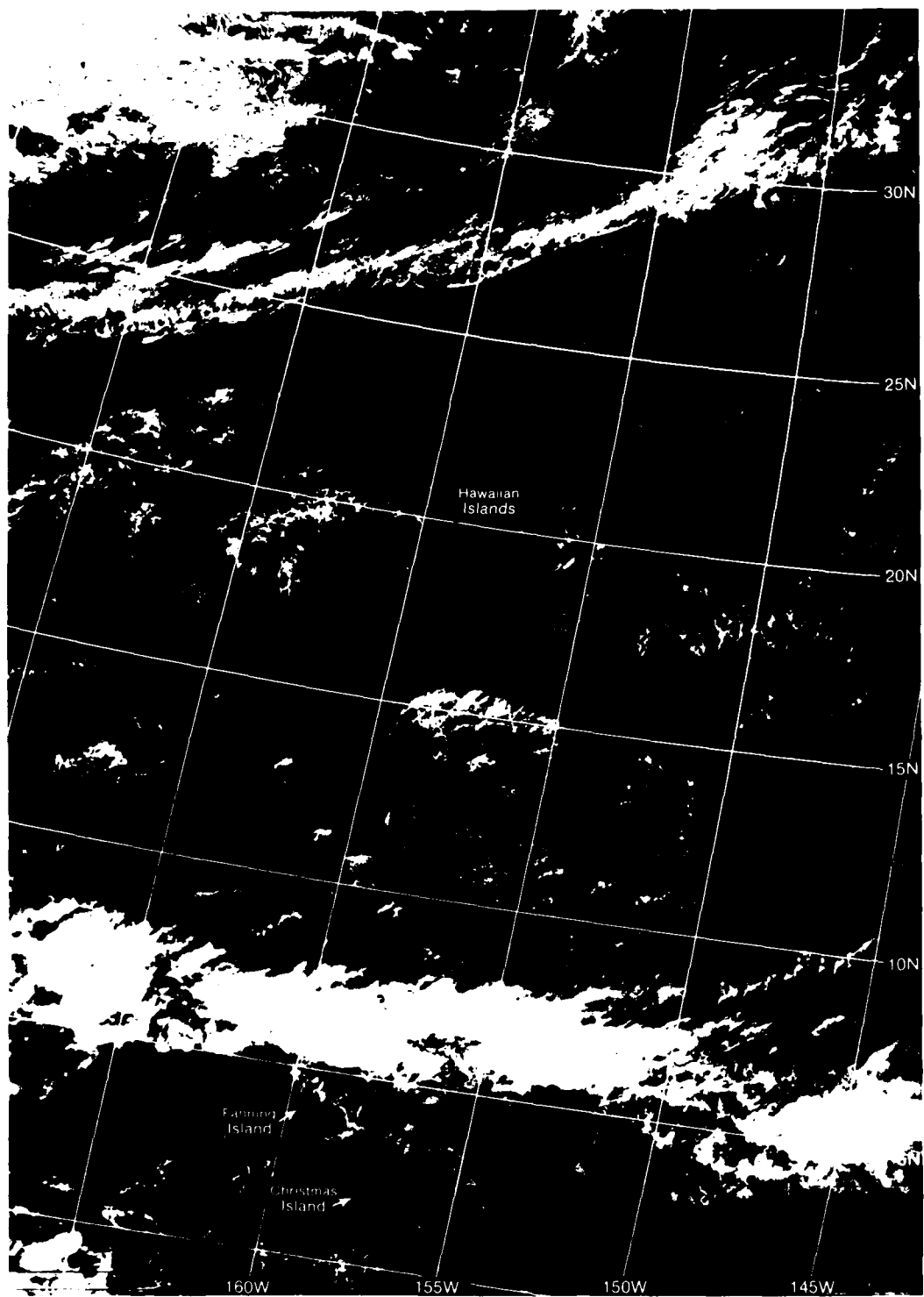
2B-5b. FNOG Surface Analysis and Wind Field. 0000 GMT 11 July 1984.



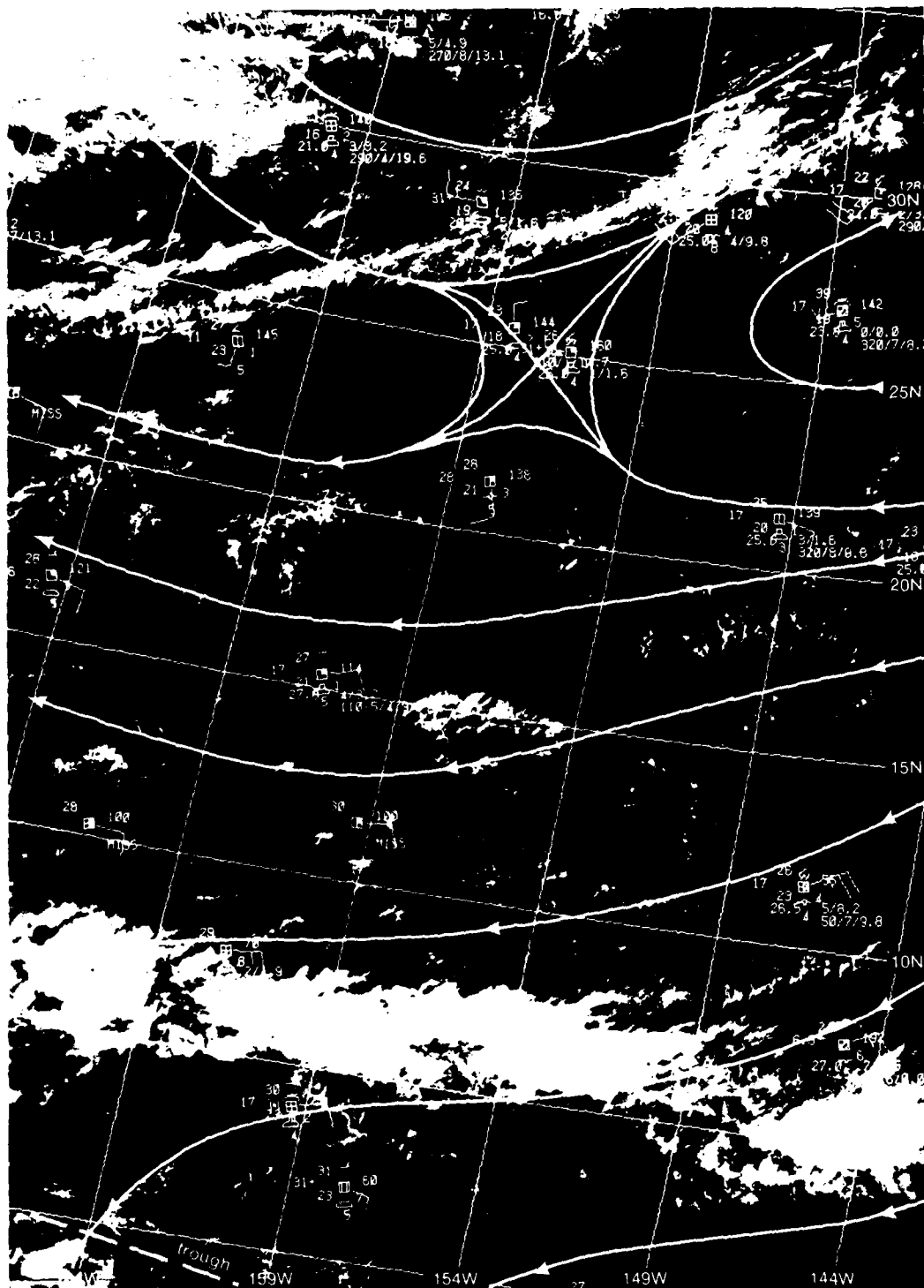
2B-6a. GOIS-W Visible Image, 2045 GMT 9 December 1977



2B-6b. FNOC Surface Analysis and Wind Field, 0000 GMT 10 December 1977



2B-7a. F-1. DMSP LF Low Enhancement. 2144 GMT 9 December 1977.



2B-7b. F-1. DMSP LF Low Enhancement. 2144 GMT 9 December 1977.
Surface Reports (0000 GMT 10 December) and Streamlines.

Case 2 Identification of Planetary Boundary Layer Height Changes from Satellite Imagery

In the eastern sector of semi-permanent anticyclones, such as off the west coast of North America, a marked increase in the height of the planetary boundary layer is often associated with the passage of a ridge line. The eastern sector of these anticyclones is generally covered by open- and closed-cell stratocumulus. Observations indicate that the stratocumulus cloud element size in these cellular cloud patterns is related to the boundary layer height—it is highest where the stratocumulus cloud element size is largest. This relationship can be used to identify ridge lines in the low-level flow field. The ridge line is located where the cloud elements in the cellular patterns change abruptly in size—from small cloud elements to large cloud elements.

Such abrupt changes in boundary layer height (which are always capped by an inversion), profoundly effect radio and radar propagation. For this reason identification of areas where boundary layer height changes occur is of great significance to Navy tactical operations.



2B-10a F-6 DMSP IF Special Enhancement. 1327 GMT 26 April 1984.

2B-10

*Ridge Line Passage
Guadalupe Island, Mexico
Tropical Eastern North Pacific
April 1984*

26 April

The DMSP infrared image at 1327 GMT (2B-10a) shows the eastern North Pacific in the region off southern California and the Baja Peninsula. The image is enhanced to emphasize contrast at the warm end of the DMSP-sensed temperatures so that clouds only slightly cooler than the sea appear white. Note that large cloud cells appear in the northern 2/3 of the image, while much smaller cloud elements dominate the lower 1/3. Smaller cloud lines are interspersed among the cellular cloud patterns, and in the northern portion, tend to define northwesterly flow which turns to northeasterly flow in the bottom 1/3 of the image.

The streamline analysis (2B-11a) superimposed on the DMSP image is based on surface observations and cloud lines. It can be seen that a ridge line is defined by the streamlines along approximately 30° N. The ridge line coincides with the transition region where cloud elements change from large to small sizes.

Guadalupe Island, near 30° N, 121° W, is perturbing the low-level flow and gravity waves are observed extending southeastward to the Baja Peninsula. These waves, which require a strong low-level inversion for formation, are aligned at a sharp angle from the surface flow. Winds therefore back with height indicating strong cold air advection, which is obviously occurring in this example. A cloud line also extends to the south-southeast in the lee of Guadalupe Island as a result of the perturbed flow below the inversion.

Sounding data from Guadalupe Island at 0000 GMT on 26 April (2B-12b) show a pronounced inversion with base at 700 m. Surface temperature is 17° C and temperature at the base of the inversion 8.2° C. The computed Lifting Condensation Level (LCL) is 946 mb. Note that the FNOC surface analysis (2B-12a) shows the ridge line to the north of Guadalupe Island.

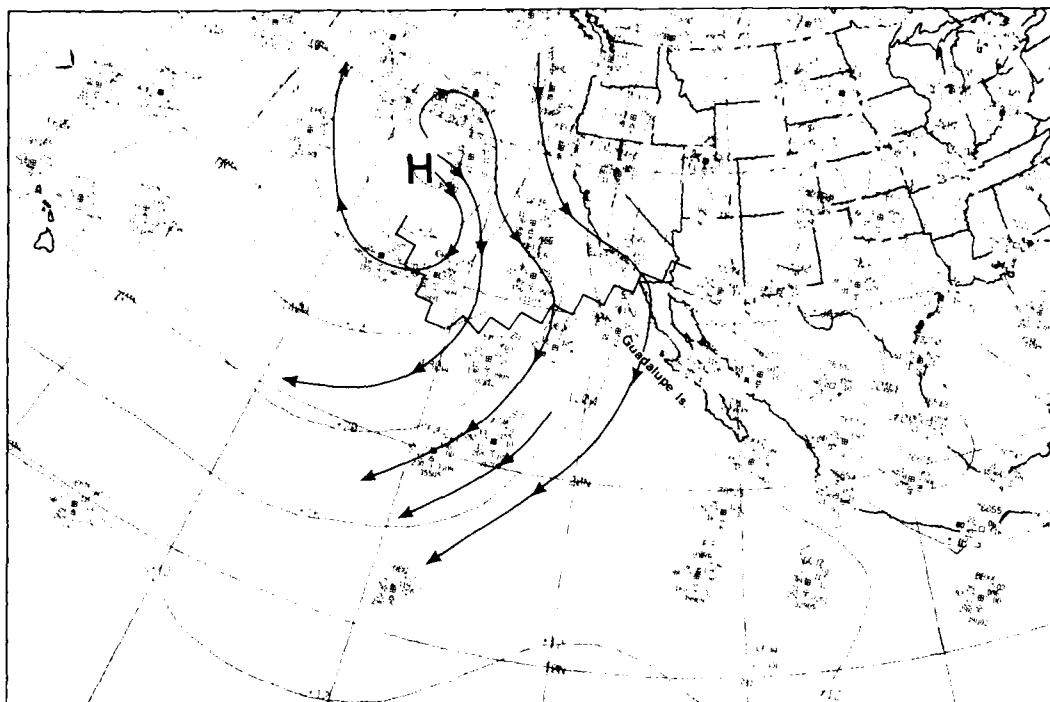
Twenty-four hours later, the ridge line has passed Guadalupe Island (2B-13a), and the sounding (2B-13b) shows a pronounced deepening of the boundary layer, from 700 to 1,500 m. Surface temperature cooled from 17° to 15.9° C, and the temperature at the base of the inversion cooled from 8.2° to 1.4° C. The LCL increased from 946 to 841 mb.

These effects illustrate the pronounced change in the height of the marine planetary boundary layer resulting from the passage of a ridge line under conditions of cold air advection.

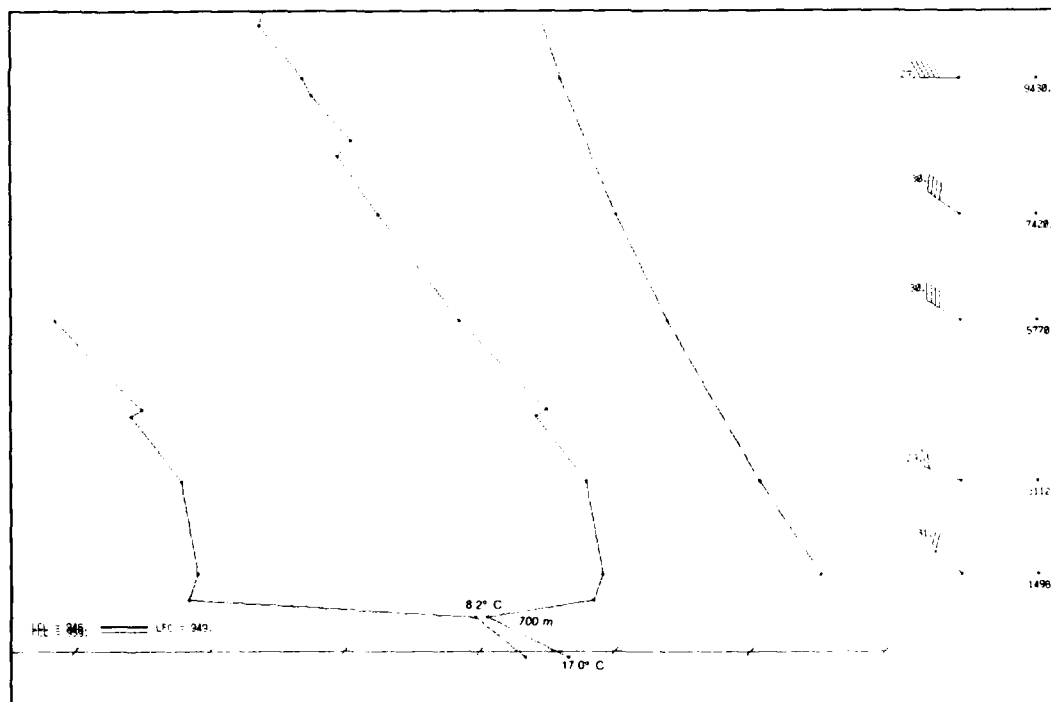
2B 10 B



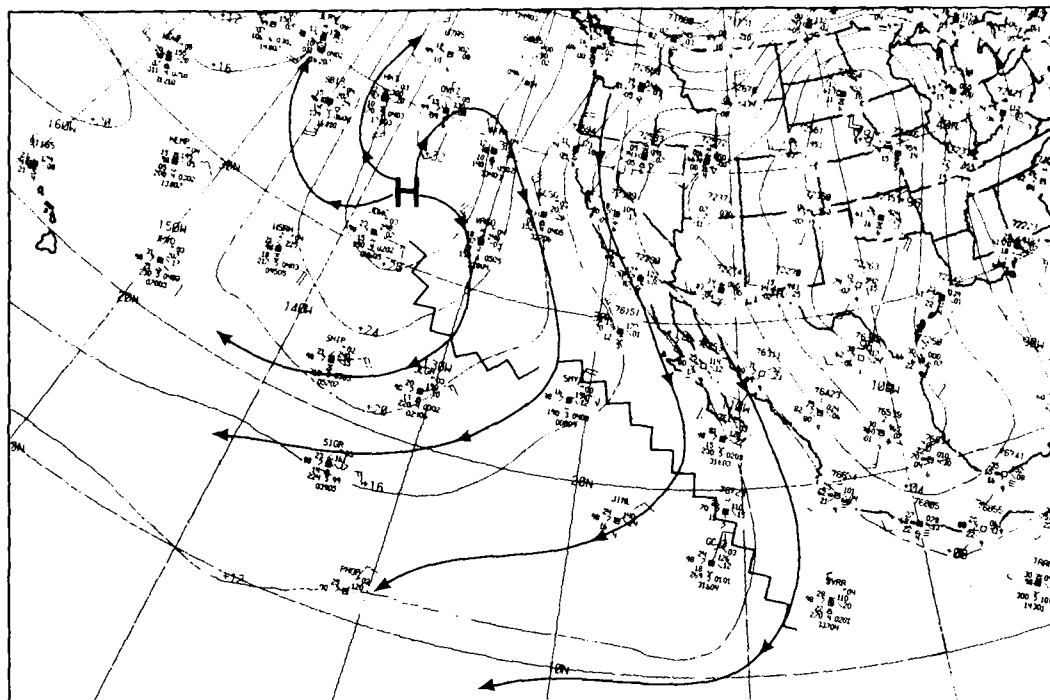
2B-11a F-6 DMSP TF Special Enhancement 1327 GMT 26 April 1984. Surface Reports (0000 GMT) and Streamlines.



2B-12a. ENOC Surface Analysis. 0000 GMT 26 April 1984.



2B-12b. RAOB. Guadalupe Island, Mexico. 0000 GMT 26 April 1984.



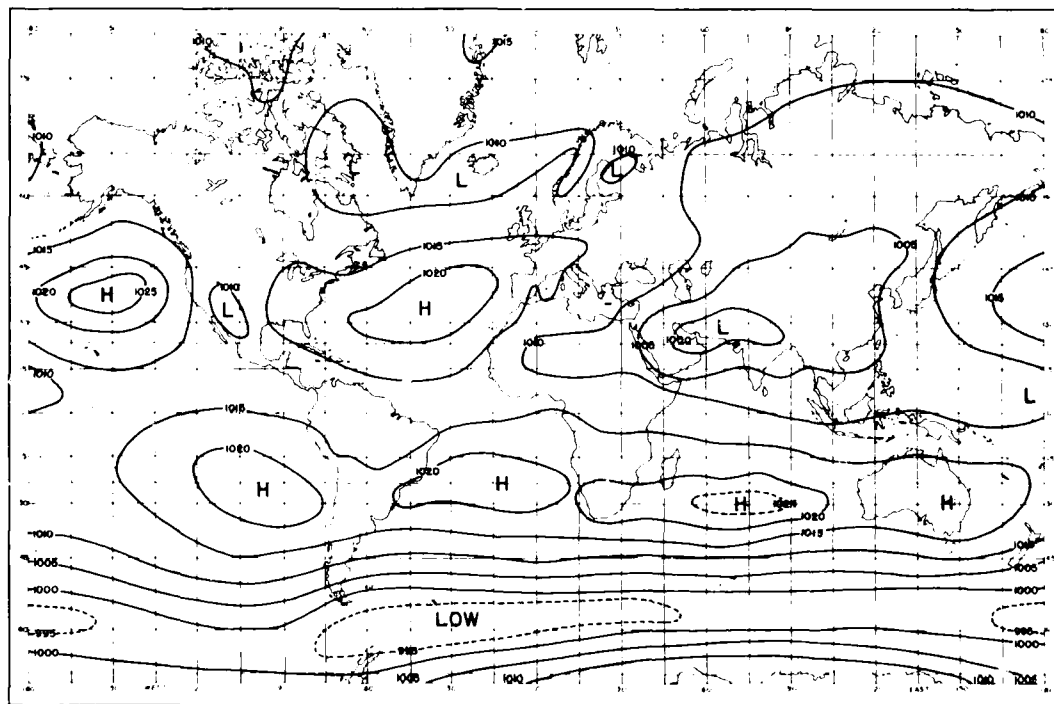
Case 3 *Use of Sunlint in Locating Ridge Lines in the Tropics*

During July, the mean sea-level pressure distribution over the North Pacific and the North Atlantic (2B-15a) shows that the center of mid-latitude surface highs and associated ridge lines are generally located between 30° and 45° N.

Occasionally, however, mid-latitude surface anticyclones are displaced well to the south of their normal position by troughs, fronts, or shear lines extending into tropical latitudes. Conventional data over oceanic regions in the tropics are often very sparse, so that locating ridge lines in the anticyclones is difficult. Satellite visible imagery from polar-orbiting spacecraft often reveal sunlint effects that permit identification and precise location of ridge lines in the anticyclones.

Reference

Haurwitz, B., and J. M. Austin, 1944: *Climatology*. McGraw-Hill Book Co., Inc., New York, 410 pp.



2B-15a Mean sea-level pressure (mb) in July. (After Haurwitz and Austin, 1944.)

*Location of a Ridge Line in Advance
of a Cold Front
Tropical Eastern North Pacific
July 1979*

9 July

The TIROS-N visible image at 2331 GMT (2B-16a) shows a cold frontal cloud band extending from the West Coast southwestward toward the Hawaiian Islands. Notice that the frontal cloud band is the boundary between the distinct stratocumulus cloud field to the north of the front and the cloud-free zone immediately to the south. In the cloud-free zone, a sunglint pattern is evident which shows linear dark areas from near 28° N, 130° W to 25.5° N, 137° W. The dark areas imply calm seas which result from a wind speed minimum along the ridge line in advance of the frontal band.

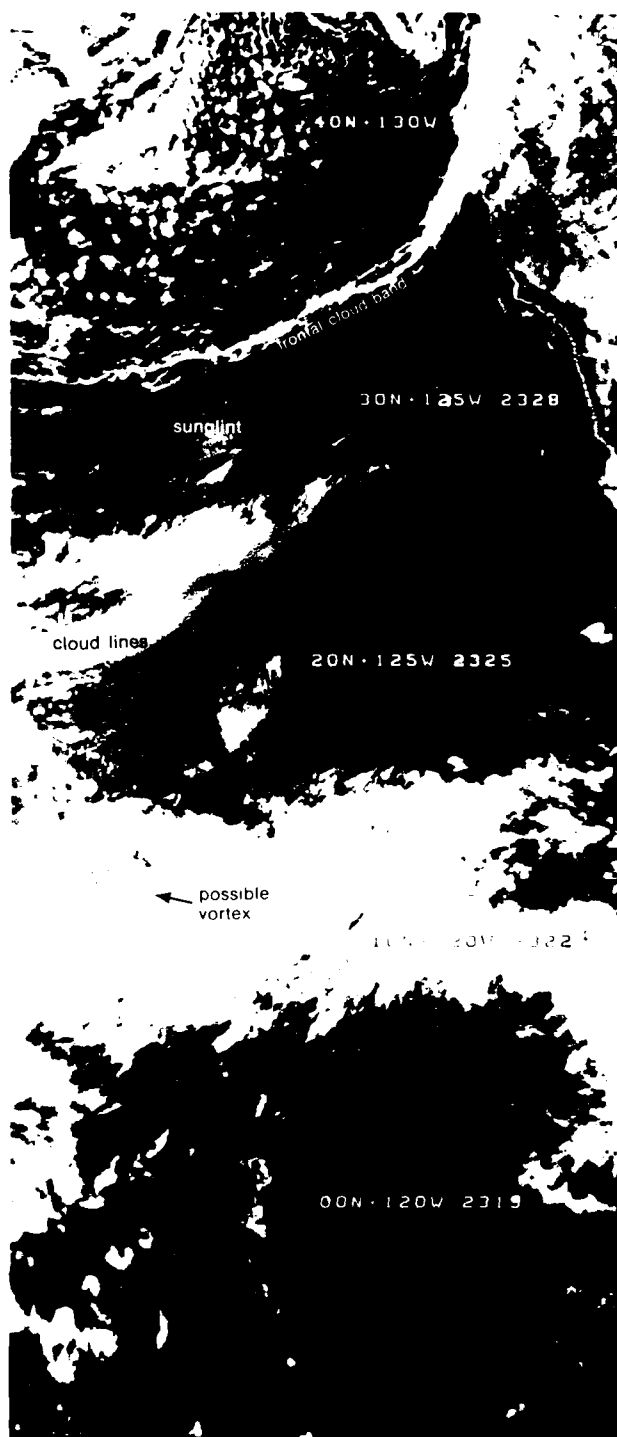
In the eastern North Pacific, ridge lines are commonly found about 1 to 4 deg in advance of frontal cloud bands, and they tend to be aligned parallel to the frontal bands over long distances. The absence of cloudiness, just south of the frontal band, from the West Coast to the extreme western edge of the TIROS-N image suggests a narrow zone of high pressure extending through the region.

The FNOC surface analysis at 0000 GMT on 10 July (2B-17a), shortly after the time of the TIROS-N image, confirms the presence of a high-pressure area over the tropical eastern North Pacific with a ridge extending to the West Coast. The location of the axis of the dark areas in the sunglint pattern is superimposed on the analysis; note that it passes through the central portion of the high-pressure area.

A close examination of cloud lines south of the ridge line, just north of the ITCZ cloudiness (2B-16a), shows the narrow spacing and streaked appearance typical of cloud line development in moderately strong flow of 15-20 kt. Wind speeds decrease markedly south of the region. This provides the shearing effect favoring vortex development within the ITCZ. This type of development appears to be in progress, judging from curvature effects in cloudiness over the region.

Important Conclusions

- 1 Clear regions in advance of frontal cloud bands in the eastern North Pacific are normally associated with ridge line axes running through the central portion of the region.
- 2 Sunglint effects can be used to substantiate the exact location of the ridge line in the segment where it occurs.



2B-16a TIROS-N Visible Image 2331 GMT 9 July 1979
Mid latitude - Tropical Coverage

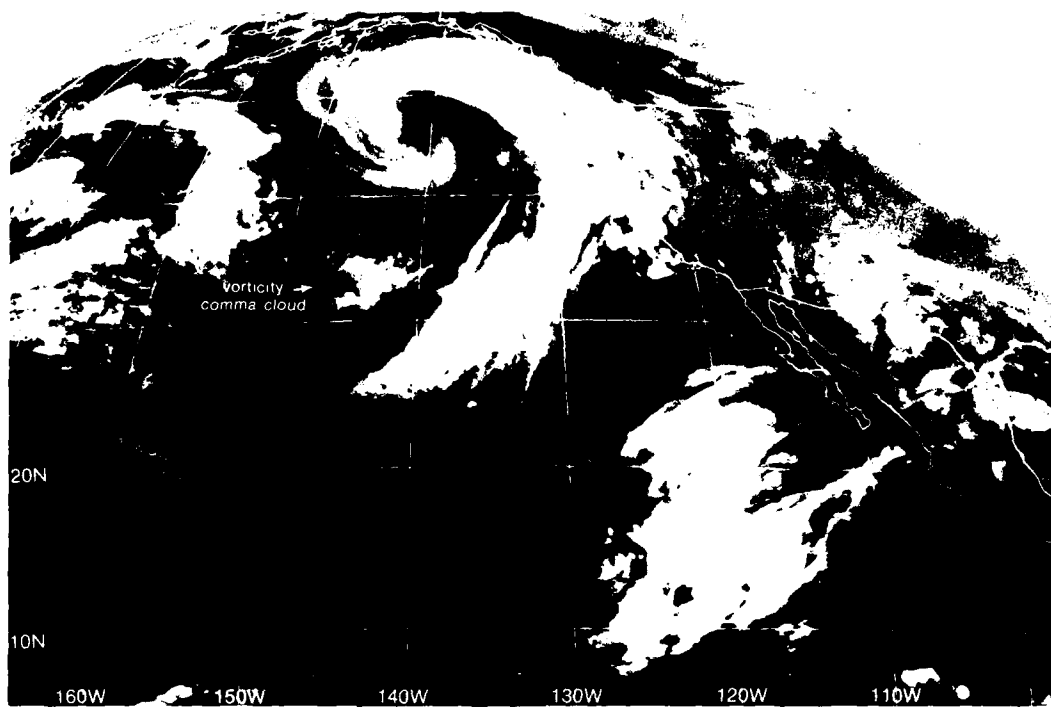
Case 4 Tropical Developments of Polar Origin

An important family of storms which affect the eastern North Pacific and the West Coast during winter and spring are upper tropospheric cyclones characterized by tracks from the southwest or south. These tropical/sub-tropical upper-level systems are unique from typical mid-latitude cyclones because they move into southern California from the south or southwest, contain large amounts of precipitable water extracted from the tropics, have maximum intensity near 200 mb, and often have heavy showers near the low center.

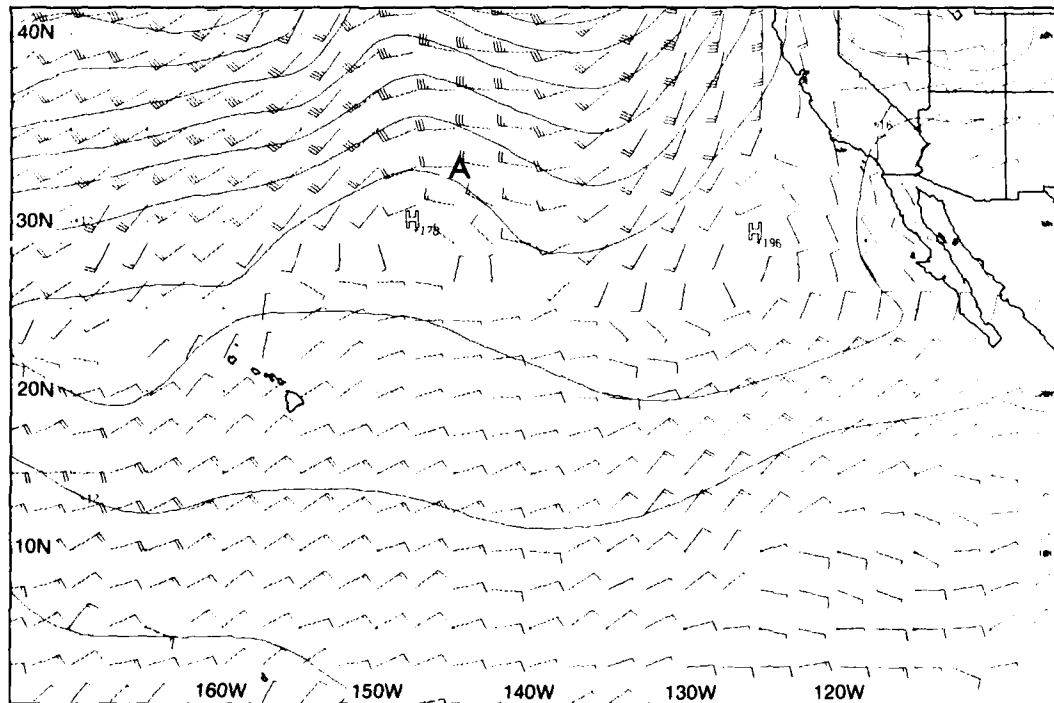
Numerical prognosis and synoptic identification of these systems are generally poor since a combination of insufficient data for initialization (with the exception of satellite winds) and inability to forecast precipitation location and amount accompany these disturbances which tap and collect abundant tropical moisture and transport it northward to mid-latitudes.

The origin of these sub-tropical tropical upper lows can be either low or mid-latitude, but they usually display features characteristic of tropical weather. Normally most intense systems originate in mid-latitudes with polar influences, penetrate equatorward, attain tropical characteristics, then swing northeast over southern California.

2B (case 4



2B-20a. GOES-W. Infrared Image. 1215 GMT 8 January 1981.



2B-20b. FNOc Surface Analysis and Wind Field. 1200 GMT 8 January 1981.

*Induced Frontal Wave (Vorticity Comma) Cyclogenesis
Tropical Eastern North Pacific
January 1981*

8 January

The GOES-W image at 1215 GMT (2B-20a) reveals a cold frontal band extending from near the Hawaiian Islands to the Pacific Coast of North America, with a cloud vortex located near 45° N, 140° W. A vorticity comma cloud **A** is evident in the cold air behind the front. The comma cloud shows no perturbation in the surface analysis and wind field (2B-20b) which indicates ridging in the region. At 500 mb (2B-21b), the comma cloud is located in a broad westerly current, and at 200 mb (2B-21a) the wind field shows that the comma system is in advance of a westerly (jet) windspeed maximum (100 kt).

9 January

Approximately 12 hours later, the GOES-W image at 2345 GMT (2B-22a) reveals that the vorticity comma cloud has merged with the southern end of the frontal zone. Such a merger usually induces frontal wave cyclogenesis. Evidence that this is occurring is the anticyclonically turning cirrostratus shield which obscures much of the frontal band to the north. The developing cloud vortex will emerge from the west edge of this shield (see NTAG, Vol. 4, Part I, Sec. 2).

The FNOC surface analysis and wind field (2B-22b) shows a sharp but weak trough development associated with the frontal wave **B**. The disturbance **B** is located in a cold trough at the 500-mb level (2B-23b). The FNOC 200-mb wind field and superimposed streamline analysis (2B-23a) is especially interesting in that it reveals a sharp upper-level trough on the west side of the frontal wave cloud pattern with diffluent winds and a divergence asymptote overlying the wave development. Such a configuration is strongly favorable for rapid intensification of the system. Note that jet-force winds are largely west of the trough axis.

By 1215 GMT, intensification is obvious in the GOES-W image (2B-24a) which reveals an emerged comma-shaped cloud defining the system **B**, and suggesting a center near 24° N, 134° W. Note that the system has tracked over 10 deg to the southeast from the initial view (2B-20a), 24 hr earlier.

The FNOC surface analysis and wind field (2B-24b) shows a low-pressure center and weak trough associated with the developing storm **B**. At the 500-mb level (2B-25b), the developing storm appears at the base of a trough. A streamline analysis of the wind field at the 200-mb level (2B-25a) continues to show diffluence in advance of a trough over the disturbance a continuing favorable pattern for intensification. Jet-force winds remain west of the trough axis.

10 January

By 1215 GMT, a well-defined cyclonic cloud signature **C** is evident on GOES-W image (2B-26a). Moderate development has taken place as indicated by increased solid-appearing cirrus cloudiness and increased cloud curvature around the upper low.

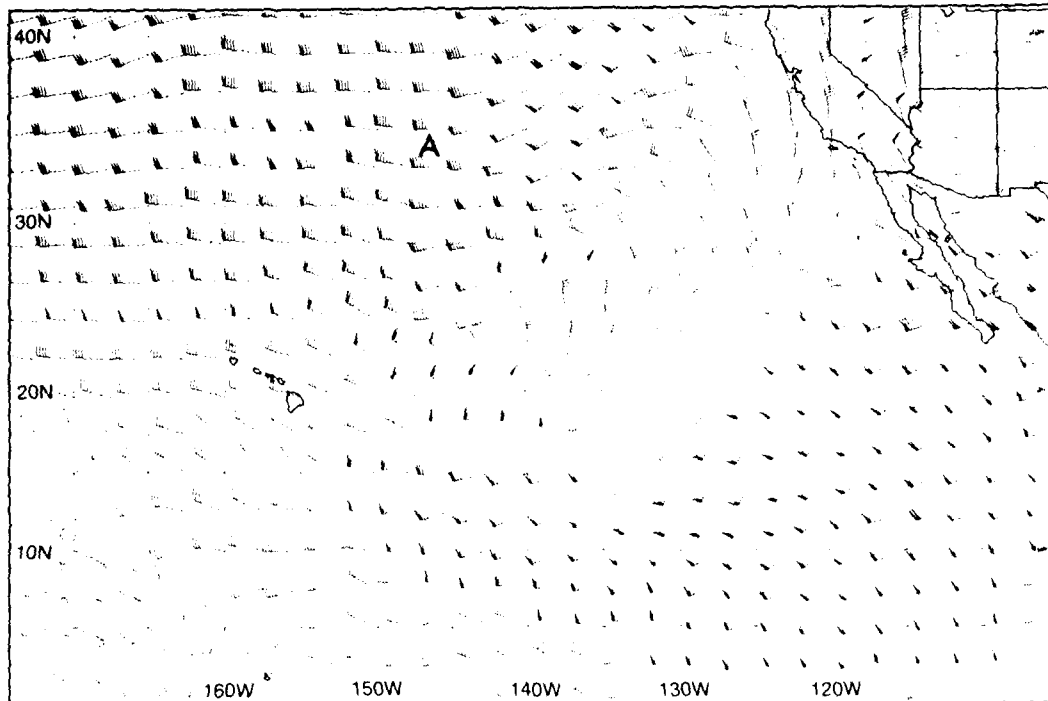
The FNOC surface analysis and wind field at

1200 GMT (2B-26b) shows that the disturbance is located in a broad low-pressure region having dual centers south of the disturbance as revealed by the satellite data. Note that, unlike mid-latitude disturbances, easterly winds are apparent both to the north and south of the storm center, similar to a tropical development.

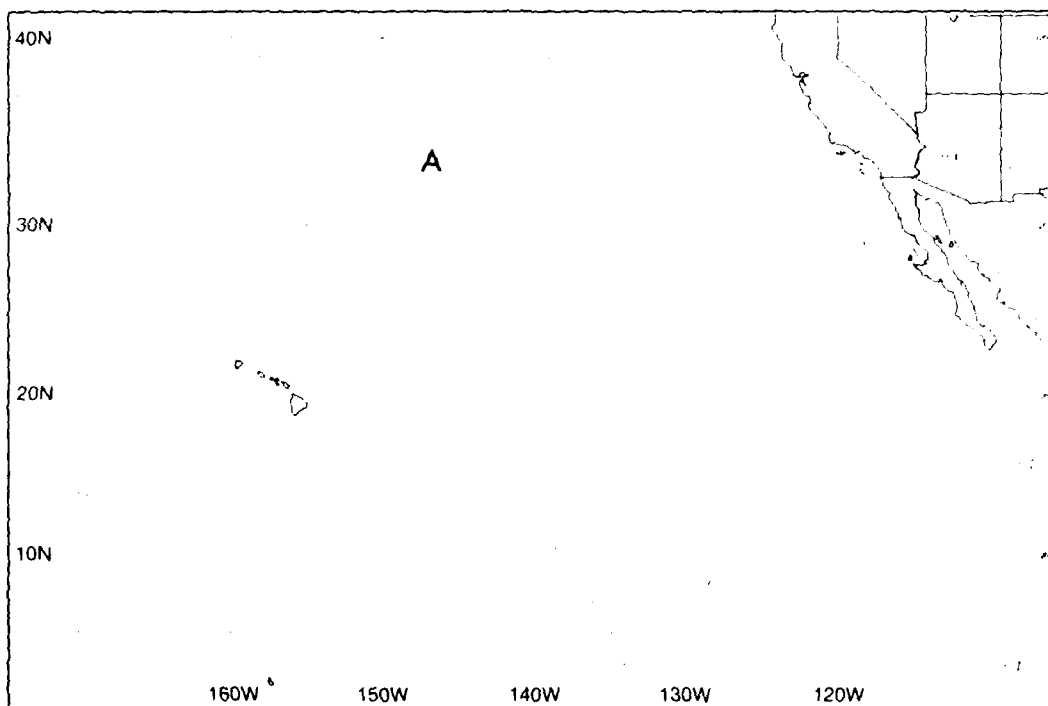
At 500 mb (2B-27b), a low-pressure center **C** is located to the northwest of the developing surface disturbance (2B-26b) a location favorable for the further intensification of the storm.

The FNOC 200-mb analysis with superimposed streamlines (2B-27a) shows that the system is ideally positioned in the positive vorticity advection region in advance of the upper-level trough, where further intensification is optimized, as jet-force winds have rotated around the trough axis to the east side. Note also pronounced speed divergence from the trough to the ridge downstream from the storm which could add to the intensification potential.

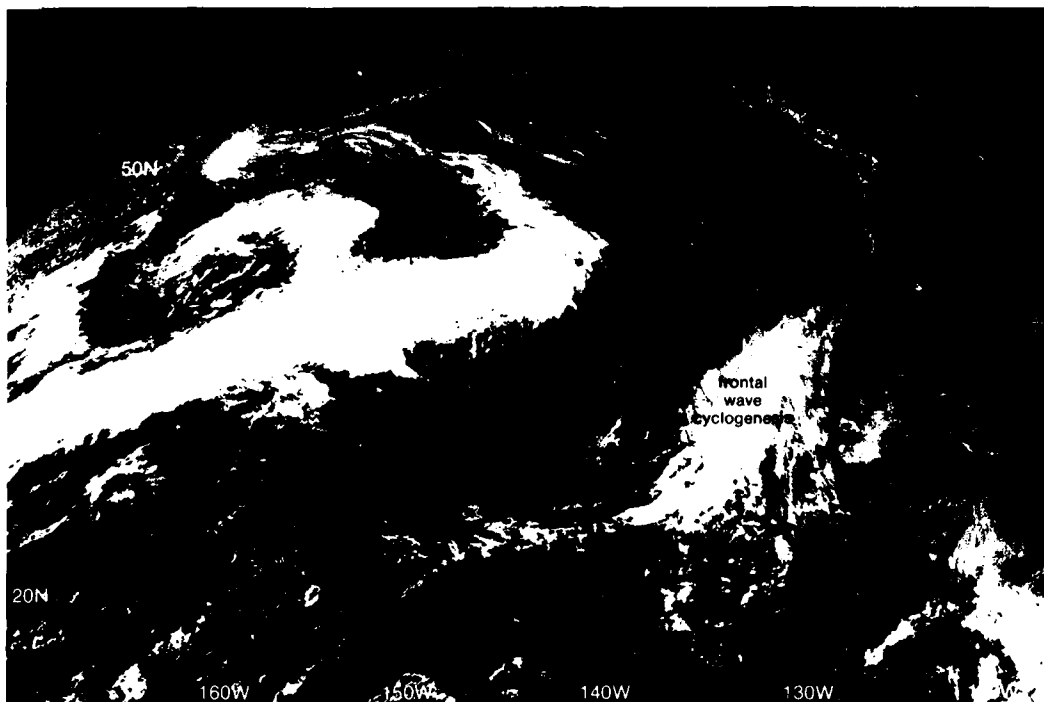
Continued on page 2B-28



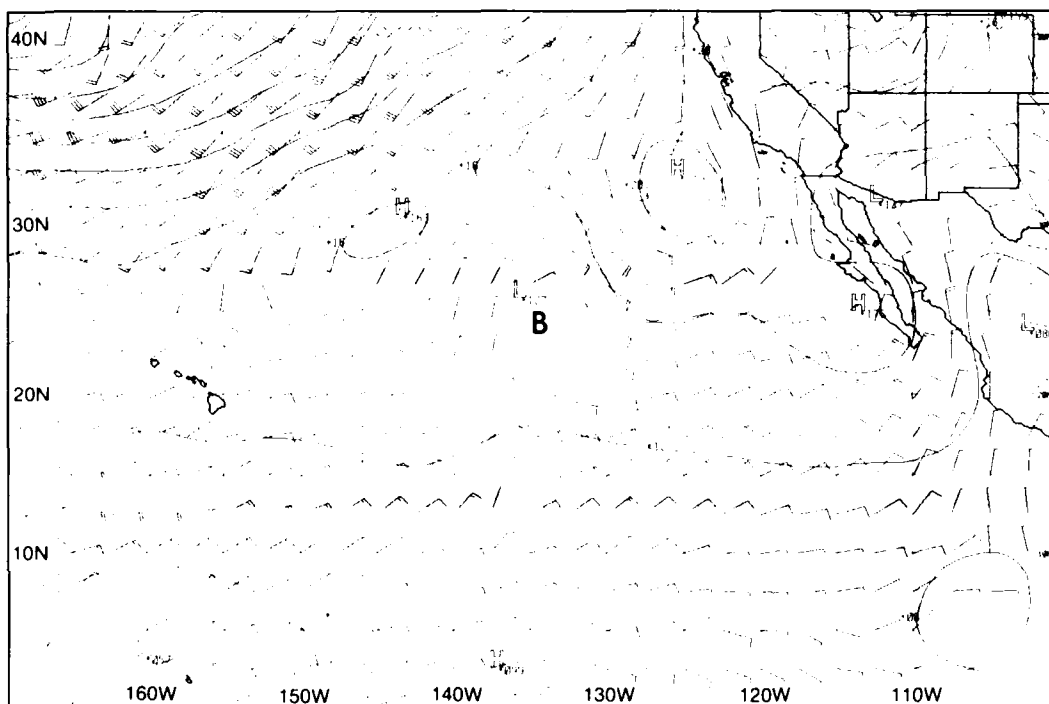
2B-21a. FNOC 200-mb Wind Field. 1200 GMT 8 January 1981.



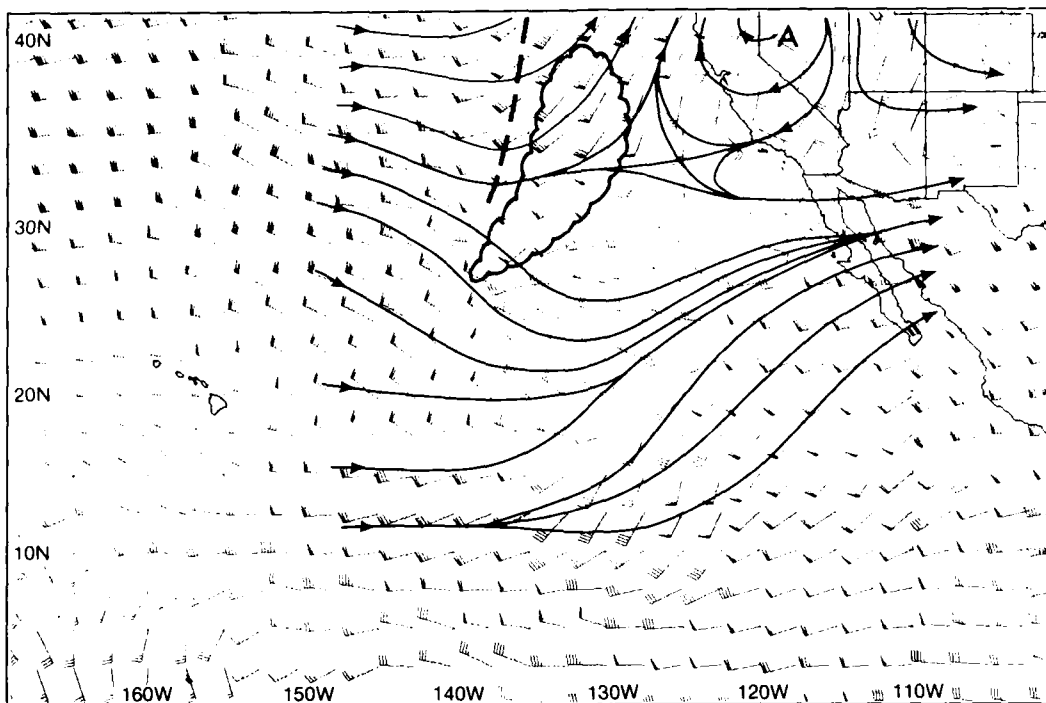
2B-21b. FNOC 500-mb Analysis. 1200 GMT 8 January 1981.



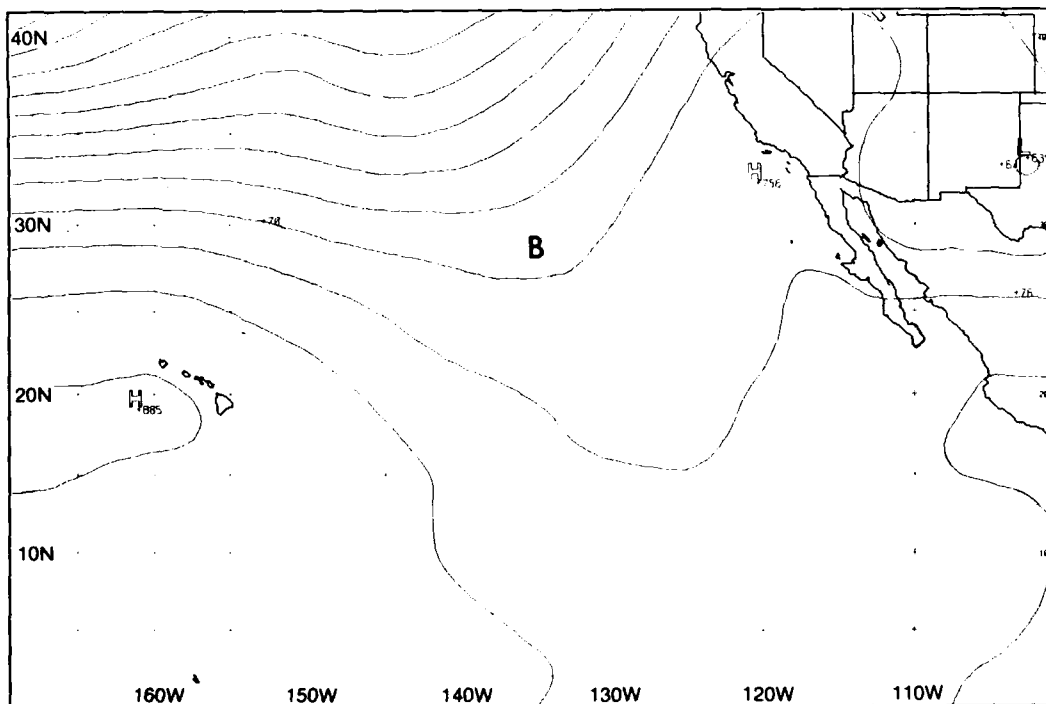
2B-22a. GOES-W. Visible Image. 2345 GMT 8 January 1981.



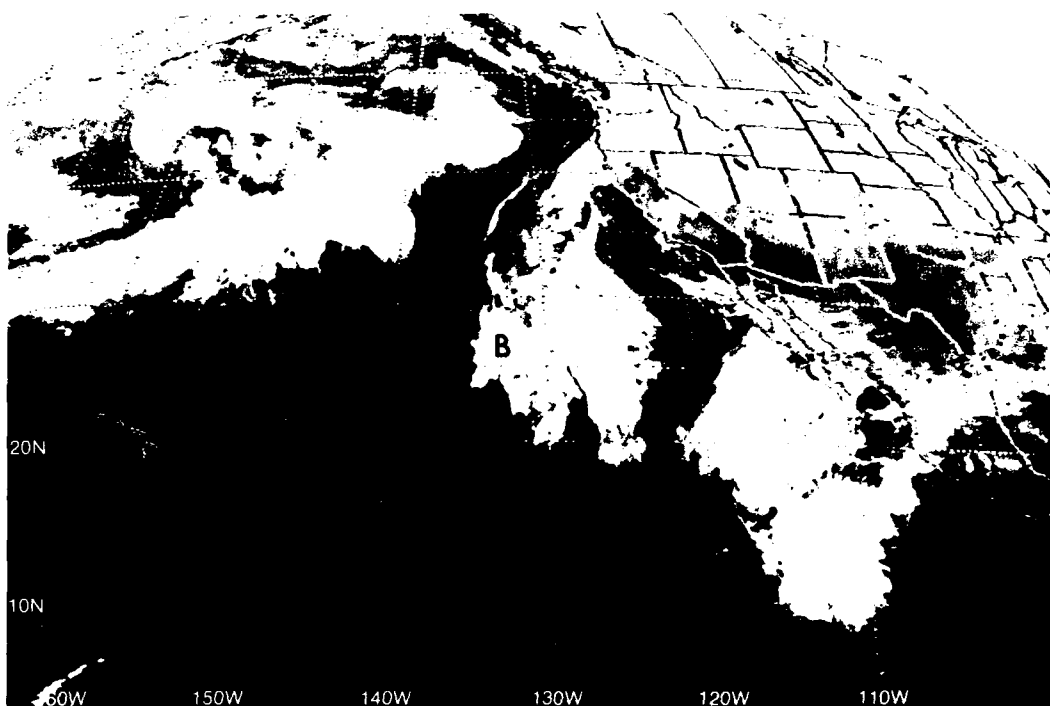
2B-22b. ENOC Surface Analysis and Wind Field. 0000 GMT 9 January 1981.



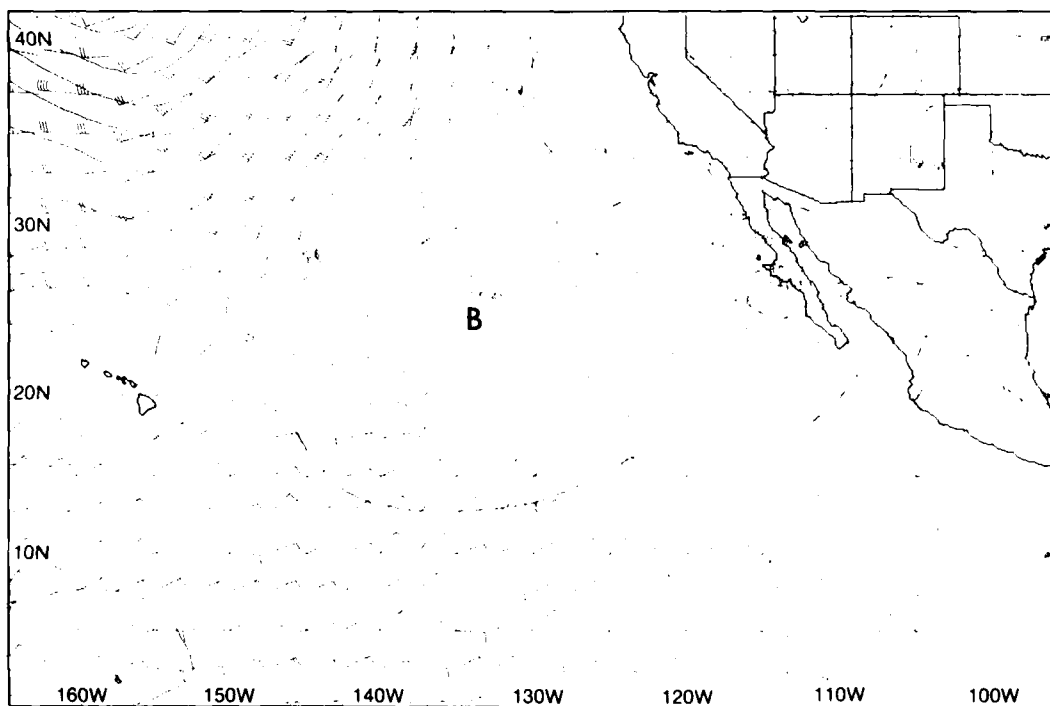
2B-23a. FNOG 200-mb Wind Field and Streamlines. 0000 GM 9 January 1981.



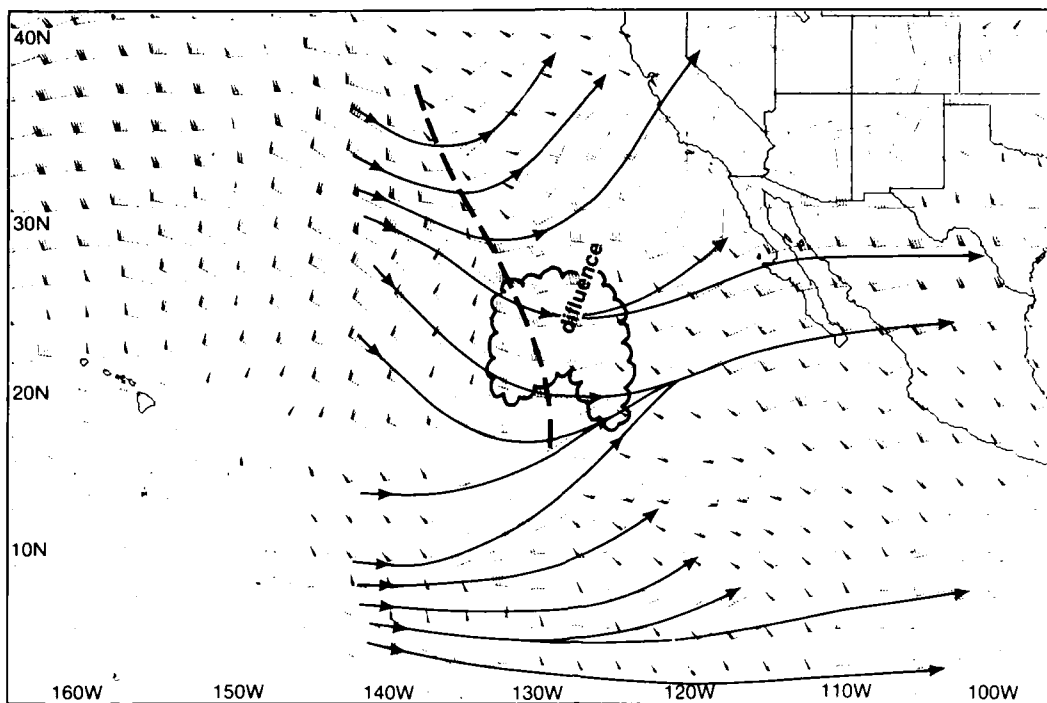
2B-23b. FNOG 500-mb Analysis. 0000 GMT 9 January 1981.



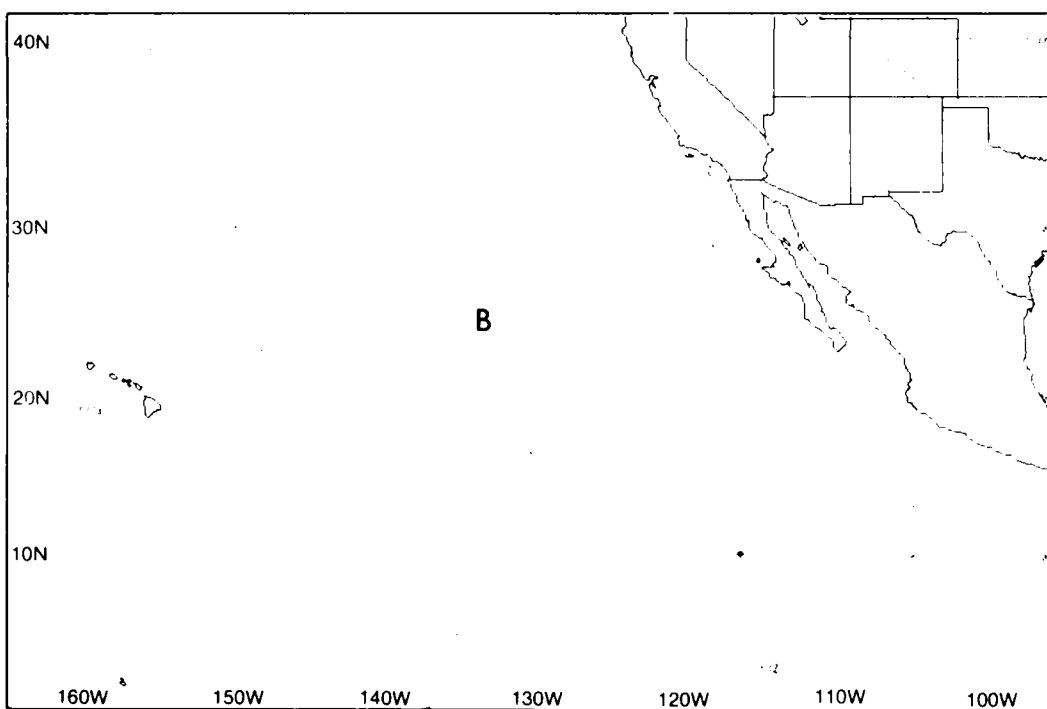
2B-24a. GOES-W. Infrared Image. 1215 GMT 9 January 1981.



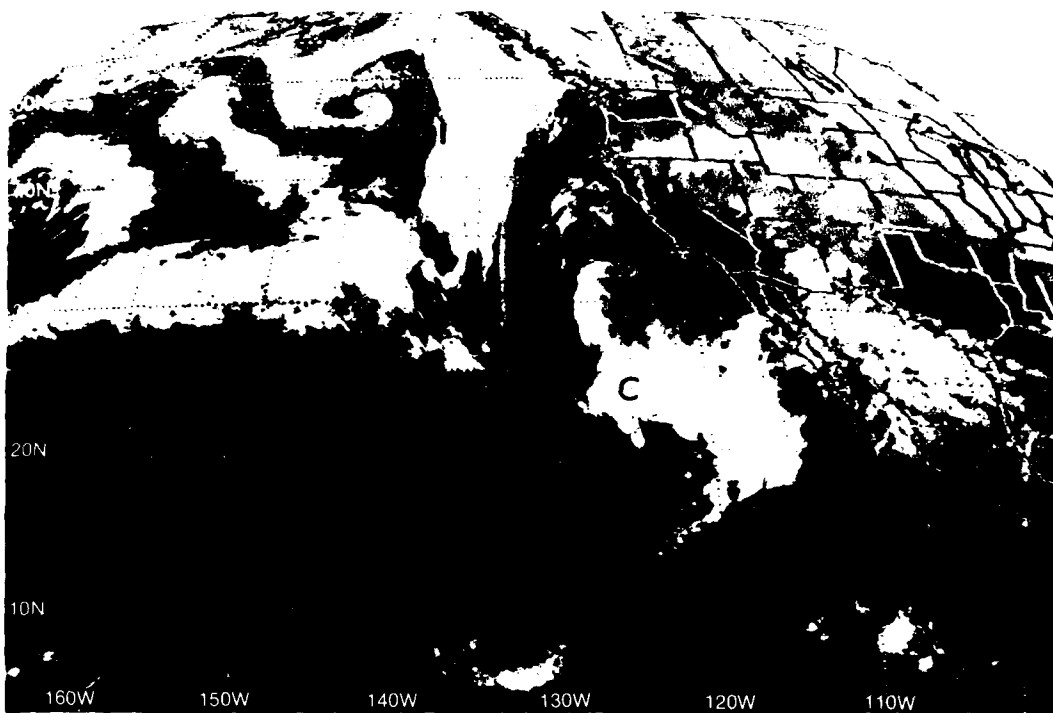
2B-24b. FNOG Surface Analysis and Wind Field. 1200 GMT 9 January 1981.



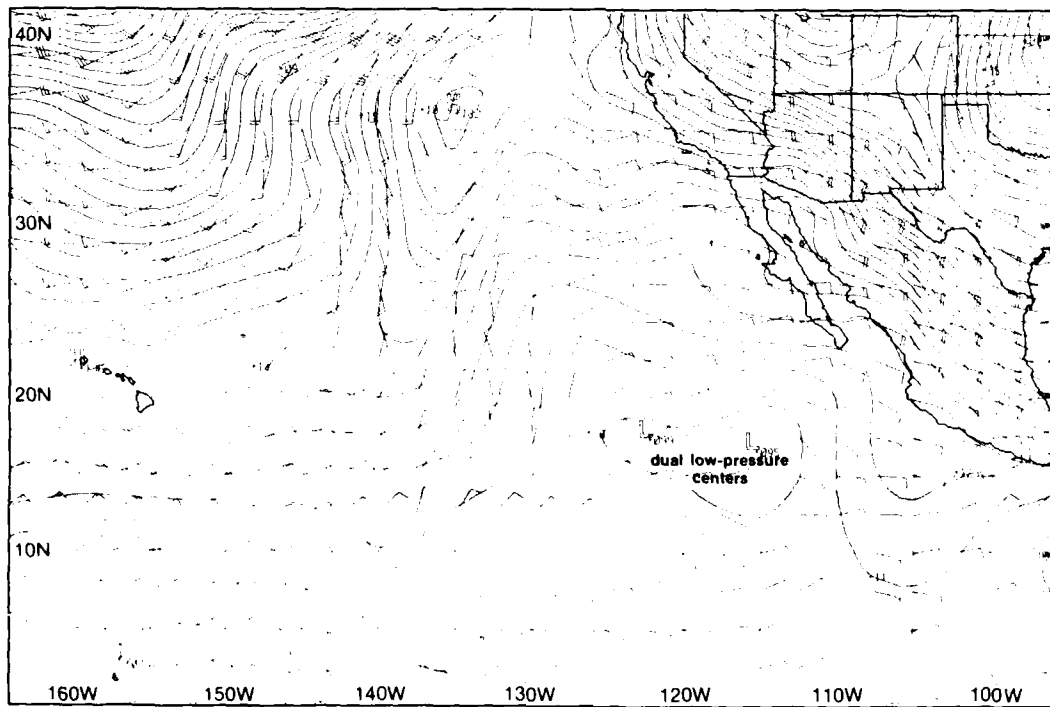
2B-25a. FNOC 200-mb Wind Field and Streamlines. 1200 GMT 9 January 1981.



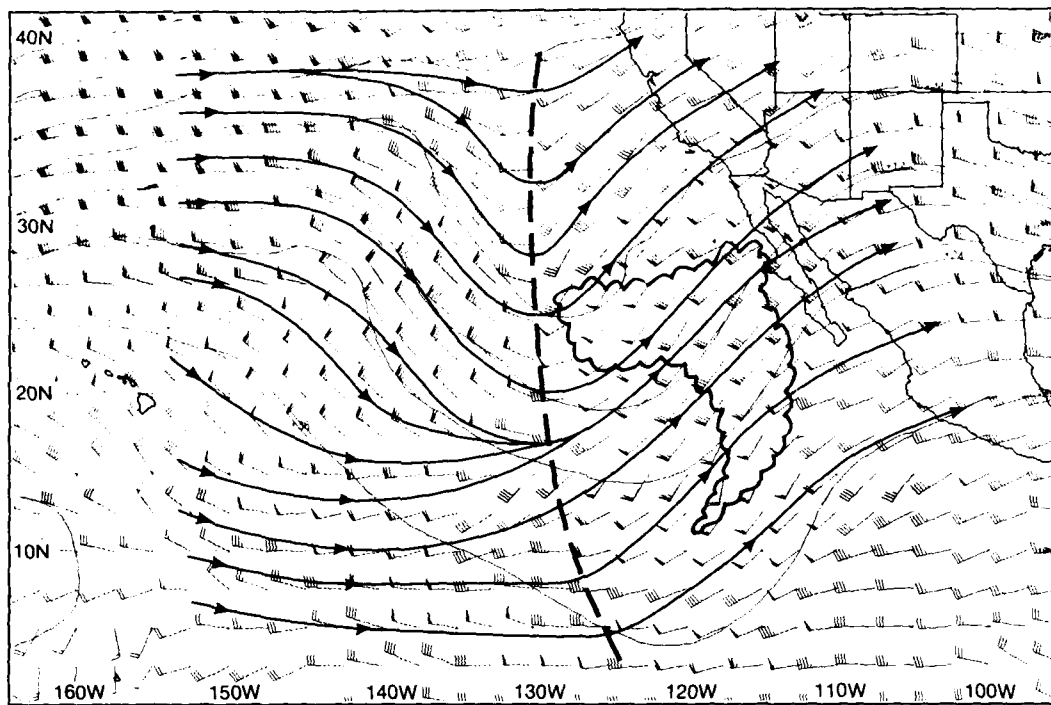
2B-25b. FNOC 500-mb Analysis. 1200 GMT 9 January 1981.



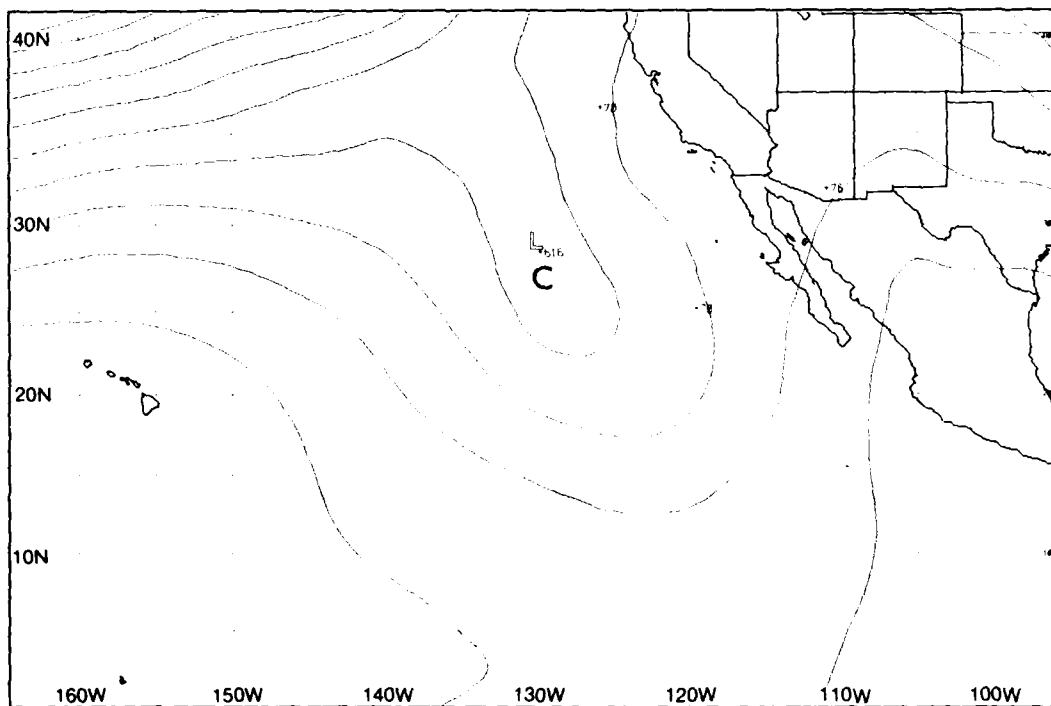
2B-26a. GOES-W. Infrared Image. 1215 GMT 10 January 1981.



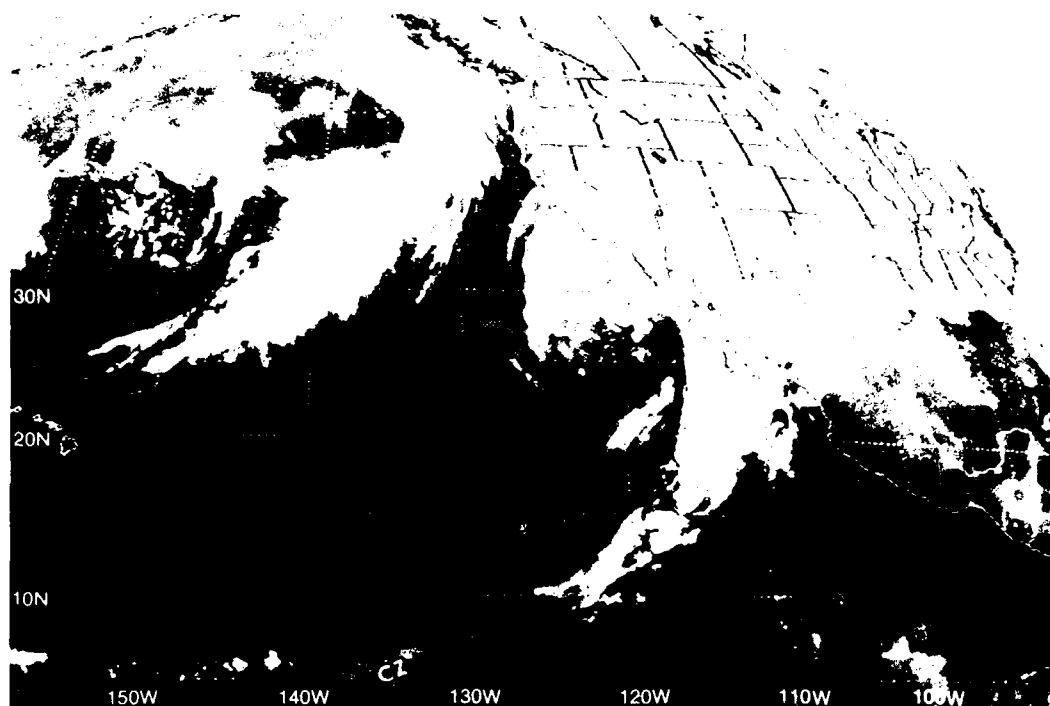
2B-26b. FNOG Surface Analysis and Wind Field. 1200 GMT 10 January 1981.



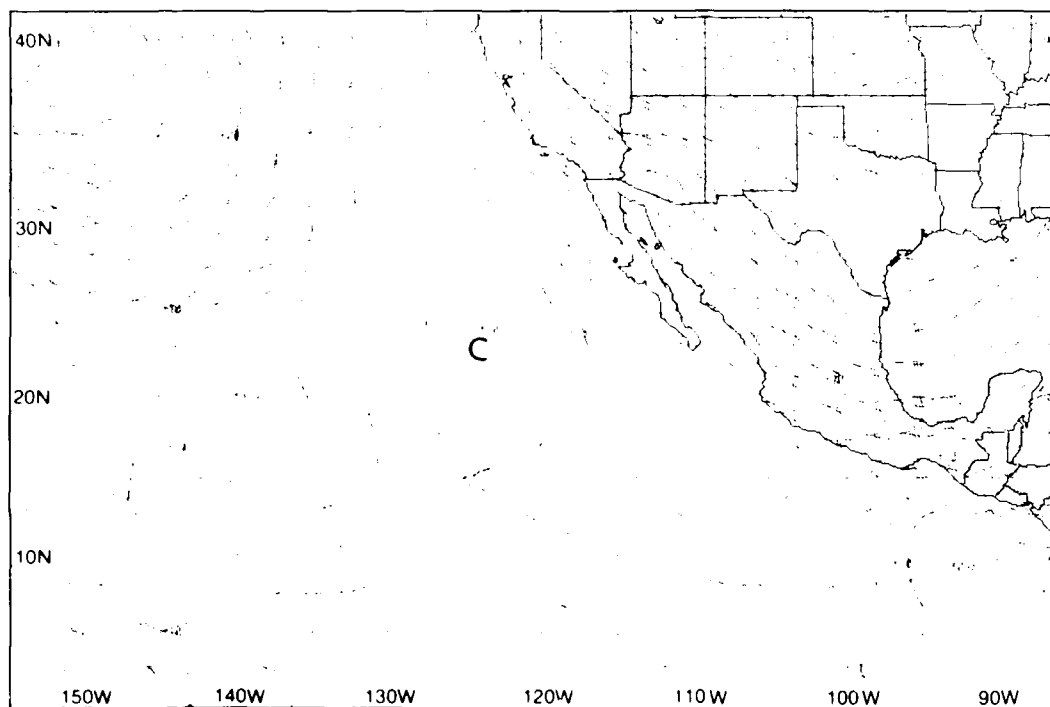
2B-27a. FNOC 200-mb Analysis and Streamlines. 1200 GMT 10 January 1981.



2B-27b. FNOC 500-mb Analysis. 1200 GMT 10 January 1981.



2B-28a GOES-W Infrared Image 1215 GMT 11 January 1981



2B-28b FNOG Surface Analysis and Wind Field 1200 GMT 11 January 1981

11 January

The low **C** attained maximum intensity at about 1215 GMT (2B-28a). Accompanying the upper-level cyclone were deep middle and high clouds, light rain, and embedded cumulonimbi. Connection of the cloud system to moisture from the equatorial convergence zone (CZ) is apparent. Unlike a typical frontal cloud system, heavy rain thunderstorms are concentrated near the upper-level circulation center. This is a common feature of these systems. Cumulonimbus clouds develop primarily as a result of cold upper tropospheric temperatures which produce unstable lapse rates. Thunderstorms near the low center are an excellent satellite identifier of the low center.

The FNOC surface analysis and wind field (2B-28b) reveals the characteristic light winds surrounding the center of this upper-level disturbance. Note that the main sensible weather events are occurring hundreds of miles from this center. Without satellite data to reveal the location of the main cloudiness surrounding the system, it would be impossible to know when and where the major weather events would occur.

It is interesting to note that, according to data on the surface analysis (2B-28b), the large spiral band extending southwestward toward the equatorial CZ is not associated with a convergence asymptote at low levels. Such a feature is a normal expectation. It is possible that the surface analysis under-estimates the existence of westerly winds south and southeast of the low center. A slight adjustment to permit this would result in a convergence asymptote near 115° W, corresponding to the location of the spiral band.

The FNOC 500-mb analysis (2B-29b) reveals the cold-core, upper-level low well offshore at its peak intensity. The low also appears strongly as a cut-off feature at the 200-mb level (2B-29a). Note the sharp anticyclonic turning of the winds at this level over the main cloud shield and the pronounced speed divergence which encourages upward vertical motion in the rain band.

12-13 January

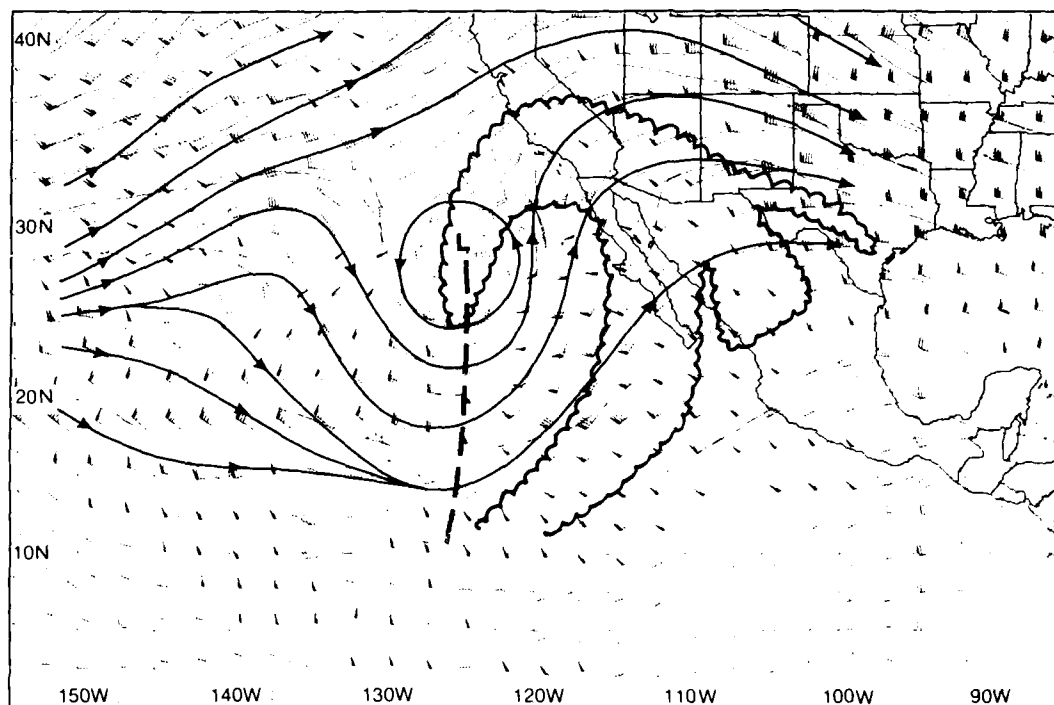
The storm **C** weakened and moved inland during this period as shown by GOES-W imagery (2B-29c and 29d). At this time the connection of the storm as a cirrus and mid-level cloud extension from the CZ was broken. This appears to be a key satellite indicator of weakening and/or transformation of the disturbance into a mid-latitude system. This normally coincides with movement of the jet core through the north-northeast sector of the low and subsequently out of the circulation.

A review of the trajectory of the storm center reveals that it moved southeastward from 8-10 January (2B-22a, 24a, and 26a) and then turned abruptly northeastward from 11-13 January (2B-28a, 29c, and 29d) to provide a "surprise" rainstorm to southern California and the southwestern United States.

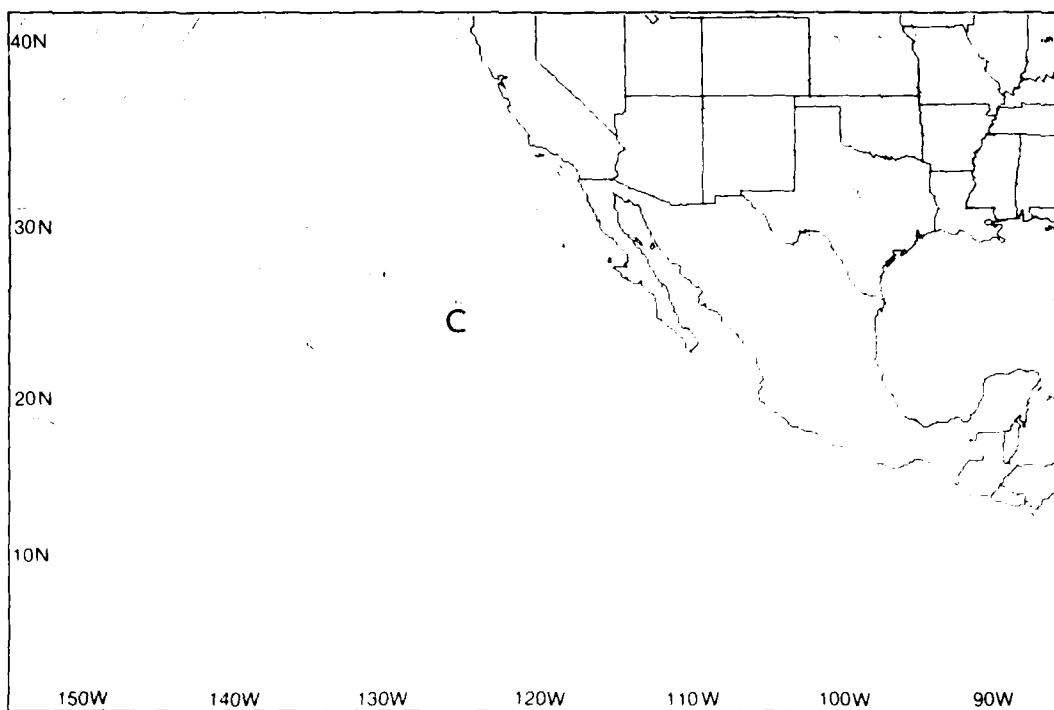
A change in direction of movement of the storm coincided with a movement of the upper-level jet core to the west side of the system around the trough axis to the east side. This is in conformance to the rule that a cyclone tends to move south (north) while a jet core is on the east (west) flank of an upper low.

Important Conclusions

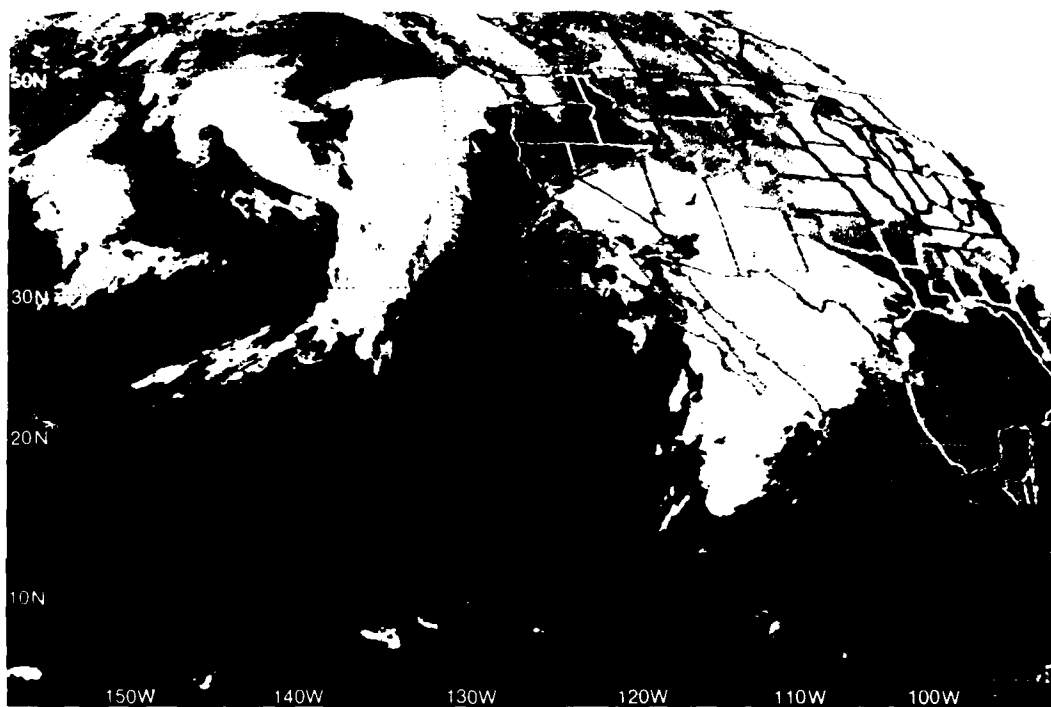
1. Satellite imagery is a key tool for identification and forecasts of upper level disturbances over data void regions of the eastern North Pacific.
2. Satellite observation and identification of upper level mid-latitude vortices is an important clue that equatorward wave energy propagation and tropical upper-low formation may take place.
3. Pre-existing upper cyclones south of 25° N serve as indicators of existing equatorial upper westerlies within which systems may develop.
4. Increasing high cloud amount and cloud curvature are good first indicators of upper-low intensification.
5. Thunderstorm cluster location is a useful method of pin-pointing the low center.
6. Existence of a cirrus cloud band emanating from tropical convection northeastward is a good indicator of jet stream motion from the southwest to the northeast sectors of the low, concurrent rapid development, and change in direction from the southeast to the northeast.
7. Cut-off of the cirrus cloud band from the tropics is a sign of upper low weakening and/or transformation of the low from a tropical to a mid-latitude disturbance.



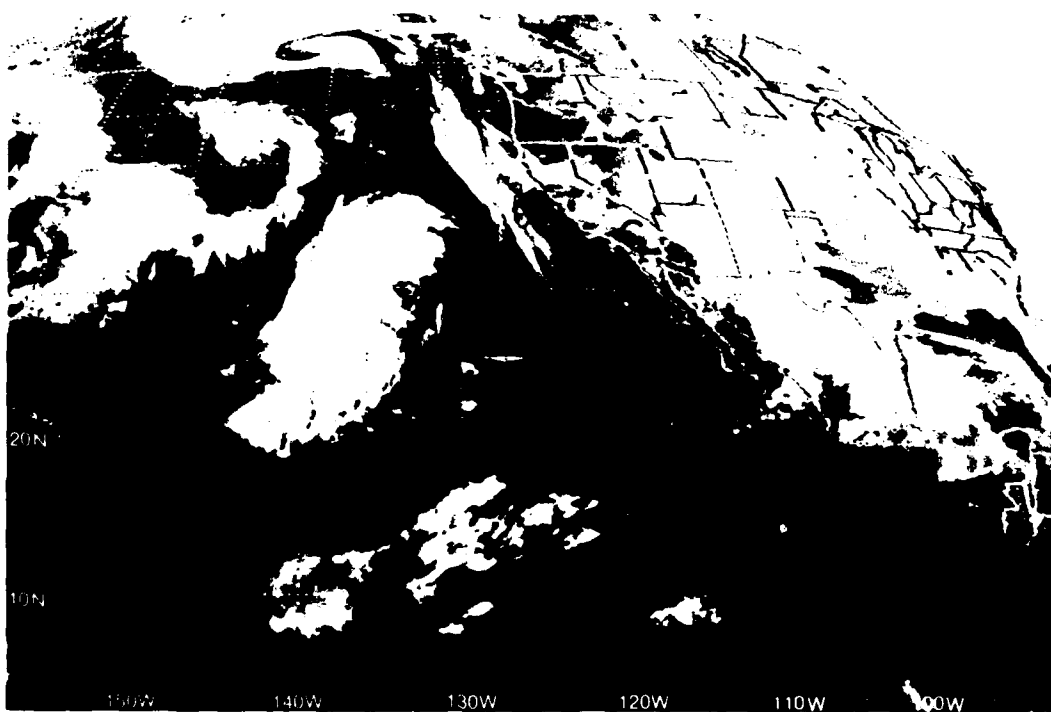
2B-29a FNOG 200-mb Analysis and Streamlines 1200 GMT 11 January 1981



2B-29b FNOG 500-mb Analysis 1200 GMT 11 January 1981



2B-29c GOES-W Infrared Image 0015 GMT 12 January 1981.



2B-29d GOES-W Infrared Image 0015 GMT 13 January 1981

Case 1 Use of Cloud Lines and Mesoscale Clear Regions as an Aid in Synoptic Analysis

When surface winds in the tropics are 15 kt or greater, stronger aloft, and show vertical speed shear but not directional shear in the lower layers, cloud line formation is normally induced. A close look at cloud line structure over a region will reveal a tendency for cloud lines to "branch" in a Y-shaped formation with the top of the Y facing in the downstream direction. This aids in resolving the 180° wind direction ambiguity.

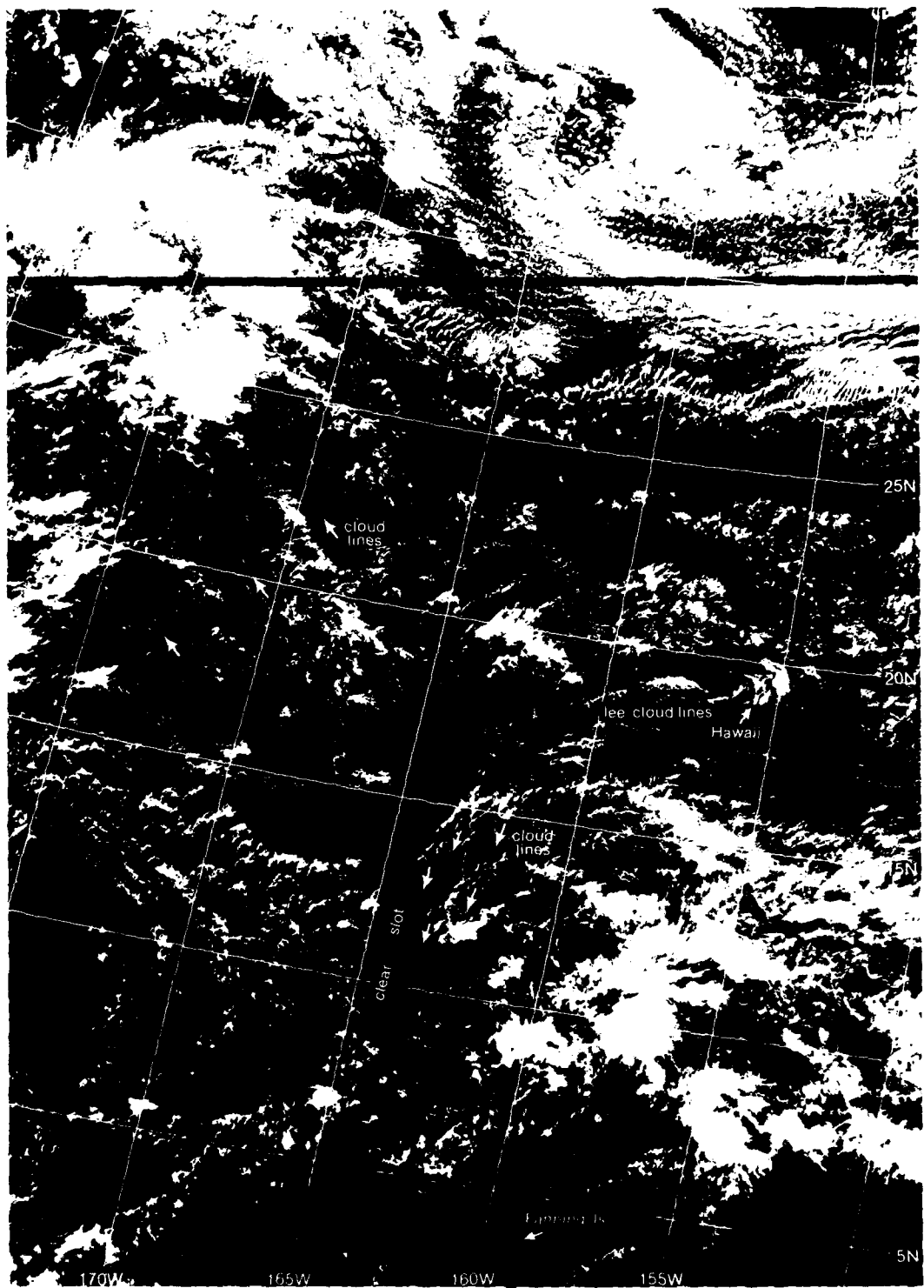
Another mesoscale effect is the tendency for an extremely well-defined clear "slot" to be formed in advance of the leading edge of cloudiness of an easterly wave. The clear slot, normally oriented in a north-south direction, defines the location of a sharp ridge line which moves with and is part of the easterly wave structure and general dynamics. In well-developed examples an upper-level trough normally overlies the position of the ridge and an upper-level anticyclone overlies convective cloudiness of the easterly wave (Fett, 1966).

The enhanced convection and tendency for curved vortical cloud lines surrounding the wave make identification of this system fairly easy.

Together these small-scale effects can be used to great advantage as guide lines in obtaining an improved synoptic analysis.

Reference

Fett, Robert, W., 1966: Upper-level structure of the formative tropical cyclone. *Mon. Wea. Rev.*, **94**(1), 9-18.



2C-2a. F-I. DMSP I-F Log Enhancement. 2119 GMT 3 November 1977.

*Identification of an Easterly Wave
Central Tropical North Pacific
November 1977*

3 November

The DMSP visible image (2C-2a) reveals a wide variety of cloud forms ranging from suppressed stratocumulus under presumably high pressure conditions to the north, to deep convection associated with disturbances and probably lower pressure near 27° N, 178° W and 10° N, 157° W.

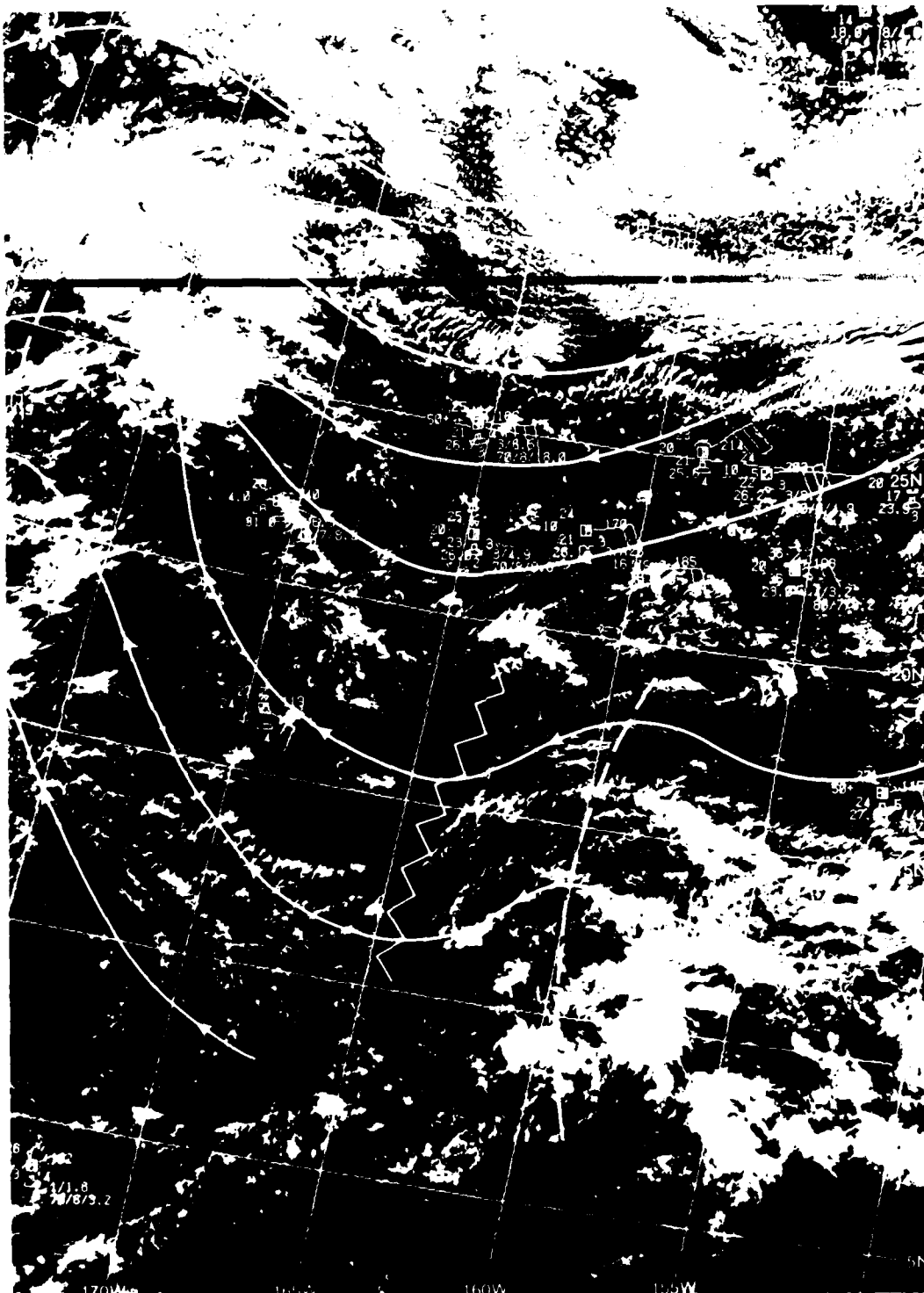
A field of cloud lines oriented northwest-southeast lead up to the northernmost disturbed area, while curving cloud lines tend to define a vortical structure surrounding the southernmost disturbance.

The island of Hawaii is located near the east central portion of the image, and Fanning Island can be identified in a sunglint region in the bottom central portion. These two geographical features permit a very accurate gridding of the entire image.

East-northeasterly flow can be deduced passing the island of Hawaii by the existence of lee cloud lines extending over 500 nmi to the west-southwest. Southeasterly flow is implied by cloud lines extending up to the northernmost disturbed region. A close examination of the cloud line field reveals the characteristic "Y-shaped" branching of some cloud elements with the Y branch open in the downstream direction. These two flow fields imply a ridge line near the leading edge of the southern disturbance. The clear slot on the leading edge of this disturbance suggests that this would be a logical position for the ridge line since this is a characteristic feature of westward moving tropical disturbances.

Surface reports and a streamline analysis based on these reports and the satellite indications, superimposed on the satellite image (2C-3a), confirm the flow pattern suggested by the cloud forms and structure appearing on the satellite imagery. One could feel quite confident about this analysis despite the lack of surface reports, almost entirely absent below 20° N.

2C-3a



2C-3a 1-1 DMSP 1F Log Enhancement 2119 GMT 3 November 1977 Surface Reports (1800 GMT) and Streamlines

Case 2 Identification of Island-Produced Cloud Plumes

Cloud plumes extending to the lee of islands have proven to be very reliable indicators of the low-level wind direction (see NTAG Vol. I, Sec. 2C).

Additional lee and corner atmospheric and sea state changes induced by trade-wind flow over island barriers under low-level temperatures inversion conditions have been documented through research aircraft flights and successfully simulated by numerical models (Fett and Burk, 1981).

In every previous example (NTAG Series) the cloud plume shown to the lee of an island was identified as a low-level phenomenon. In this example, an apparent cirrus cloud plume is mistakenly identified as island-produced.

Reference

Fett, R. W., and S. D. Burk, 1981: Island Barrier Effects as Observed by Satellite and Instrumented Aircraft and Simulated by a Numerical Model. *Mon. Wea. Rev.*, **109**(7), 1527-1541.



2C-6a Enlarged View FIV-33 DMSP EE Low Enhancement 1819 GMT 24 June 1975

*Deep Convection Cirrus Debris -
Mistaken as an Island-Produced
Cloud Plume
Hawaiian Islands
June 1975*

24 June

The DMSP visible image (2C-6a) is an enlargement of the region surrounding the island of Hawaii. The left hand border of this image was the actual border of non-enlarged data obtained on this pass.

It is of great interest to note the light gray cloud plume leading from the lee of the island to the west. This cloud plume is aligned perfectly with the general direction of low-level cloud lines suggesting an east-southeasterly flow direction past the island.

The uniform "smokey" structure of this cloud plume is not usually observed. Normally cloud lines or plumes in the lee of Hawaii are highly reflective and obviously low-level in nature (see NTAG, Vol. I, Sec. 2C, Case 5).

A DMSP infrared image (2C-7a) was also available at the same time as the visible image. The infrared image reveals that the cloud plume is very cold (white tones cold temperatures) suggesting a cirriform structure. This is also suggested by the characteristic transverse banding apparent along the plume in the DMSP visible image (2C-6a).

An apparent logical conclusion would be that this is a rare example of an upper-level cirrus plume generated by a lifting action of moist, high-level air as it moved over the island barrier. The expectation would be for sounding data to reveal moist, high-level air in strong easterly flow.

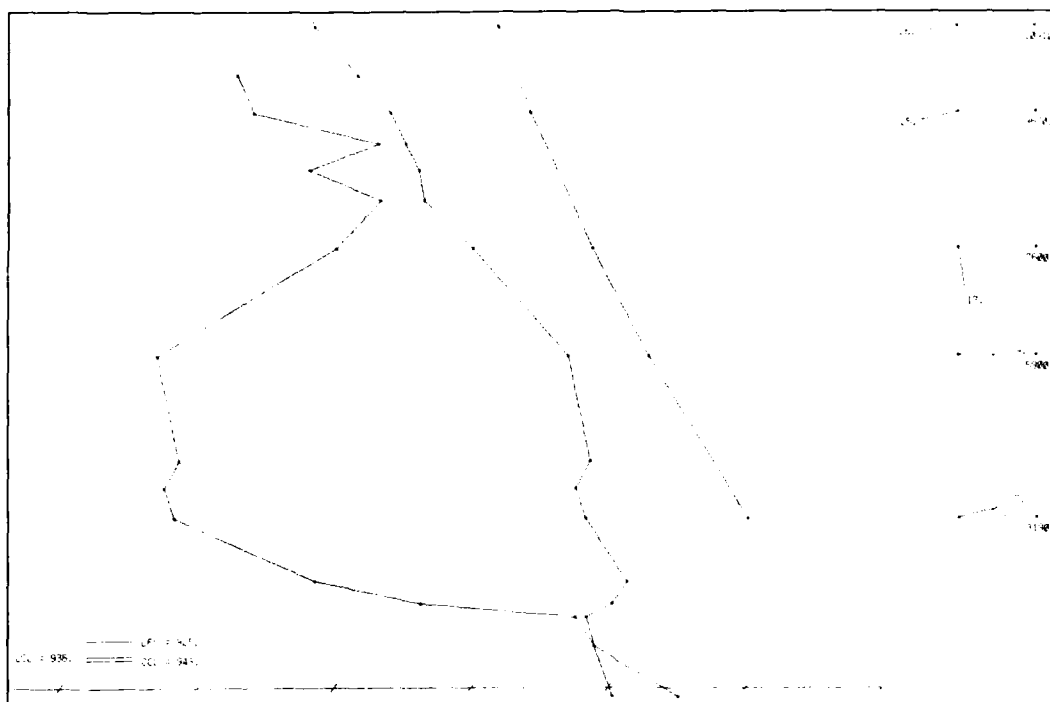
Sounding data at Hilo (2C-8a) reveal very moist, upper-level conditions from 9,670 to 10,910 m (280 to 230 mb) at 0000 GMT on 24 June, which seems to fit the possibility of cirrus clouds perfectly. Unfortunately the winds near this level are from the wrong direction they are blowing eastward (25-30 kt) rather than westward! At 0000 GMT on 25 June, about 6 hr after the time of DMSP imagery, moist conditions (2C-8b) are similarly implied at about 9,710 m (275 mb). However, winds near this level, again, are strong northwesterly (30 kt), obviously from the wrong direction to produce a cirrus cloud plume west of the island.

The discrepancy is resolved through a mosaic of the IR image on this date, over the island, with the image from the adjoining pass to the west (2C-9a). The mosaic reveals that the cloud plume over Hawaii emanated from cloudiness spawned from deep convective activity southwest of Hawaii and advected over Hawaii in westerly flow. The location of the cirrus plume in the lee of Hawaii was due to the advective process fortuitously superimposed over the island of Hawaii, creating the appearance of a lee cloud formation due to easterly flow aloft.

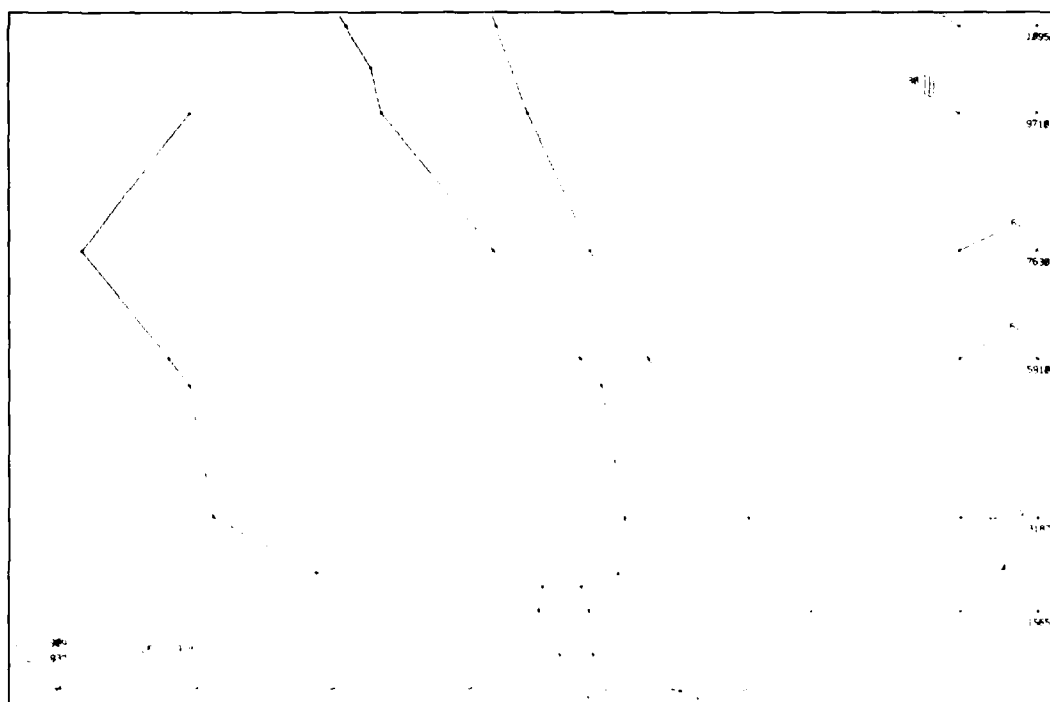
2C6A



2C-7a. Enlarged View. FIV-33. DMSP TS Normal Enhancement. 1819 GMT 24 June 1975.



2C-8a. RAOB Hilo, Hawaii 0000 GMT 24 June 1975.



2C-8b. RAOB Hilo, Hawaii 0000 GMT 25 June 1975.

Section 3

Tropical Western Pacific Ocean

3A Introduction

Tropical Western Pacific Ocean	3A-1
--------------------------------------	------

3B Synoptic-scale Case Studies

1 Cold Surges Associated with the Winter Monsoon	3B-1
Development of a Cold Surge	
South China Sea	
December 1974	3B-4
2 Mesoscale Use of Cloud Lines and Anomalous	
Gray Shades in the Tropics	3B-25
Identification of a Weak Cyclonic Circulation	
Tropical Central Pacific	
June 1974	3B-26
3 Tropical Air Fog	3B-31
Tropical Air Fog	
Gulf of Tonkin	
December 1978 and January 1980	3B-32
4 Use of Convergence Bands in the Tropics	
to Locate Surface Troughs	3B-37
Locating the Surface Trough Line	
in a Weak Tropical Disturbance	
Tropical Western Pacific	
November 1977	3B-38
5 Use of Sunlight in Determining the Position	
of the Southern Equatorial (Monsoon) Trough	3B-41
Identification of the Monsoon Trough	
Tropical Southwest Pacific	
February 1985	3B-44

3C Mesoscale Case Studies

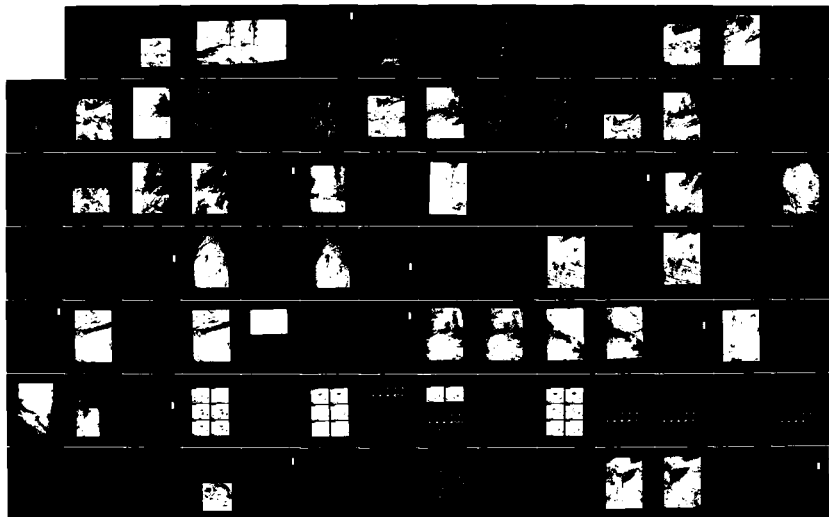
1 Cloud Line Configurations in the Lee of Islands	
Under Low-level Inversion Conditions	3C-1
Island Lee Cloud Formation Under Statically Unstable	
Low-level Conditions	
Tropical Central Pacific	
January 1974	3C-2
2 Streamline Analysis Using the Buffer Zone	
and Monsoon Trough Concepts and Satellite	
Imagery Interpretation	3C-5
Locating a Buffer Zone and Monsoon Trough Axes	
Tropical Southwest Pacific	
August 1974 and August 1979	3C-6

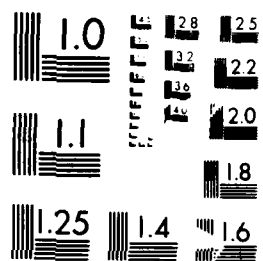
<i>3 Detection of Mountain Gap Winds over Coastal Areas from Slingline Patterns</i>	3C-11
Mountain Gap Winds Southeast Asia July 1973	3C-12
<i>4 Mesoscale Convective Systems in the Tropics</i>	3C-15
Mesoscale Convection Systems Induced by Land Breeze Convergence Tropical Western Pacific December 1978	3C-16

AD-A183 046

NAVY TACTICAL APPLICATIONS GUIDE VOLUME 6 PART 1
TROPICAL WEATHER ANALYSIS... (U) BOWMAN (WALTER A) CO PARK
RIDGE YL R H FETT ET AL. AUG 86 NEPRF-TR-86-02-U6-PT-2
UNCLASSIFIED N00228-85-C-3398 F/G 4/2 NL

2/3





MICROCOPY RESOLUTION TEST CHART
NBS 1010-A

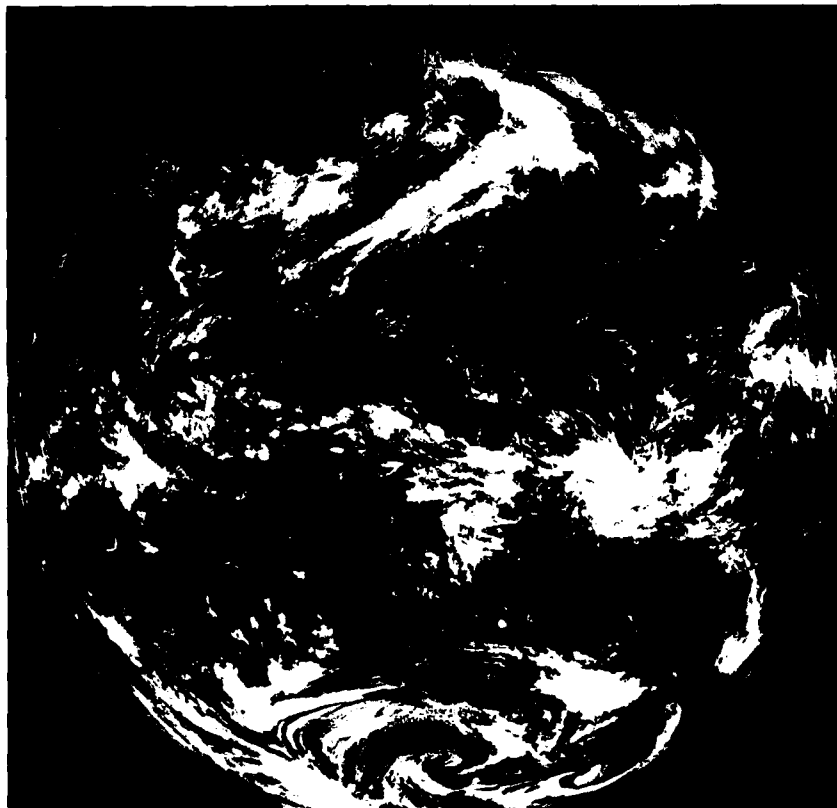
Tropical Western Pacific Ocean

The tropical western Pacific Ocean north of the equator is characterized by easterly to northeasterly flow in winter turning to northwesterly flow in a buffer zone near the equator. The active streamline trough area at this time lies in the Southern Hemisphere near 15° S, passing just south of New Guinea and over northern Australia. Strong northeast monsoon conditions exist over the region from Taiwan to the South China Sea. The pattern reverses in summer west of 150° E as southeasterly flow from the Southern Hemisphere crosses the equator and turns in a buffer region to southwesterly flow which converges in a monsoonal trough passing through the Philippines and into the South China Sea. East of 150° E easterly flow predominates.

Unlike the tropical Atlantic Ocean, tropical cyclone activity is evident on both sides of the equator and sometimes simultaneously.

The Navy meteorologist can use many weather satellite techniques in this region to significantly improve analysis and short-range forecast capabilities. Included in this section are discussions of some of those techniques including meaning and interpretation of anomalous gray shades; use of cloud lines or streets to determine flow direction; sunglint interpretation; and island barrier effects. The Japanese GMS view of the region (3A-1a), in a winter situation, shows a frontal penetration into the South China Sea and an active cloud convergence zone in the Southern Hemisphere with a tropical cyclone near the Solomon Islands.

3A-1a. GMS.
Visible Image.
0233 GMT
15 February 1979.

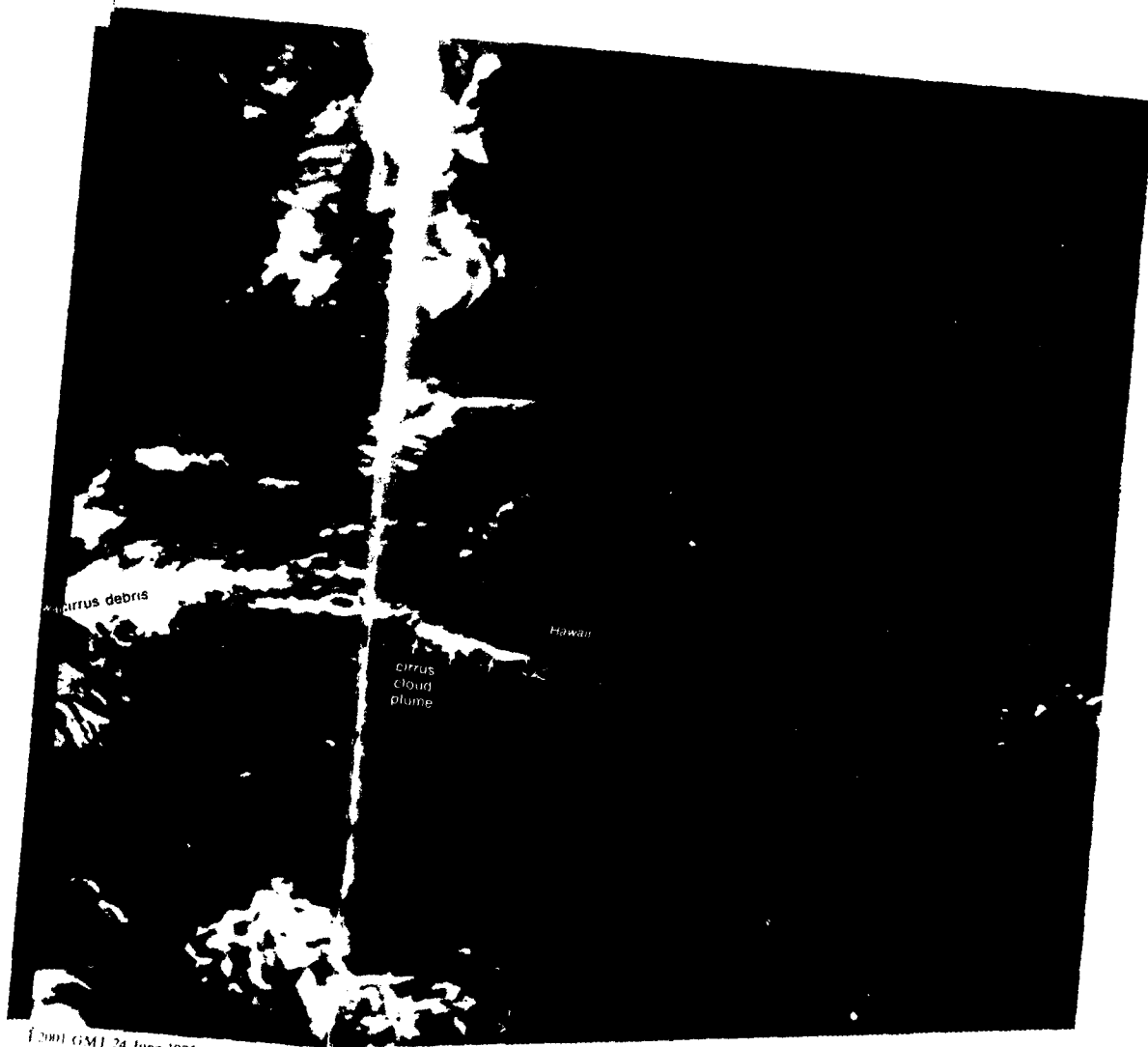


3A-1



2C-9a. FIV-33. DMSP IS Normal Enhancement. Mosaic of 1819 GMT and 2001 GMT 24 June 1975.

A.



2001 GMT 24 June 1975

B.

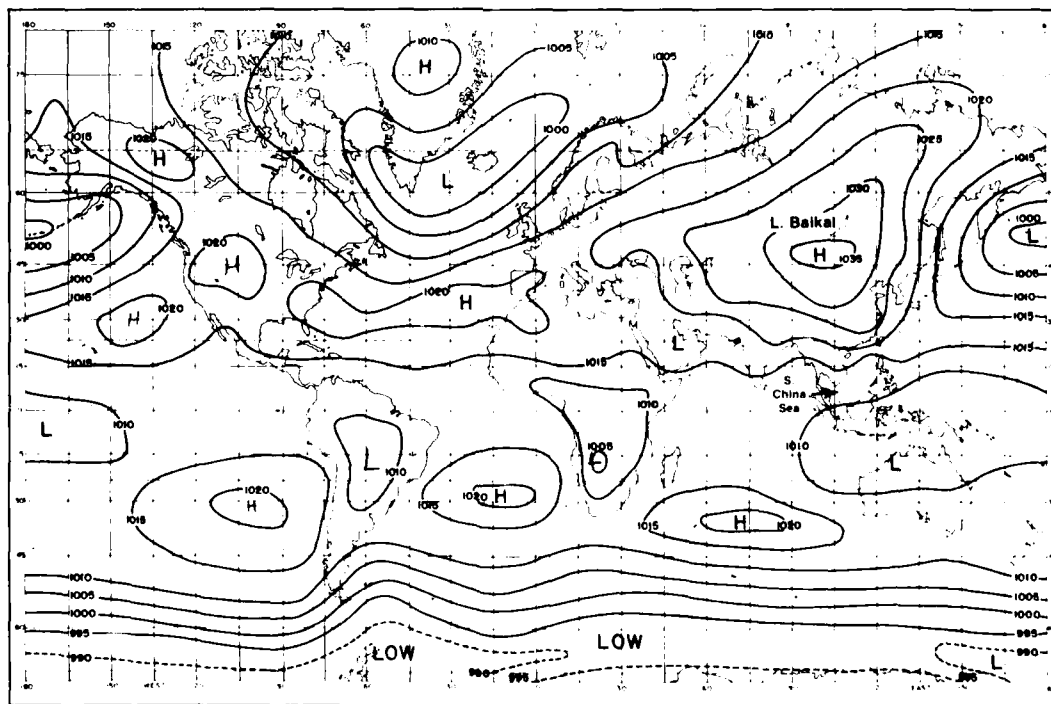
2C-9

Case 1 Cold Surges Associated with the Winter Monsoon

With the onset of the Northern Hemisphere winter, intense surface high pressure develops over the East Asia continental region south of Lake Baikal (3B-1a). The dominating characteristics of this anticyclone are quite evident.

The anticyclone is sustained and intensified by strong radiational cooling over the frozen land mass and by consistent cold air advection. Outflow from the anticyclone provides strong, steady, northeasterly monsoon winds along the east Asian coast, and across the South China Sea. The influence of the winds extends through the area of the maritime continent, which consists of the Indonesian and Malaysian Islands (Houze *et al.*, 1981a). The occurrences of cold air outbreaks accompanied by increased northeasterly winds and the weather associated with them are referred to as cold surges.

In general, a cold surge in the East Asia region may be detected by the occurrence of either a sharp drop in surface temperature; a minimum temperature notably below the seasonal average; a strengthening of the northerly winds; or any combination of these events (Chang *et al.*, 1979).

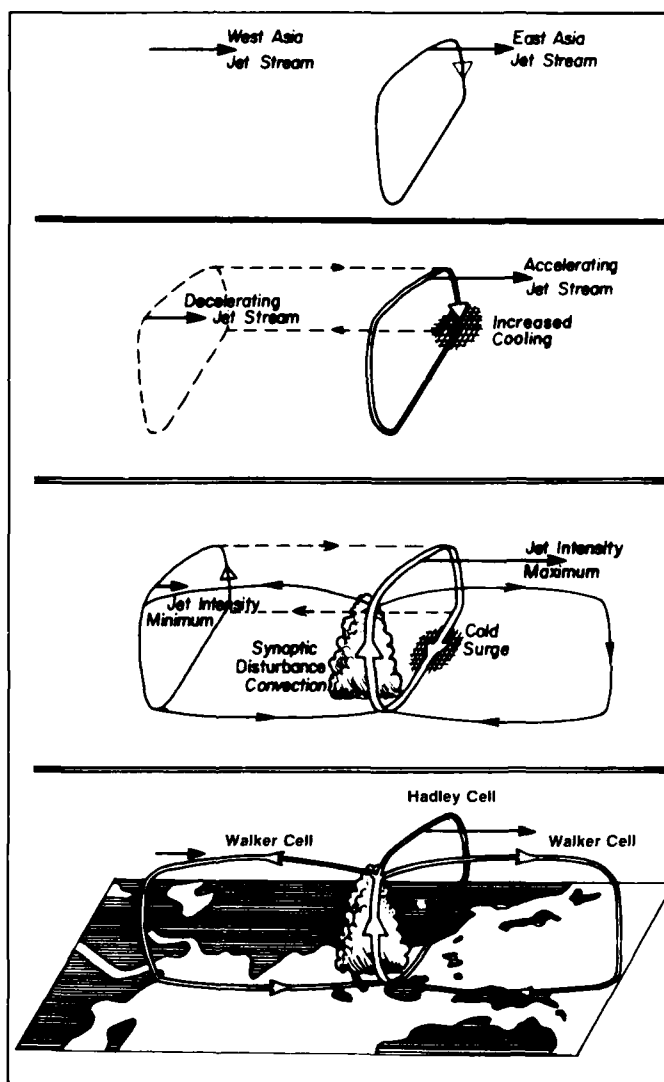


3B-1a. Mean sea-level pressure (mb) in January. (After Haurwitz and Austin, 1944.)

The vast amounts of heat energy transferred from the ocean to the atmosphere during convection associated with cold surges make this one of the major energy sources of the winter atmosphere. The winter monsoon itself may be viewed as a Hadley cell circulation with combined Walker cells in the equatorial regions, as depicted in the schematic (3B-2a) which shows the stages of Hadley and Walker cell development during a cold surge event. The Hadley circulation consists of lower tropospheric northeasterly flow; a strong heat source and ascending motion in the equatorial trough region near the north Borneo coast; and a strong heat sink and descending motion in the East Asia-North China region.

The Walker cells develop to the east and west of the equatorial zone of ascent (3B-2a). Convective cloudiness forms in the equatorial ascending region. Outflow aloft diverges east and west as part of the Walker cell circulation with main areas of descent in the equatorial Central Pacific

3B-2a. Schematic diagrams showing the effect of a cold surge passage on the Hadley and Walker circulations. Intensities of jet streams represented by relative lengths and intensities of circulations by relative width. (After Chang *et al.*, 1979.)



and along the east coast of Africa. The enhanced upper-level poleward flow of the Hadley cell results in a strengthening of the East Asia jet stream located over Japan. On the other hand, as convective cloudiness develops, as a result of a cold surge, the Walker cell circulation is strengthened resulting in a decrease of jet stream intensity at lower latitudes to the west. After the surge passes, convection in the maritime continent will increase thereby sustaining the circulation. The strong convection, however, will only last about one day following the surge passage. From the above considerations it can be seen that although cold surges are initiated in the northern mid-latitudes they may influence a large equatorial region and the large-scale motions occurring in that region.

Cold Surge Effects

Cold surge effects can often be deduced from satellite data through noting a sudden increase in convective activity over Vietnam. This occurs because of frictional convergence due to increased low-level onshore flow.

At the furthest extremity of the cold surge in its southward progression (near Borneo), other studies (Houze *et al.*, 1981; and Johnson, 1982) have shown an increase in offshore land breeze cloudiness due to increased convergence with the strong northeasterly flow. Chang *et al.* (1979), found that the surge will continue equatorward unless interaction with a synoptic-scale disturbance at lower latitudes occurs. When this happens the cold surge acts to intensify deep convection due to convergence of the strong northeasterly flow and easterly trades. The strong convection will later dissipate as the northeasterly flow weakens or as cold air advection, which lags the wind increase, stabilizes the area.

Forecast Techniques

Cold surges are associated with the approach of an upper-level trough over northern Japan. One technique used in forecasting a cold surge is that a surge can be expected within one or two days when the 500-mb winds over Lake Baikal are northwesterly (suggesting a trough approaching Japan), and the 500-mb temperatures are below -30°C at 40°N . Riehl (1968) offered another rule indicating that when a pressure difference of $>10\text{ mb}$ occurs between 30°N , 115°E and Hong Kong, a cold surge would begin in 48 hours.

References

- Chang, C. P., J. E. Erickson, and K. M. Lau, 1979: Northeasterly cold surges and near-equatorial disturbances over the Winter Monex Area during December 1974. Part I. Synoptic Aspects. *Mon. Wea. Rev.*, **107**, 812-829.
- Haurwitz, B., and J. M. Austin, 1944: *Climatology*. McGraw-Hill Book Co., Inc., New York, 410 pp.
- Houze, R. A., S. G. Geotis, F. D. Marks, Jr., and A. K. West, 1981a: Winter Monsoon convection in the vicinity of North Borneo. Part I. Structure and time variation of the clouds, wind, precipitation. *Mon. Wea. Rev.*, **109**, 1595-1614.
- Johnson, R. H., 1982: Vertical motion in near-equatorial winter monsoon convection. *J. Meteorol. Soc. Japan*, **60**, 682-689.
- Riehl, H., 1968: Surface winds over the South China Sea during the northeast monsoon season. Navy Weather Research Facility Tech. Pap. No. 22-68, 24 pp.

*Development of a Cold Surge
South China Sea
December 1974*

3 December

The NMC surface analysis at 0000 GMT (3B-4b) shows a 1064-mb high over Asia, southwest of Lake Baikal. Strong northerly surface winds up to 30 kt are reported in the eastern portion of the high, west of Korea. Winds are notably light and variable in the South China Sea.

A stationary front is analyzed nearly parallel to the southeast coast of China, through Hong Kong. The front extends east-northeastward over Taiwan, where it becomes an active cold frontal system associated with a 1000-mb low east of Japan. A more detailed analysis (Chang *et al.*, 1979) showed that the front moved past Hong Kong by 0300 GMT.

The surface pressure difference between 30° N, 115° E and Hong Kong is about 12 mb, which according to Riehl's (1968) criteria, suggests a cold surge into the South China Sea within 48 hours.

Note that wind reports are already suggesting a cold air outbreak flowing into the Sea of Japan and the Yellow Sea. This is also strongly indicated on the NMC 850-mb analysis (3B-4a) which shows isotherms perpendicular to isopleths in that region.

At 500 mb (3B-5b), northwesterly flow is shown over Lake Baikal with a trough approaching Japan. The -30° C isotherm is very close to 40° N but has not passed south of it over China to indicate an imminent cold surge event. A blocking situation seems to be suggested near 160° E with a ridge line extending to a high pressure center near 65° N, 170° E. The effect of such a block would tend to encourage cold surge flow over an extended period.

At 200 mb (3B-5a), a 130-kt jet streak is shown crossing over North Korea and the northern island of Japan.

The NOAA-3 visible image mosaic at about 0300 GMT (3B-6a) reveals overcast cloudiness north of the stationary front (3B-4b) extending deep into China and over the western Pacific south of Japan. Note the sudden termination of cloudiness to the west between roughly 22° to 33° N, and 101° to 106° E. This is the precise boundary where the terrain rises abruptly, giving way to the mountains of Tibet and high terrain of provinces to the north.

Very little cloudiness is apparent over Vietnam and the South China Sea except for convective clusters along the equatorial convergence zone (CZ).

The DMSP infrared image at 1509 GMT (3B-7a) reveals the typical cloud line development that occurs when frigid air flows over much warmer water in the coastal region of the Soviet Union northeast of Korea. The isotach analysis shows that winds over the water are much stronger than over the land. This should be anticipated not only because of less friction over water but also as a result of the violent mixing process that occurs during a cold air outbreak which brings stronger winds from aloft down to the surface layers.

3B-4

4 December

The NMC surface analysis at 0000 GMT (3B-8b) shows the beginning of the cold frontal penetration into the South China Sea. The 1016-mb isobar now lies close to Hong Kong indicating a pressure rise of about 5 mb over the past 24 hr in response to the cold surge event. The light southerly winds apparent in the anticyclonic flow over the South China Sea on the previous analysis (3B-4b) have now given way to northeasterlies, apparently as a result of the anticyclone's southward shift.

The NMC 850-mb analysis (3B-8a) now shows cold air advection at this level extending offshore of China and into the South China Sea.

At 500 mb (3B-9b), the short-wave trough appears to have moved over the Yellow Sea while the low-pressure center at 50° N, 142° E has moved eastward a few degrees. This maintains the northerly flow over Lake Baikal. The -30° C isotherm has now moved south of 40° N in a segment over the Sea of Japan, fulfilling the criteria for a cold surge event in the South China Sea within 48 hr. (Riehl's criterion, however, had predicted this 24 hr earlier.) The Omega block near 160° E persists and is undoubtedly responsible for the relatively slow movement of the major low-pressure system north of Japan.

The NMC 200-mb analysis (3B-9a) shows a cyclonically turning 130 kt jet streak circling the elongated low-pressure system north of Japan.

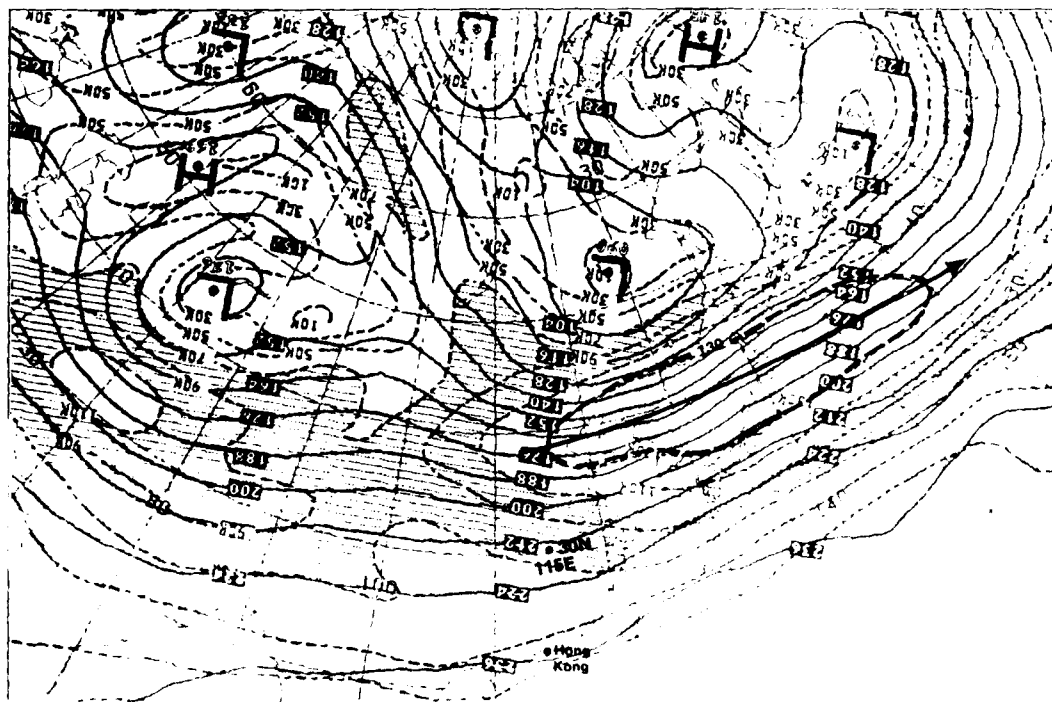
The NOAA-3 visible image mosaic at about 0300 GMT (3B-10a) shows cloudiness advancing slightly further into the South China Sea and it appears more solid, possibly containing shower activity.

The DMSP visible image acquired at 0030 GMT (3B-11a), shows that heavy overcast cloudiness has advanced southward to about 20° N. Strong surface winds (30 kt) associated with the surge over the open water are observed just north of Luzon (Philippines).

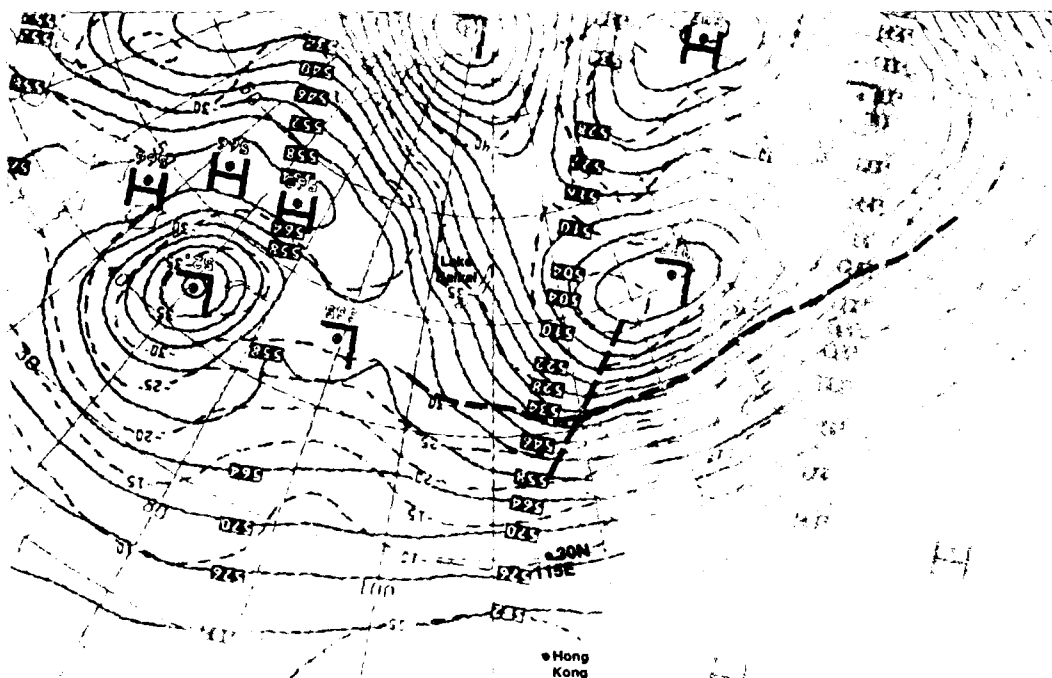
A streamline showing the flow of cold air moving over the Yellow Sea to the South China Sea, where a merger with normal northeast monsoon flow occurs, is quite revealing. Note that higher wind speeds in the surge region over the water are 2-3 times as strong as over land. This again is chiefly attributable to the strong mixing occurring over the water, bringing strong winds from aloft to the sea surface.

The land breeze cloud line extending offshore of southern Vietnam is indicative of light synoptic-flow conditions and indicates that the surge has not yet reached this region.

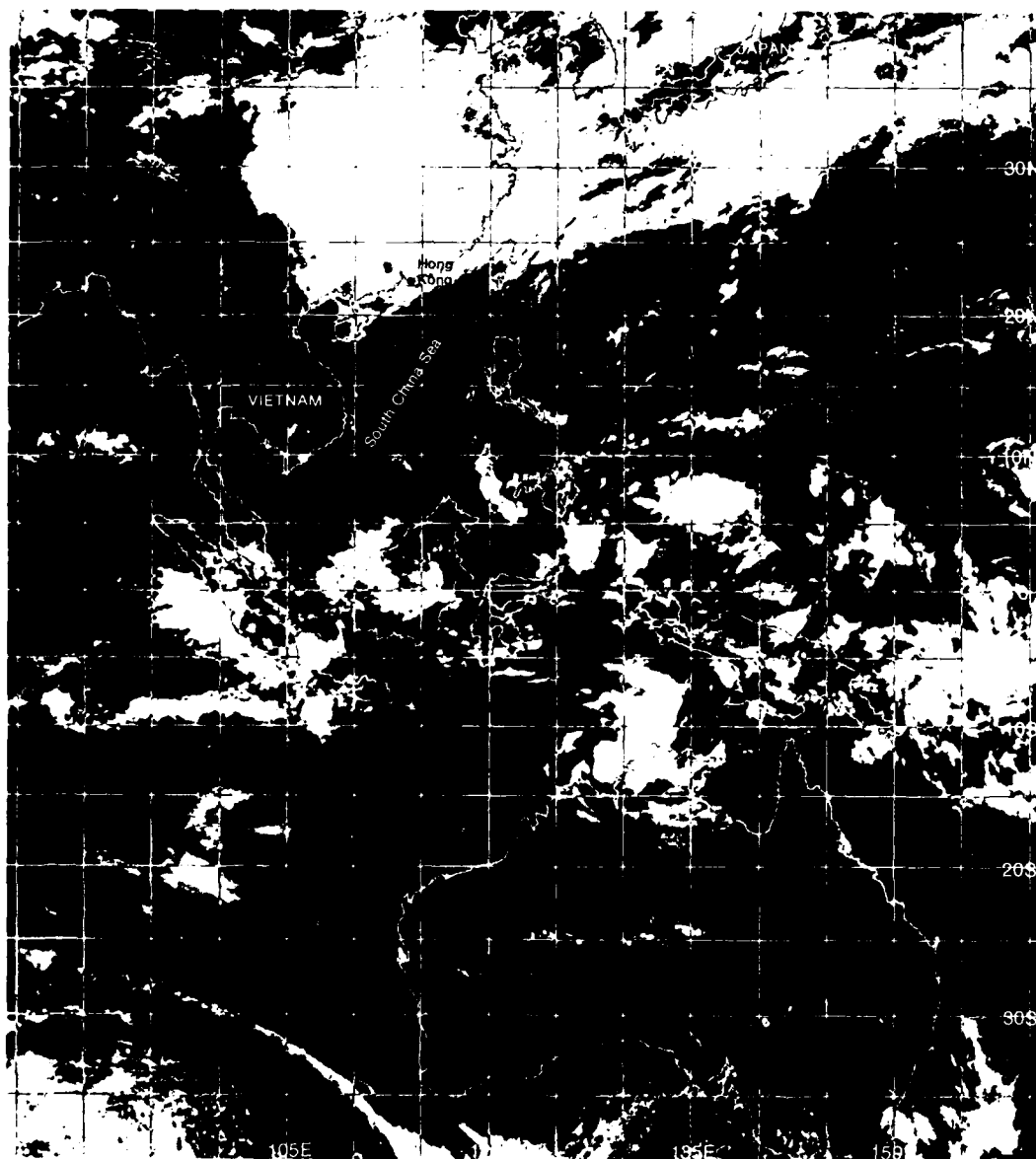
Continued on page 3B-12



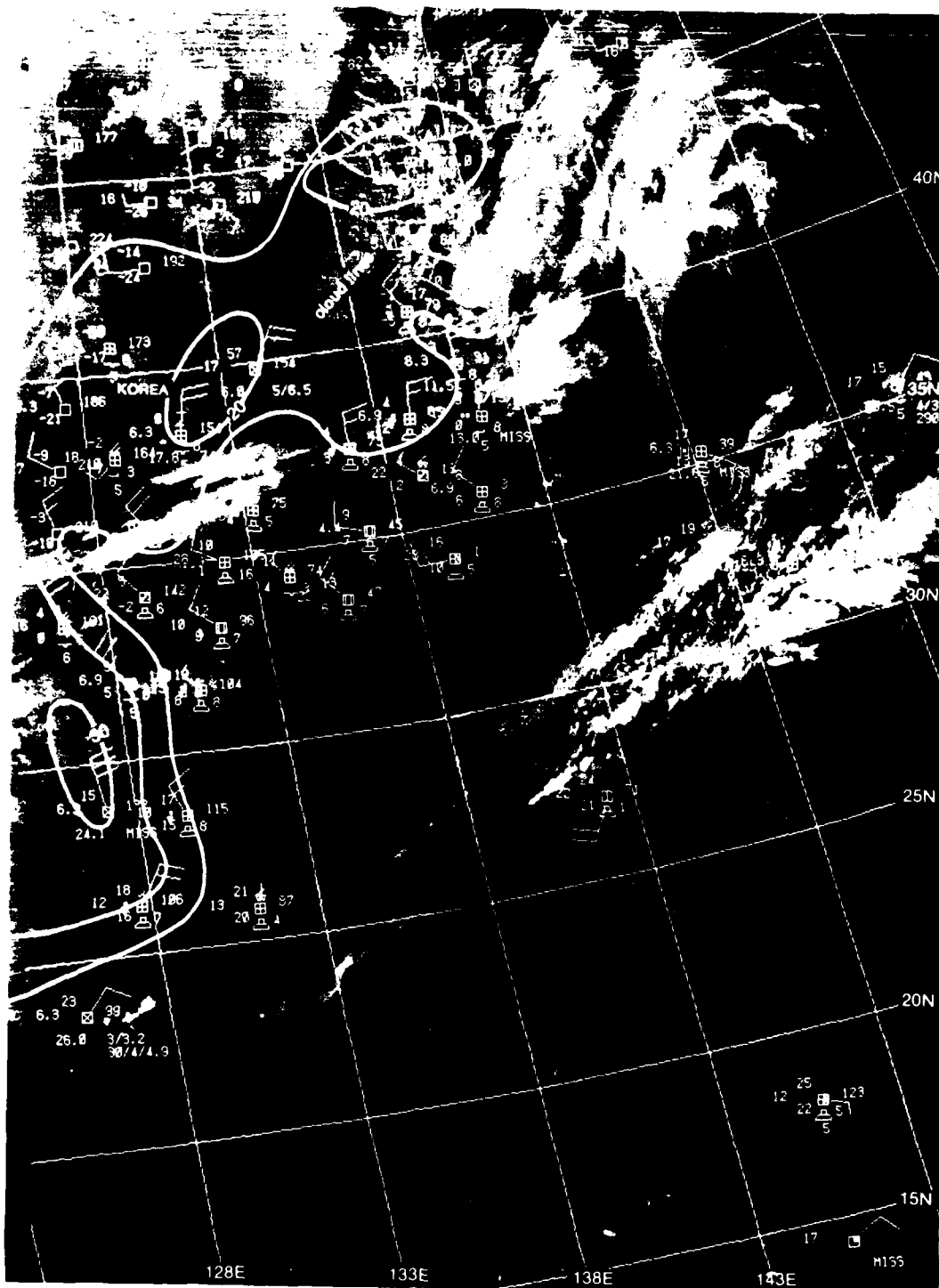
3B-5a. NMC 200-mb Analysis. 0000 GMT 3 December 1974.



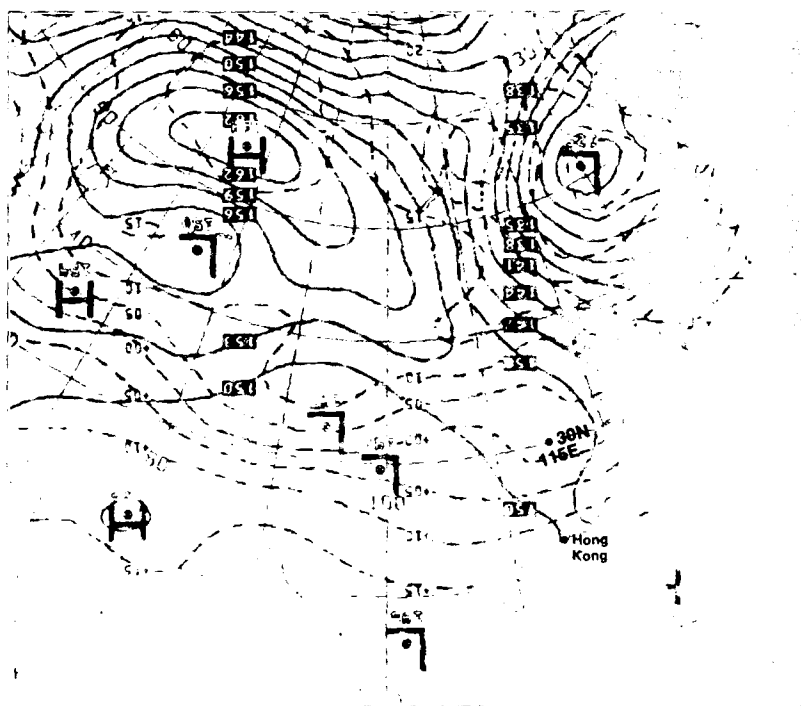
3B-5b. NMC 500-mb Analysis. 0000 GMT 3 December 1974.



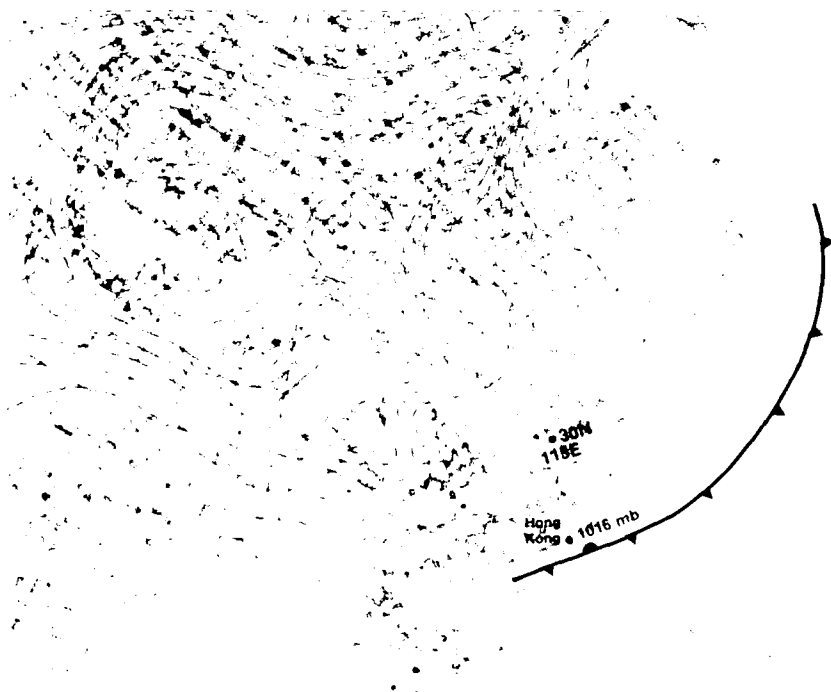
3B-6a. NOAA-3 Visible Image Mosaic. 0300 GMT 3 December 1974.



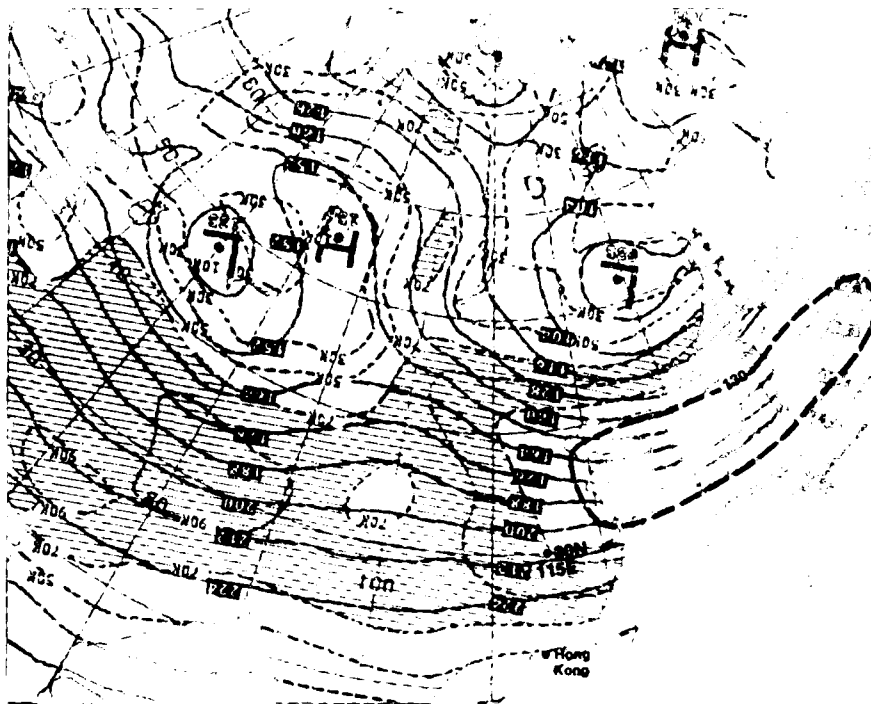
3B-7a FIV-31 DMSP IF Normal Enhancement 1509 GMT 3 December 1974 Surface Reports (1800 GMT) and Isotachs



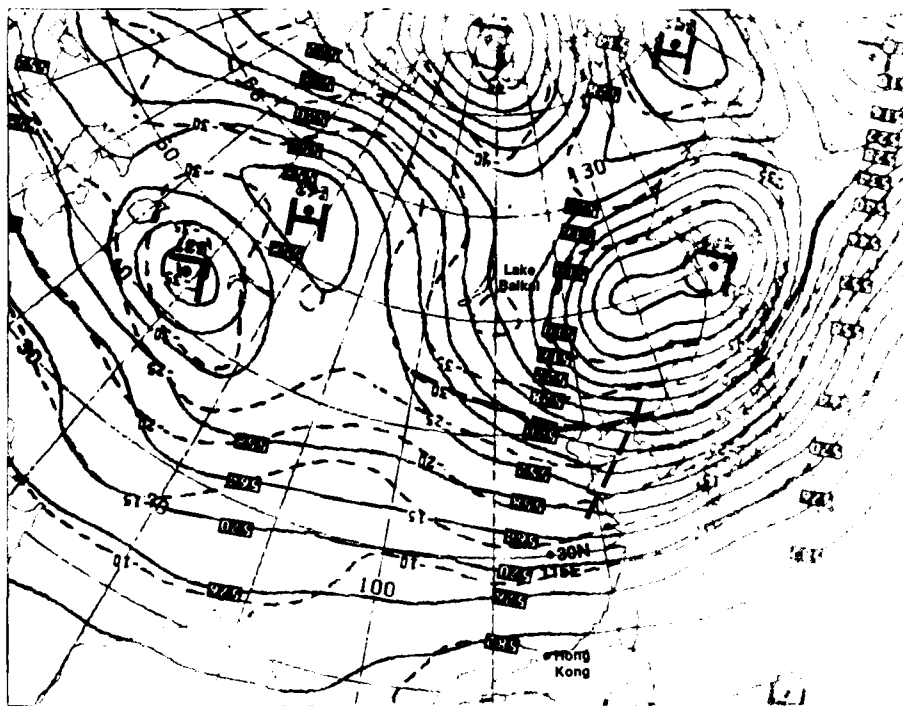
3B-8a. NMC 850-mb Analysis. 0000 GMT 4 December 1974.



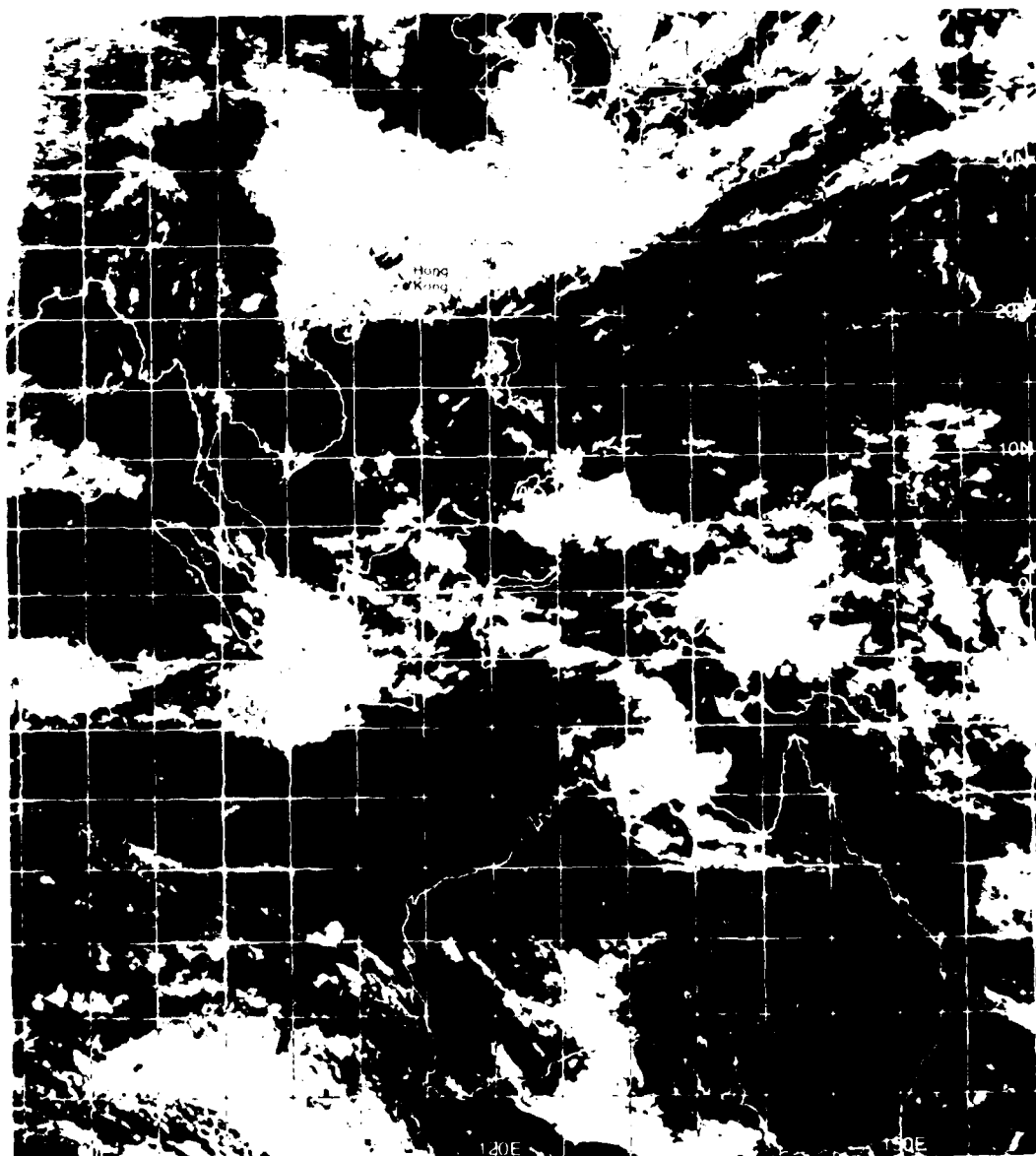
3B-8b. NMC Surface Analysis. 0000 GMT 4 December 1974.



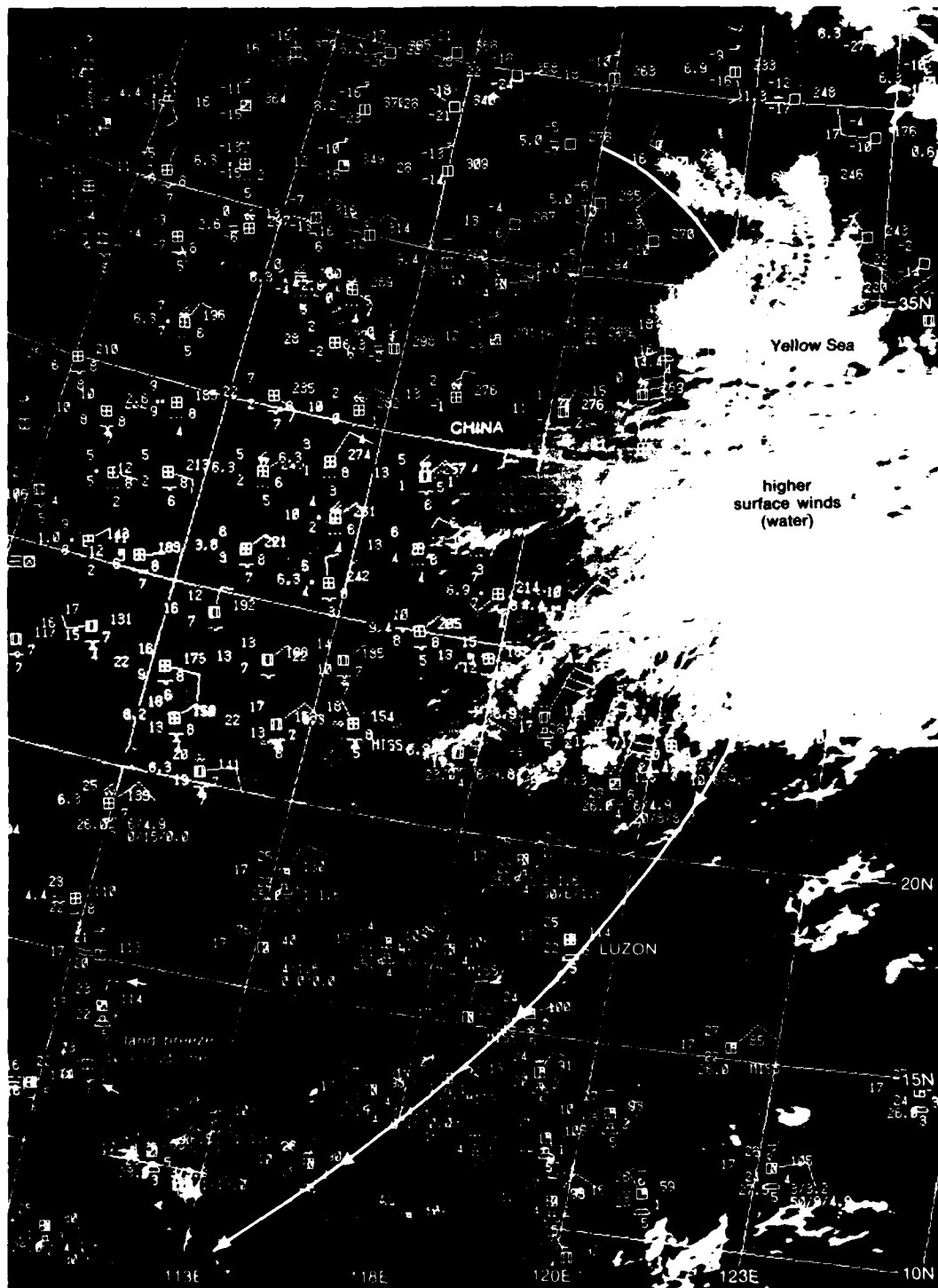
3B-9a. NMC 200-mb Analysis. 0000 GMT 4 December 1974.



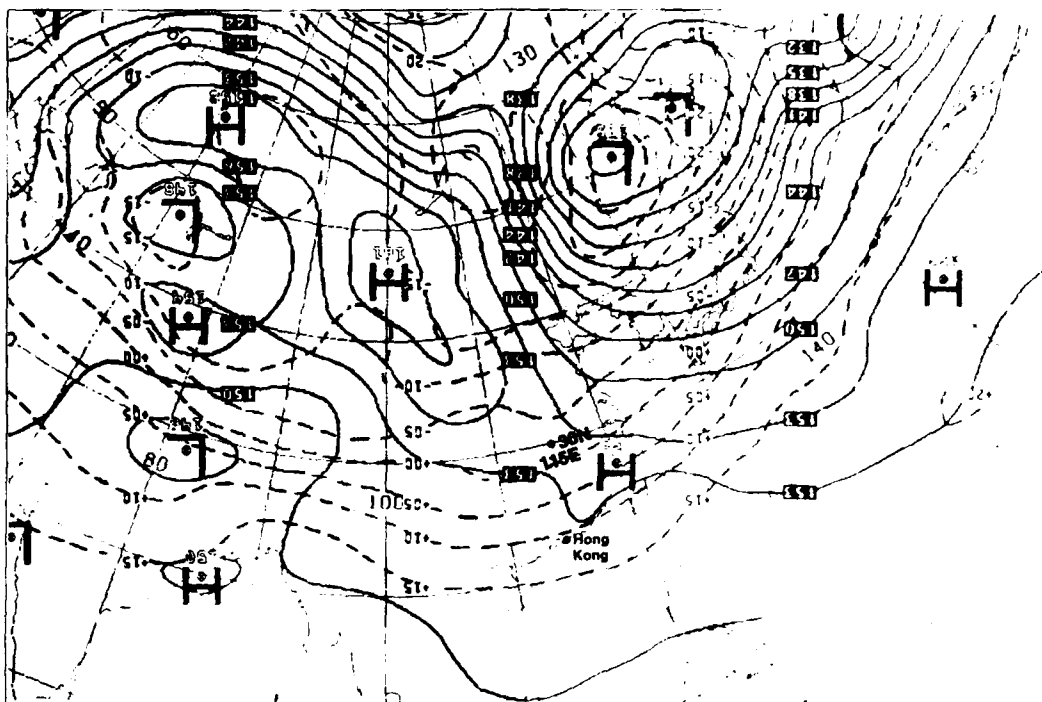
3B-9b. NMC 500-mb Analysis. 0000 GMT 4 December 1974.



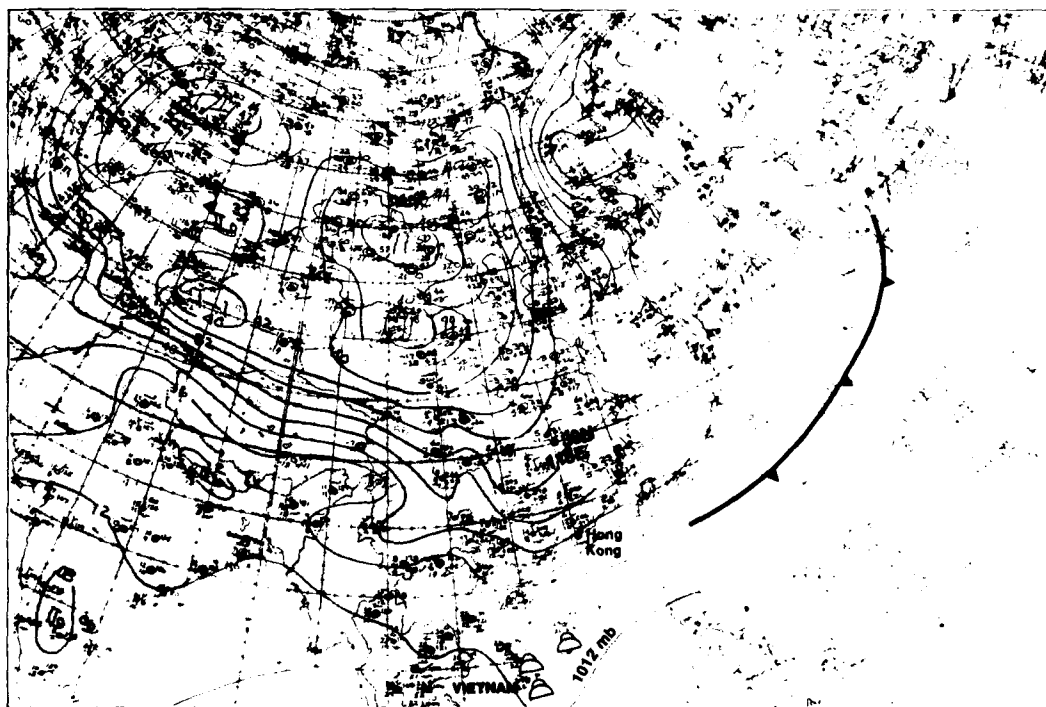
3B-10a NOAA-3 Visible Image Mosaic 0300 GMT 4 December 1974



3B-11a FTV-29 DMSP LF Low Enhancement 0030 GMT 4 December 1974. Surface Reports (0000 GMT) and Streamlines.



3B-12a. NMC 850-mb Analysis. 0000 GMT 5 December 1974.



3B-12b. NMC Surface Analysis. 0000 GMT 5 December 1974.

5 December

The NMC surface analysis at 0000 GMT (3B-12b) shows that the 1012-mb isobar, which had been over Hong Kong on 3 December has moved southward to southern Vietnam. Cumulus congestus reported at sea and along the coast of Vietnam indicates that the surge has reached the region. Temperatures and dew points, however, show little change over that shown on the analysis of 3 December (3B-4b), prior to the surge. This finding is consistent with that of Chang *et al.* (1979), who concluded that a freshening of the northeast monsoon flow due to the cold surge precedes a temperature decrease over the same region. They indicate that such a decrease, "if it occurs, is confined to the western portion of the South China Sea." Due to air/sea interaction, the air further east, having a long over-water trajectory, is modified too much to show a large temperature/dew point difference.

The NMC 850-mb analysis (3B-12a) shows little further evidence of cold air advection into the South China Sea, with the 15° C isotherm only slightly further south of the position shown 24 hr earlier (3B-8a).

The NMC 500-mb analysis (3B-13b) continues to show the Omega block near 160° E. The effect on the movement of the low-pressure center is drastic, resulting in a retrograde westward movement of about 5 deg in comparison to its position 24 hr earlier (3B-9b). The blocking action keeps cold air moving from northern latitudes to the region off the China coast.

At 200 mb (3B-13a), a jet streak remains south of the low-pressure center north of Japan with intensity increased to 150 kt.

The NOAA-3 visible image mosaic at about 0300 GMT (3B-14a) shows movement of frontal cloudiness southward to Luzon with increased convection in the South China Sea and along the coast of Vietnam. This cloudiness change, though subtle in the NOAA-3 imagery, indicates movement of cold surge effects southward to at least 10° N.

The DMSP visible image at 0011 GMT (3B-15a) shows cold surge cloud lines still being generated in the Yellow Sea and in the Sea of Japan. Jet stream cirrus cloudiness is apparent near the northern edge of overcast cloudiness sweeping across the Yellow Sea past the southern top of Korea.

The flat appearance of overcast cloudiness south of the jet stream cirrus suggests subsidence as the dense, cold air spreads southward.

A streamline analysis of surface reports superimposed on the DMSP image (3B-15a) shows that this subsidence is occurring under anticyclonically-turning flow with a ridge line passing through the center of this cloudiness.

In the southwest portion of the DMSP image, easterly trade wind flow is shown which merges with the surge in the South China Sea after passing over the Philippine Islands.

6 December

The NMC surface analysis at 0000 GMT (3B-16b) shows 25-kt winds extending to about 10° N. Cumulus congestus, rain, and rainshowers, along the coast of Vietnam suggest the influence of a cold surge in progress. Low pressure is analyzed in the middle of the South China Sea, but without a great deal of evidence from previous history or from indicated pressure reports in the vicinity. It is possible that the low was analyzed-in on the basis of the 25-kt wind report, indicating a lack of understanding by the analyst that a cold surge was in progress over the region and that strong winds associated with such surges do not require and, in fact, are not associated with low pressure.

At 850 mb (3B-16a), a dome of high pressure is seen to have pushed southward toward Hong Kong and the 15° C isotherm is located south of Hainan Island. Pronounced cold air advection is still indicated from Korea southward to Hong Kong.

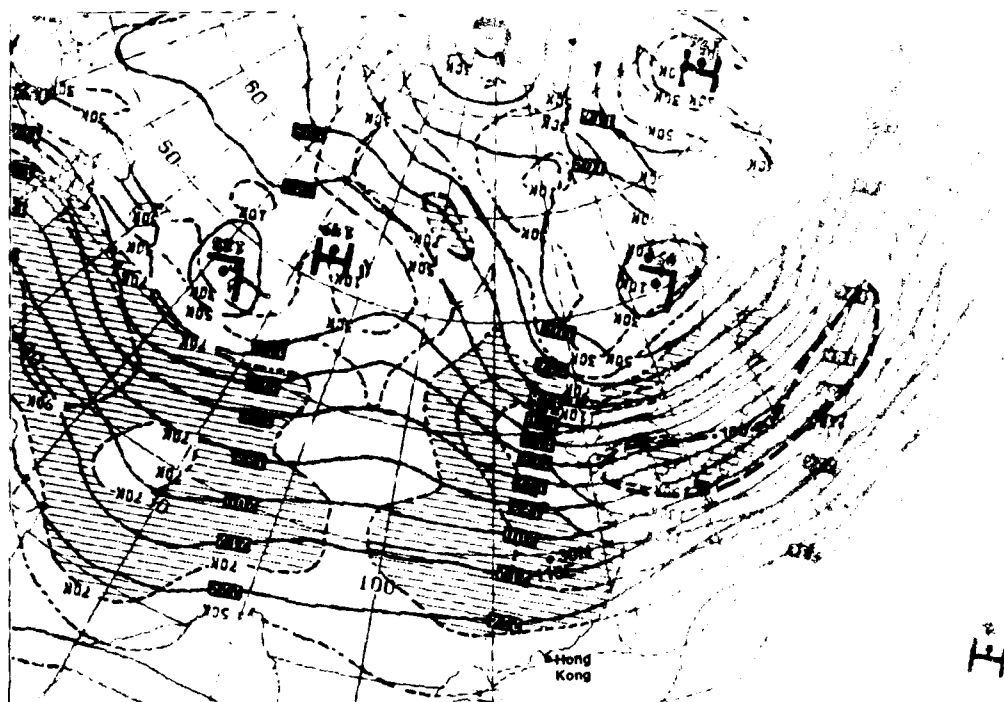
At 500 mb (3B-17b), the blocking pattern near 160°-165° E is still shown to persist and the low-pressure system north of Japan has moved eastward from its previous position (3B-13b) by only about 4 deg, which maintains the northwesterly flow over Lake Baikal. The -30° C isotherm now extends southward past 40° N into Korea and Central Japan, indicating a well-advanced cold surge event.

The NMC 200-mb analysis (3B-17a) continues to show a strong jet streak, now with maximum winds of over 170 kt, anchored in the southern portion of the trough extending from the low north of Japan.

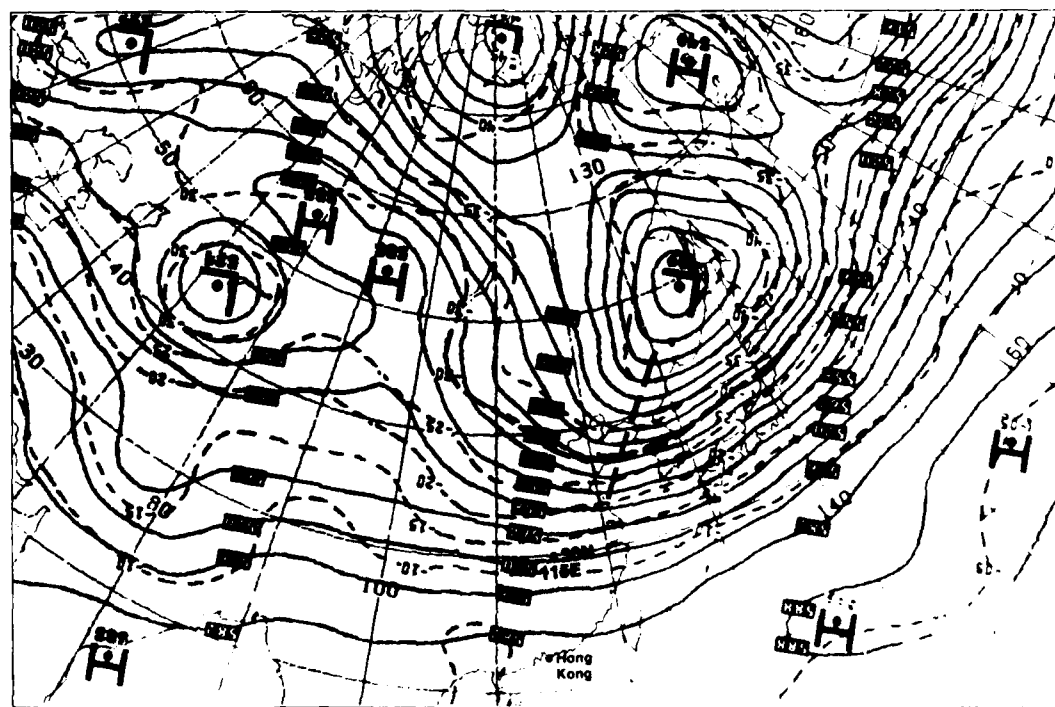
The NOAA-3 visible image mosaic at about 0300 GMT (3B-18b) reveals considerable cloudiness over the northern portion of the South China Sea except along the China coast where strong subsidence and clear skies occurred as Hong Kong experienced its coldest temperature. An analysis of surface temperatures by Chang *et al.* (1979; 3B-18a), revealed that the temperature gradient was greatest in the northern South China Sea, as Hong Kong recorded its lowest temperature; however, winds from the surge preceded the cooling effect and had reached southward to southern Vietnam (3B-16b). Convective cloudiness along the equatorial CZ has increased dramatically as increased convergence caused by the cold surge has affected the area.

The DMSP visible image at 2353 GMT (3B-19a) shows a closer view of cloud forms observed in the NOAA-3 image (3B-18b). The streamline analysis shows that the initial overcast cloudiness extending offshore tends to dissipate in the ridge line region where winds turn from northwesterly to northeasterly. A convergence of surge winds with easterly trades is shown in the southeast portion of this image and coincides with the region of enhanced ITCZ convection. Note that along the eastern coastline of Japan, cloud lines develop in preferred regions with some regions being clear of cloudiness for as much as 50 n mi offshore. The cloud lines form first in channel areas or in the lee of valleys. Wind speeds at the surface in these regions are much higher than nearby clear regions which lie in the lee of mountainous terrain.

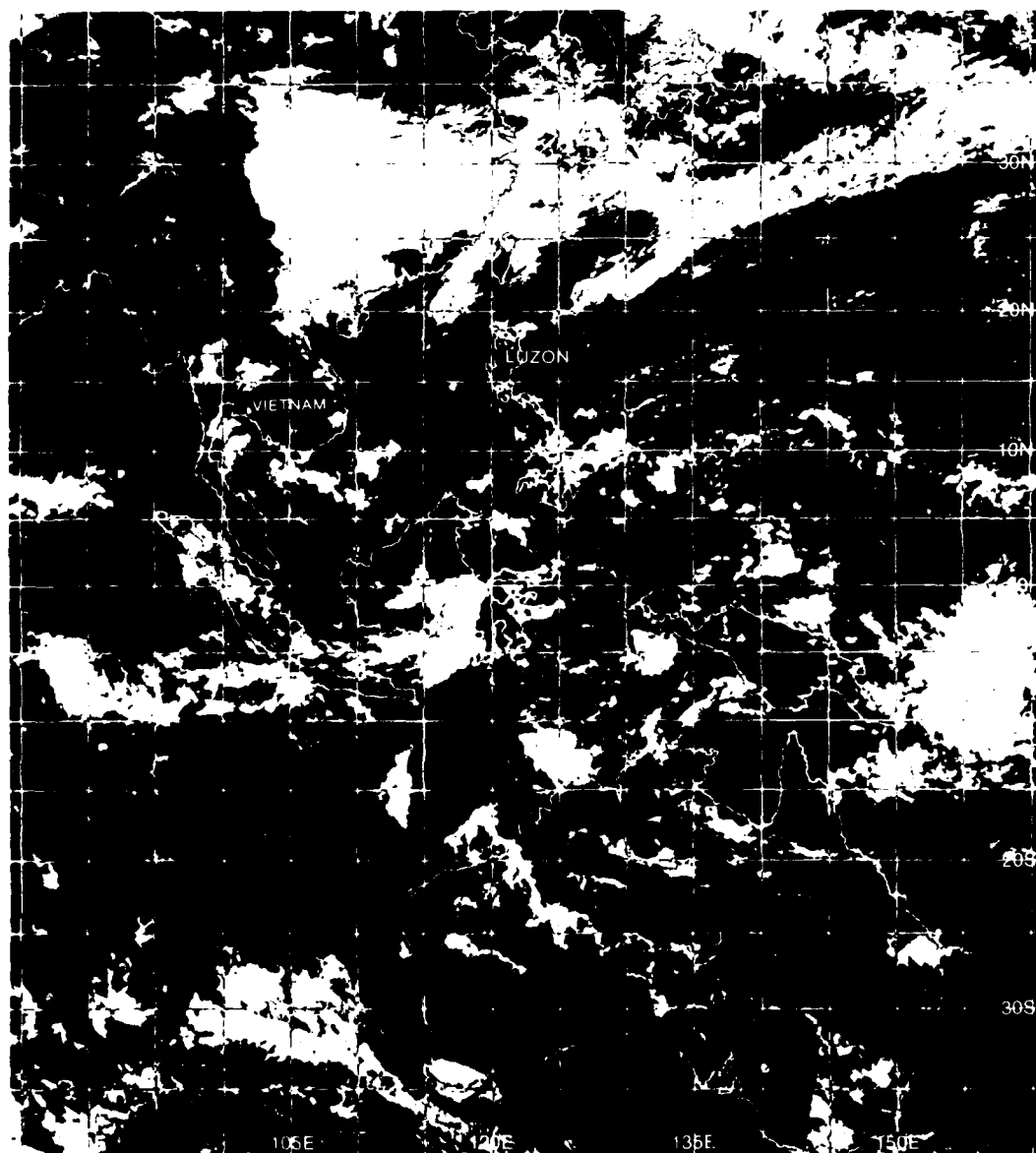
Continued on page 3B-19



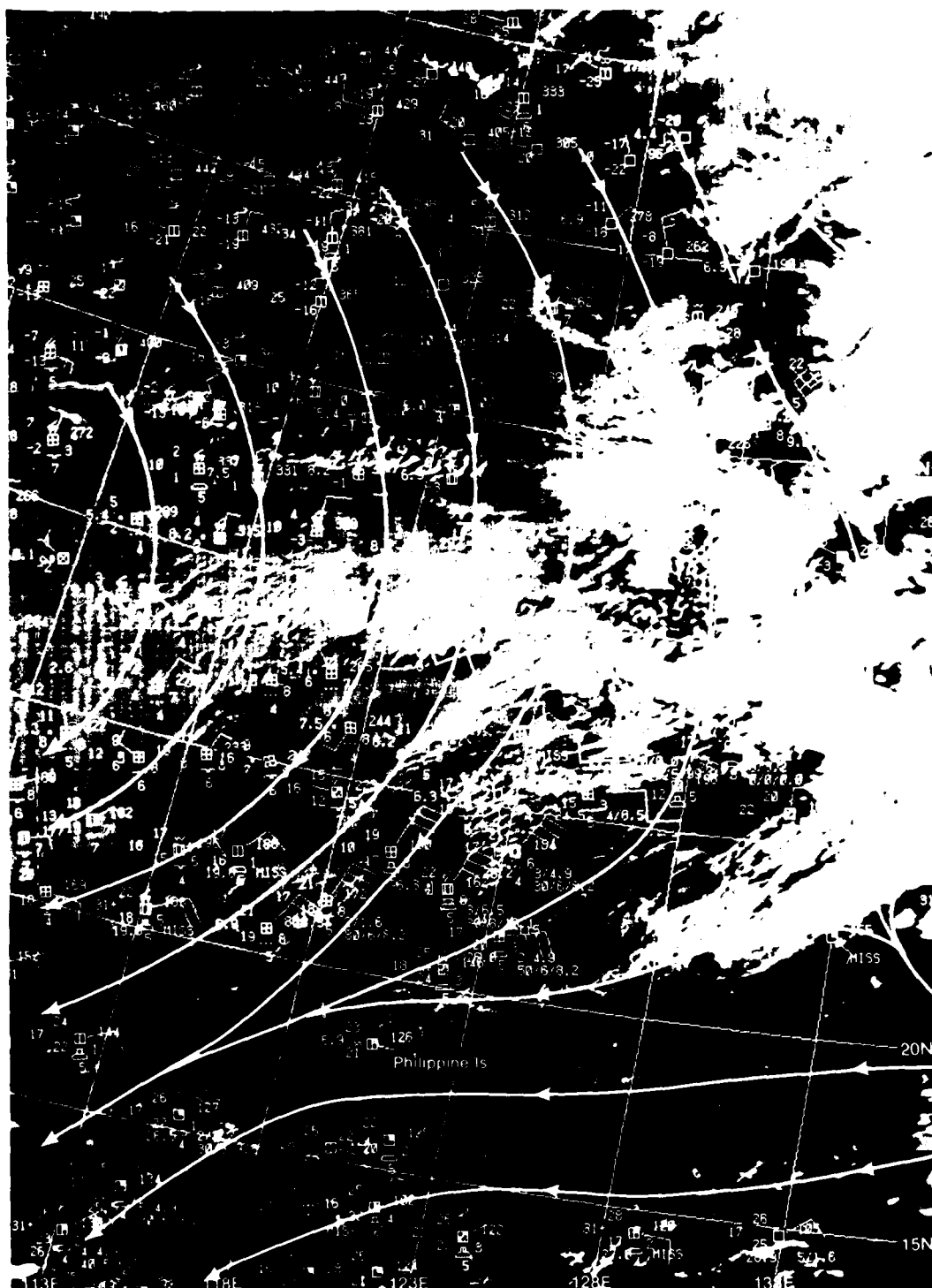
3B-13a. NMC 200-mb Analysis. 0000 GMT 5 December 1974.



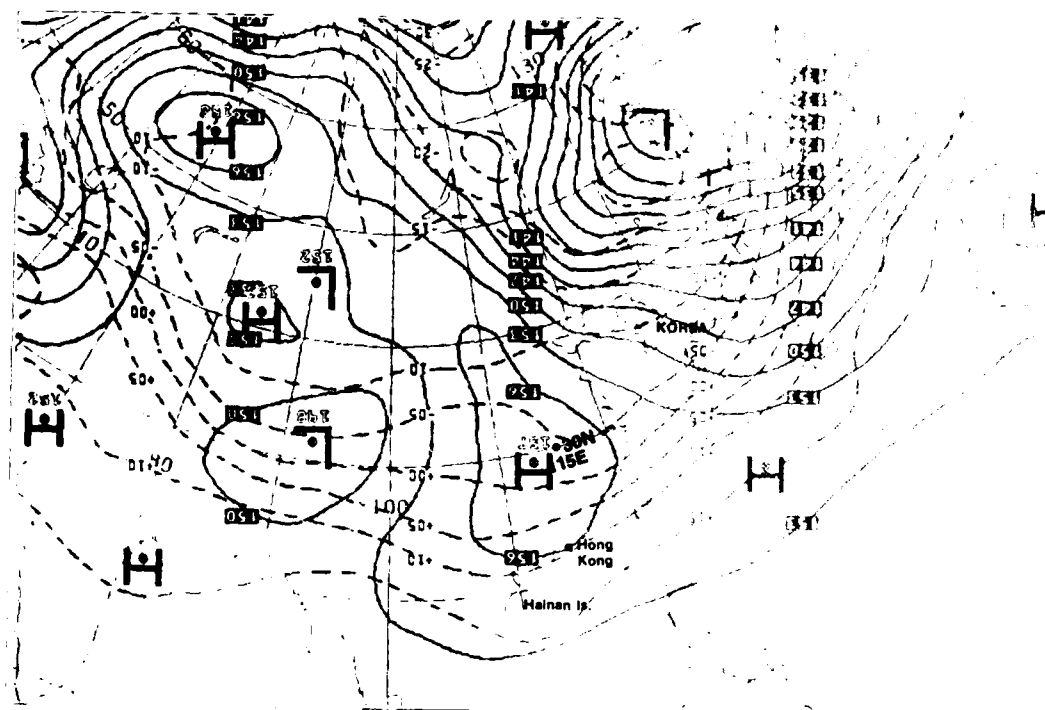
3B-13b. NMC 500-mb Analysis. 0000 GMT 5 December 1974.



3B-14a NOAA-3 Visible Image Mosaic, 0300 GMT 5 December 1974.



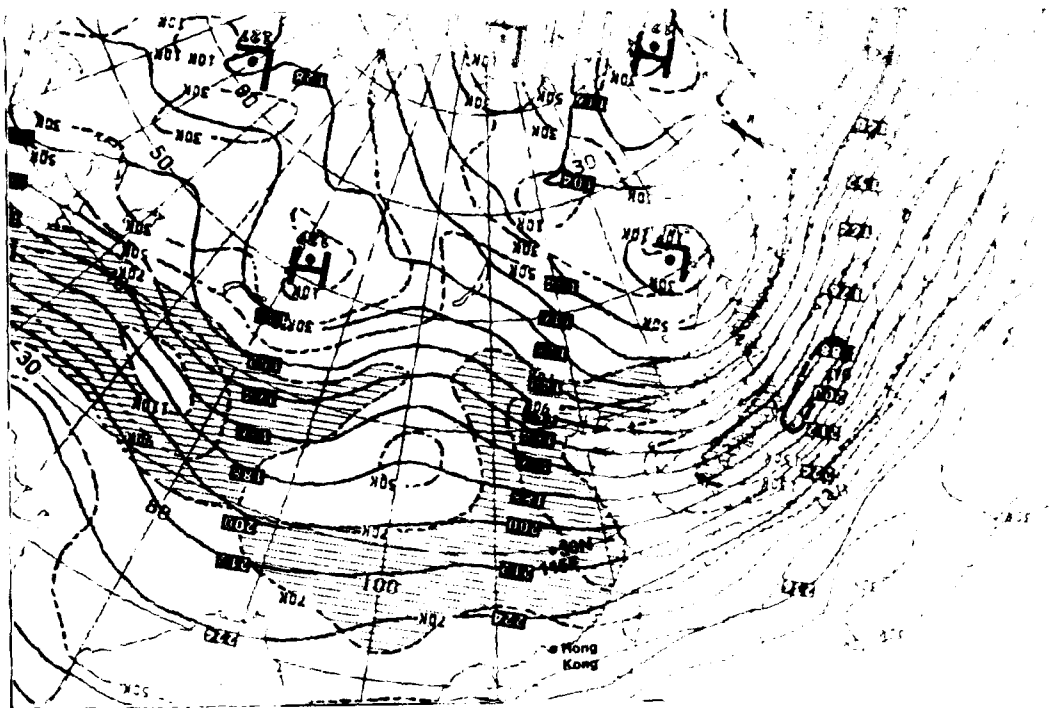
3B-15a FIV-29 DMSP L1 Low Enhancement 0011 GMT 5 December 1974. Surface Reports (0000 GMT) and Streamlines.



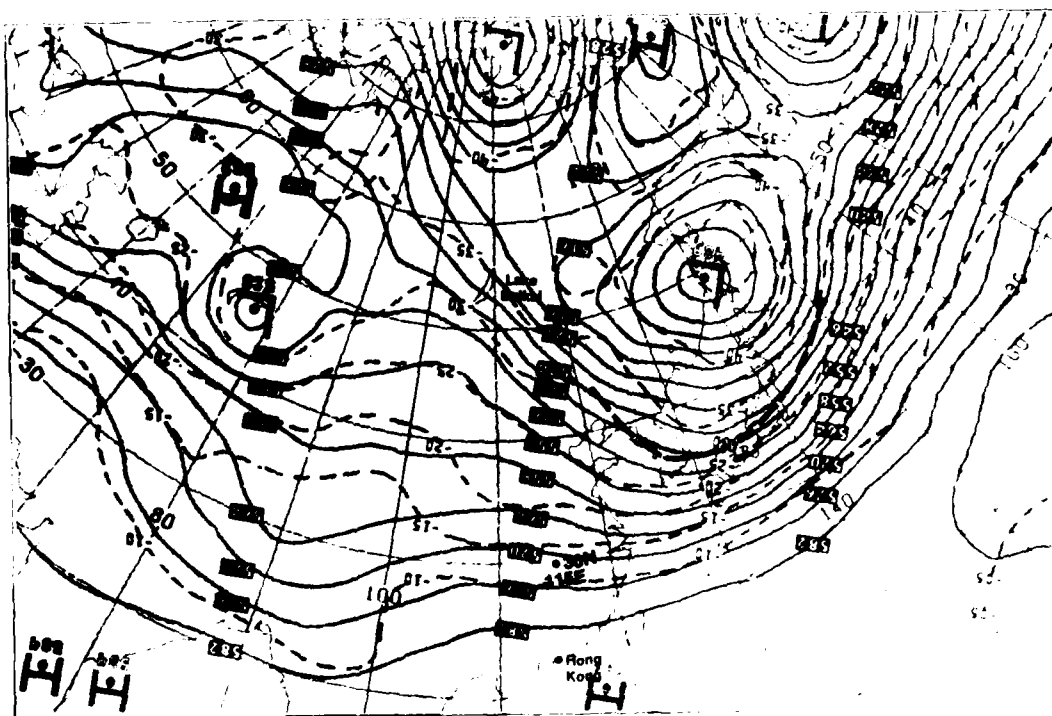
3B-16a. NMC 850-mb Analysis. 0000 GMT 6 December 1974.



3B-16b. NMC Surface Analysis. 0000 GMT 6 December 1974.

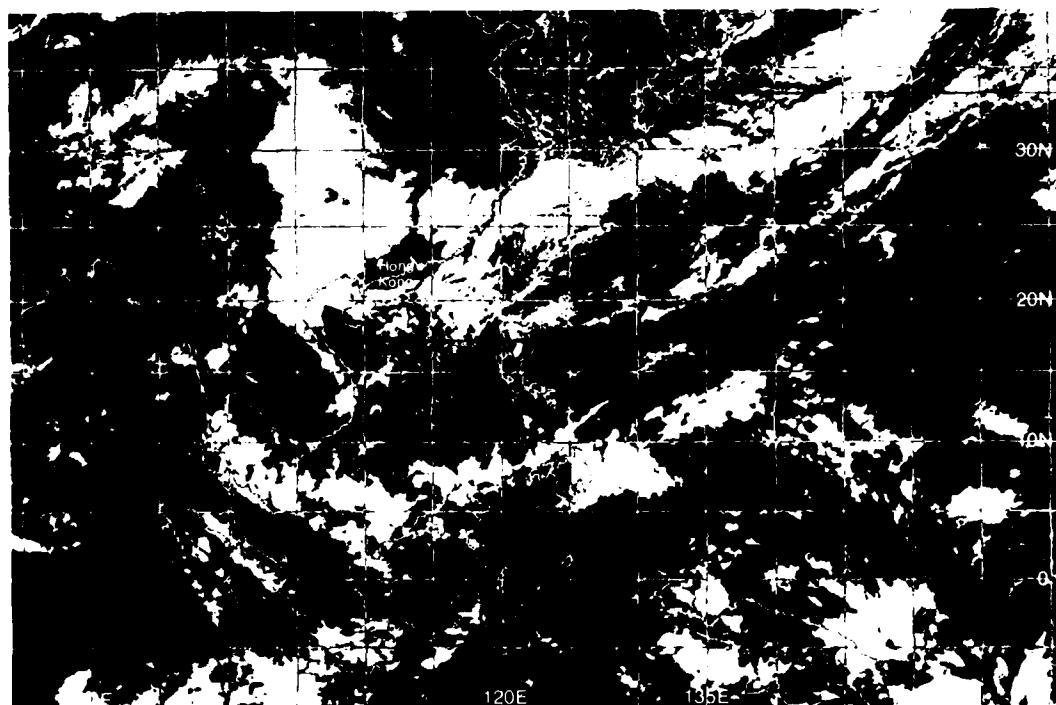
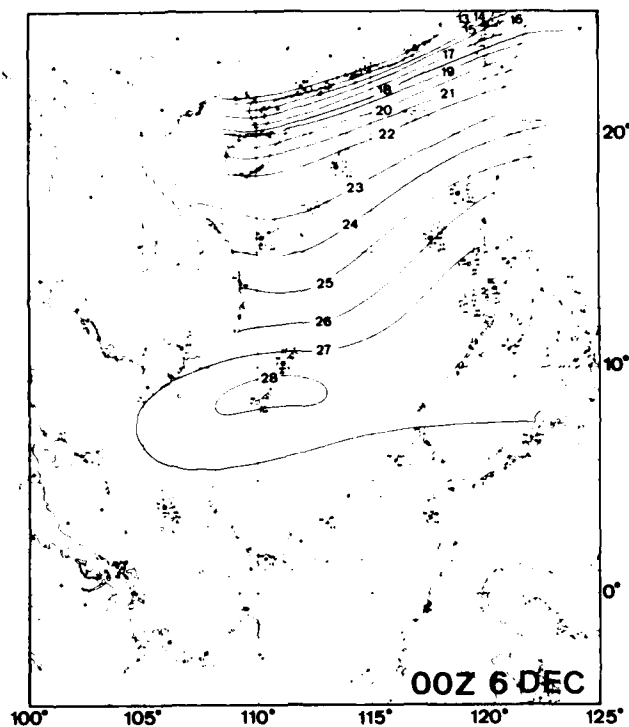


3B-17a. NMC 200-mb Analysis. 0000 GMT 6 December 1974.

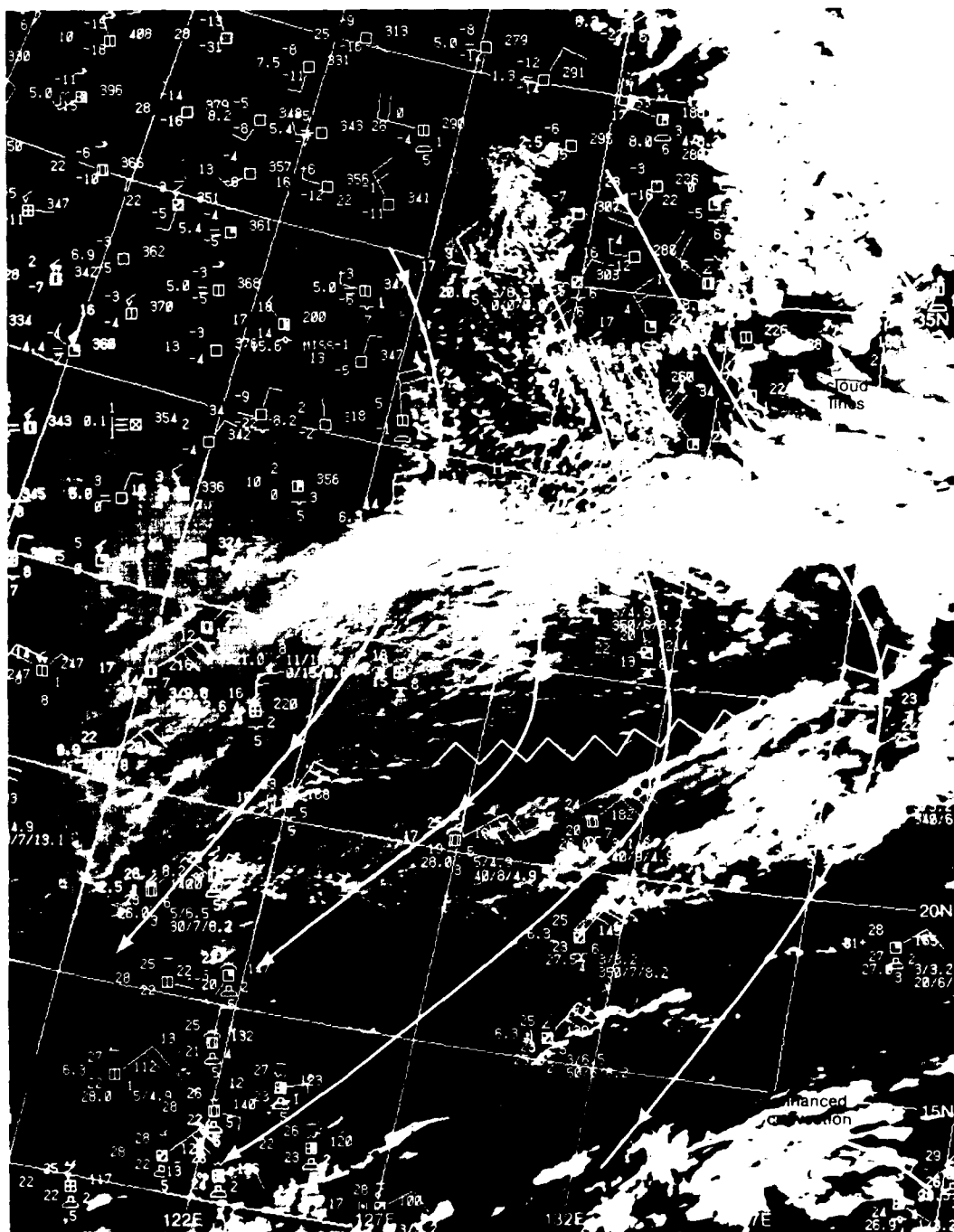


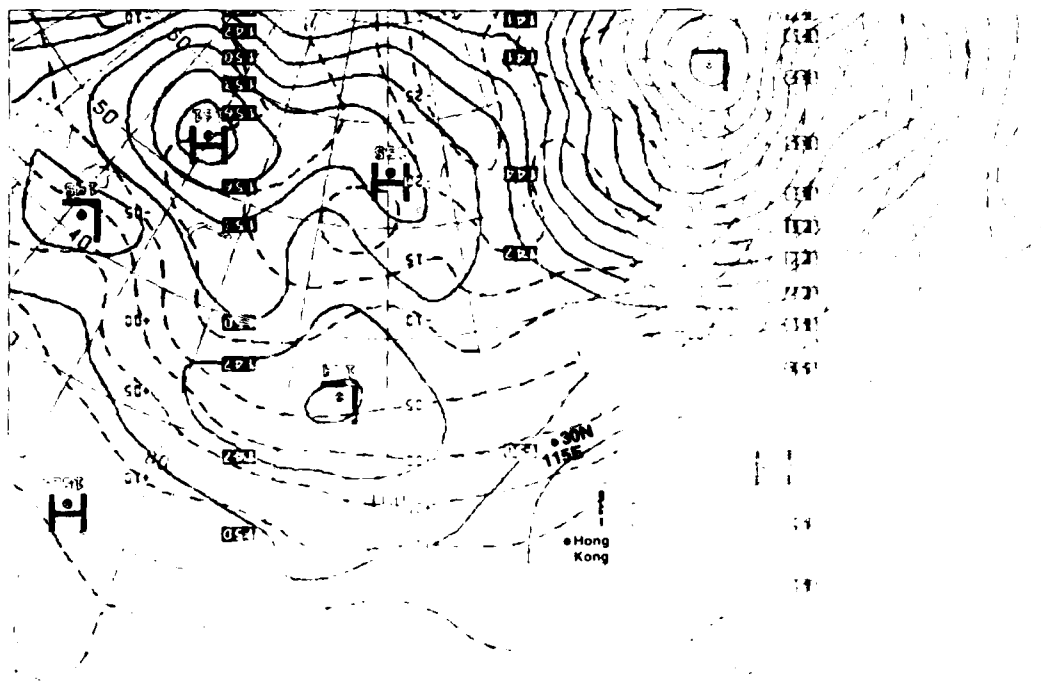
3B-17b. NMC 500-mb Analysis. 0000 GMT 6 December 1974.

3B-18a. Surface Temperature Analysis.
0000 GMT 6 December 1974
(After Chang *et al.*, 1979.)

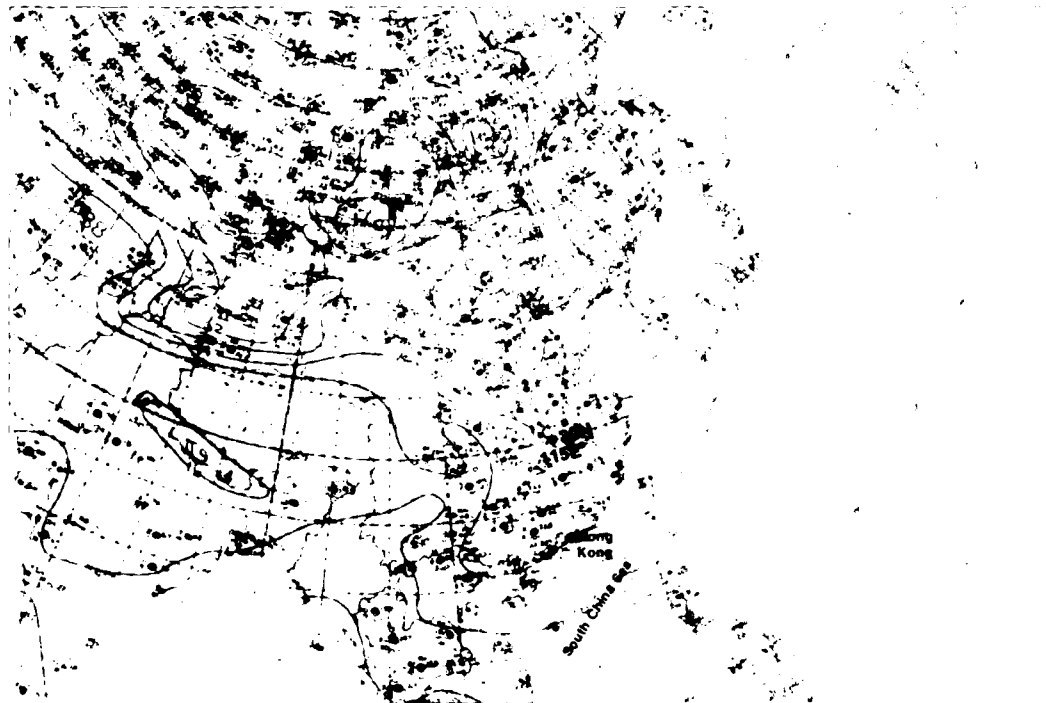


3B-18b. NOAA-3. Visible Image Mosaic. 0300 GMT 6 December 1974.





3B-20a NMC 850-mb Analysis 0000 GMT 6 December 1974



3B-20b NMC Surface Analysis 0000 GMT 6 December 1974

7 December

On this last day of the cold surge, the NMC surface analysis at 0000 GMT (3B-20b) omits the erroneously analyzed low in the central South China Sea, and the pressure gradient is shown to have relaxed considerably in the northern South China Sea. However, high pressure is building up again in the north for another surge (which followed on 9-12 December).

At 850 mb (3B-20a), the high-pressure dome has dropped further south associated with the advance of the surge, and cold air advection into the northern South China Sea has ceased.

The NMC 500-mb analysis (3B-21b) shows a dissipation of the block along 160° E, but the low over Japan still persists in roughly the same position. (By 8 December the low moved rapidly eastward). Northwesterly flow still persists over Lake Baikal.

The NMC 200-mb analysis (3B-21a) shows the jet streak with 170-kt wind maximum still at the base of the low near 140° E.

The NOAA-3 visible image mosaic at about 0300 GMT (3B-22b) reveals renewed indications of cold surge effects off Korea and Japan in the form of cloud lines emanating from coastal regions. A detailed surface temperature analysis (Chang *et al.*, 1979; 3B-22a) shows that a tongue of cold air has now moved past Vietnam to the northwest coast of Borneo. Heavy overcast cloudiness covers most of China and increased cloudiness appears offshore over Taiwan.

To the south, the equatorial CZ appears more intense with a disturbed area northwest of Borneo. It is suggested by Chang *et al.* (1979), that the disturbance intensified as a result of increased convergence and cyclonic shear caused by a confluence of winds from the cold surge into the disturbed region. Such an intensification is also suggested by cirrus streamers appearing in the DMSP visible image in the region south of Vietnam (3B-23a). The cirrus suggest increase outflow aloft forced by lower-level convergence and the accompanying release of latent heat through the convective process. Surface winds and the streamlines tend to support this hypothesis in showing that the strong winds are not driven by a low-pressure center, and the cirrus outflow area is many miles from any center of circulation associated with the disturbance.

Chang *et al.* (1979), also noted that the sudden apparent increase in intensity diminished shortly after the time of the DMSP image, as the cold air tongue (depicted in 3B-22a) protruded into the region of the disturbance. The diminished intensity was short-lived, however, as the cold temperature effects receded, and the disturbance again showed signs of intensification.

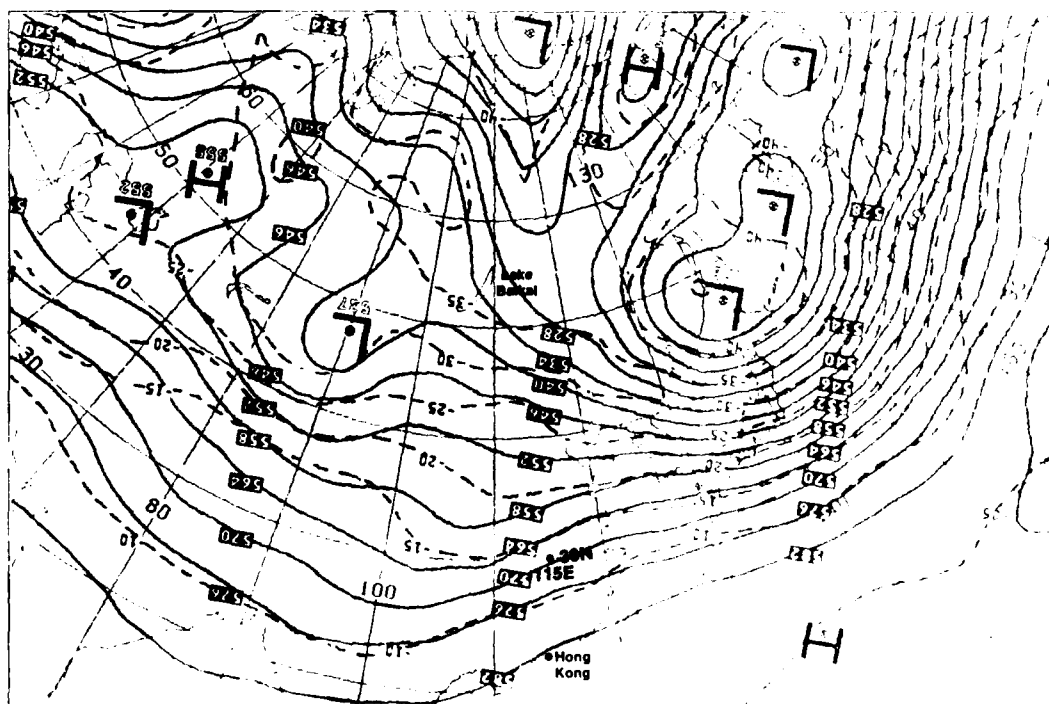
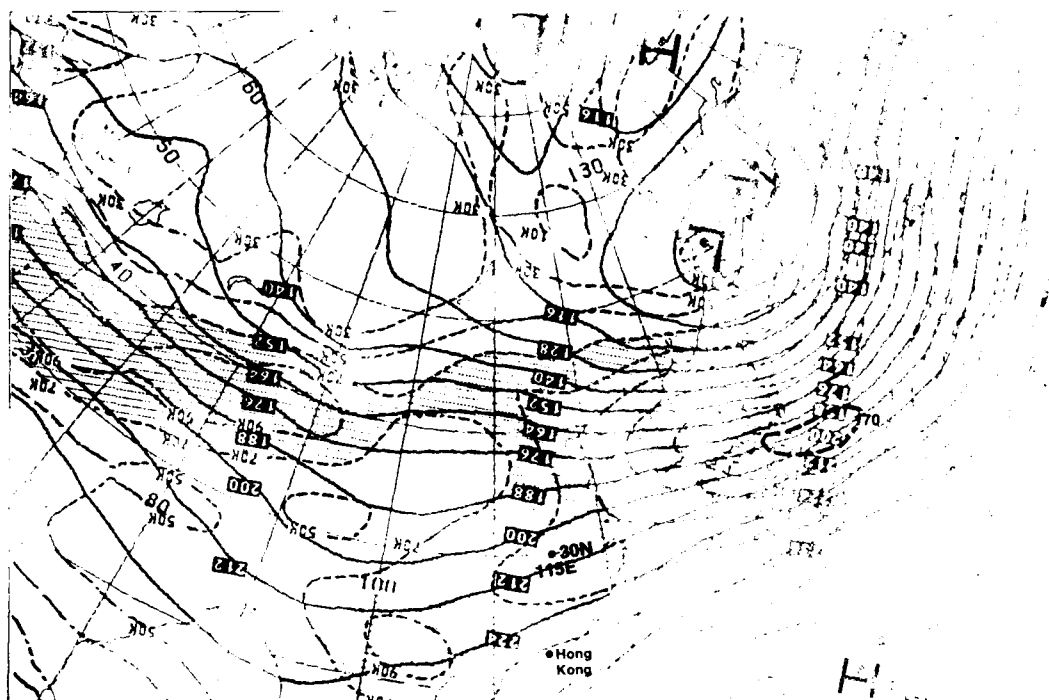
A final DMSP view of the disturbance at 0040 GMT on 9 December (3B-23b) shows intense cirrus outflow, and the streamlines, at this time, indicate a closed circulation. The storm, however, failed to achieve tropical storm intensity.

Important Conclusions

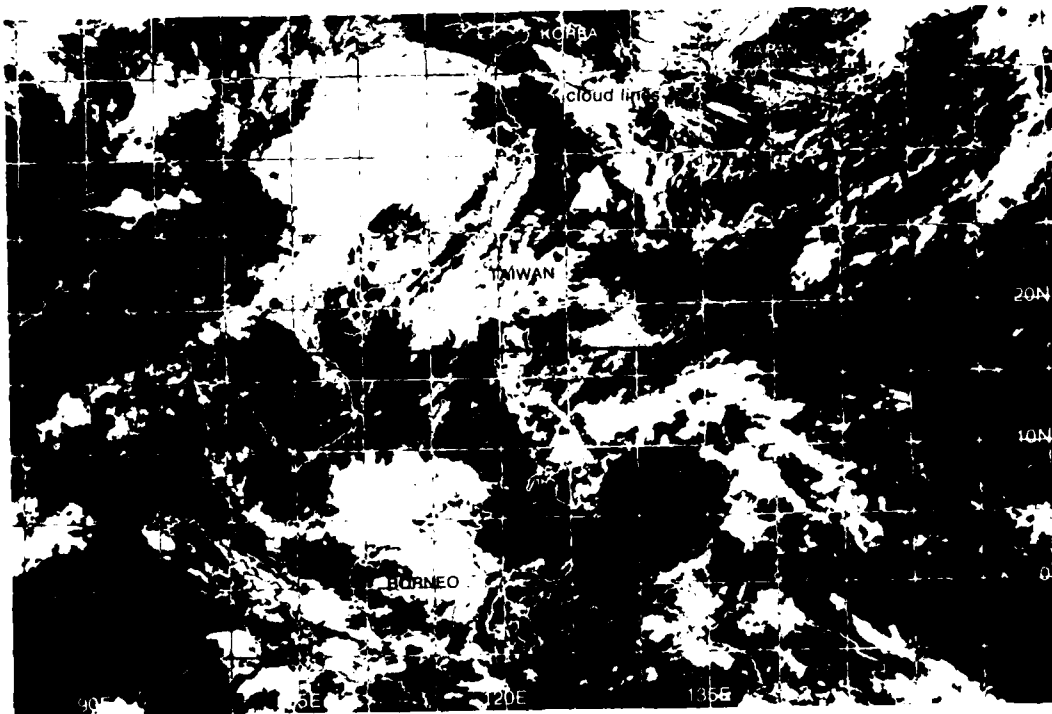
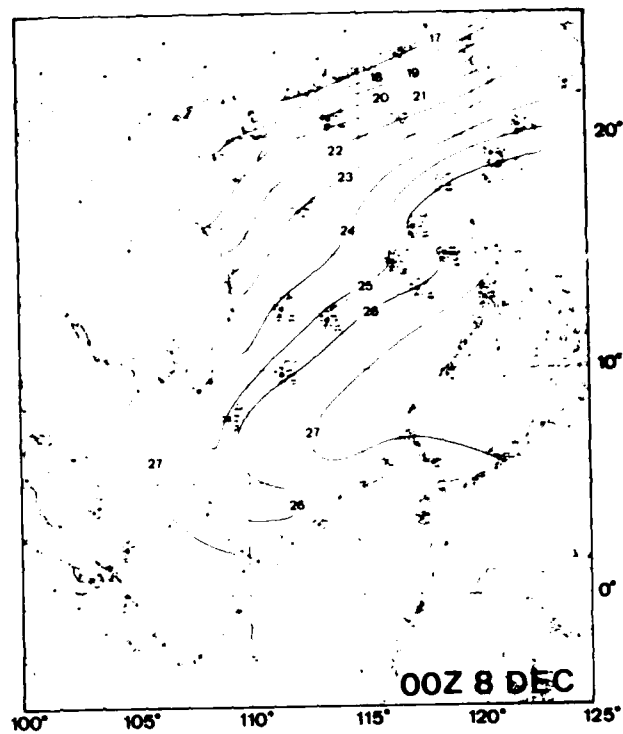
1. Cold surges off the coast of Asia have an important influence in the intensification of tropical convection and of tropical disturbances.
2. Cold surges are most easily detected by noting the locations of stronger than normal winds over the ocean regions during the period of the northeast monsoon, especially in the absence of low-pressure centers.
3. Because of rapid modification of cold air over-running warmer water, it is often difficult to detect a cold surge in tropical latitudes by a temperature decrease.
4. The most reliable method of predicting the possibility of a cold surge into the South China Sea, within 24 hr, is to note the following evidence:
 - a. Winds at 500 mb over Lake Baikal are northwesterly.
 - b. A trough at 500 mb is approaching Japan.
 - c. A strong pressure gradient exists between a low near Japan and a high to the southwest of Lake Baikal.
 - d. The -30° C isotherm is beginning to move south of 40° N over western Asia.
 - e. A pressure gradient of -10 mb exists between Hong Kong and 30° N, 115° E.
 - f. Jet streaks (>130 kt) at 200 mb persist for at least 3 days over Japan.
5. The 850-mb analysis is a good indicator of low-level cold air advection.
6. Strong winds from a cold surge precede any indication of falling temperatures and at times temperatures never do fall, particularly in those regions where air has had a long over-water trajectory.
7. Cooler temperatures associated with a cold surge are most likely to be noted near the coast of Vietnam in the South China Sea.
8. Blocking action, as detected at the 500-mb level, near 160° E, appears important in anchoring low pressure in the region north of Japan, and thereby providing a stationary channel for cold northerly winds to surge southward over an extended period.

References

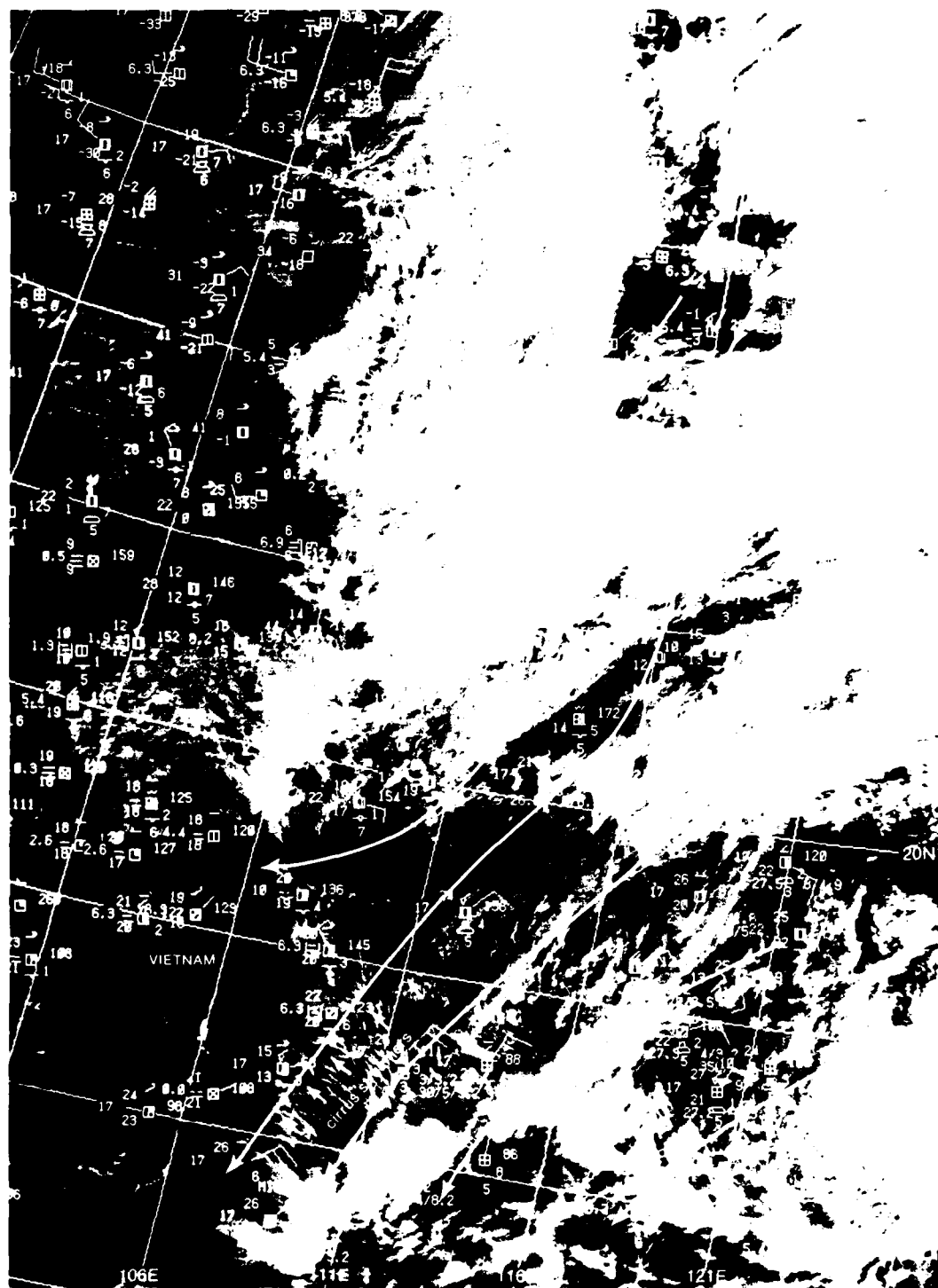
- Chang, C. P., J. E. Erickson, and K. M. Lau, 1979. Northeasterly cold surges and near-equatorial disturbances over the Winter Monex Area during December 1974. Part I, Synoptic Aspects. *Mon. Wea. Rev.*, **107**, 812-829.
- Riehl, H., 1968. Surface winds over the South China Sea during the northeast monsoon season. Naval Weather Research Facility Tech. Pap. No. 22-68, 24 pp.



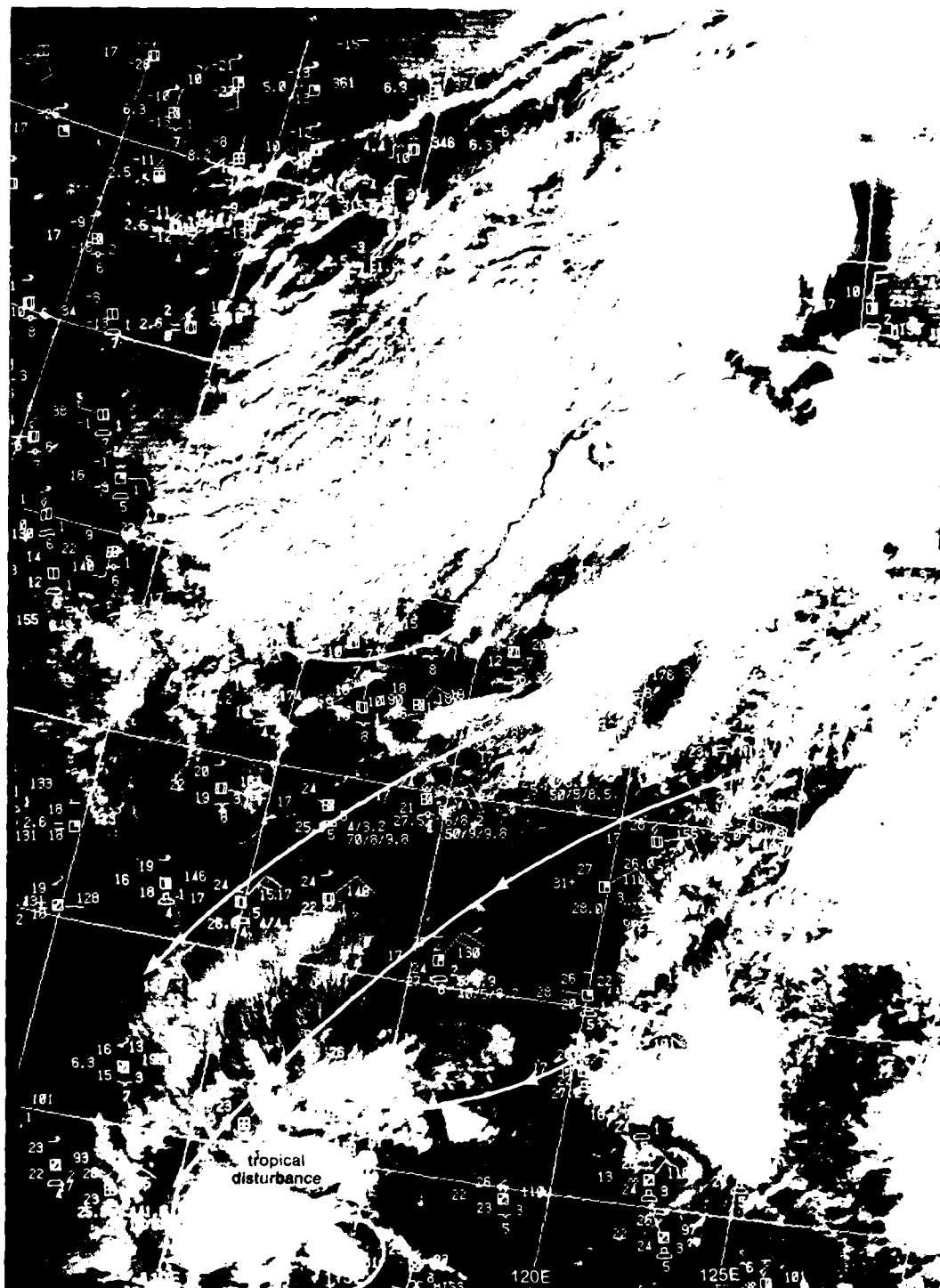
3B-22a Surface Temperature Analysis
0000 GMT 7 December 1974
(After Chang *et al.*, 1979)



3B-22b NOAA-A Visible Image Mosaic 0300 GMT 7 December 1974



3B-23a FTV-29 DMSP LF Low Enhancement, 0058 GMT 8 December 1974, Surface Reports (0000 GMT) and Streamlines.



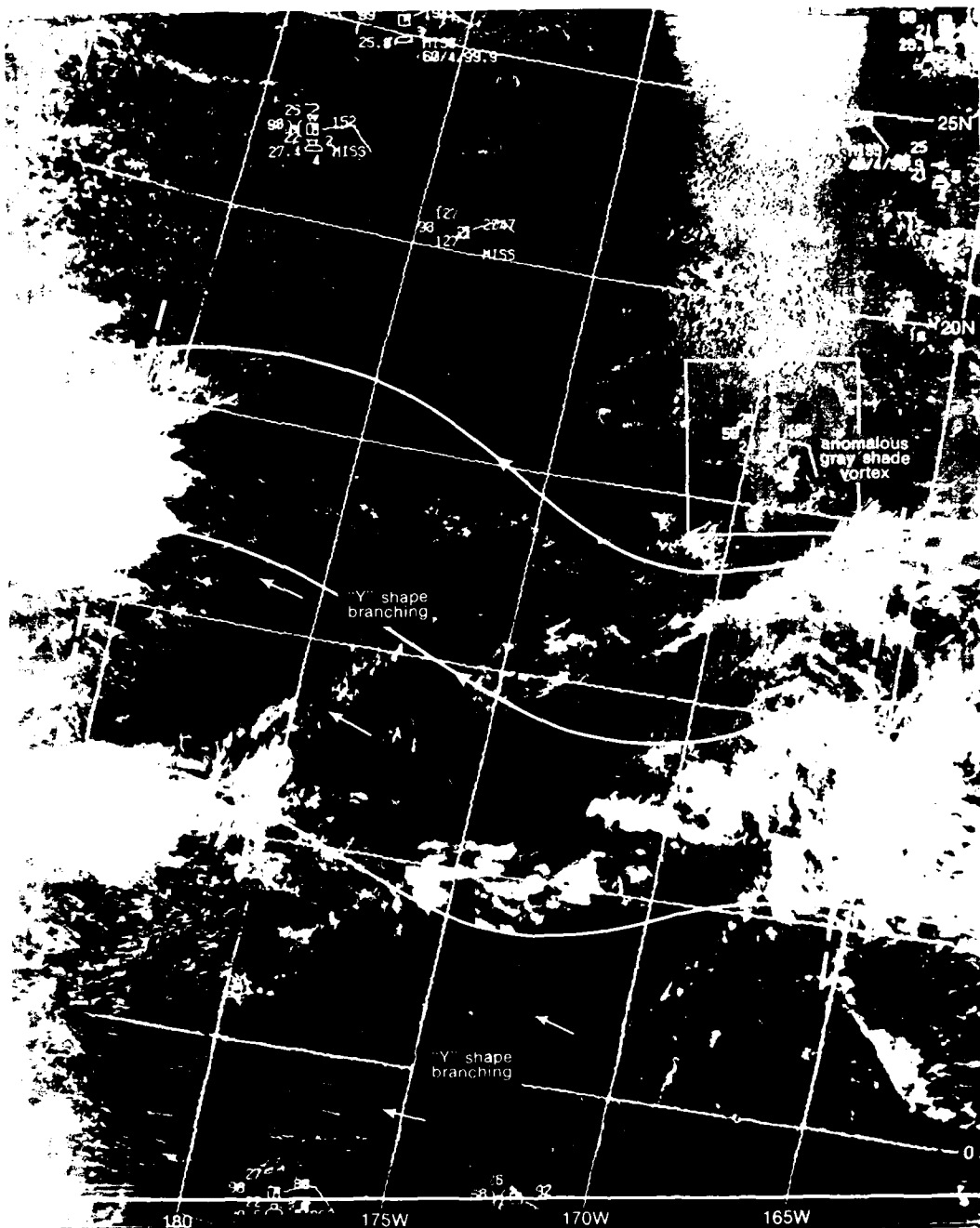
3B-236 F14-29 DMSP LF Low Enhancement 0040 GMT 9 December 1974 Surface Reports (0000 GMT) and Streamlines.

Case 2 Mesoscale Use of Cloud Lines and Anomalous Gray Shades in the Tropics

Cloud lines in the tropics are good indicators of low-level (gradient wind-level) wind direction. In addition, in satellite visible imagery, the appearance of the characteristic "Y-shaped" branching on the downstream end of a cloud line is useful for resolving the 180 deg ambiguity in determining the direction of the flow.

Weak vortices or upper-level trough axes are sometimes defined by the spiral pattern of satellite-observed anomalous gray shades and embedded cloud bands.

Together these indicators can improve synoptic analysis in regions of few conventional observations.



3B-26a FTV-29 DMSP LF Low Enhancement. 2011 GMT 29 June 1974. Surface Reports (1800 GMT) and Streamlines

*Identification of a Weak Cyclonic Circulation
Tropical Central Pacific
June 1974*

28 June

The DMSP visible image (3B-26a) reveals a fairly inactive convergence zone (CZ) between 4° to 15° N, and 170° to 180° W. Note that the surface winds (ship reports) on either side of the CZ are easterly. Using cumulus cloud lines as additional indicators of basic low-level flow, it can be inferred that easterlies prevail throughout the area from south of the Equator to mid-latitudes. The characteristic "Y-shaped" branching on the downstream end of several cloud lines resolves the sense of direction as easterly.

The cloud cluster near 7° N, 165° W does have some weak banding on the northern side suggesting the possibility of a weak easterly wave. About 25° further west, a typical spacing between wave phenomena of the CZ, a second wave is implied by heavy convective activity extending up to 15° N.

This example supports other evidence indicating that weak tropical waves or easterly waves are found in the Pacific as well as the Atlantic tropical areas, where they are well documented.

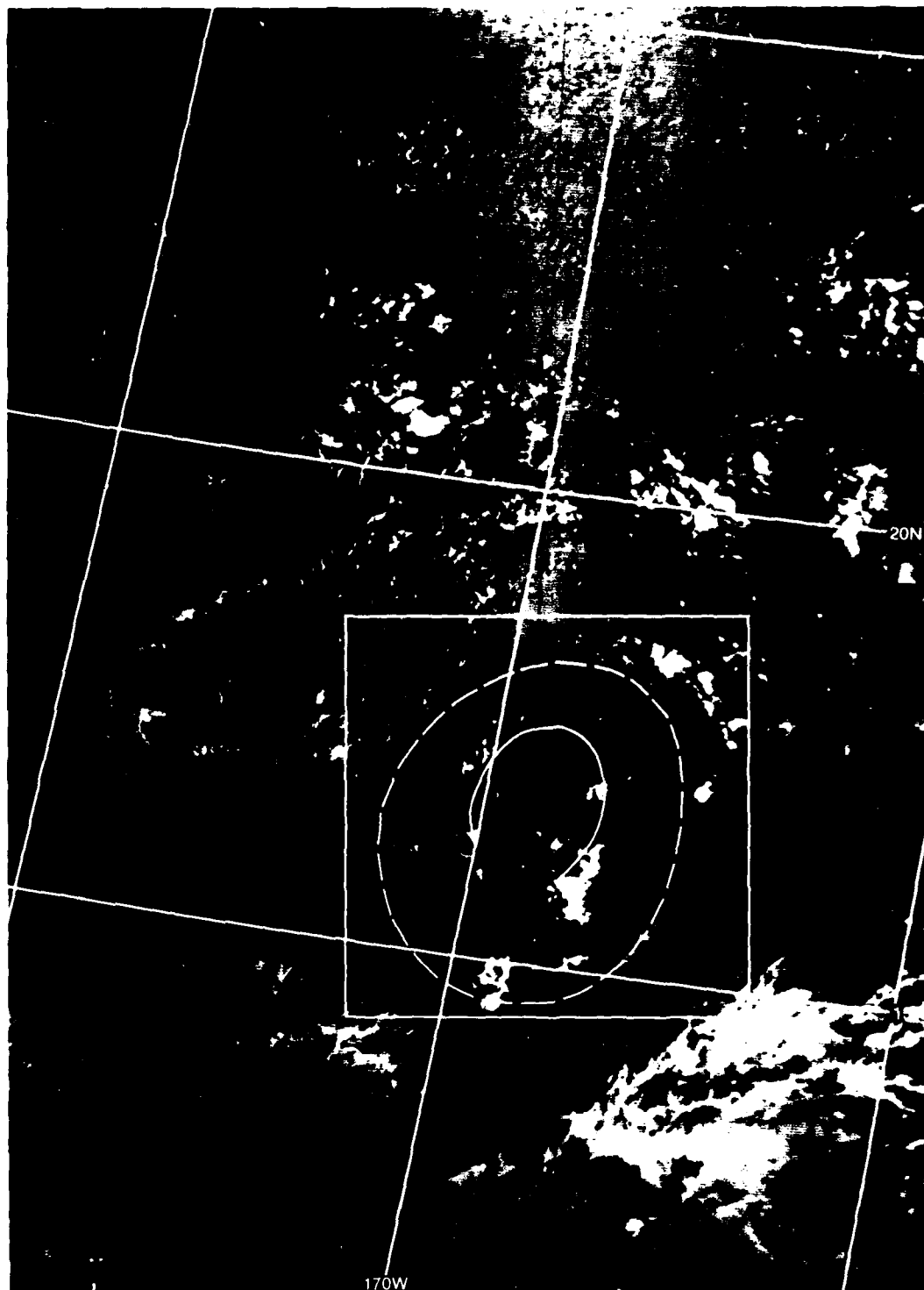
A close examination of the area near 16.5° N, 170° W (3B-27a) reveals a weak cyclonic circulation (vortex) defined partially by curving cumulus cloud bands and partially by darker gray shades indicative of a high moisture concentration, blocking underlying sunlight. Since low-level flow is easterly through this area, a vertical shear is implied suggesting the presence of an upper-level trough or vortex. This possibility is confirmed by RAOB data (3B-28a and 28b) from Johnson Island (16.7° N, 169.5° W) and from Midway Island (28.2° N, 177.4° W), which show strong jet force westerlies (55 kt) to the south at Johnson and light (10 kt) northeasterlies to the north at Midway about 4 hr after the time of the DMSP image.

The FNOG 500-mb analysis at 1200 GMT on 29 June (3B-29a) clearly shows the Tropical Upper Tropospheric Trough (TUTT) passing westward through the Hawaiian Islands to the vicinity of Johnson Island.

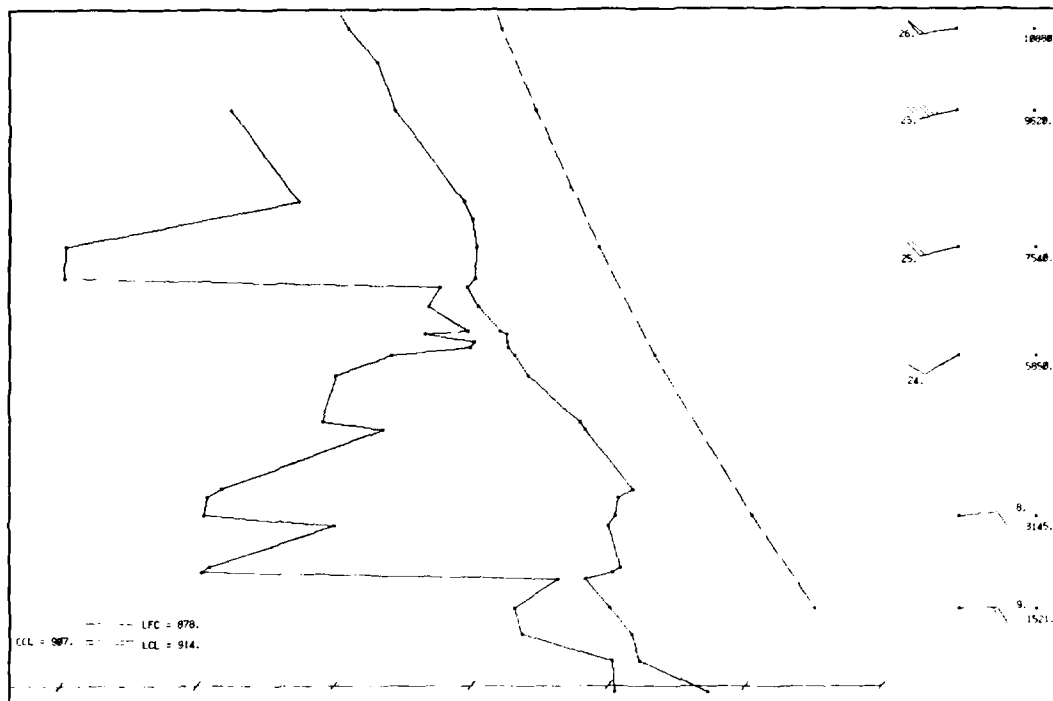
Important Conclusions

1. Weak easterly waves embedded in easterly flow to the north and south of the wave location do occur in the tropical Central Pacific.
2. Y-shaped branching on the downstream end of cloud lines is a useful tool in determining low-level wind direction.
3. Anomalous gray shades in regions where upper-level troughs pass over sunlight regions can be useful in determining trough presence and location.
4. Weak tropical waves can be detected by noting areas of more intense convection preceded by cyclonically curving cloud elements defining an axis, or centers along an axis, of positive relative vorticity.

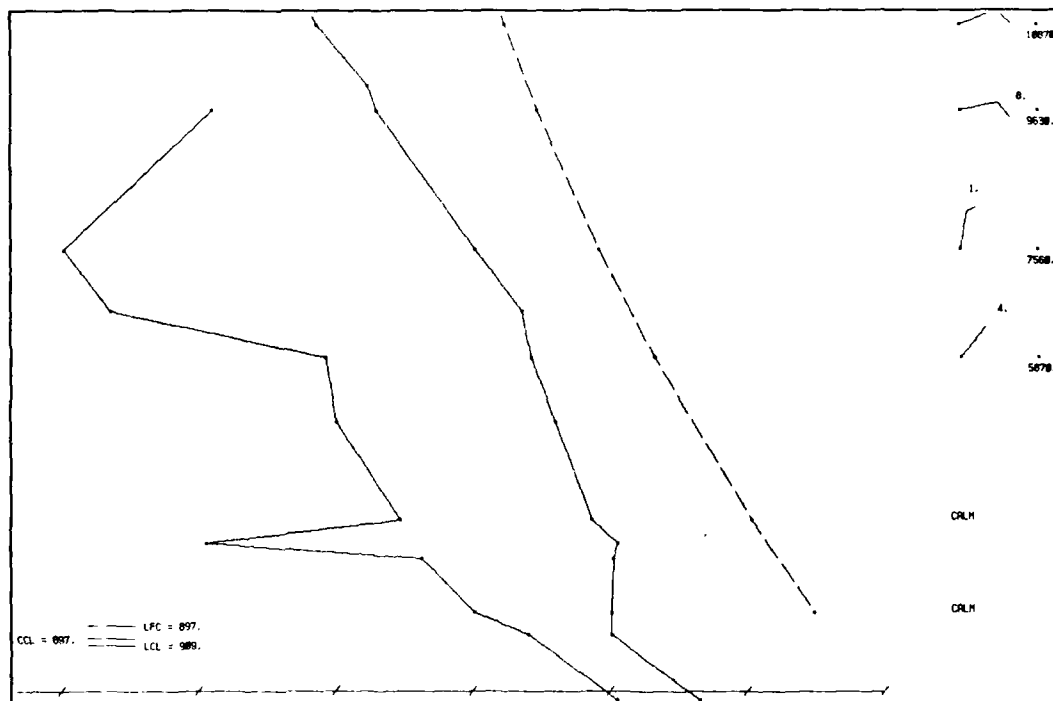
3B-26-B



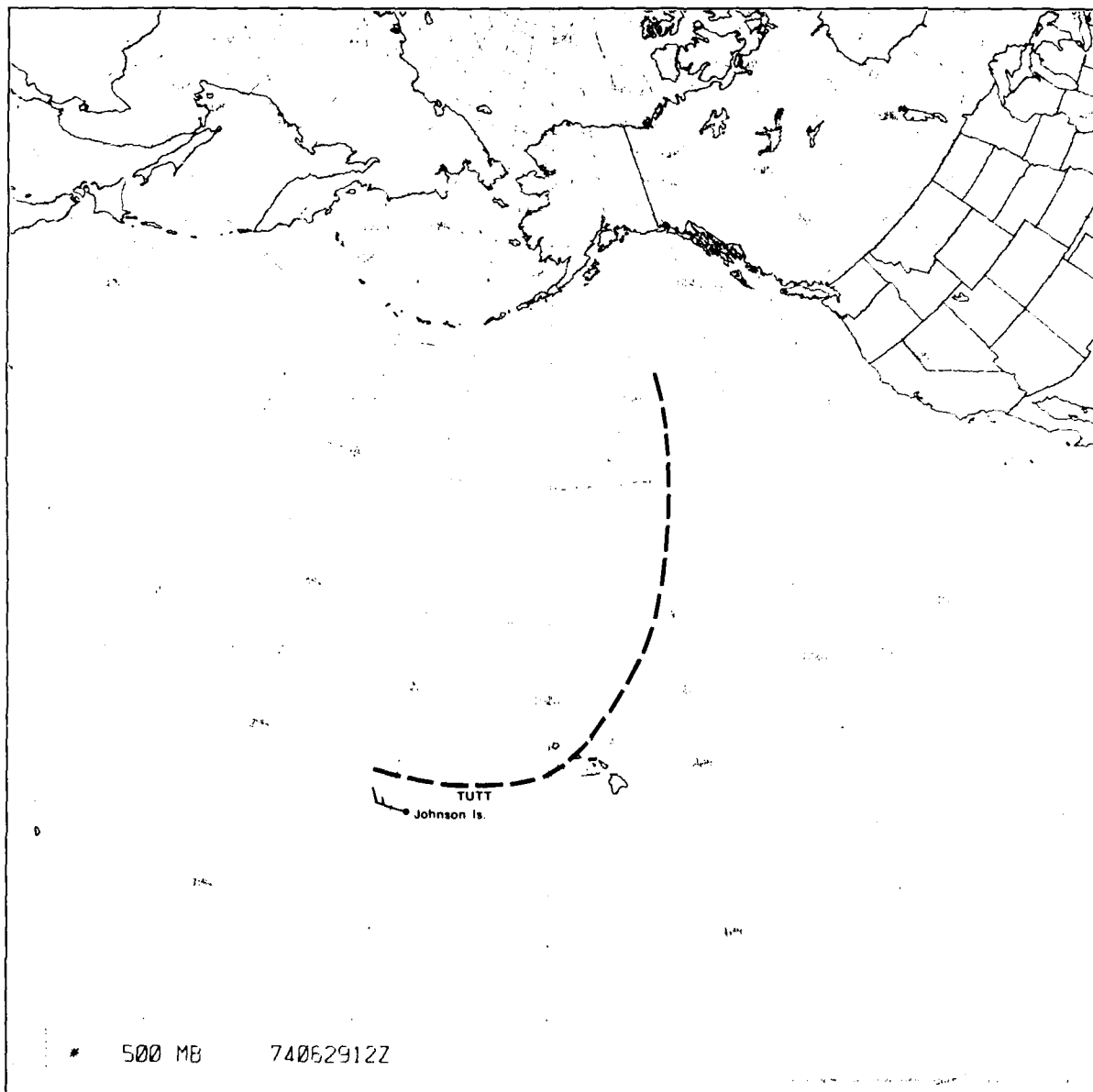
3B-27a FTV-29, DMSP LF Low Enhancement, 2011 GMT 29 June 1974.



3B-28a. RAOB. Johnson Island. 0000 GMT 29 June 1974.



3B-28b. RAOB. Midway Island. 0000 GMT 29 June 1974.

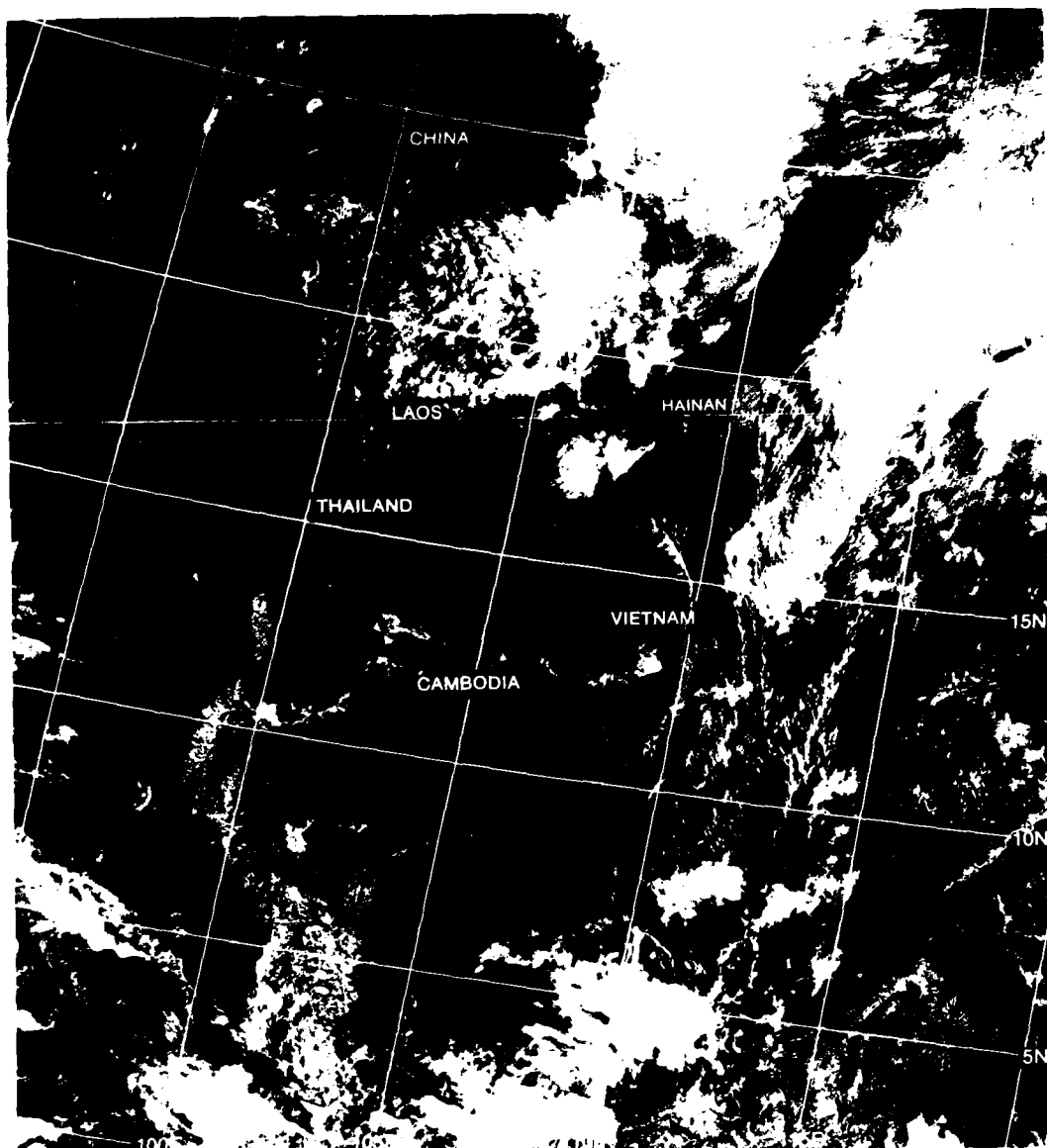


3B-29a FNOG 500-mb Analysis 1200 GMT 29 June 1974

Case 3 Tropical Air Fog

The tropics are normally thought of as fog-free areas. However, during winter months, fog can form over tropical or semi-tropical ocean areas as warm, moist tropical air is advected northward around the western portion of high pressure systems. The tropical air is cooled to saturation as it passes over increasingly cooler water to the north.

3B Case 3



3B-32a. F-2. DMSP LF Low Enhancement. 0347 GMT 24 December 1978.

*Tropical Air Fog
Gulf of Tonkin
December 1978 and January 1980*

24 December 1978

The DMSP visible image at 0347 GMT (3B-32a) shows a generally fog-free day over Southeast Asia. Lakes and streams and land topography are crisply delineated. Note that the appearance of such features over relatively low elevations in Thailand, Laos, Cambodia, and Vietnam does not appear less clear than over much higher elevations such as a mountainous region of China near the top central portion of the image. (Overcast cloudiness is banked up against the foothills of this region from the east).

29 January 1980

The DMSP visible image of the region (3B-33a) shows a significant change in clarity over northern Thailand, Laos, and Vietnam. The area to the north, over China, however, appears largely unaffected.

Also immediately noticeable is the gray shade extending eastward over the Gulf of Tonkin, which nearly obscures Hainan Island.

Surface reports superimposed on the DMSP image (3B-33a) reveal the wide-spread fog and poor visibilities (in statute miles) present on this day. One could immediately deduce and reasonably analyze for the poorer visibility areas based only on the gray shade information appearing in the DMSP image.

Since the depiction is for an early morning (0830 LST) view, it is easy to explain the fog over the land as an effect due to radiational cooling under clear night-time sky conditions. However, this logic cannot explain the extensive occurrence of fog over the South China Sea.

A RAOB from Da Nang (16° N, 108.2° E) at 0000 GMT (3B-34a) reveals a boundary-layer height of about 1,466 m (850 mb). The sounding stabilizes above this level as the air becomes much dryer. Wind speeds increase rather strongly within the boundary layer from 10 to 35 kt at 1,466 m (850 mb). The fact that these strong winds do not extend to the surface is an indication of the stabilizing effect of cold air near the ground. Still some possibility of advection of the fog from the land to the sea is suggested by the sounding which reveals westerly winds blowing from the land to the sea.

For fog to persist over the sea at a land air temperature of about 19° to 20° C implies that the sea surface temperature in the Gulf of Tonkin region be no warmer than these same values. Otherwise the fog would be dispersed by turbulent mixing and heat flux from the sea to the air.

An FNOG regional sea surface temperature analysis for 0000 GMT (3B-34b) reveals that temperatures, indeed, were considerably warmer than the air temperature over land—ranging in values from 22° to 24° C, or 2 to 4 deg higher than land temperatures. This suggests that fog advected over the water could not persist and that the major source of the fog over the South China Sea was not advection from land but

through some other mechanism.

The FNOG surface analysis for the region (3B-35a) shows the tight packing of isobars associated with extremely cold air and high pressure to the north over China. A trough of low pressure extends from east of Japan southwestward past Taiwan to Hainan Island. A ridge of high pressure extends from east of the Philippines into the South China Sea.

Weak southerly flow comes around the periphery of the high, in the South China Sea, into the trough to the north.

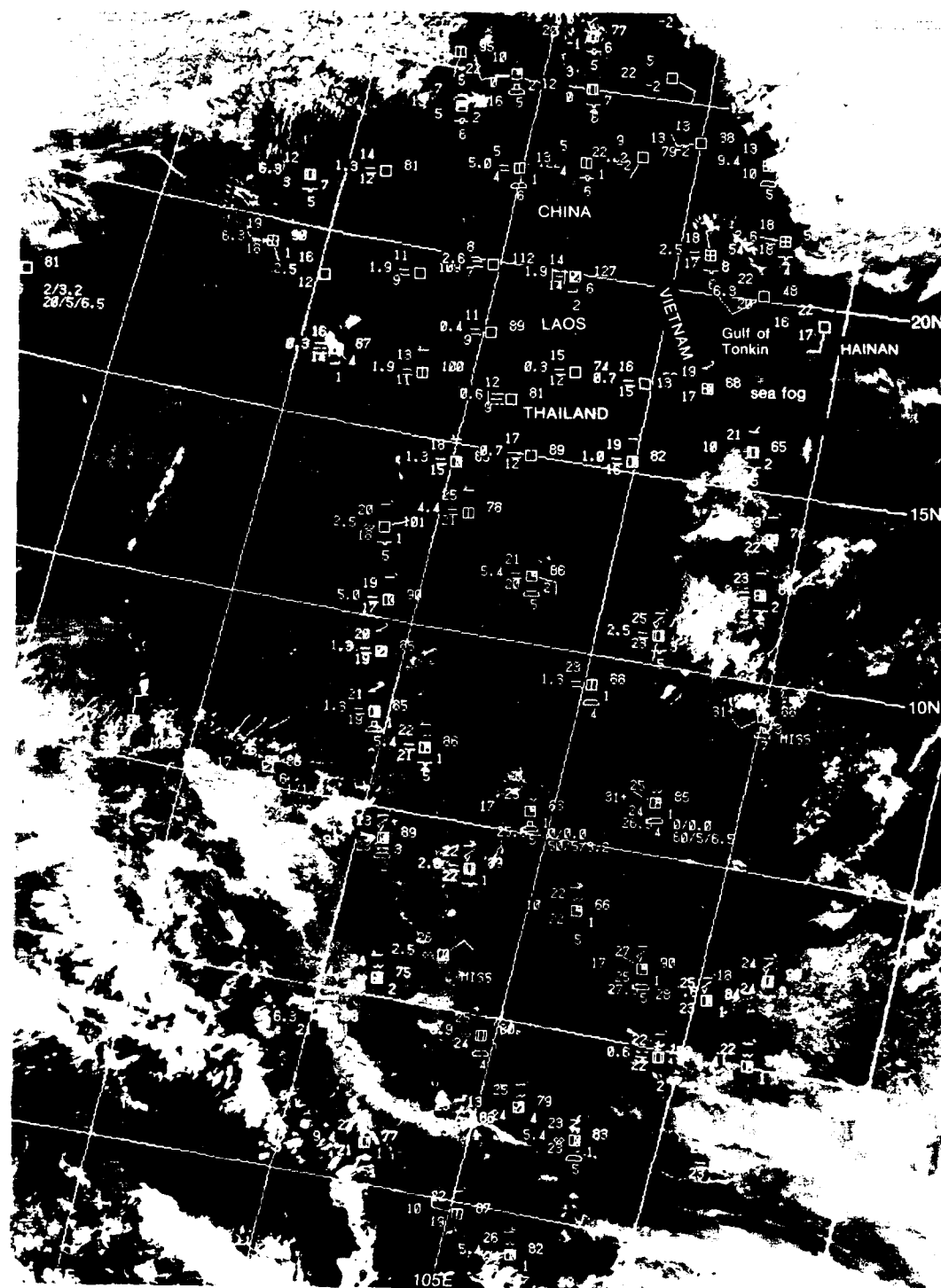
Dew point temperatures over the southern South China Sea are about 24° C, and dry bulb temperatures are only a few degrees higher. Comparing these temperatures to the sea surface temperature analysis (3B-34b) indicates that the maritime air over the South China Sea would reach saturation very rapidly, after being advected north of 15° N, due to cooling of the air by the sea. This could account for the widespread fog noted in that region which becomes denser (judging by the gray shade values (3B-33a) the further north the air is advected over increasingly cooler water. Fog formed in such a manner is referred to as tropical air fog (Byers, 1974).

Important Conclusions

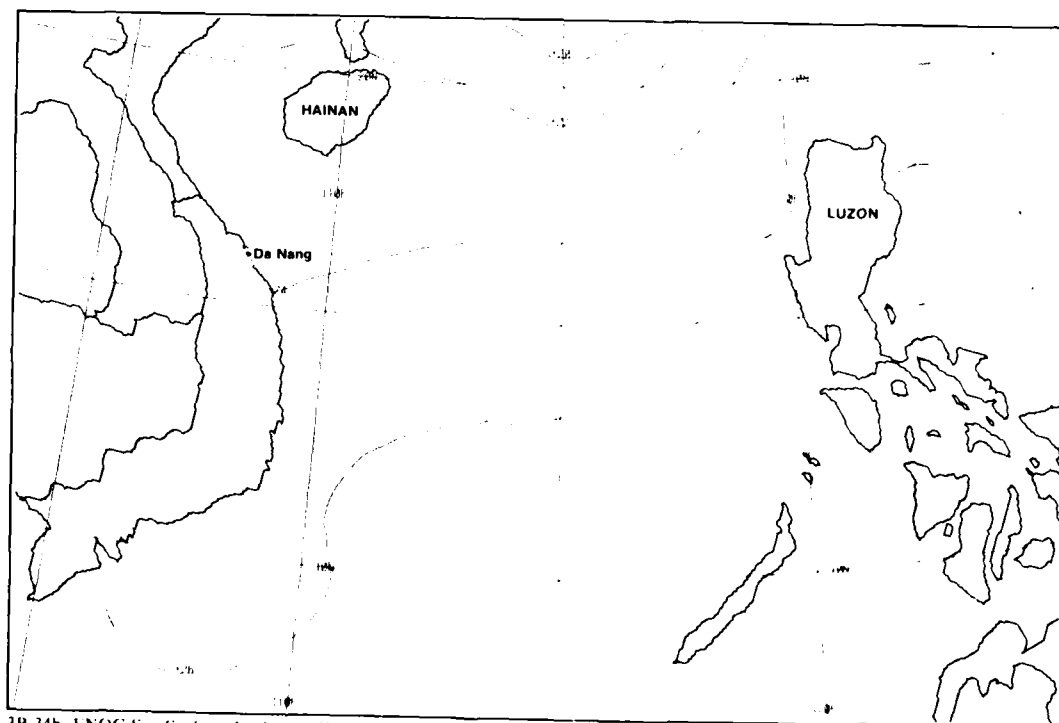
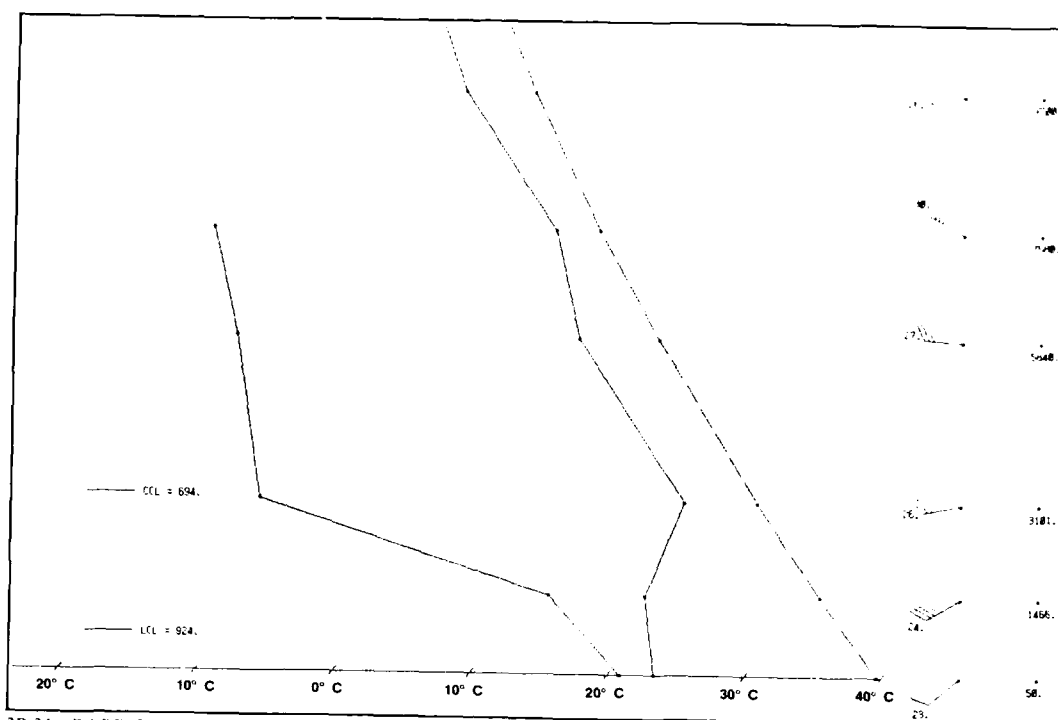
1. Widespread fog over the South China Sea can occur in winter months due to the advection of moist tropical air northward over increasingly cooler water.
2. A good way to predict the occurrence of such fog is to note when conditions for advection of moist tropical air from the south into the South China Sea are likely to occur. When the tropical air is close to saturation, fog can be anticipated to the north.
3. The presence of fog over land can often be determined by visual inspection of DMSP high resolution visible imagery, and noting regions where underlying terrain features, lakes and streams, are blurred or obscured in comparison to fog-free views.

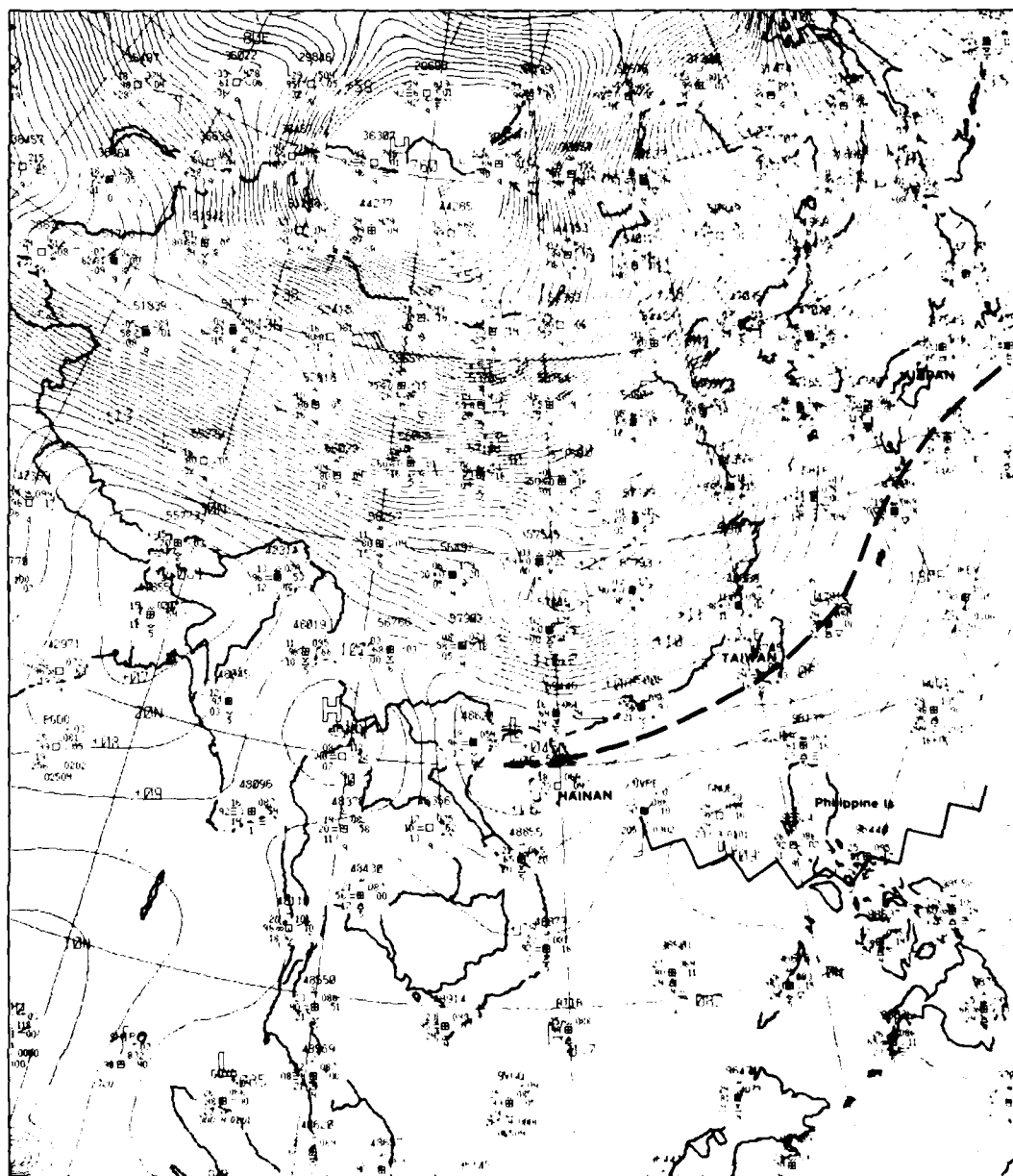
Reference

Byers, H. R., 1974. *General Meteorology*. McGraw-Hill Book Co., Inc., New York and London, p. 645.



3B-33a F-2 DMSP LF Low Enhancement 0238 GMT 29 January 1980 Surface Reports (0000 GMT)



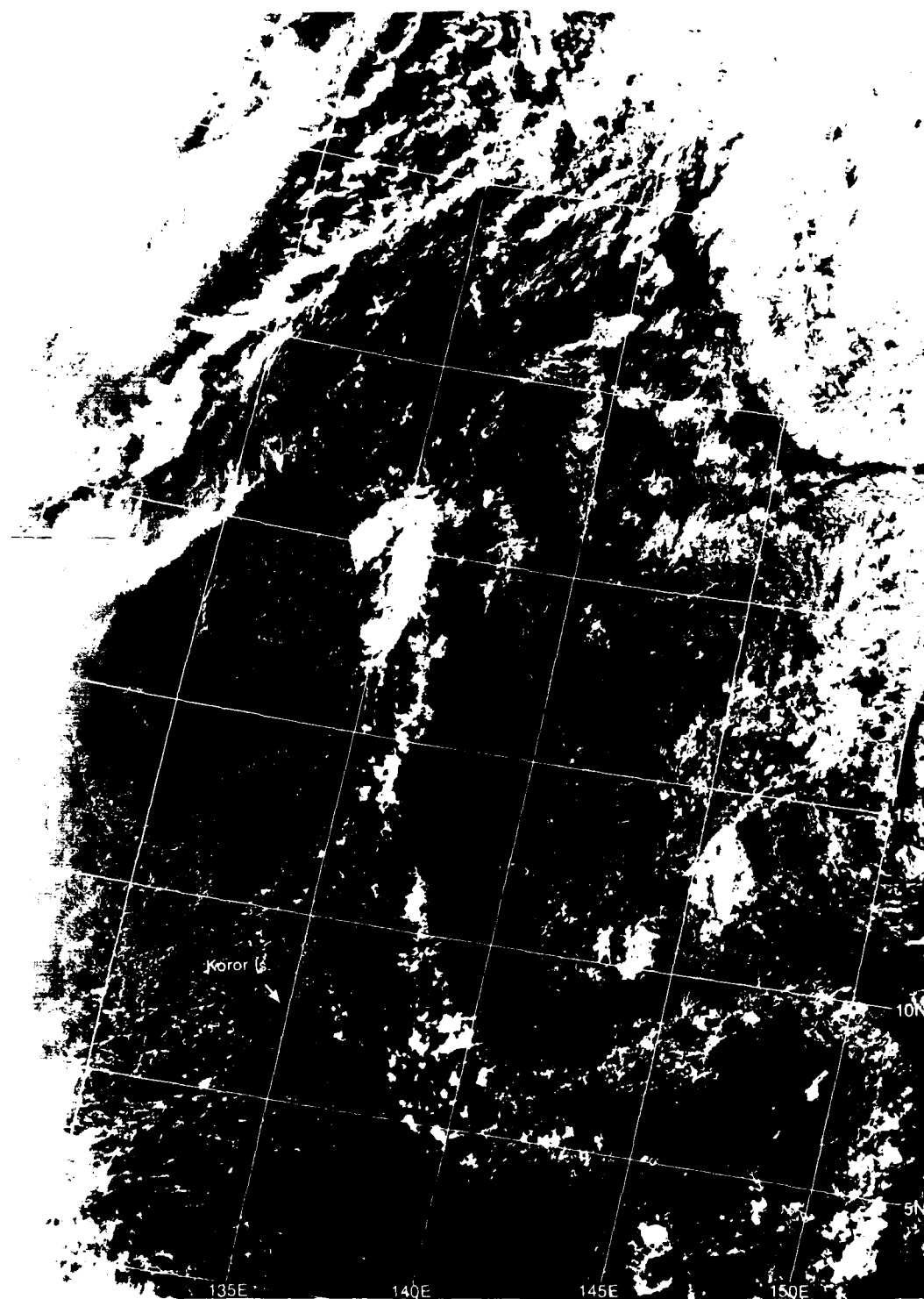


3B-35a LNOG Surface Analysis 0000 GMT 29 January 1980

*Case 4 Use of Convergence Bands in the Tropics
to Locate Surface Troughs*

Cloud bands leading into tropical depressions from points a thousand miles or more from the center are normally found to be associated with asymptotes of convergence in the low-level flow or with trough lines connecting cyclonic centers.

3B (anc-4)



3B-38a. F-2. DMSP LF Low Enhancement. 2150 GMT 17 November 1977.

*Locating the Surface Trough Line
in a Weak Tropical Disturbance
Tropical Western Pacific
November 1977*

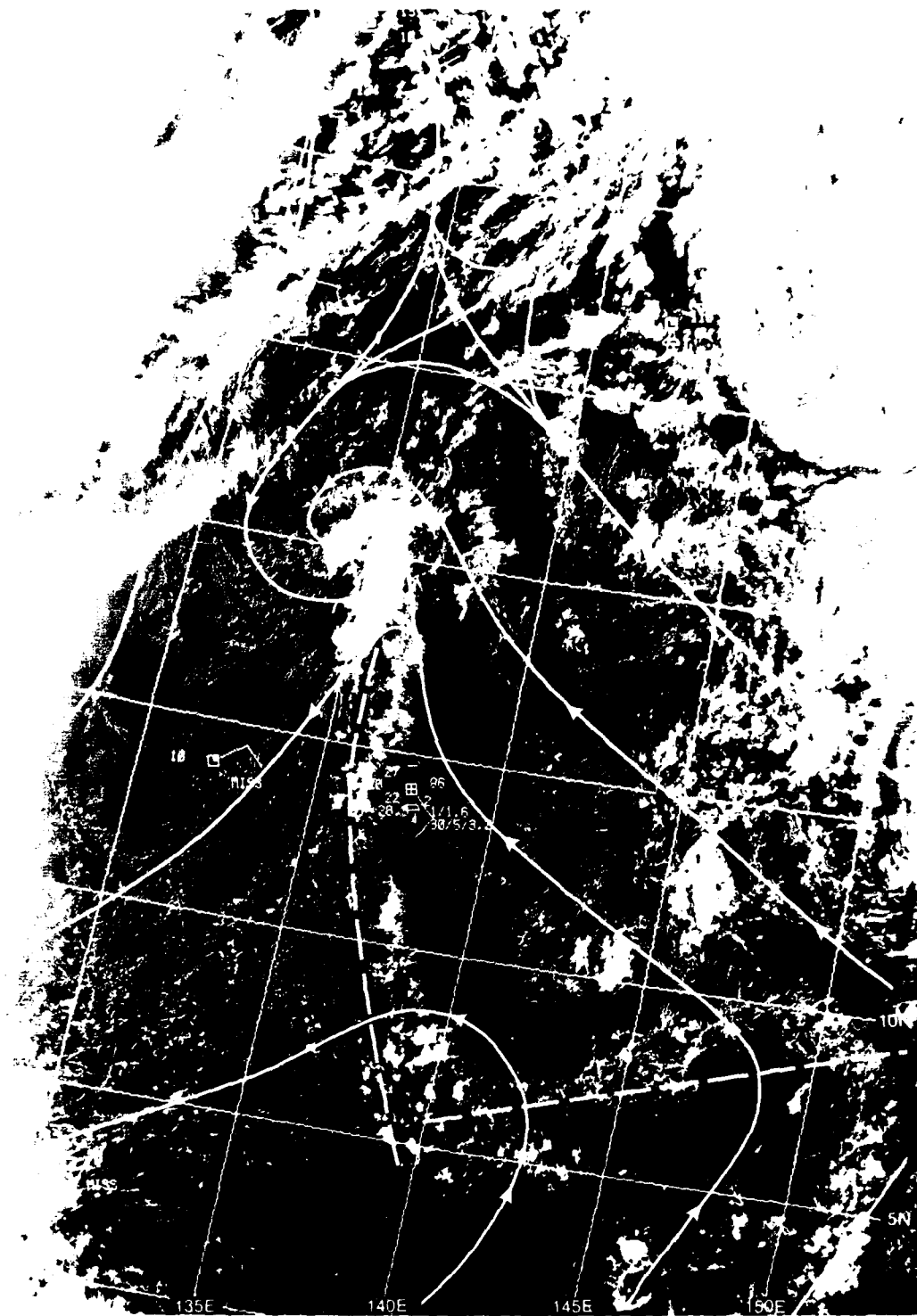
17 November

The DMSP visible image (3B-38a) reveals a tropical depression with center near 20°N, 134°E. This depression never intensified to tropical storm status.

Of immediate interest is the long north-south oriented cloud band leading to the storm from over 1,500 n mi distance to the south. Also of interest is the heavy cloud band forming the tail of the storm comma cloud, also pointing to the south.

The superimposed streamline analysis based on surface reports and low cloud alignment (3B-39a) reveals that the long cloud band is located due east of a trough line, while the heavy convective comma tail corresponds to the location of an asymptote of convergence associated with a hyperbolic point southeast of the storm center. These are logical positions for the trough and convergence asymptote, which repeat in other synoptic situations on a reliable basis. The features, therefore, can be a great assistance in synoptic analysis, particularly, when other conventional reports are not available.

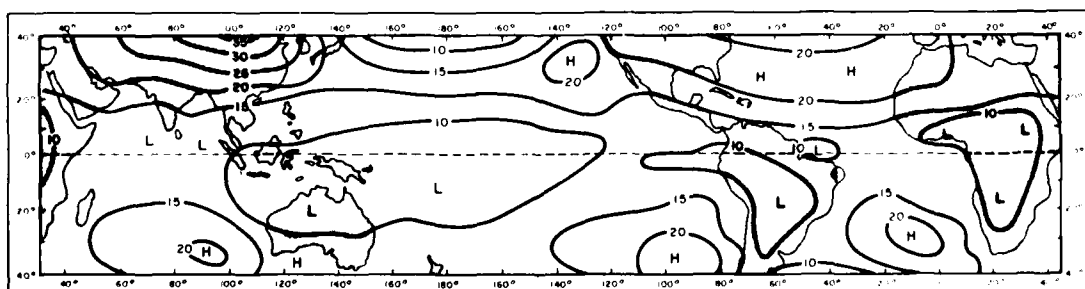
3B-38 B



3B-39a 1-2 DMSP-11 Low Enhancement 2150 GMT 17 November 1977 Surface Reports (1800 GMT) and Streamlines

Case 5 *Use of Sunlint in Determining the Position of the Southern Equatorial (Monsoon) Trough*

The seasonal mean sea-level pressure over the tropics (3B-41a) shows a broad elongated trough extending from near the equator in the eastern Pacific westward to the Australian-Indonesian region during the month of January.



3B-41a. Mean sea-level pressure (mb). (After Crutcher and Davis, 1969.)

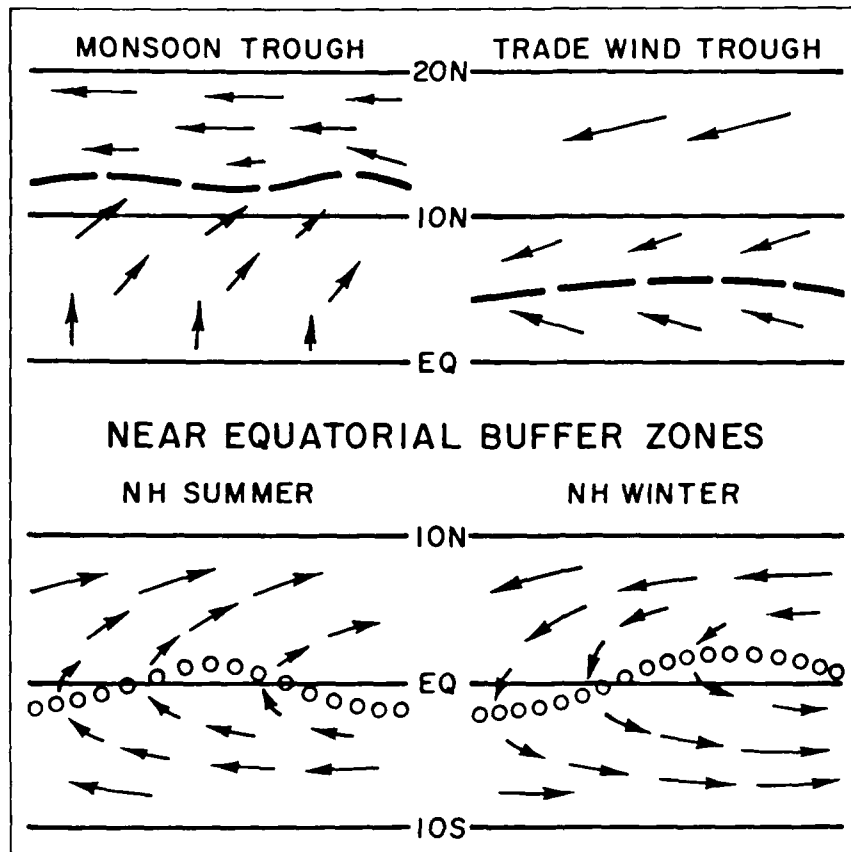
This broad depiction is not very useful in delineating details of the gradient wind flow (3B-43b) over the same region, which shows a reversal of wind direction from easterly north of the equator to westerly south of the equator in the region of Indonesia and New Guinea. A streamline trough is additionally defined south of these westerlies extending from near the Fiji Islands (18° S, 178° E) through northern Australia and into South Africa.

The circulation involving easterly trade wind flow crossing the equator and changing direction to westerly is referred to as a "buffer zone" (Conover and Sadler, 1960) while the streamline trough having westerlies on the equatorward side and easterlies on the poleward side is referred to as a "monsoon trough." In the eastern Pacific, the northeast and southeast trades merge without change of direction to form what is called the "Trade Wind Trough" (Atkinson, 1971). The various configurations are illustrated schematically (3B-43a). Note the reversal of flow in the buffer zone transitioning from Northern Hemisphere summer to Northern Hemisphere winter.

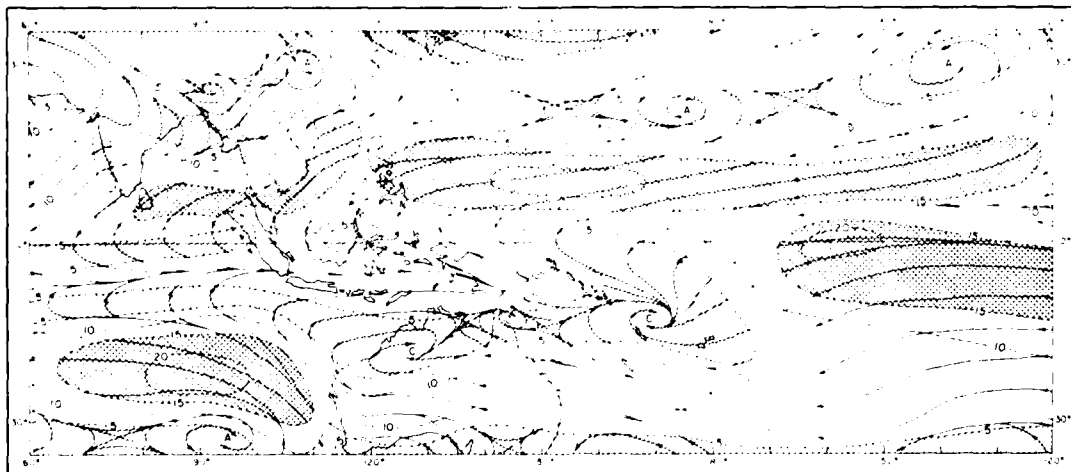
A feature of the monsoonal trough is that a distinct isotach minimum lies along its axis. Sun glint data from polar-orbiting satellites during the winter should therefore be very useful in locating the exact position of this trough axis at a particular latitude, since minimum wind speed regions over the ocean should reflect sun glint more brilliantly than adjacent rougher sea regions. By combining the satellite input with available ship reports a significantly improved analysis can often result.

References

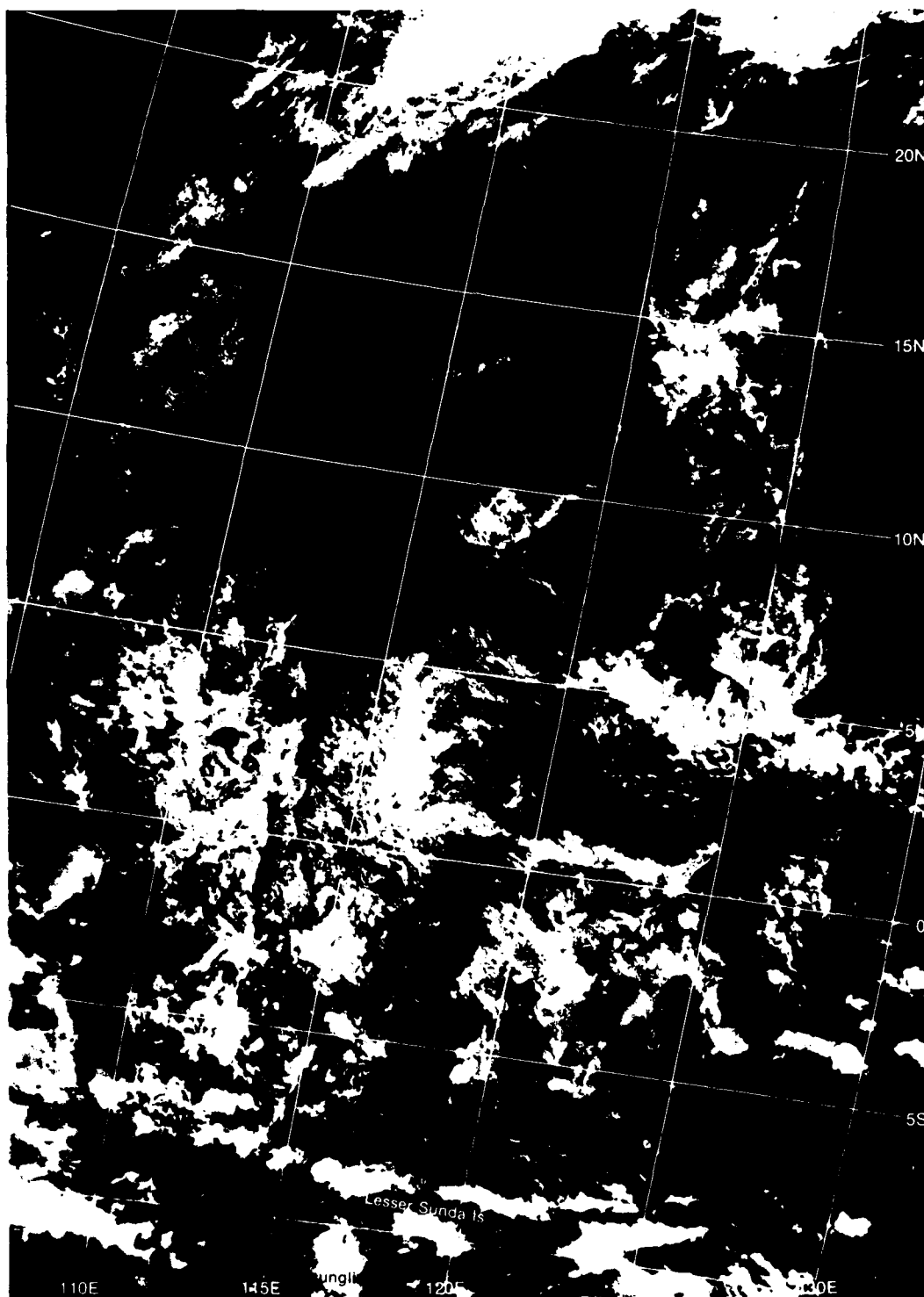
- Atkinson, G. D., and J. C. Sadler, 1970: Mean Cloudiness and gradient level-wind charts over the tropics, AWS Tech. Report 215, Vol. I (Text), Vol. II (Charts).
- Conover, J. L.T., and J. C. Sadler, 1960: Cloud patterns as seen from altitudes of 250 to 850 miles - preliminary results, *Bull. Am. Meteorol. Soc.*, **41**(6), 291-297.
- Atkinson, G. D., 1971: Forecaster's Guide to Tropical Meteorology, Air Weather Service Tech Report 240, Hq. AWS, Scott AFB, IL., pp. 360.
- Crutcher, H. L., and O. M. Davis, 1969: U.S. Navy Marine climatic atlas of the World, Vol. VIII, "The World," NAVAIR 50-1C-53, Naval Weather Service Command



3B-43a. Schematic representation of monsoon and trade-wind type troughs and near-equatorial buffer zone in the tropics (After Atkinson, 1971)



3B-43b. Resultant gradient-level wind for January (After Atkinson and Sadler, 1970)



3B-44a. F-7, DMSP LF Low Enhancement 0628 GMT 8 February 1985.

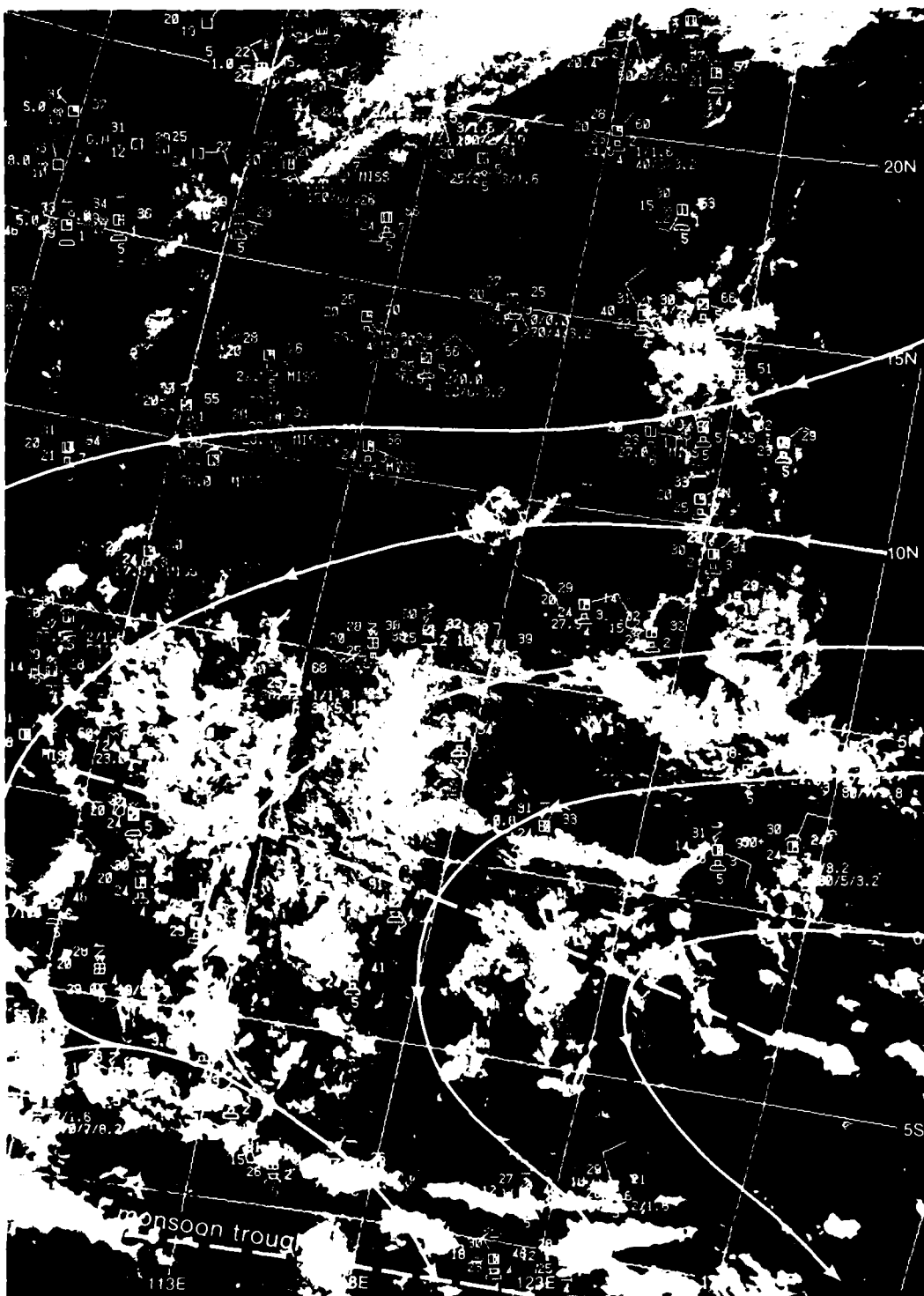
*Identification of the Monsoon Trough
Tropical Southwest Pacific
February 1985*

8 February

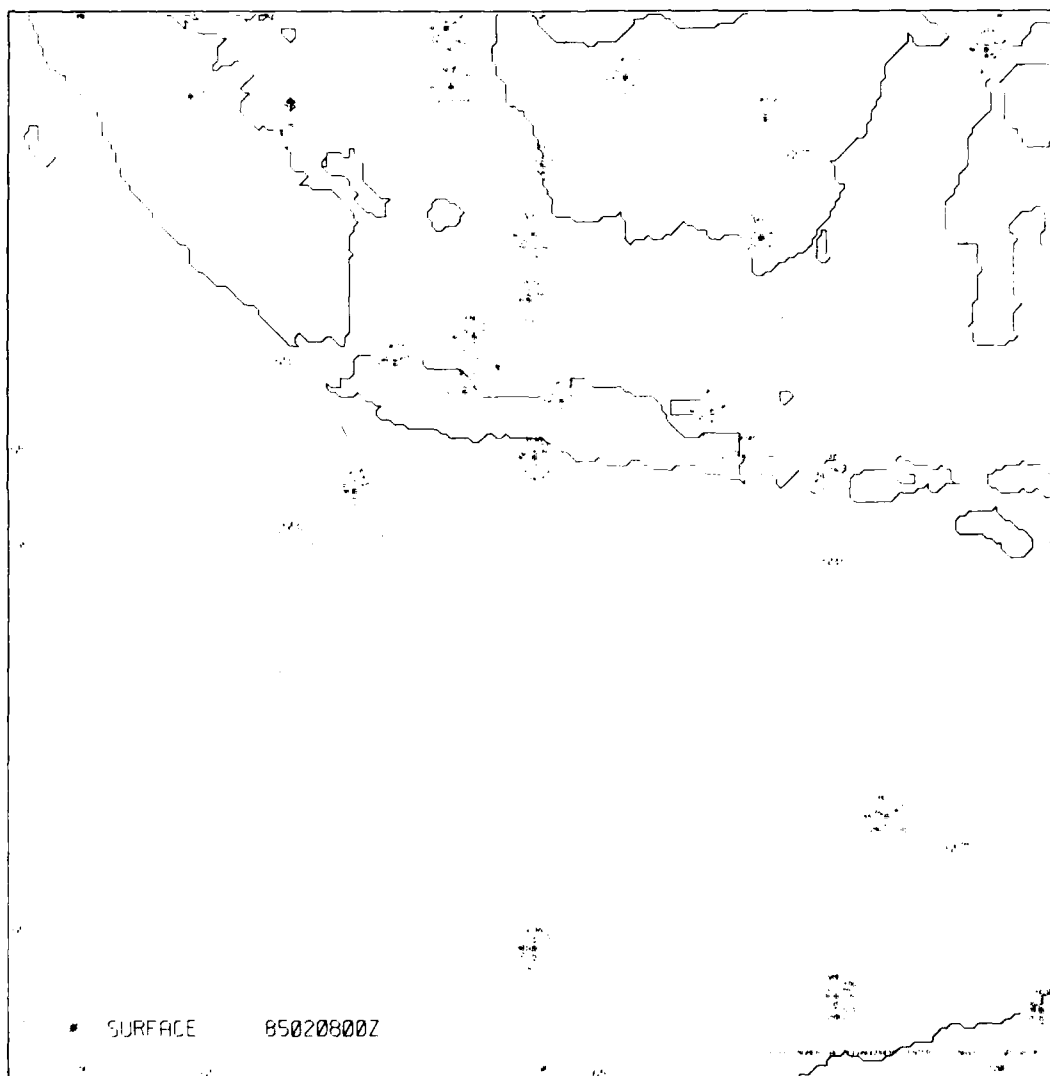
The DMSP visible image (3B-44a) extends southward over Borneo and past Java and the Lesser Sunda Islands. Brilliant sunglint reflection occurs south to the Lesser Sunda Islands at the bottom of the image near 12° S. As can be seen from the depiction of the resultant gradient wind flow (3B-43b), this is very near the mean position of the streamline trough for that time of year.

The streamline analysis, based on surface reports and superimposed on the DMSP image (3B-45a), reveals the flow pattern defining the buffer zone and suggests an east-west trough axis defining the exact location of the monsoon trough passing through the position of the brilliant sunglint.

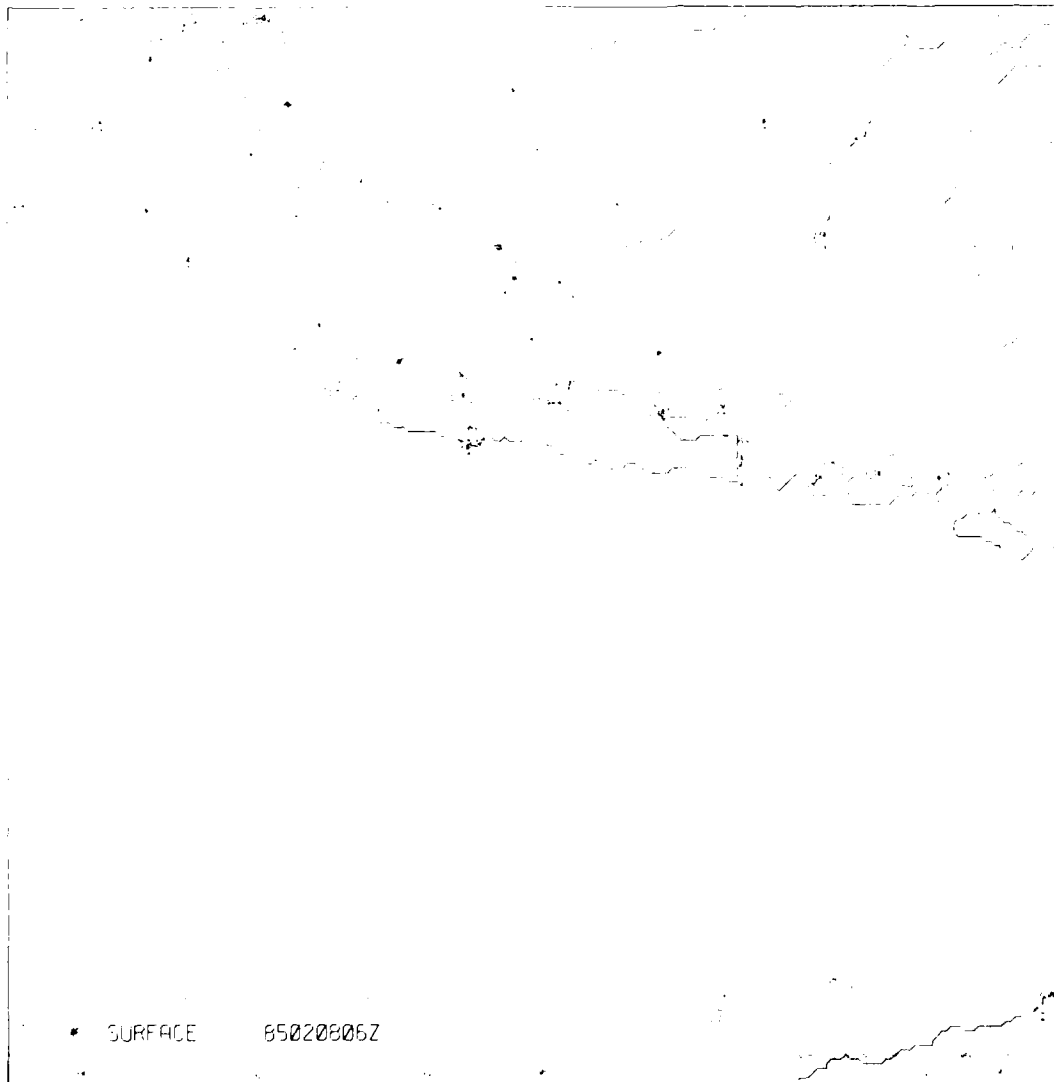
The JNOC surface analyses at 0000 and 0600 GMT (3B-46a and 47a) show two low-pressure centers just south of the Lesser Sunda Islands with higher pressure to the north and south, fully substantiating implications of trough locations derived from the DMSP image.



3B-45a F-7, DMSP LF Low Enhancement, 0628 GMT 8 February 1985. Surface Reports (0600 GMT) and Streamlines



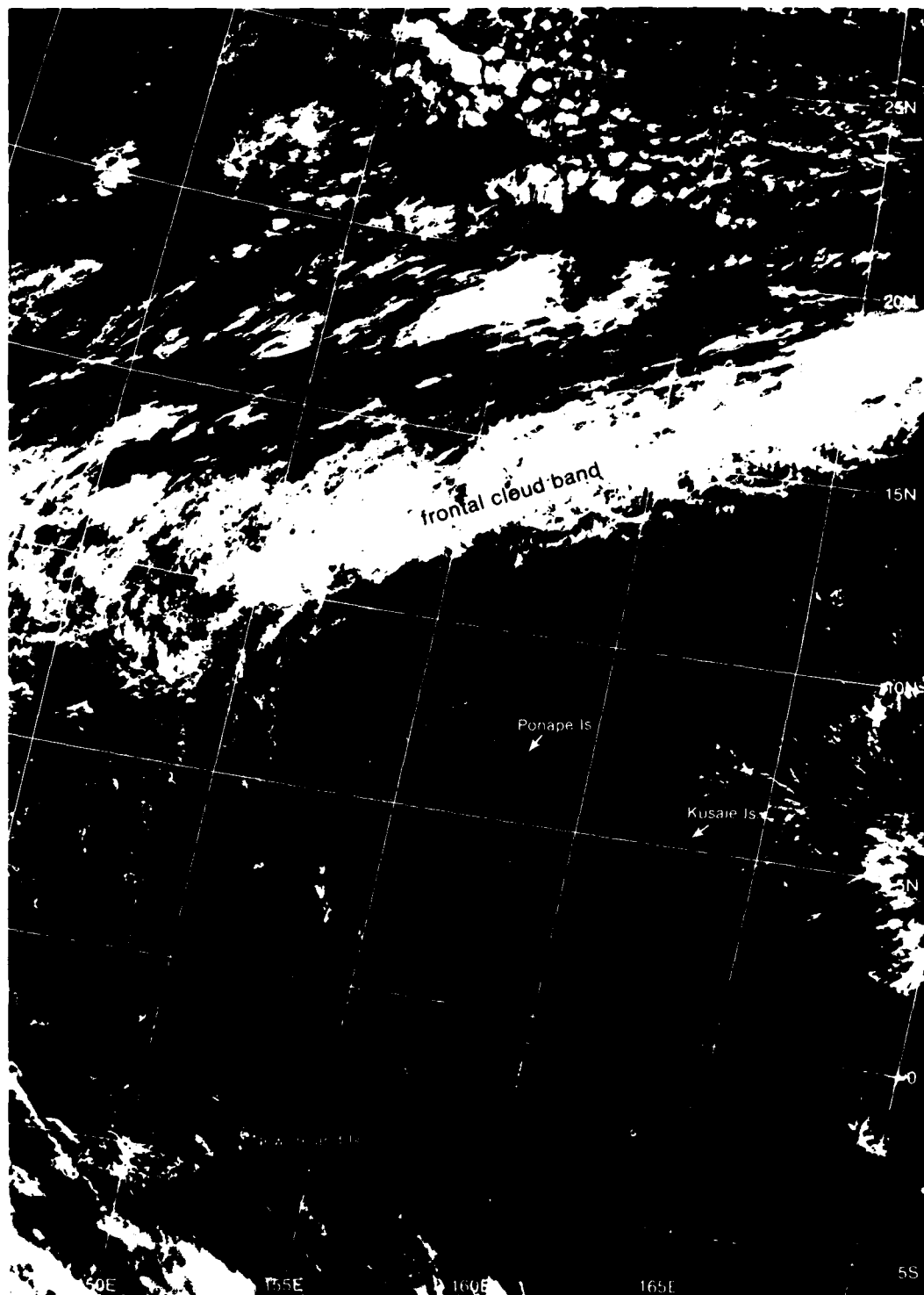
3B-46a FNOG Surface Analysis 0000 GMT 8 February 1985



3B-47a ENOC Surface Analysis 0600 GMT 8 February 1985

*Case 1 Cloud Line Configurations in the
Lee of Islands Under Low-level
Inversion Conditions*

When island topography rises to near the base of a low-level inversion, or rises above this base, air flowing past the island is forced around the sides rather than over the island. Downstream effects may become perturbed giving rise to Von Karmen vortices, or if the inversion interface is especially pronounced, cloud formations may separate in a "ship wake" configuration (see NTAG Vol. 1, Sec 2C). The particular effect depends on many variables including the shape of the island, vertical shear, stability, moisture, and sea surface temperature variations.



3C-2a. FIV-28, DMSP LF Low Enhancement, 0157 GMT 16 January 1974

*Island Lee Cloud Formation Under
Statically Unstable Low-level Conditions
Tropical Central Pacific
January 1974*

16 January

The DMSP visible image (3C-2a) reveals a band of frontal clouds extending down into tropical latitudes. The rope-like cloud structure at the leading edge of the frontal band defines the surface frontal position.

A sharp surface ridge normally precedes frontal movement. Ponape and Kusaie Islands show lee effects, indicating southeasterly low-level flow past these locations (see enlargement, 3C-3b).

The surface observations and streamline analysis superimposed on the DMSP image (3C-3a) confirm the existence of a ridge line in advance of the front while the frontal band is located along an asymptote of streamline convergence.

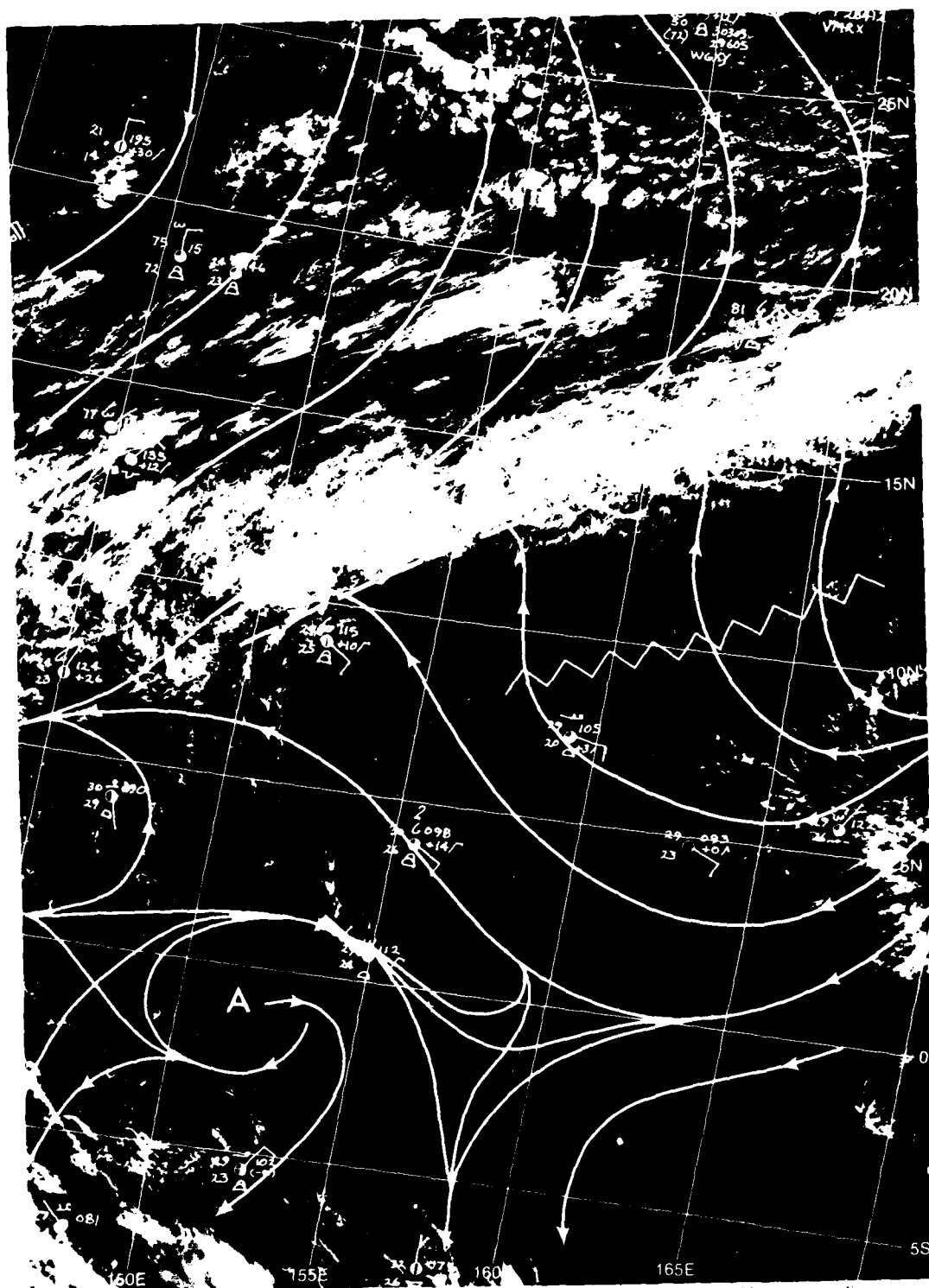
The flow pattern past Kusaie and Ponape Islands has resulted in lee cloud line formations (3C-3b) exhibiting a "split-V" configuration similar to the appearance of a ship's wake in the ocean. Such formations occur when an extremely sharp inversion exists near the top of the island's highest terrain (see NTAG, Vol. 1, Sec. 2C).

The 0000 GMT sounding for Ponape (3C-3c) reveals such a condition at 3,200 ft (900 mb). Ponape's highest altitude is indicated to be 2,595 ft., close enough to the base of the inversion to result in such an effect.

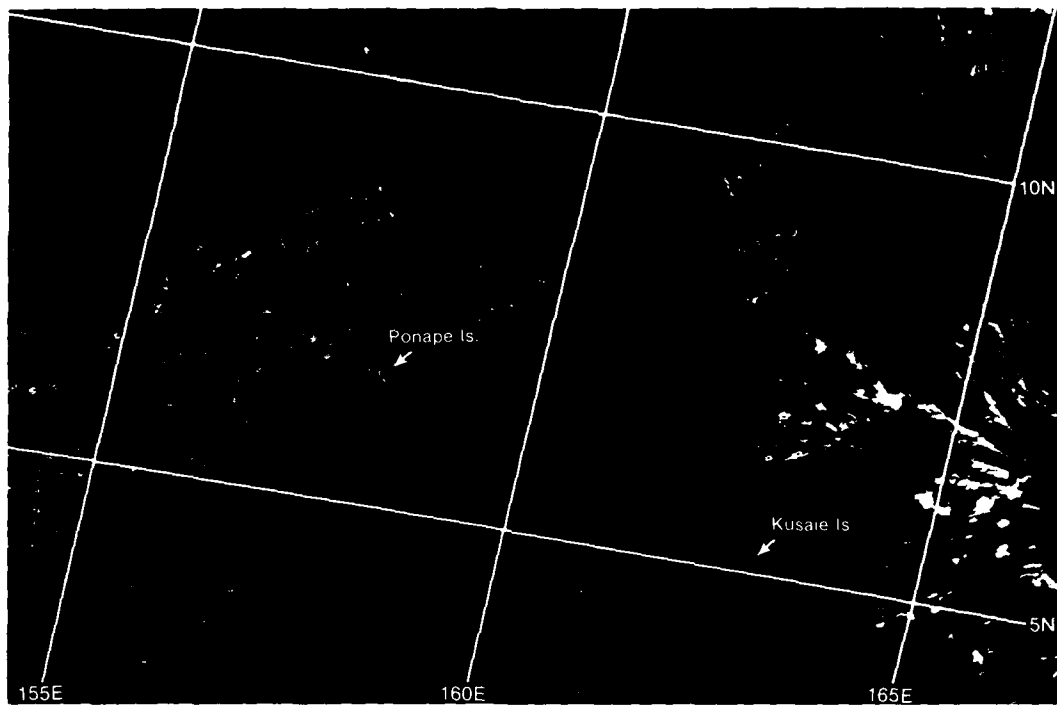
Important Conclusions

1. The "split-V" cloud line formation forms under a statically unstable local environment and denotes the existence of an especially sharp inversion near the top of the island's highest terrain.
2. Island lee cloud line formations, exhibiting a "split-V" configuration, are useful in delineating the direction of low-level flow.

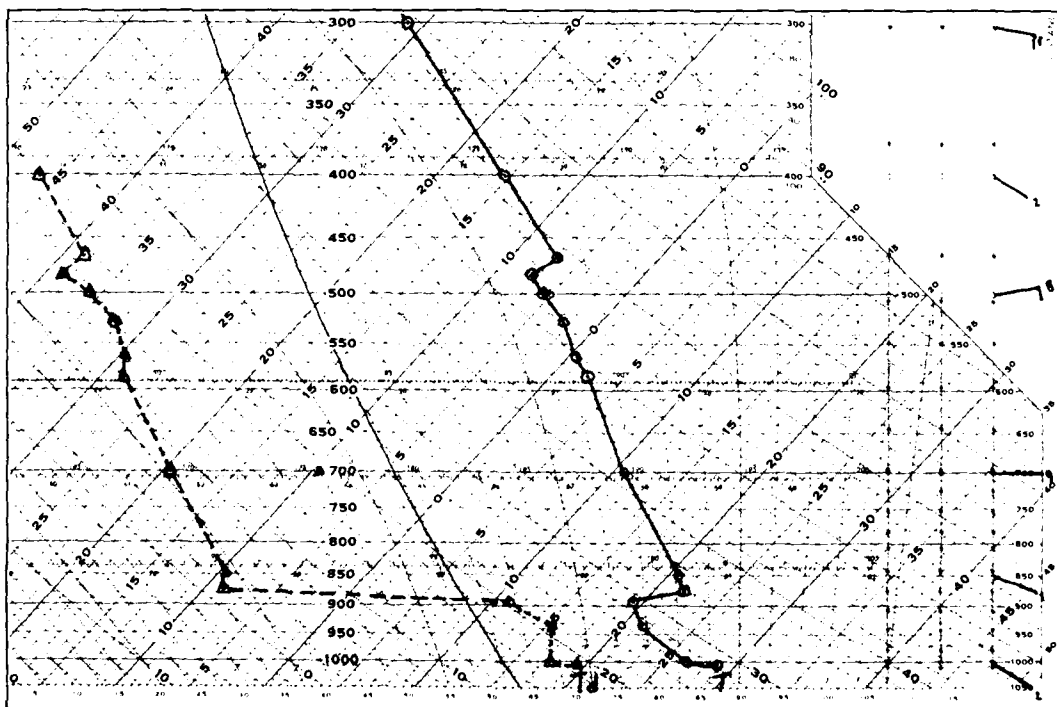
3C2B



3C-3a. FIV-28. DMSP LE Low Enhancement. 0157 GMT 16 January 1974. Surface Reports (0000 GMT) and Streamlines.



3C-3b. Enlarged View. FTV-28. DMSP LF Low Enhancement. 0157 GMT 16 January 1974.



3C-3c. RAOB. Ponape Island. 0000 GMT 16 January 1974

*Locating a Buffer Zone
and Monsoon Trough Axes
Tropical Southwest Pacific
August 1974 and August 1979*

15 August 1974

The DMSP visible image (3C-6a) reveals the islands of Borneo, Celebes, Morotai, and Halmahera, which lie very near the equator. One would expect the buffer zone axis to be located running east-west somewhere in the vicinity of these islands.

The reflective pattern around the islands of Morotai and Halmahera immediately enable one to deduce the presence of southerly low-level flow. This is verified by surface observations and the streamline analysis superimposed in 3C-7a. A buffer zone axis is defined near the equator consistent with climatological expectations.

Southwesterly flow continues north of the buffer zone until nearly 15° N, where easterly winds are encountered on the northern side of the convergence zone (CZ) cloudiness defining the position of the monsoon trough. Two tropical storms are evident, embedded as circulations along the monsoon trough axis.

5 August 1979

Five years later, a DMSP visible image of the same region (3C-8a) reveals that similar flow patterns are evident. The arc cloud line apparent on the south coast of Obo, and convective cloud lines streaming northward on the east and west side of Halmahera, indicate southerly flow, blocked by a low-level inversion, resulting in air flowing around, rather than over the islands at low levels.

Convergence zone cloudiness to the north would suggest that this southerly flow turns southeastward through the convergence zone cloudiness and then becomes easterly or southeasterly to define a monsoon trough on the north side of the cloudiness.

Surface observations and a streamline analysis superimposed on the DMSP image (3C-9a) confirm that this pattern did exist. Note that Tropical Depression #11, as designated by the Joint Typhoon Warning Center (JTWC), has formed along the monsoon trough on the northern edge of the CZ cloudiness.

Important Conclusions

1. The concept of the buffer zone and monsoon trough is a useful aid in streamline analysis over the tropics.
2. Satellite indications of low-level flow revealed by barrier effects and cloud vortex centers are useful indicators in fine-tuning a streamline analysis based on sparse surface observations.

3C-4

Case 2 Streamline Analysis Using the Buffer Zone and Monsoon Trough Concepts and Satellite Imagery Interpretation

During the Northern Hemisphere summer, a "buffer zone" as defined by Conover and Sadler (1960), is created near the equator where the easterly trade wind flow from the Southern Hemisphere changes direction to westerly as it moves into the Northern Hemisphere. The westerlies again change direction to easterlies near 10°-15° N, defining a streamline axis referred to as the monsoon trough (3C-5a). From a satellite perspective, the monsoon trough axis is frequently found near the northern edge of the convergence zone cloudiness where tropical depression formation is favored (Fett, 1968).

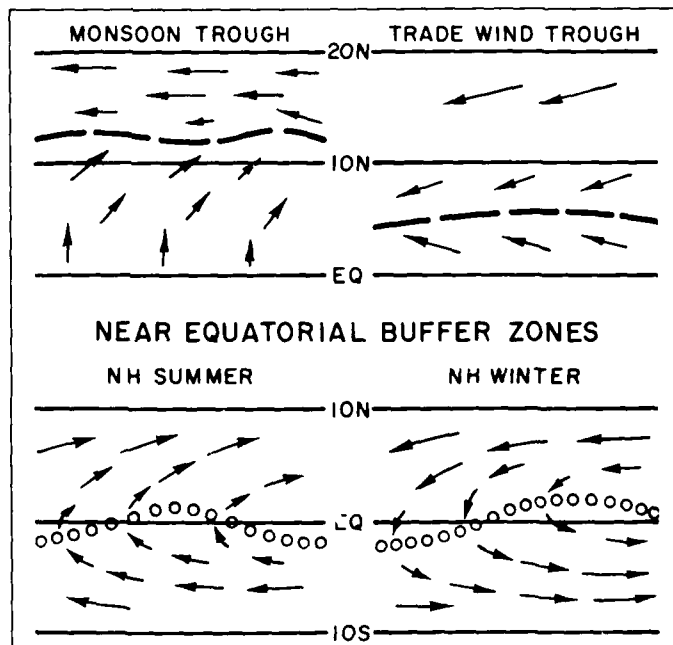
The Northern Hemisphere summer buffer zone occurs characteristically in all areas of the world except the central and western North Atlantic and the North Pacific between longitudes 120° W and 140° E. In those regions, Southern Hemisphere easterlies converge on crossing the equator with Northern Hemisphere easterlies, creating what is referred to as the "trade wind trough" (3C-5a).

It is especially useful to have these concepts in mind when analyzing satellite imagery, making use of additional detail in the satellite images to fine-tune placement of the buffer zone and monsoon trough axis.

References

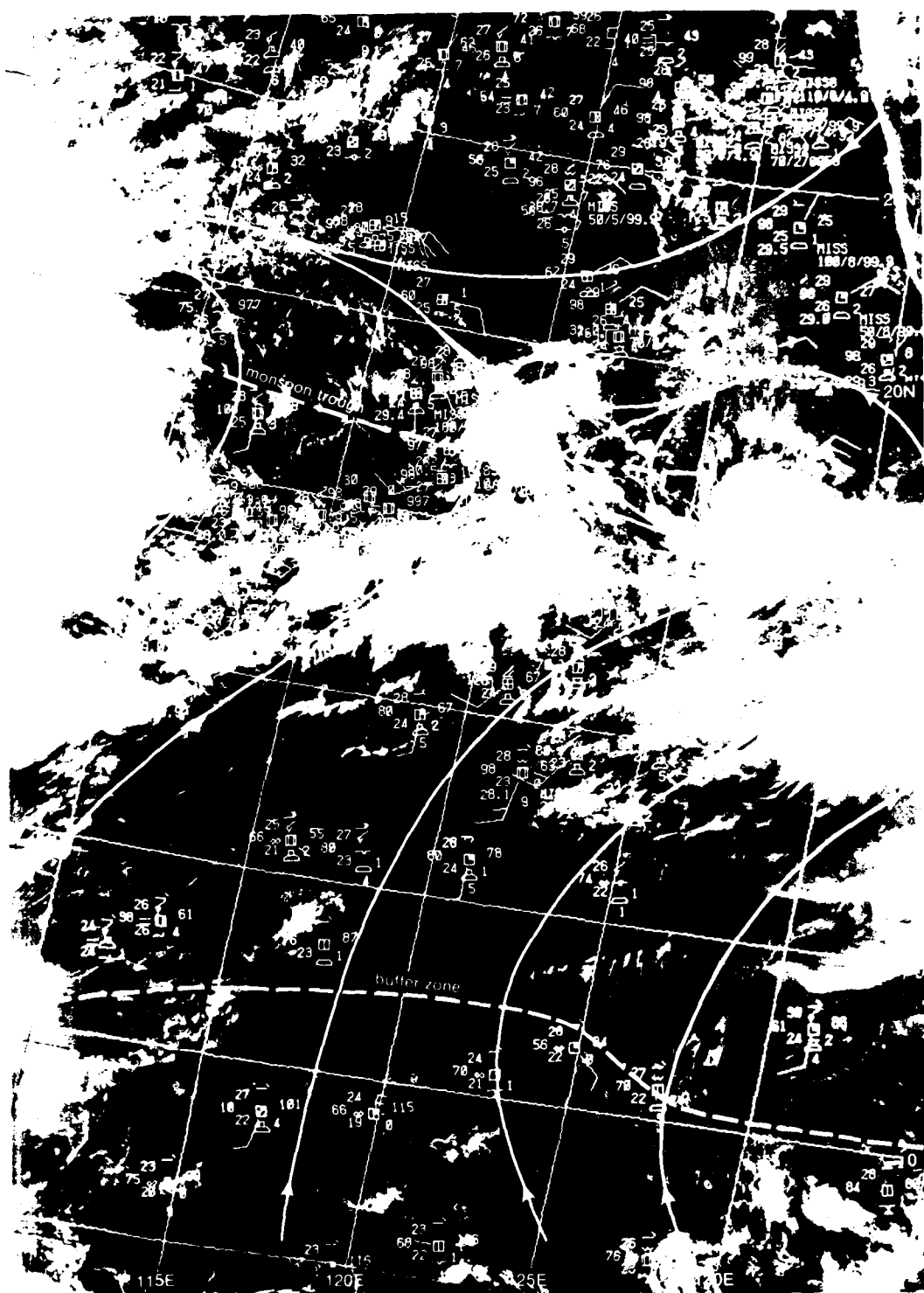
- Atkinson, G. D., 1971: Forecaster's Guide to Tropical Meteorology, Air Weather Service Tech Report 240, Hq. AWS, Scott AFB, IL, pp. 360.
 Conover, J. H., and J. C. Sadler, 1960: Cloud patterns as seen from altitudes of 250 to 850 miles - preliminary results. *Bull. Am. Meteorol. Soc.*, **41**, 291-297.
 Fett, R. W., 1968: Typhoon formation within the zone of the intertropical convergence. *Mon. Wea. Rev.*, **96**, 106-117.

3C-5a. Schematic representation of monsoon and trade-wind type troughs and near-equatorial buffer zone in the tropics (After Atkinson, 1971)

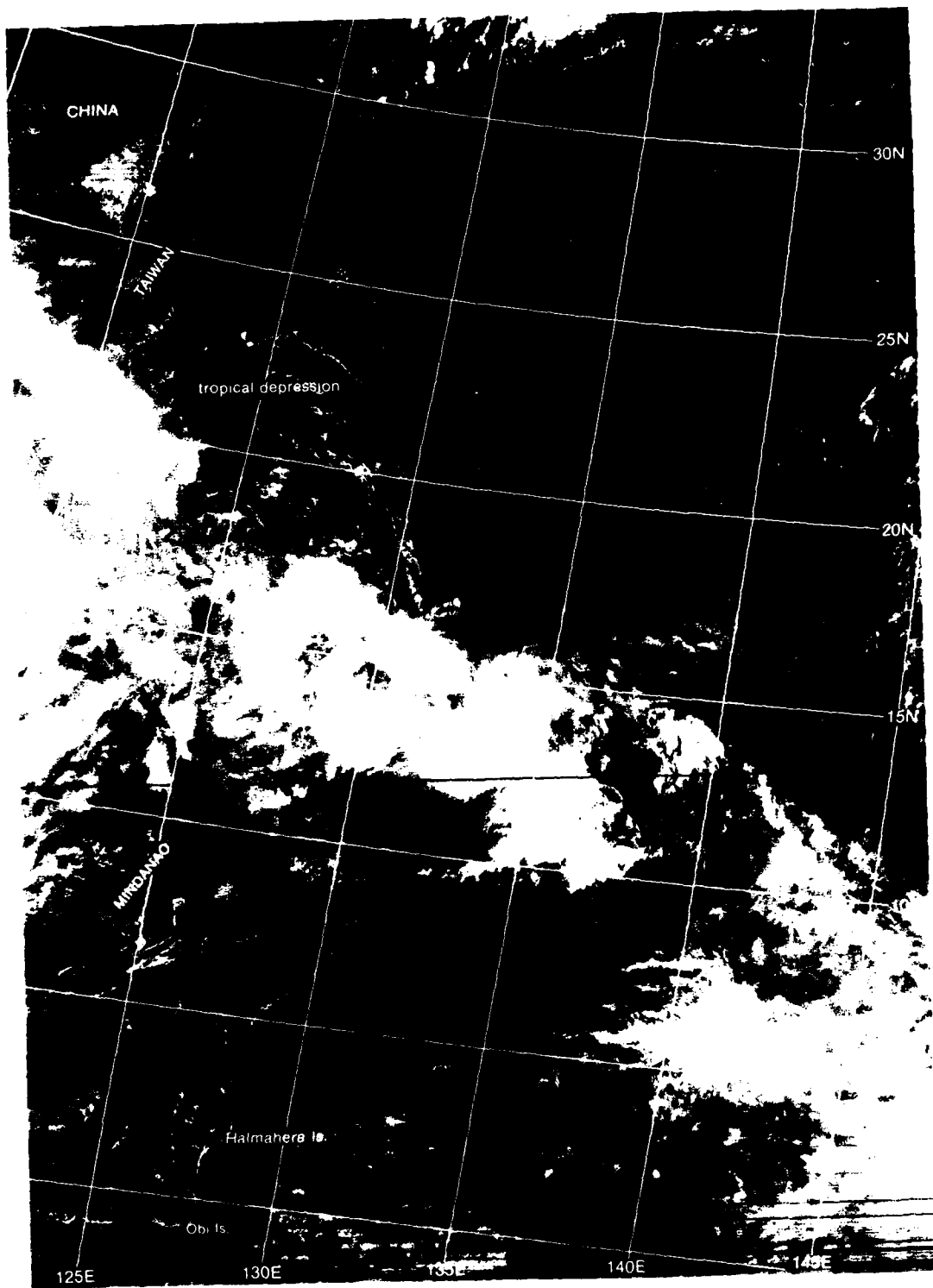




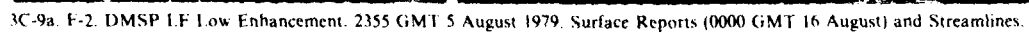
3C-6a FIV-29 DMSP FF Low Enhancement 0029 GMT 15 August 1974.



3C-7a F14-29 DMSP F14-29 Low Enhancement 0029 GMT 15 August 1974. Surface Reports (0000 GMT) and Streamlines



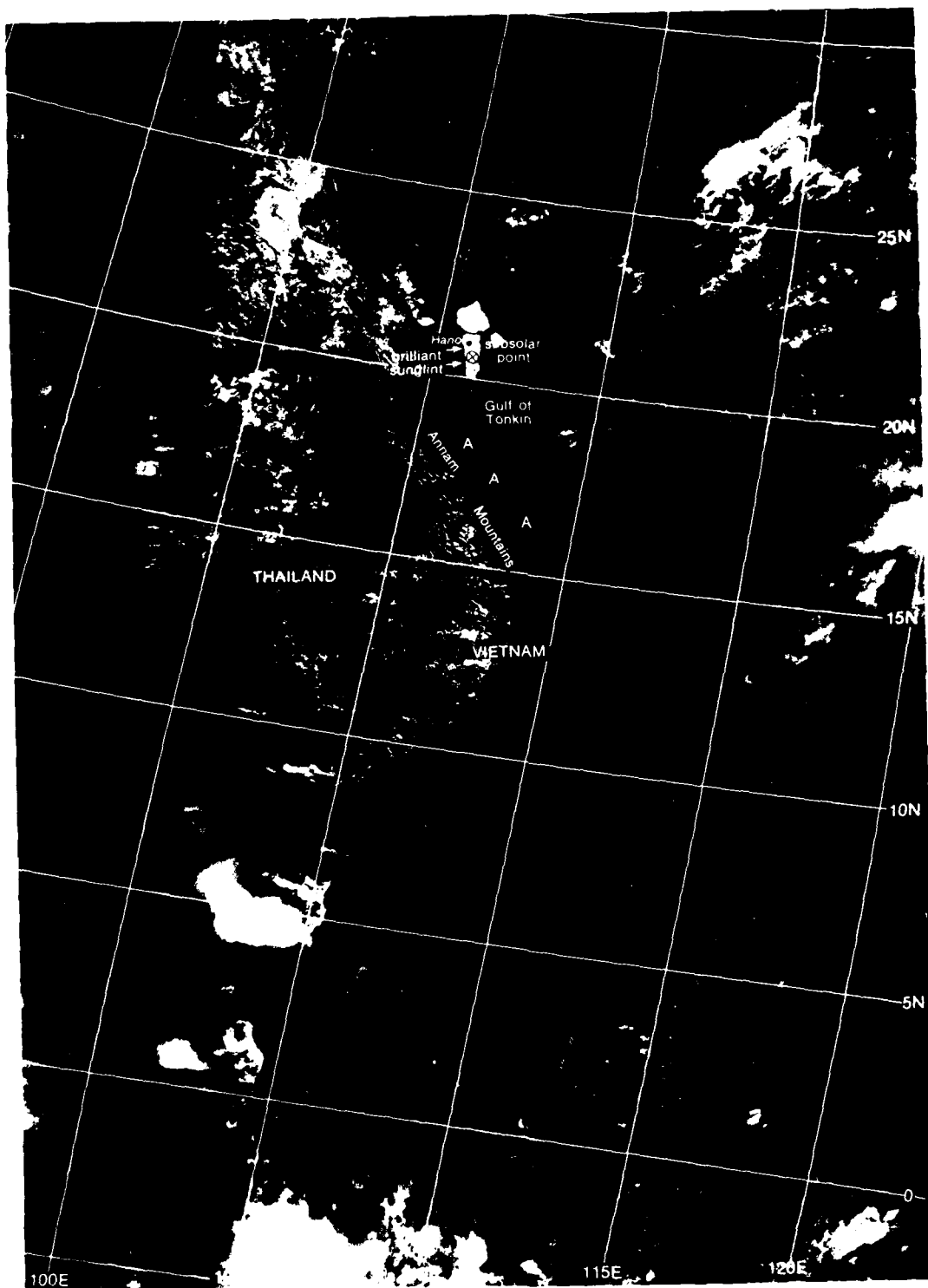
3C-8a. F-2, DMSP LF Low Enhancement. 2355 GMT 5 August 1979.



Case 3 Detection of Mountain Gap Winds over Coastal Areas from Sunlint Patterns

Under offshore flow conditions, where a coastal mountain range has gaps and valleys which lead to the ocean, winds are observed to be stronger in the valley regions (due to the Venturi effect) than in mountain lee areas, which act as a barrier to the winds. The stronger winds produce rougher seas over the adjacent coastal waters and, when sunlint is present, these areas can be distinguished from adjoining calmer areas in the sunlint pattern (see NTAG Vol. 1, Sec. 2A).

3C Case 3



3C-12a FIV-28 DMSP LF Low Enhancement 0500 GMT 20 July 1973

*Mountain Gap Winds
Southeast Asia
July 1973*

20 July

The DMSP visible image (3C-12a) is a view of Southeast Asia during the season of the Southwest Monsoon. Westerly or southwesterly flow can easily be deduced from the cloudiness pattern which shows fair weather cumulus over the western slopes of the Annam coastal mountain range, while the coastal areas are clear due to subsiding downslope flow. Row alignment of cumulus cloud patterns over Thailand (lower left portion of picture) is suggestive of west-southwesterly flow.

In the DMSP image, the subsolar point is located very near the subsatellite point, just south of Hanoi (near 21° N, 106° E). Brilliant sunglint over the flooded Red River delta area is so intense that the scanning radiometer is adversely affected in its ability to record consistent reflectance over the eastern half of the scanning swath, which appears darker than it should.

The gray shade patterns A in the Gulf of Tonkin present a problem for interpretation which is clarified through a comparison with ERTS-I imagery acquired approximately two hours earlier (3C-13a). This figure is a mosaic of two adjacent ERTS images from Channel 4 (0.5-0.6 μ m) and shows a portion of the same section of the northern Vietnam coastline appearing in the DMSP image. Arrows on the ERTS mosaic correspond to similar locations on the enlarged DMSP image (3C-13c). It will be noted that the light gray shade streaks appearing at the end of the arrows in the DMSP image appear as dark gray streaks in the ERTS mosaic. This type of reversal is consistent with reflective effects of calm seas, as viewed by satellite from different perspectives with respect to the sun. At the time of the DMSP image acquisition, the subsolar point was over the DMSP subsatellite track, near Hanoi, as indicated by the X. As the satellite progressed northward, over the Gulf of Tonkin, the subsolar point was essentially stationary and the specular point was very close to the subsatellite point throughout the entire portion of the satellite track. Calm seas show greater reflectance in such circumstances at points near the primary specular point or near the center of a sunglint pattern.

Two hours earlier, however, at the time of the ERTS imagery, the subsolar point was to the east at 20.5° N, 139.5° E (not shown). Hence, the specular points for the ERTS imagery were also well to the east of the ERTS subpoint track. Calmer areas in ERTS data at the edge of a sunglint pattern should therefore appear darker than surrounding seas, and this is precisely the effect shown in 3C-13a. (Refer to NTAG, Vol. 1, Sec. 2A, for technical discussion of sunglint patterns.)

The fact that the calmer areas coincide in the two types of images, despite the two hour time differential, suggests a common cause. On a topographical map of this area (3C-13b), gray shade positions have been lightly superimposed over the Gulf of Tonkin. It can be seen that many of the gray shade patterns are in the immediate lee of mountain peaks. Calm or relatively

calm seas extending for some distance offshore in the lee of such features is consistent with a barrier effect similar to that seen and documented in the lee of mountainous islands (see NTAG, Vol. 1, Sec. 2C). The persistence of calm narrow streaks on the water's surface long distances seaward is attributed to a downward turbulent mixing of air from aloft which is heated as it ascends adiabatically over heated elevated terrain (Annam Mountains). A thermal stratification results in the lee of such a feature which can persist great distances downstream. The explanation for this effect was first suggested by Deardorff (1976) who indicated that the "wind shadow seems due to the associated stable stratification that both protects the wake from significant lateral mixing, and micrometeorologically causes weak winds at small heights."

Not all of the gray shade plumes are due to sunglint patterns. For example, the reflective plume north of the northernmost arrow in the ERTS mosaic (3C-13a) extends from the mouth of a river and is obviously caused by water turbidity. Such plumes have been photographed by the astronauts on numerous occasions. Several other smaller plumes to the south are identified that coincide with river exit points.

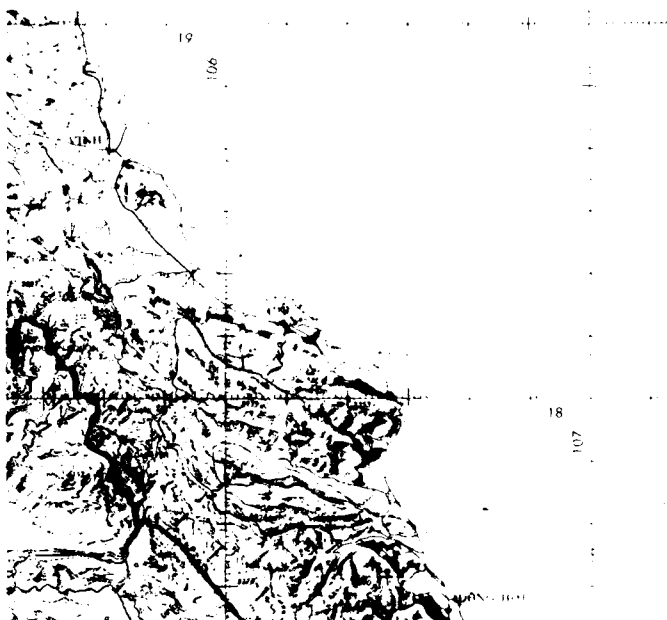
Note that the reflectivity of the northernmost turbid plume decreases by at least an order of magnitude where it passes into the dark, calm, swath depicted by the northernmost arrow. Such a decrease would be anticipated because more of the sun's rays are reflected away from the spacecraft's sensor in this calmer region in comparison to adjacent rougher seas.

Reference

Deardorff, S. W., 1976: Island wind shadows observed by satellite and radar. *Bull. Am. Meteorol. Soc.*, **57**(10), 1241-1242.



3C-13a. FRIS. Visible Image Mosaic. 0248 GMT. 20 July 1973.



3C-13b. Topographic map
of the northern
Vietnam coastal region.



3C-13c. Aerial photograph
DMSP/OLS data from
0500 GMT, 10/20/82
Northern Vietnam coastal region.

Case 4 *Mesoscale Convective Systems in the Tropics*

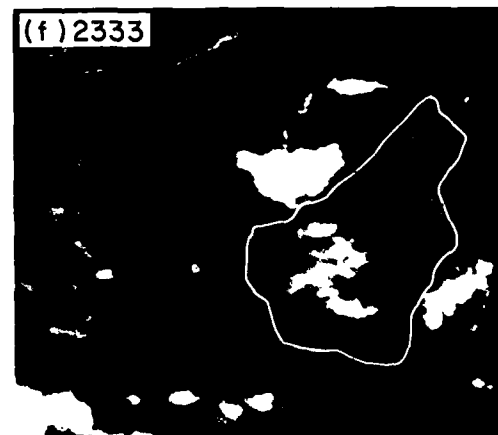
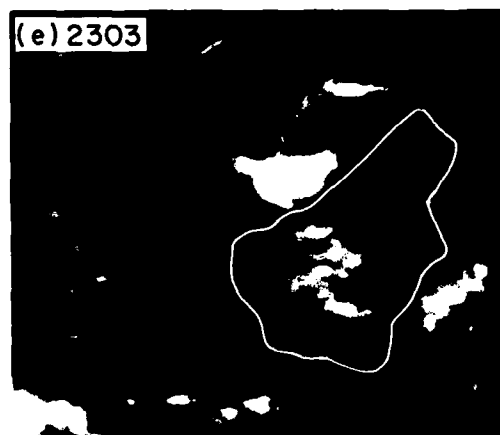
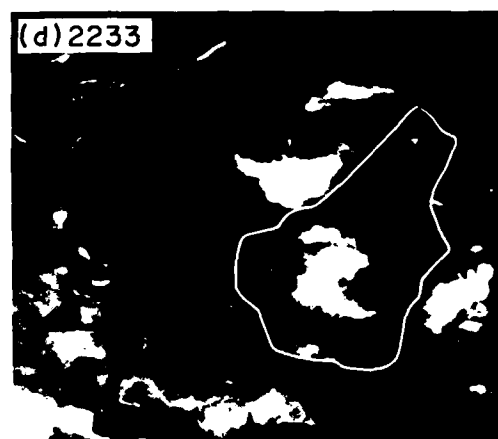
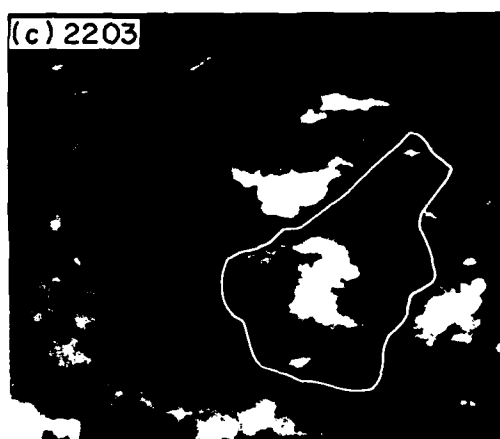
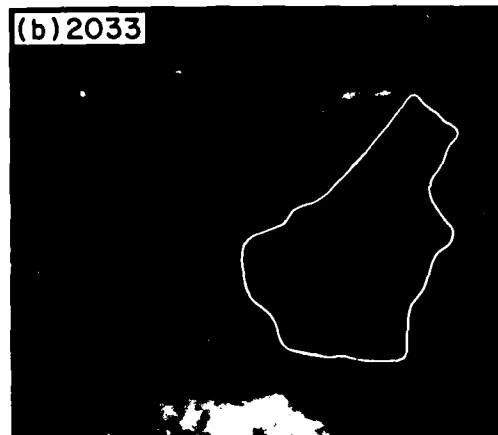
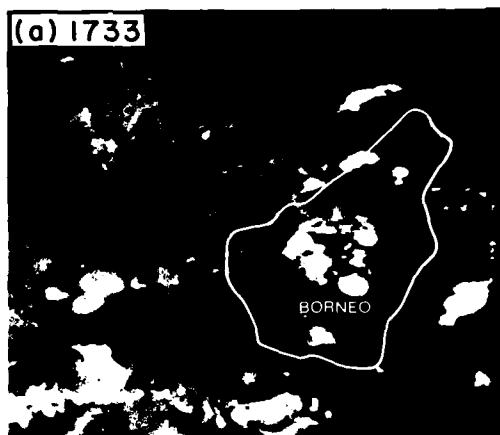
Winter monsoon cloud cover and precipitation over the maritime continent (i.e., Malaysia, Indonesia, and surrounding seas) take place largely in mesoscale convective systems (or cloud cluster) initiated by low-level convergence associated with local diurnal land- and sea-breeze circulations (e.g., Johnson, 1982). These cloud clusters exhibit a life cycle similar to those of mesoscale cloud systems found elsewhere in the tropics (e.g., Houze, 1982).

The typical cloud cluster life cycle commences with the formation of a group of convective cells, which evolves into a system composed of a combination of convective cells and mesoscale stratiform precipitation within the area covered by a mesoscale upper-level cloud shield, observed by satellite. As the system ages, the precipitation becomes increasingly stratiform and less convective, then ceases. The upper-level cloud persists for several more hours, slowly thinning and finally dissipating (Churchill and Houze, 1984).

This study presents a typical cloud cluster life cycle as revealed by a group of cloud clusters that occurred over the South China Sea on 10 December 1978. The discussion is based on Churchill and Houze (1984).

References

- Churchill, D. D., and R. A. Houze, Jr., 1984: Development and structure of winter monsoon cloud clusters on 10 December 1978. *J. Atmos. Sci.*, **41**, 933-960.
Houze, R. A., Jr., 1982: Cloud clusters and large-scale vertical motions in the tropics. *J. Meteorol. Soc. Japan*, **60**, 396-414.
Johnson, R. H., 1982: Vertical motion of near-equatorial winter monsoon convection. *J. Meteorol. Soc. Japan*, **60**, 682-690.



3C-16a. GMS-1. Infrared Images. 1733-2333 GMT 9 December 1978.

*Mesoscale Convection Systems Induced by Land Breeze Convergence
Tropical Western Pacific
December 1978*

9-10 December

Satellite imagery of the upper-level cloudiness in the vicinity of Borneo and the South China Sea from 1733 GMT on 9 December to 1530 GMT on 10 December 1978 is shown in 3C-16a, 17a, and 17b. The corresponding schematics (3C-17c) show the evolution of the family of cloud clusters (labeled A-J) that developed along the north coast of Borneo and over the South China Sea.

The 10th of December 1978 was characterized by the onset of a cold surge over the South China Sea. During a cold surge, northeasterly monsoon surface winds over the South China Sea increase in speed in conjunction with the passage of an upper-level trough in central China, and cloudiness and precipitation are enhanced along the north coast of Borneo (Ramage, 1971; Chang and Lau, 1980; Johnson and Priegnitz, 1981). At 0000 GMT on 10 December 1978, 30-kt (15 m s^{-1}) northeasterly surface winds over the South China Sea extended southward to 6°N (3C-18b). By 1200 GMT they reached 1°N (3C-18c), indicating the intensifying cold surge. Clusters A, B, and C were penetrated by aircraft (an Electra and a P3) between 0900 and 1100 GMT as indicated by the flight tracks (3C-18a, i, k). Low-level convergence centered near 3.5°N , 114°E (3C-18b), and an apparent increase in upper-level diffluence over the north coast of Borneo between 0000 and 1200 GMT (3C-19a and 19b) is consistent with the development of this group of cloud clusters. At middle and upper levels the flow was easterly over the north coast of Borneo, in a pattern typical of the winter monsoon (3C-19a, 19b, 19c, and 19d).

Cluster B dominated the family of clusters (3C-21b). This cluster was apparently triggered by the low-level convergence of the diurnal land breeze with the northeasterly monsoonal surface flow just off the north coast of Borneo. After 1731 GMT (3C-21b, a), cluster B grew until the area covered by its cirrus shield reached a maximum on the next day at about 0533 GMT (3C-21b, h). During this period of growth, the southeastern boundary of the cirrus shield was stationary along the coast of Borneo, while the western and northern boundaries expanded outward. Cluster I, also seen developing at 1733 GMT (3C-21b, a), never attained as great an areal extent as B. By 2303 GMT 10 December, while cluster B was still actively expanding, cluster I was decreasing in size.

Extensive changes occurred in the cloud patterns between 0233 and 0833 GMT 10 December (3C-21b, g-i). Cluster B developed a northern arm connecting with the remains of cluster I, while separate new clusters, A, C, and J, formed. During the next three hours (3C-21b, i-k), clusters A, B, and C were penetrated by the Electra and P3. Active growth continued on the western, northern, and northeastern borders of B during this time. However, at about the time that typical diurnal low-level flow reversed from offshore to onshore (3C-21a), the southeastern border of B disintegrated, while new clusters D, E, F, G, and H appeared just inland from the coastline. (Note

similar behavior over the Makassar Strait, along the east coast of Borneo, where new clusters also formed in a line just inland from the edge of a weakening cluster (3C-20a, g-i).

Further descriptions of cloud clusters A and B are as follows:

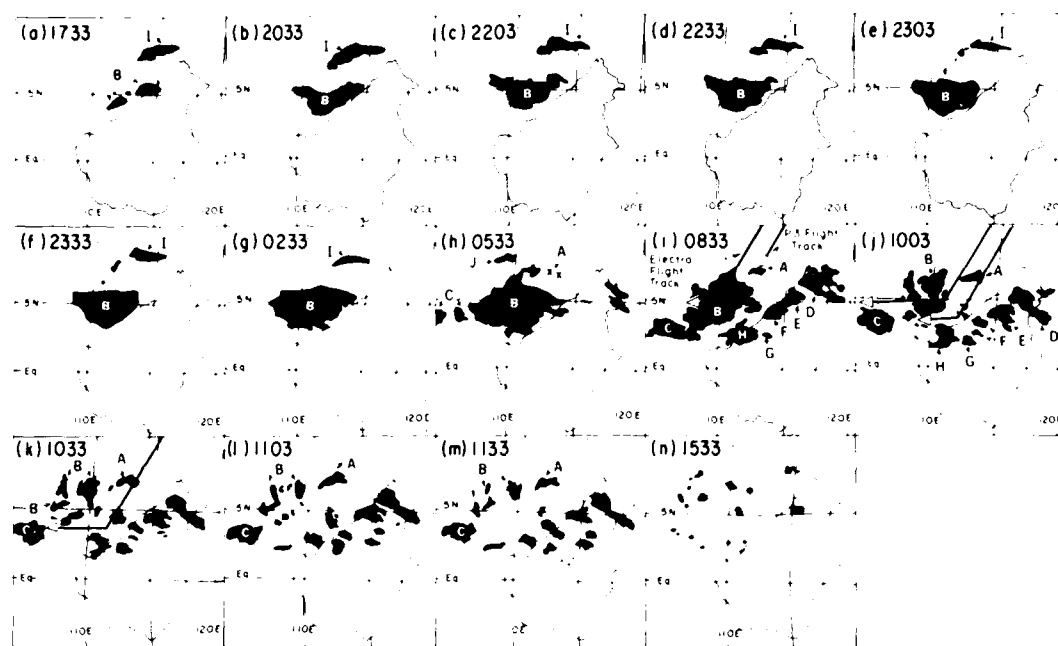
(1) *Cloud cluster A* Cloud and weather observations were reported by a research ship (4k, *Shirshov*), located beneath cluster A. From 0500 to 0700 GMT 10 December, the ship reported (3C-22a) building cumulus evolving into cumulonimbus with cirriform tops. A moderate rainshower had begun by 0700 GMT, and 0.9 of the sky was covered by low- and middle-level cloud. At 0800 GMT heavy thunderstorm activity was reported. By 0900 GMT, the thunderstorm had ended, though some rain fell at the ship during the next hour. From 0900 to 1100 GMT, the ship reported middle cloud and cirrus, presumably the cloud deck of A, combined with cumulonimbus covering 0.9 of the sky. Throughout the period of 1100 to 1200 GMT, rain was seen reaching the sea in the distance, but not at the ship. At 1200 GMT 4k, *Shirshov* recorded a 6-hr precipitation total of 11 mm. Then, a clearing trend brought fair weather for the next few hours.

Note that cluster A was forming between cluster B and the remnants of cluster I at 0533 GMT (3C-22b, h). Surface and sounding data taken at 4k, *Shirshov* suggest that convective downdraft outflows similar to those that appeared to produce the cloud arc lines may have been involved in triggering cluster A. The hourly surface data at the ship showed a drop in wet-bulb potential temperature from 298.5 to 296.5 K between 0600 and 0700 GMT. The ship sounding reported for 0600 GMT (3C-23a) showed the low wet-bulb equivalent potential temperature at the surface at the base of a shallow stable layer similar to that of convective downdraft outflow air seen elsewhere in the tropics (Houze and Betts, 1981). The sounding observed at 4k, *Shirshov* earlier in the day (3C-23b) and dropwindsondes obtained just prior to (3C-23c) and just after (3C-23d) the P3 aircraft penetration of cluster A show the undisturbed stratification.

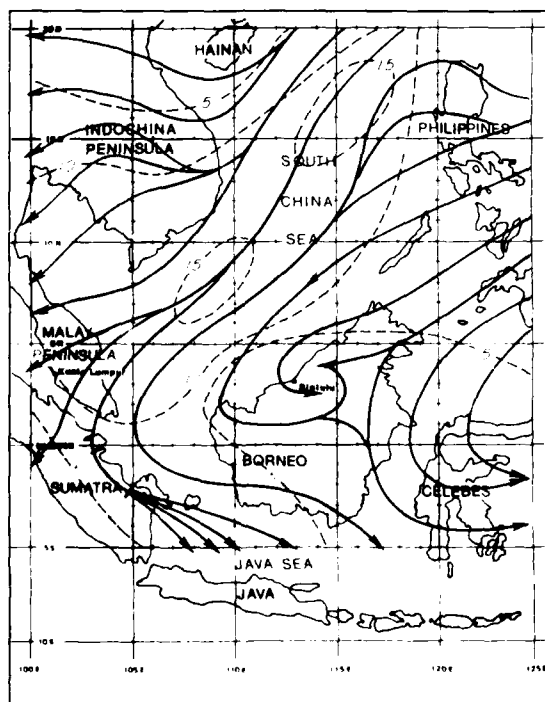
Continued on page 3C-24



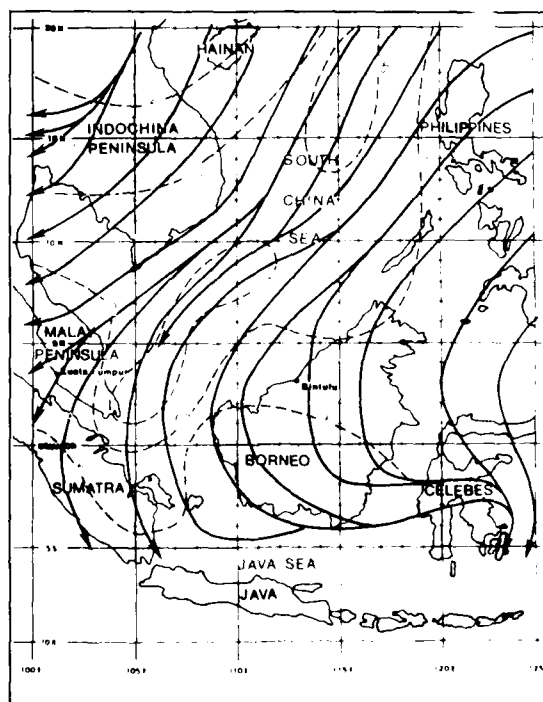
3C-17a GMS-1 Infrared Images 0233-1103 GMT 10 December 1978



3C-18a. Schematics of AMS-1 infrared images, 9-10 December 1978



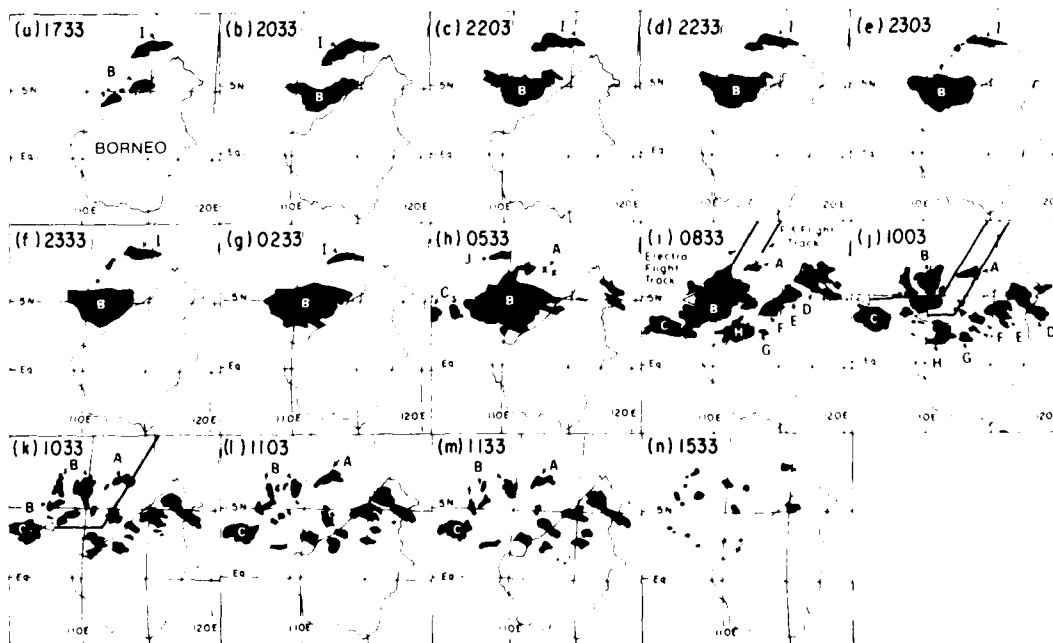
3C-18b. Surface streamlines and isotachs ($m sec^{-1}$)
0000 GMT 10 December 1978



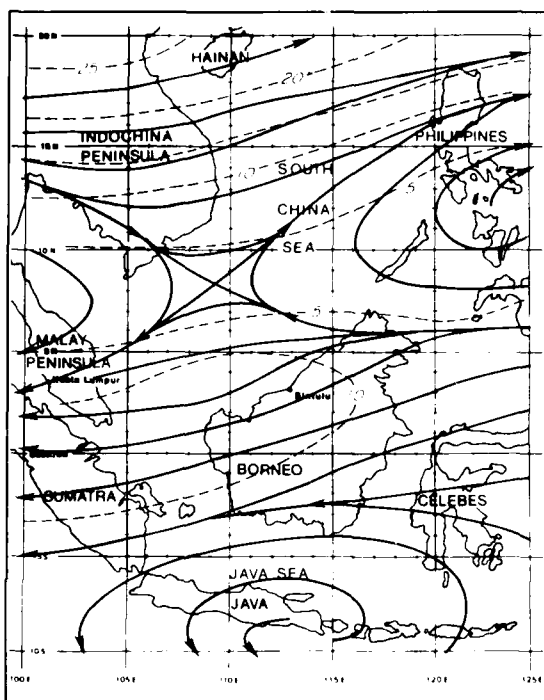
3C-18c. Surface streamlines and isotachs ($m sec^{-1}$)
1200 GMT 10 December 1978



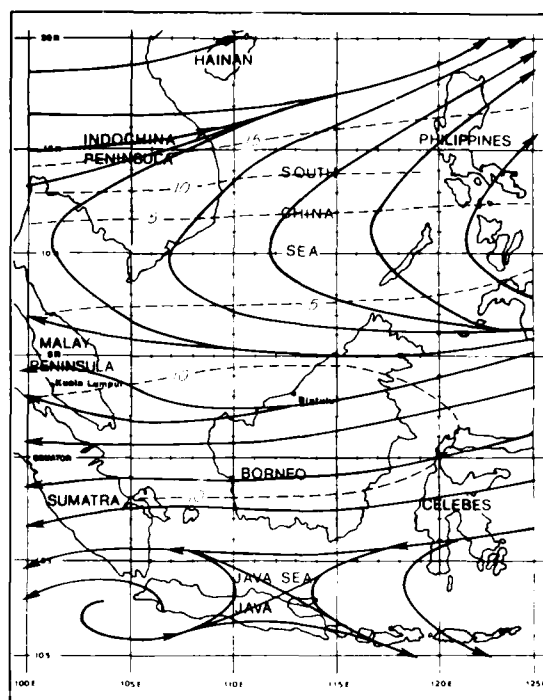
3C-17b. GMS-I. Infrared Images. 1133 1503 GMT 10 December 1978.



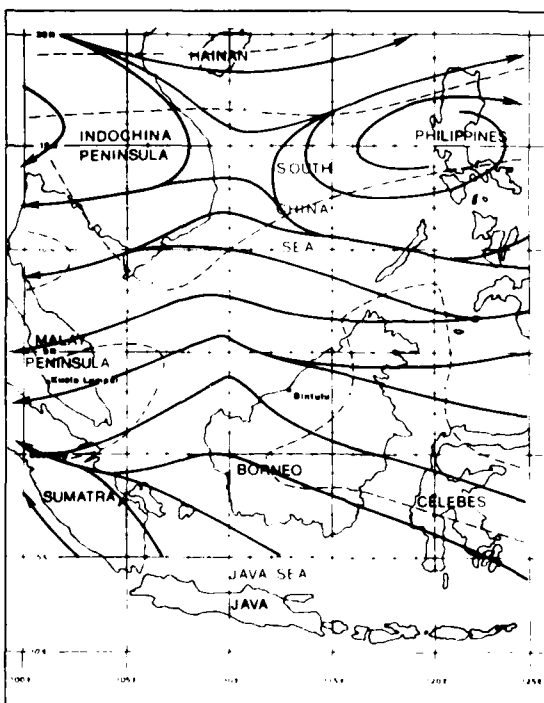
3C-17c. Schematics of GMS-I infrared images. 9 10 December 1978.



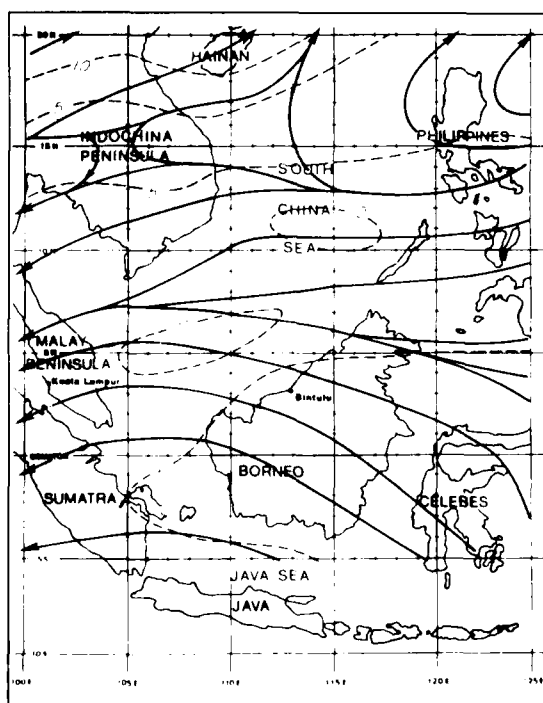
3C-19a. 200-mb streamlines and isotachs (m sec⁻¹)
0000 GMT 10 December 1978.



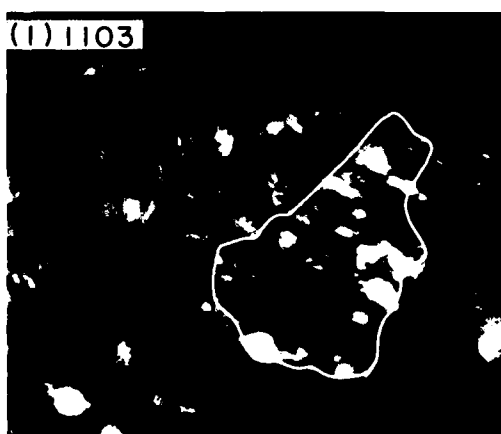
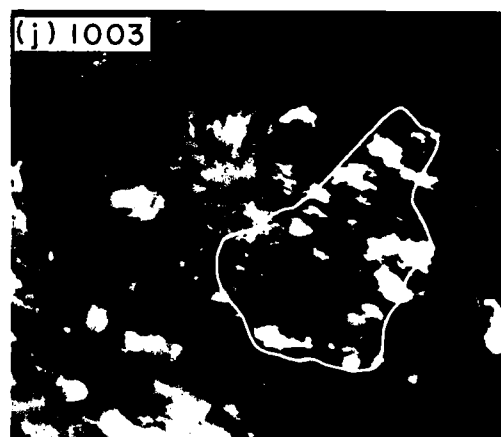
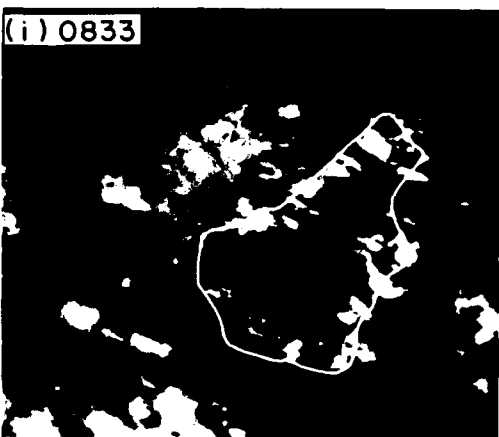
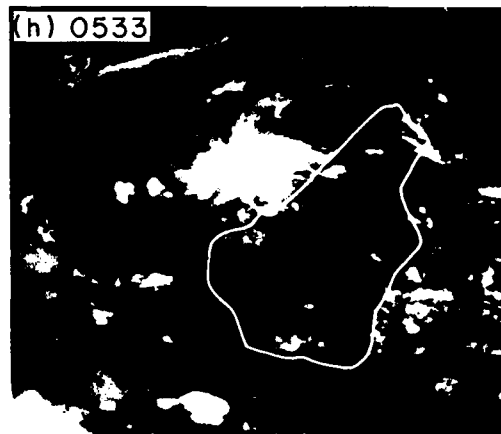
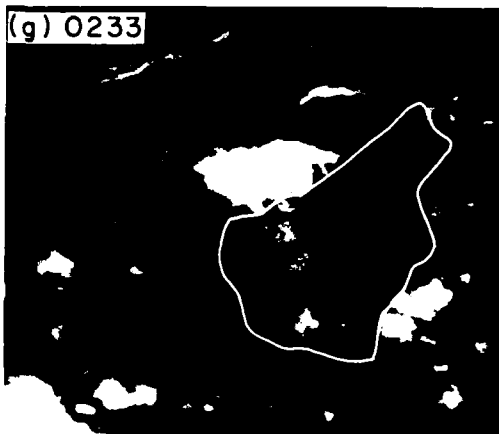
3C-19b. 200-mb streamlines and isotachs (m sec⁻¹)
1200 GMT 10 December 1978.



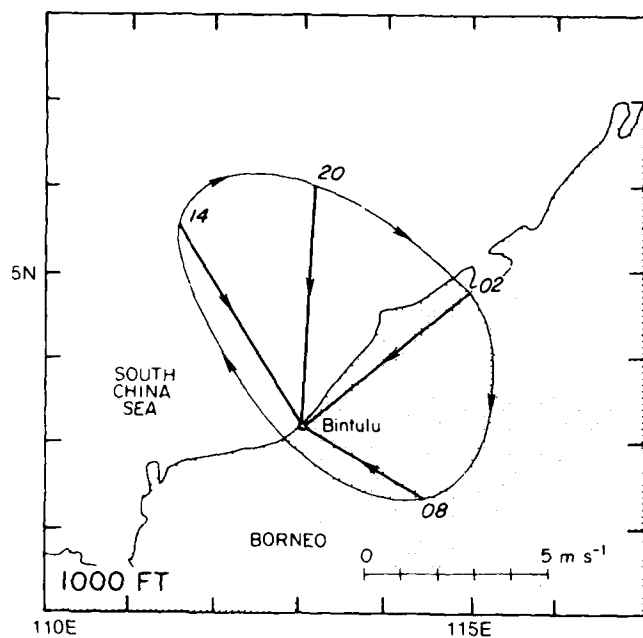
3C-19c. 500-mb streamlines and isotachs (m sec⁻¹)
0000 GMT 10 December 1978.



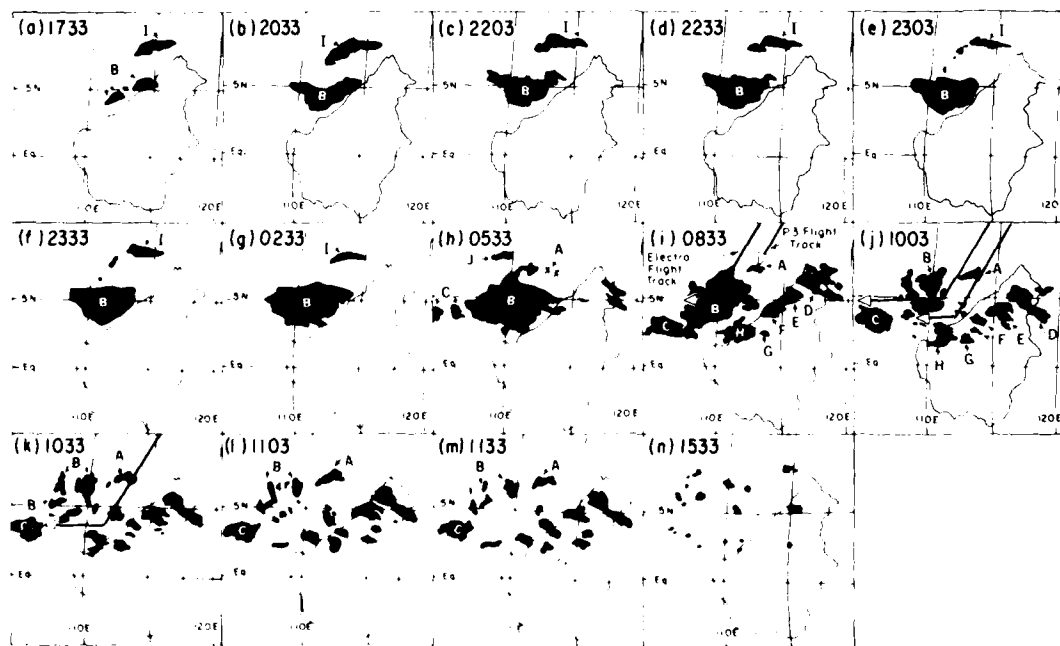
3C-19d. 500-mb streamlines and isotachs (m sec⁻¹)
1200 GMT 10 December 1978.



3C-20a GMS-1 Infrared Images, 0233-1103 GMT 10 December 1978.



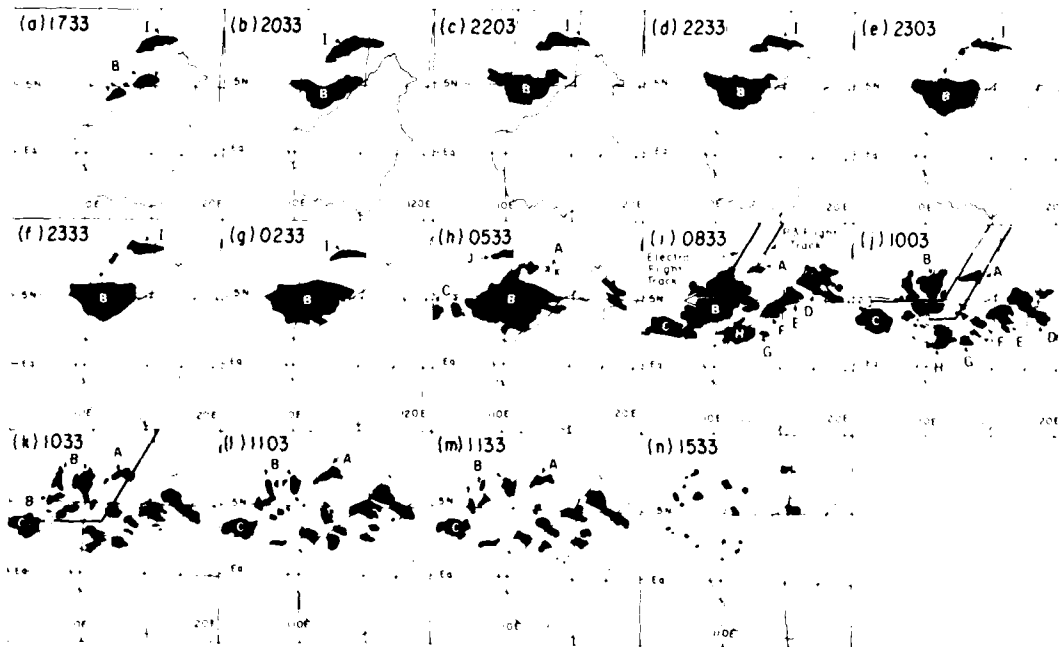
3C-21a. Hodograph of winds at 1,000 ft for Bintulu. 0200, 0800, 1400, and 2000 LST averaged over December 1978.



3C-21b. Schematics of GMS-I infrared images, 10 December 1978.

WW										
CH										
CM										
CL										
Nh										
	05	06	07	08	09	10	11	12	13	14

3C-22a. 4A. *Shirshov* clouds and weather beneath cluster A
10 December 1978.



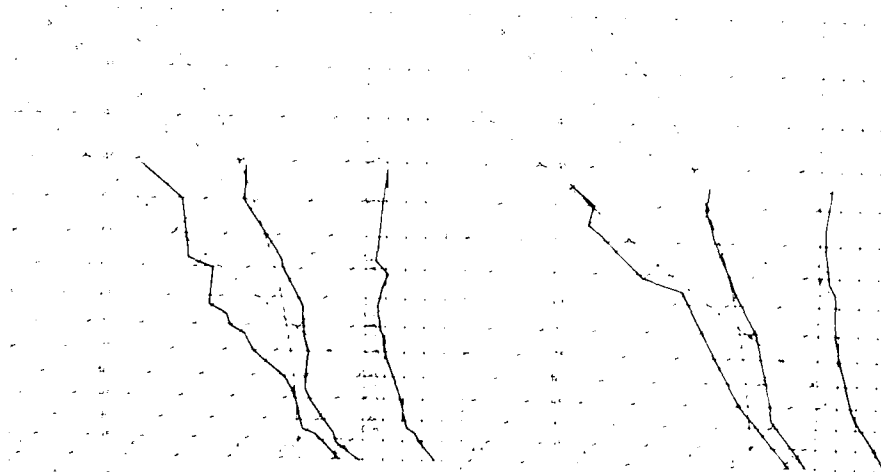
3C-22b. Schematics of GMS-I infrared images 9-10 December 1978.

ENVIRONMENTAL SOUNDINGS FOR CLUSTER A
10 DECEMBER 1978



3C-23a - 14 Skew-T log-P sounding for
0600 GMT 10 December 1978

3C-23b - 14 Skew-T log-P sounding for
0600 GMT 10 December 1978

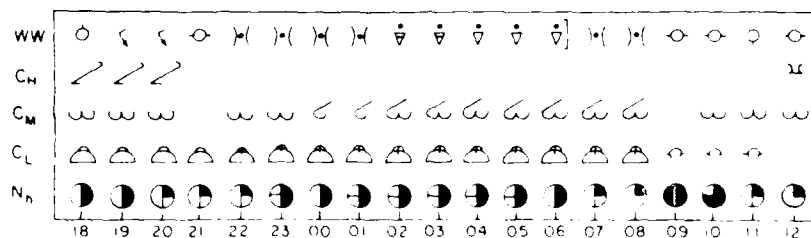


3C-23c - P3 dropwindsonde for
0859 GMT 10 December 1978

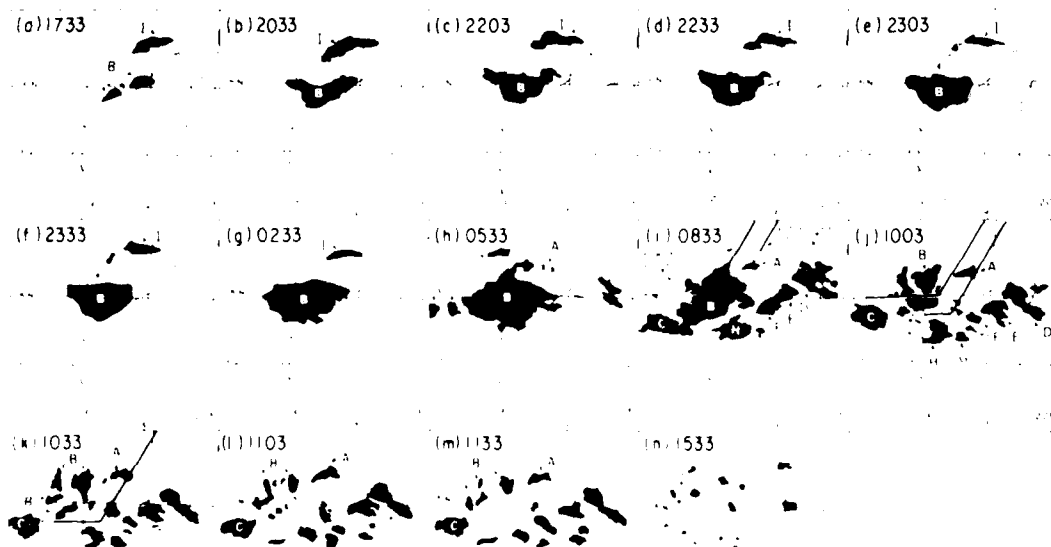
3C-23d - P3 dropwindsonde for
0914 GMT 10 December 1978

(2) *Cloud cluster B* Clouds and weather observations beneath cluster **B** were reported by another research vessel (*4k Korolov*) (3C-24a). Radiosondes from the ship and other sources show the WMONEX (Winter Monsoon Experiment) mean and 0000 GMT 10 December 1978 soundings for the ship (3C-25a and 25b). The latter was obtained just before cluster **B** (3C-24b) moved over the ship, and it strongly resembles the mean sounding. However, the two P3 dropwindsondes (3C-25c and 25f) and the two *4k Korolov* soundings obtained along the track of the Electra research aircraft between 0800 and 1000 GMT (3C-25d and 25e) sampled a very old, decaying part of the stratiform region of cluster **B**. In other words, the soundings in the decaying stratiform region (3C-25c through 25f) showed marked deviation from the main structure seen in 3C-25a and 25b. This

deviation was evidently produced by an unsaturated downdraft below the stratiform cloud base of cluster **B**. Each of these soundings was a typical mesoscale downdraft sounding (Zipser, 1977) characterized by a low-level subsidence inversion with the dew point depression decreasing with height up to the base of the stratiform cloud, approximately 500 mb.

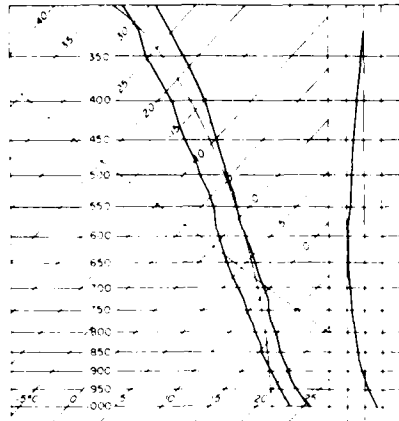


3C-24a. *4k Korolov* clouds and weather beneath cluster **B**, 10 December 1978.

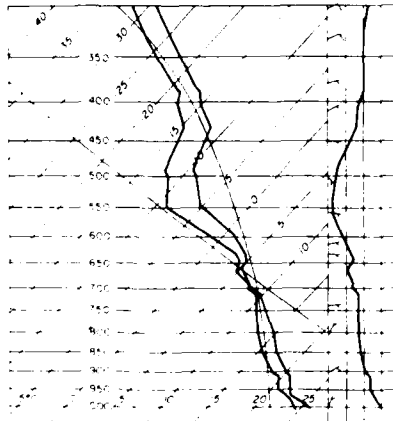


3C-24b. Sequence of 14 GMS satellite images of cluster **B**, 10 December 1978.

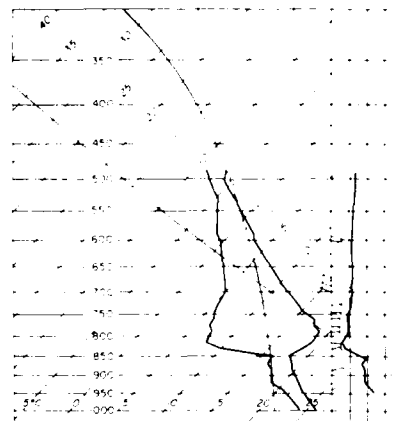
ENVIRONMENTAL AND MEAN SOUNDINGS
FOR CLUSTER B
10 DECEMBER 1978



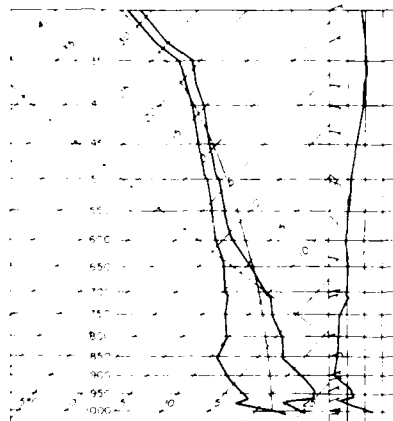
3C-25a. AK. Korolov Mean winter
MONEX sounding.



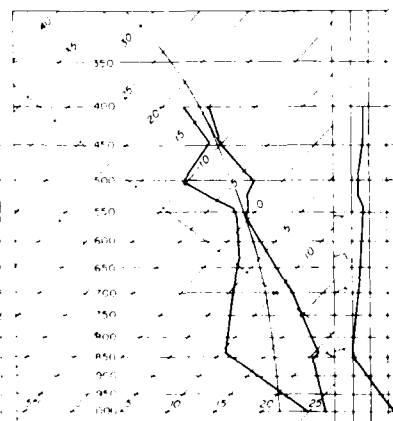
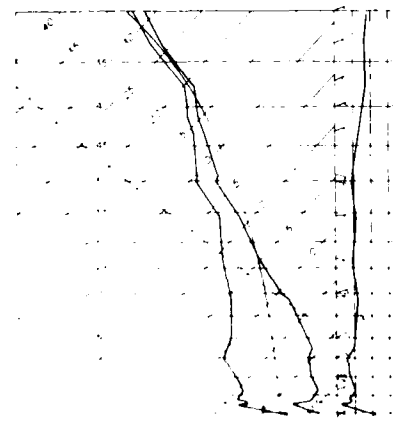
3C-25b. AK. Korolov sounding for
0000 GMT 10 December 1978.



3C-25c. P2 dropwindsonde for
0940 GMT 10 December 1978.



3C-25d. AK. Korolov sounding for
0800 GMT 10 December 1978.



3C-25f. P3 dropwindsonde for
1000 GMT 10 December 1978.

Important Conclusions

1. The dominant cluster observed off the north Borneo coast was initiated when a group of convective cells formed in response to a land-breeze convergence flow pattern associated with upper-level diffluence.
2. During the mature stage of this cluster, the stratiform rain area became nearly surrounded by a broken line of convective cells of various intensity. The greatest concentration of intense cores was maintained in a generally stationary region on the southeast side of the cluster, where the land-breeze convergence was located, while convection on the northwest side of the cluster propagated out to sea.
3. The stratiform precipitation area of the cluster appeared to be formed and maintained by a combination of three processes: dying convective cells being transformed into stratiform structures, hydrometeors being advected from the tops of active cells into the stratiform precipitation region, and condensation in the mesoscale updraft contributing to the growth of hydrometeors falling as stratiform rain. About 46% of the total precipitation from this cluster fell as stratiform rain.
4. Other cloud clusters that occurred on this day generally formed around the periphery of the large land breeze-generated cluster and were of smaller size. Convective downdraft outflows found in the regions between the old and new clusters may have been involved in triggering the new clusters.

References

- Chang, C.-P., and K. M. Lau, 1980: Northeasterly cold surges and near equatorial disturbances over the Winter MONEX area during December 1974. Part II: Planetary-scale aspects. *Mon. Wea. Rev.*, **108**, 298-312.
- Chang, C.-P., B. K. Cheang, and G. T. Chen, 1981: Regional Synoptic Analysis during Phase I of Winter MONEX. Department of Meteorology, Naval Post-graduate School, Monterey, CA 93940, pp. 285.
- Houze, R. A., Jr., and A. K. Betts, 1981: Convection in GATE. *Rev. Geophys. Space Phys.*, **19**, 541-576.
- Houze, R. A., Jr., S. G. Geotis, F. D. Marks, Jr., and A. K. West, 1981: Winter monsoon convection in the vicinity of North Borneo. Part I: Structure and time variation of the clouds and precipitation. *Mon. Wea. Rev.*, **109**, 1595-1614.
- Johnson, R. H., and D. L. Priegnitz, 1981: Winter monsoon convection in the vicinity of North Borneo, Part II: Effects of large-scale fields. *Mon. Wea. Rev.*, **109**, 1615-1628.
- Ramage, C. S., 1971: *Monsoon Meteorology*. Academic Press, New York, pp. 271.
- Zipser, E. J., 1977: Mesoscale and convective-scale downdrafts as distinct components of squall-line circulation. *Mon. Wea. Rev.*, **105**, 1568-1589.

Section 4

Tropical Indian Ocean

4A Introduction

Tropical Indian Ocean	4A-1
-----------------------------	------

4B Synoptic-scale Case Studies

1 Low-level Jets	4B-1
The Somali Low-Level Jet	
Somalia, East Africa	
June 1979	4B-4
2 Detection of Surface Ridge Lines in Infrared Imagery ...	4B-9
Surface Ridge Line	
Arabian Sea	
April 1980	4B-10

4C Mesoscale Case Studies

1 Detection of Sea Breeze Offshore Subsidence	
Regions in Daytime Infrared Imagery	4C-1
Sea Breeze	
Persian Gulf	
March 1983	4C-2
2 Fog Formation over Cold Upwelled Coastal Waters	4C-5
Coastal Fog	
Arabian Peninsula Southern Coast	
July and August 1981	4C-6
3 Island Barrier Effects	4C-9
Island Barrier Effects Revealed by Sunlight Patterns	
Socotra Island Eastern Arabian Sea	
June 1979 and June 1983	4C-10
4 Detection of Oil Spills in Sunlight	4C-15
Damaged Oil Fields	
Persian Gulf	
June 1983	4C-16
5 Differentiation of Phenomena of Atmospheric	
Origin from Oceanographic Origin in	
Satellite Imagery	4C-19
Dust Storm	
Red Sea	
June 1973	4C-20

Tropical Indian Ocean

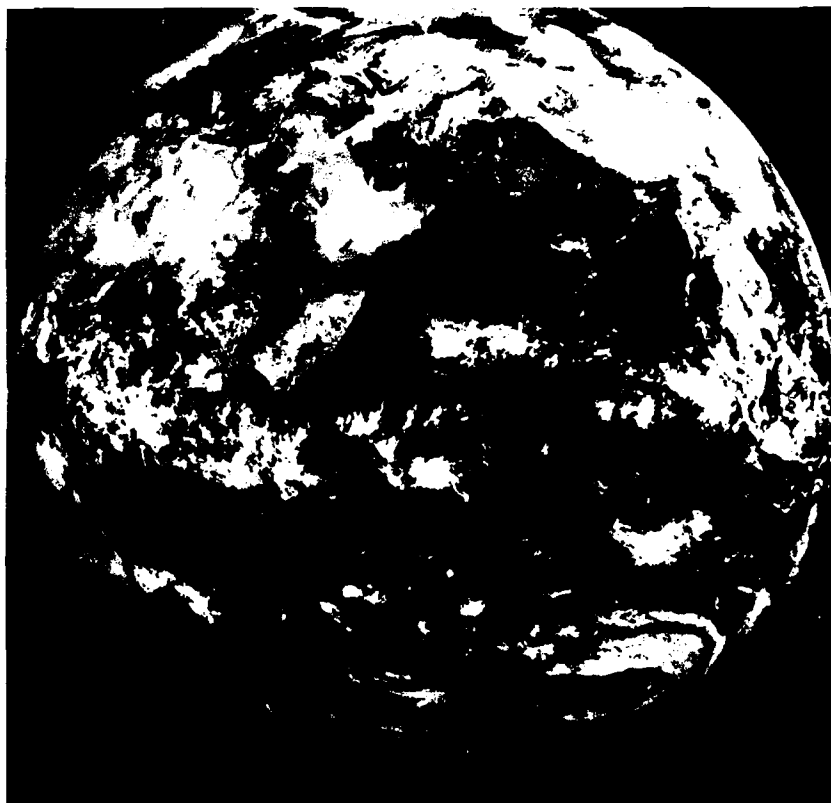
The tropical Indian Ocean is characterized by the famed northeast (winter) and southwest (summer) monsoon seasons with transitions in the spring and fall (see NTAG, Vol. 5, Parts 1 and 2).

The northeasterly winds of the Northern Hemisphere turn counterclockwise near the equator to northwesterly winds in a buffer zone similar to that existing over the tropical western Pacific Ocean. This wind regime does a complete reversal by summer as southeasterly winds from the Southern Hemisphere turn clockwise to southwesterly in an equatorial buffer zone.

A GOES-Indian Ocean image (4A-1a) shows an April view of the region. Dark streaks south of convergent cloud bands indicate calm seas and the location of the equatorial trough on this date. Note the extremely clear conditions over India indicating that the southwest monsoon has not yet been initiated in that region. It has started, however, over Southeast Asia where abundant convective cloudiness is evident.

This section includes a number of examples of Indian Ocean weather as detected by satellite and includes other interesting examples of other effects including dust storm activity and the detection of oil spills by satellite.

4A-1a. GOES-Indian Ocean.
Visible Image.
0730 GMT
23 April 1979.



Case 1 Low-level Jets

Low-level jets with wind speeds concentrated in the lowest 2 km of the atmosphere have been detected in a number of locations. One of the earliest described was that found in the south to central United States extending from Texas to Nebraska (Polson, 1958). Low-level jets are also observed over the western Arabian Sea off Somalia, the west coast of the United States, and along the coast of western Africa.

Formation of Low-level Jets

Wexler (1961) explained the formation of the jet as a dynamic effect originating from easterly trade wind flow being deflected anticyclonically northward into the Mississippi Valley by the high escarpment of Central America and the foothills of the Rocky Mountains. According to the potential vorticity expression

$$\frac{f + \zeta}{D} = \text{constant}$$

where f is the coriolis parameter, ζ is the relative vorticity, and D is the column thickness, as air moves northward in adiabatic motion, f increases, while D remains constant. This implies that the relative vorticity must decrease to maintain the required constant ratio. Increasing anticyclonic vorticity if converted into anticyclonic shear, implies a high speed current at the western boundary of the flow, which correlates with the observed position of the low-level jet.

In the Indian Ocean, a low-latitude jet was documented by Findlater (1969). This jet requires the following precursors for formation: (1) the southeast trades of the Southern Hemisphere; (2) a strong, narrow, cross-equatorial flow over East Africa and the western edges of the Indian Ocean; and (3) the southwest monsoon over the Arabian Sea. The presence of these components collectively result in the formation of the East-African or Somali jet.

Since the coriolis force is very small at low latitudes, the vorticity theorem is inadequate to explain jet formation in near-equatorial regions. Some other type of forcing must be involved. Bannon (1982), with a numerical model, successfully simulated known details of the East-African jet and concluded "that large-scale mass, source-sink forcing present to the east of the model geography drives the low-level circulation."

The source of the jet was determined to be southeasterly trade wind flow from the region east of the Malagasy Republic (Madagascar) in the Southern Hemisphere. The mountains of East Africa act to block this flow and play a crucial part in intensifying the speed of the current. Heat lows over Saudi Arabia and India act as atmospheric sinks which tend to draw the flow northeastward into India.

Northerlies associated with the heat low over Saudi Arabia appear crucial in causing the separation of the jet from the coast of Somalia near 11° N. The model simulated positions of relative wind maxima and minima which related well to known maxima near Madagascar, over Zambia, Zimbabwe, and off the coast of Somalia. Southwest monsoon winds over the Arabian Sea were also shown to be notably stronger than winds in the southeast trades, as is commonly observed.

Low-level jets have also been detected in other regions of the world, most notably along the west coast of the United States and along the coast of western Africa. Jet formation in these regions occurs commonly during the summer period under a normal situation of high pressure at sea to the west with a thermal low inland. Northerly winds along the coast subside in their straight southward movement and produce warming of the air, lower pressure, and low inversion height near the coast.

The rise of the inversion to the west is often steep. For example Brost *et al.* (1982), report that on 12 June 1979, the mixed layer depth was only 180 m near shore in the San Francisco region but rose to 800 m at a distance 150 km out to sea. The increased pressure gradient below the sloping inversion implies a sudden increase to higher wind speeds in the

same region reaching values as much as 26 kt (13 m sec^{-1}) going from above the inversion to below the inversion. It is the slope of the inversion, therefore, which is thought to be an important factor in the development of the low-level jet in these regions.

Finally, Hsu (1979) describes mesoscale jets that can form over flat coastal regions when the prevailing geostrophic flow is less than 10–12 kt ($5\text{--}6 \text{ m sec}^{-1}$) and blows preferably from land to sea; when the wind directional shear within the boundary layer is less than 80° ; and when air temperatures over nearby waters are at least 5°C warmer than over land.

Under such circumstances a cold pool of air may develop over land at night creating a mesoscale low-level inversion below a mesoscale inversion at a slightly higher level. Jet-like winds develop between the inversion layers over land as a venturi effect. Under conditions of offshore flow the jet is normally found between 100–600 m and extends from 40–50 km inland to a few km offshore (see Sec. 1C, Case ?).

Diurnal Variations

It has been noted that the low-level jet is normally much weaker during daylight hours, and increases in speed rather dramatically at night. This is true of the low-level jet in all locations.

Blackadar (1957) attributed this variation to an inertial oscillation of the ageostrophic wind (such as sea breezes) at the top of the boundary layer. Turbulent mixing during the daytime decreases boundary layer momentum below the geostrophic value. This acts to retard the wind at that level. After sunset, cooling of the land stabilizes the atmosphere so that mixing no longer occurs. The ageostrophic wind component at the top of the boundary layer, then, acted upon by coriolis force, undergoes an inertial oscillation as it turns toward the geostrophic wind direction. As the geostrophic and ageostrophic winds become aligned, the wind at the top of the boundary layer accelerates, normally becoming super-geostrophic in the process, thereby creating an important jet maximum during the evening hours.

Upwelling is very intense along the coast of Somalia during the period of the southwest monsoon. The land-sea temperature difference during daylight hours can be as much as $20^\circ\text{--}30^\circ \text{C}$. The strong sea breeze, which develops as a result of the temperature contrast in this region, acts to retard the low-level jet during daylight hours. During night-time the land-sea temperature difference becomes very small, and the reverse circulation of the land breeze begins to develop. Additionally, because of mountains in the region, cold katabatic winds develop, flowing seaward down the mountains, in the direction of the land breeze.

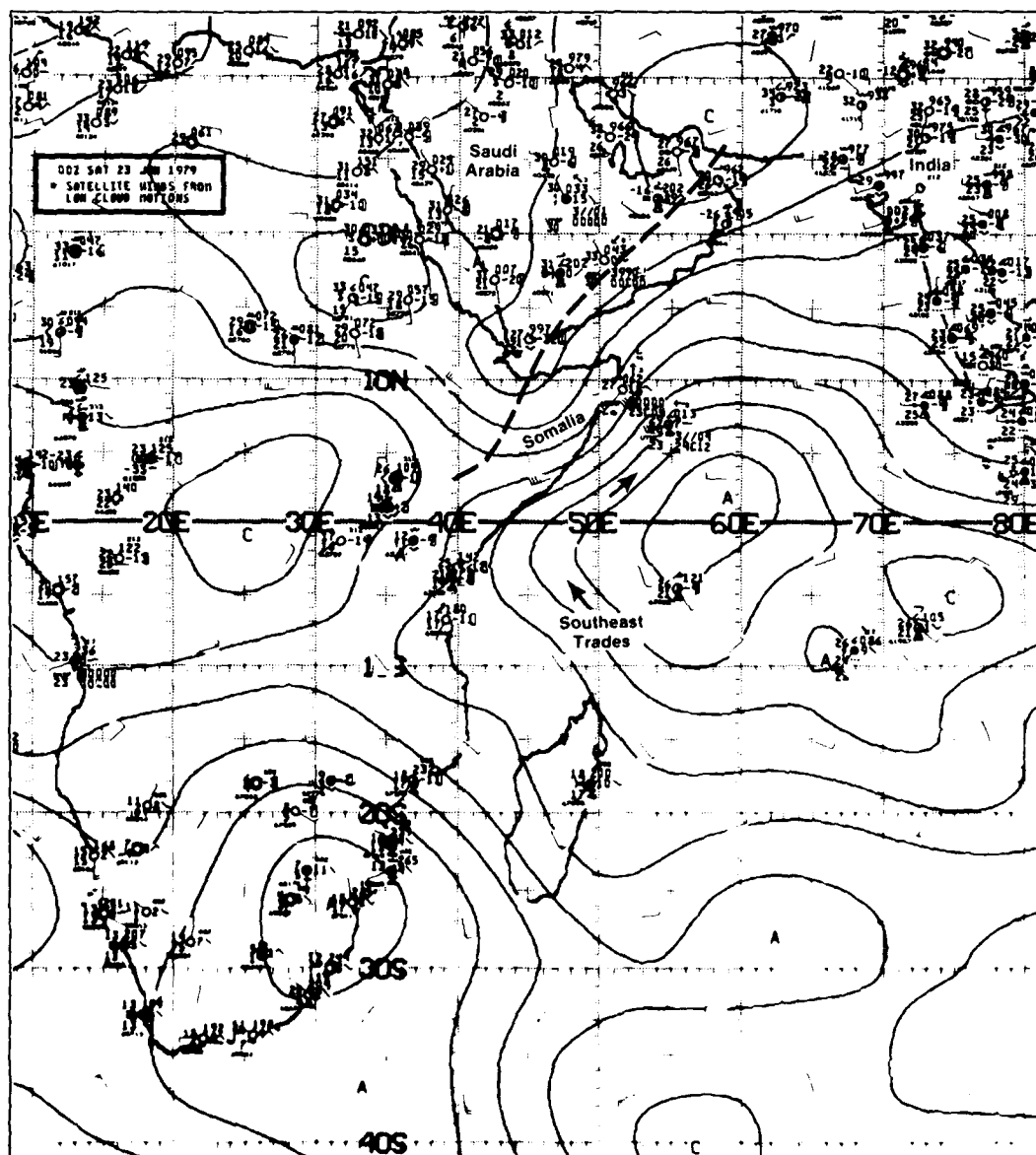
This combined effect acts to accelerate the Somali jet during night-time hours leading to the jet maximum, which is normally double the strength observed during daylight hours (Hsu, 1981).

References

- Bannon, P. R., 1982: On the Dynamics of the East African Jet. III: Arabian Sea Branch. *Jour. Atmos. Sci.*, **39**, 2267–2278.
- Blackadar, A. K., 1957: Boundary layer wind maxima and their significance for the growth of nocturnal inversions. *Bull. Am. Meteorol. Soc.*, **38**(5), 283–290.
- Brost, R. A., D. H. Lenschow, and J. C. Wyngaard, 1982: Marine Stratocumulus Layers. Part I: Mean Conditions. *Four. Atmos. Sci.*, **39**, 800–817.
- Findlater, J., 1969: A major low-level air current near the Indian Ocean during the northern summer. *Quart. J. Roy. Meteorol. Soc.*, **95**, 362–380.
- Hsu, S. A., 1979: Mesoscale nocturnal jetlike winds within the planetary boundary layer over a flat, open coast. *Boundary Layer Meteorology*, **17**(4), 485–494.
- Hsu, S. A., 1981: Diurnal variation of the low-level jet in Somalia. Condensed Papers and Meeting Report, "International conference on early results of FGGF and large-scale aspects of its monsoon experiments, Tallahassee, FL, 12–17 Jun 1981", 12-63-12-67.
- Polson, R. K., 1958: Sunrise Wind—How to find and use it. *Bus. and Comm. Aviation*, Feb. 1958, 42–44.
- Wexler, H., 1961: A boundary layer interpretation of the low-level Jet. *Tellus*, **13**, 368–378.

References

- Findlay, A. G., 1866. *A directory for the navigation of the Indian Ocean*. London, Richard Holmes Laurie, pp. 1062.
- Hsu, S. A., 1981. Diurnal variation of the low-level jet in Somalia. Condensed Papers and Meeting Report, "International conference on early results of FGGF and large-scale aspects of its monsoon experiments. Tallahassee, FL, 12-17 Jun 1981", 12-63-12-67.



4B-4a NMC Tropical Surface Streamline Analysis 0000 GMT 23 June 1979

*The Somali Low-Level Jet
Somalia, East Africa
June 1979*

23 June

The NMC surface streamline analysis for 0000 GMT (4B-4a) shows the basic elements forcing the Somali low-level jet. The southeast trades turn to southwesterly as they cross the equator and increase in wind speed as much as 45 kt off the coast of Somalia, and then flow at somewhat reduced speed toward India. A closed circulation over the Persian Gulf has associated trough lines extending northeastward to northern India and southwestward across Saudi Arabia.

The FNOG surface analysis for the same time (4B-5a) gives a slightly different portrayal of conditions, indicating a low-pressure center over the southern Red Sea region and in south-central Saudi Arabia. Northerly winds over Saudi Arabia and the Red Sea converge with strong southwesterlies near the southern Saudi Arabian coast.

The DMSP visible image acquired at 0818 GMT (4B-6a) shows cloudiness over the region. Anticyclonic turning of the southeasterly trades is clearly depicted by the curvature of cloud lines which can be traced from well south of the equator to the northern coastal area of Somalia. The fine nature, close spacing, and long length of the cloud lines is characteristic of high surface wind speed conditions as verified in the surface analyses (4B-4a and 5a).

The sudden clearing of cloud forms in the region, outlined on the DMSP image offshore of Somalia, corresponds to the cold upwelled water which rings the "prime eddy," a warm anticyclonic ocean feature located semi-permanently in that position during the southwest monsoon (Findlay, 1866). Cloud lines disappear over the cold water but reappear over the warm prime eddy where the air is again heated from below.

Note that cloudiness apparently associated with the Somali jet extends well inland. A sudden break in this cloudiness occurs over Somalia near 8.5° N, the location of the Nogal Valley, which runs nearly perpendicular to the coastline. Such a break indicates strong downward motion of the flow into the valley, causing the observed dissipation of cloudiness. As such this clear zone is indicative of a low-level jet over the region.

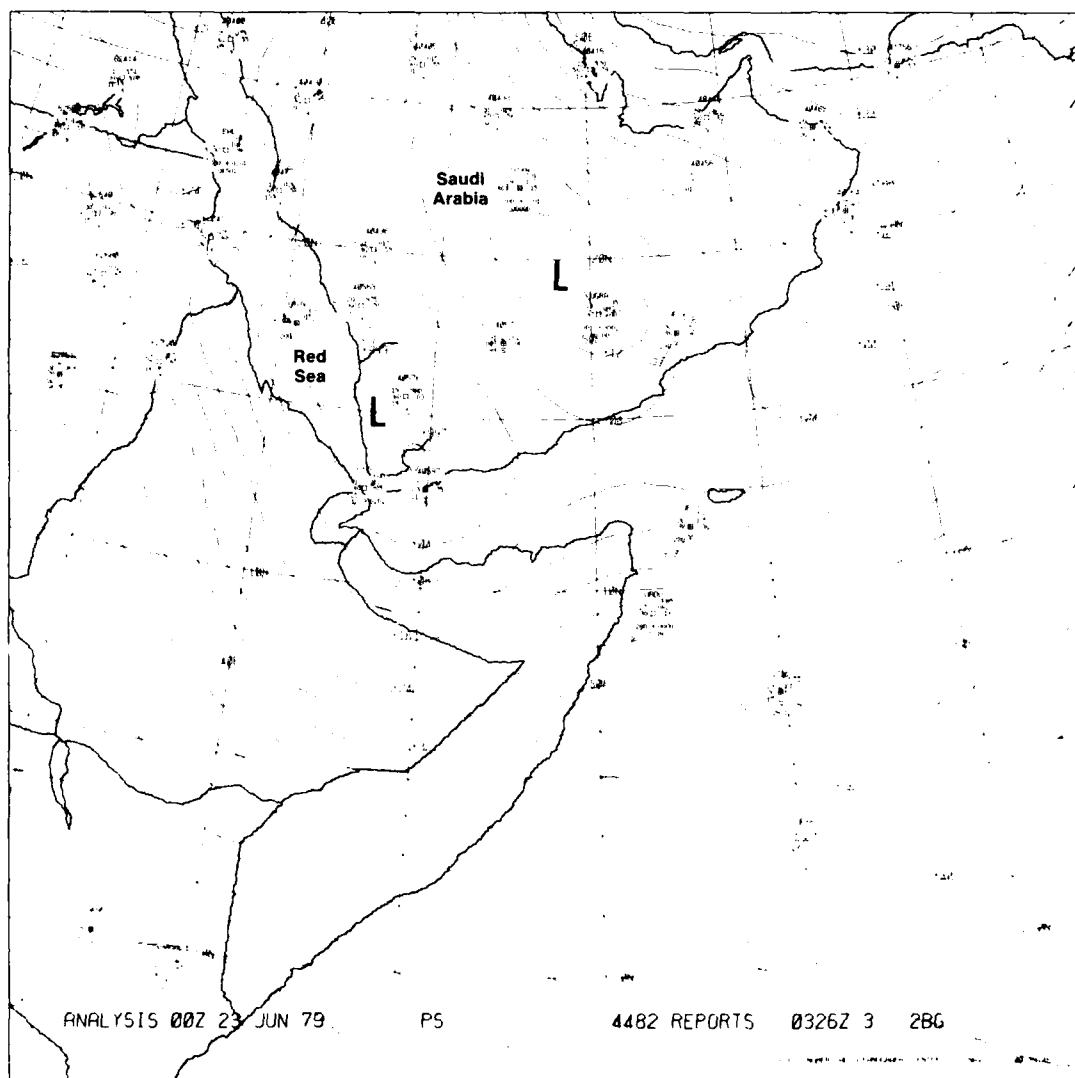
Gardo, Somalia (9.5° N, 49.1° E), is located just to the north of the Nogal Valley. The RAOB from Gardo at 0055 GMT (0355 LST; 4B-7b) suggests a thin surface layer in which the wind increases very rapidly from calm to 20 kt (10 m sec⁻¹). The temperature shows a nearly adiabatic lapse rate in this region. From 100 m to about 1,200 m an adiabatic layer exists, in which the wind speed increases steadily from 20 kt to 60 kt (10–30 m sec⁻¹). This is the peak speed of the Somali jet. The lapse rate stabilizes in this region at the base of an inversion which extends from about 1,200 to 1,700 m. The dew point decreases fairly rapidly from near the top of the inversion as the temperature lapse rate again returns to adiabatic. Wind direction veers from southwest and west below the inversion layer to northwest and north above this layer.

During the day, the surface layer (4B-7c) behaves superadiabatically; with about 20–30 kt (10–15 m s⁻¹) wind speed, a condition which exists only between the surface and 100 m. Above this height, an adiabatic layer with steady wind speeds of 30–40 kt (15–20 m sec⁻¹) prevails up to 1,500 m, and a subsidence inversion is located from 1.5 to about 2.0 km. Above 2 km, adiabatic conditions again prevail. These features imply a four-level structure characteristic of the atmosphere over Somalia in the region of the jet. Note that the wind blows from southwest to west below the inversion layer. Wind speed shear is largest in the surface layer. Above the inversion layer, wind speed decreases to less than 20 kt (10 m sec⁻¹). It can be seen that the jet effect is much reduced during daylight hours. Note that vertical mixing has tended to sharpen the inversion, which appears much more pronounced in comparison to the sounding acquired during night-time hours (4B-7b).

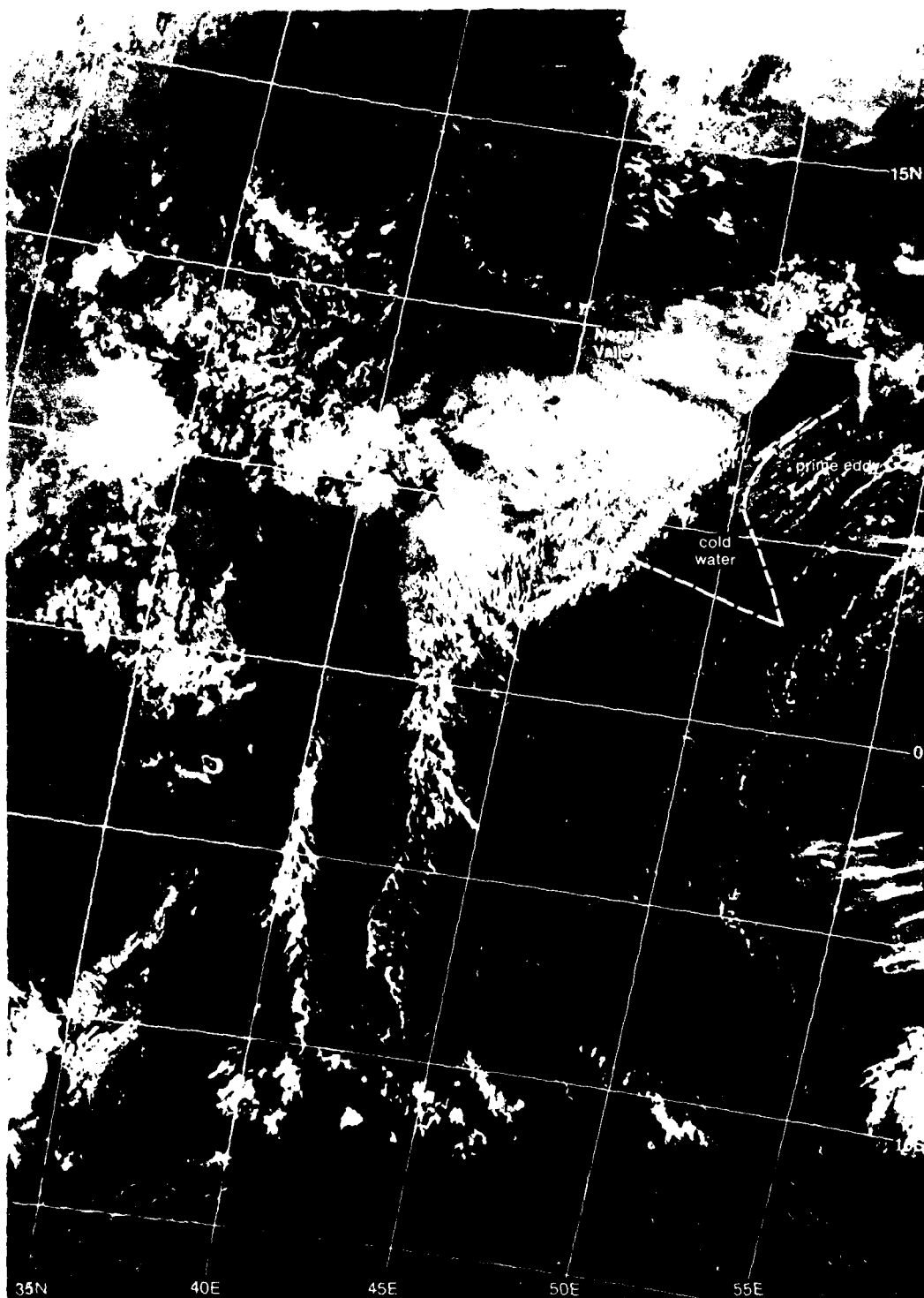
The DMSP visible image of the region on the following day (4B-7a) shows virtually identical conditions to the preceding day (4B-6a). Note in particular the clear slot over the Nogal Valley and the clear region offshore of Somalia outlining the upwelled water surrounding the prime eddy. These conditions imply strong southwesterly flow at low-levels across Somalia and the adjacent coastal region. Ship reports (4B-7a) over the western Arabian Sea show 30–40 kt southwest winds that confirm the presence of strong southwest monsoon flow on this date.

Important Conclusions

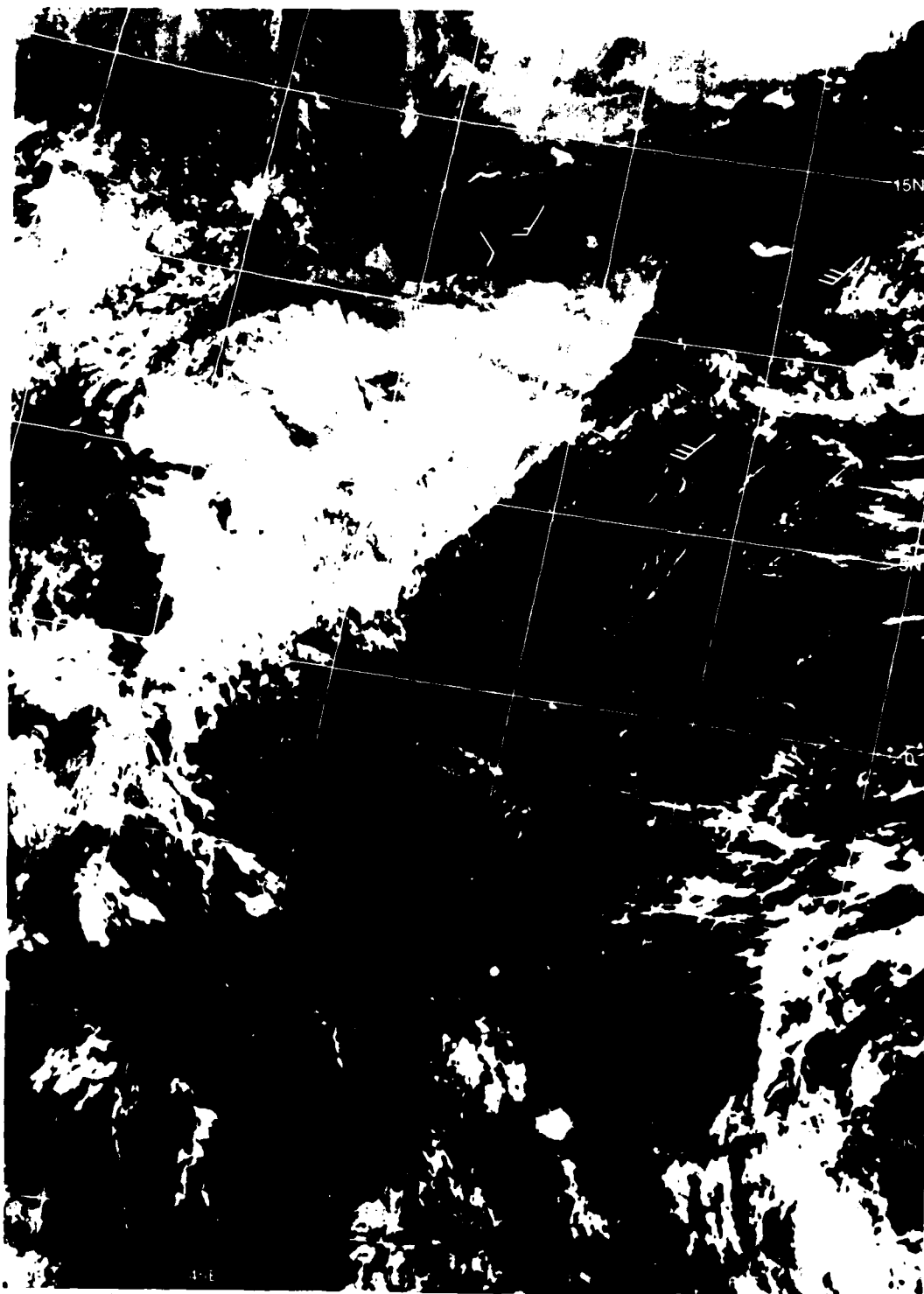
1. The East-African or Somali jet has a low-level wind maximum at the base of an inversion generally below 1,500 m over Somalia.
2. The Somali jet's existence can easily be inferred from satellite data by tracing cloud lines turning anticyclonically over the Arabian Sea off the coast of Somalia and noting the distinct clear slot formed over land by the evaporation of clouds in downslope motion from the southwest over the Nogal Valley.
3. Soundings over Somalia during the occurrence of Somali jet conditions reflect a distinct four level structure: surface, adiabatic, inversion, and again adiabatic. The Somali jet lies near the base of the inversion.
4. Cold upwelled water off the coast of Somalia and the position of the prime eddy are clearly shown in satellite daytime DMSP visible images by the absence of clouds over the cold water and the quick return to abundant cloudiness over the warm waters of the prime eddy.



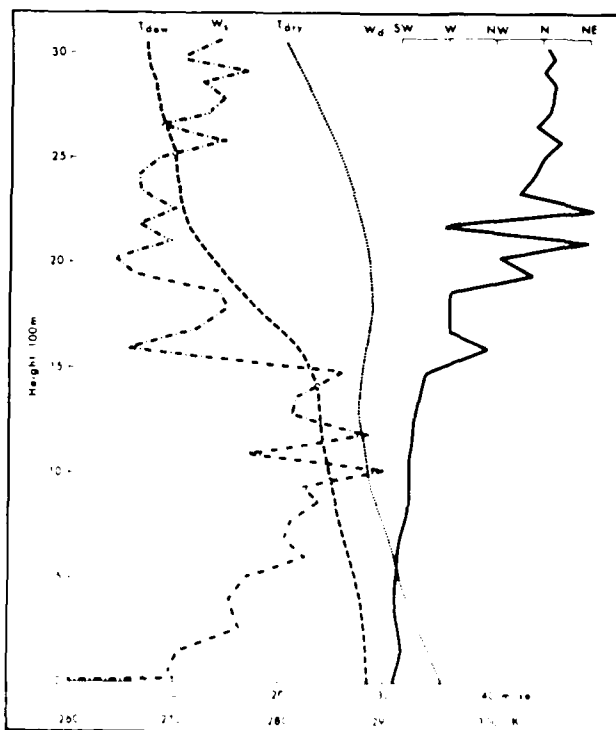
4B-5a FNOG Surface Analysis 0000 GMT 23 June 1979



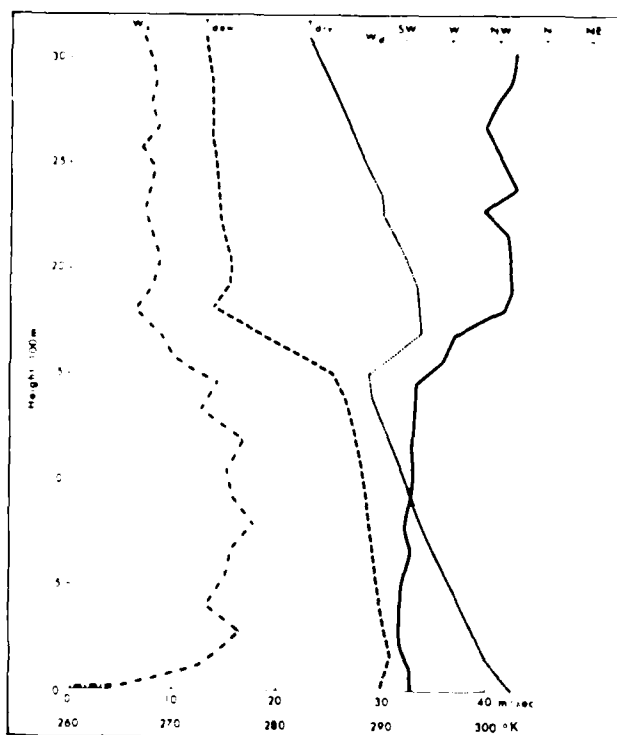
4B-6a F-1 DMSP 1F Low Enhancement, 0818 GMT 23 June 1979



4B-7a F1 DMSP F1 Low Enhancement 0759 GMT 24 June 1979. Surface Wind Reports (1200 GMT)



4B-7b RAOB Gardo, Somalia
0055 GMT (0355 LST)
23 June 1979
(After Hsu, 1981)



4B-7c RAOB Gardo, Somalia
0055 GMT (0355 LST)
23 June 1979
(After Hsu, 1981)

Case 2 Detection of Surface Ridge Lines in Infrared Imagery

During late March through early April each year the Indian Ocean is in its spring transition from the dry northeast monsoon (winter) to the wet southwest monsoon (summer). Areas of high pressure slowly transit the northern Arabian Sea during this period. The location and progress of the highs can be followed in infrared imagery. Since the central regions of these high pressure systems have light surface winds, there is a minimum of mechanical mixing in the surface layers of the ocean. The surface waters, therefore, will warm rapidly during daytime insolation and become "hot" areas that can be detected in daytime infrared imagery.

AD-A183 046

NAVY TACTICAL APPLICATIONS GUIDE VOLUME 6 PART 1

3/3

TROPICAL WEATHER ANALYSIS (U) BOWAN (WALTER A) CD PARK

RIDGE IL R W FEIT ET AL AUG 86 NEPRF-TR-86-02-U6-PT-2

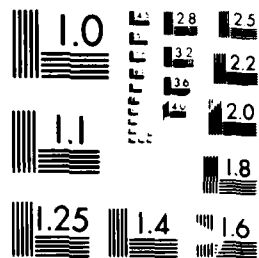
UNCLASSIFIED

NO0228-85-C-3398

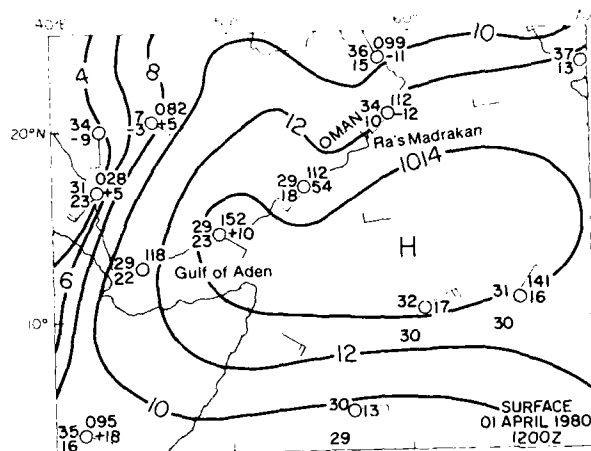
F/G 4/2

NL

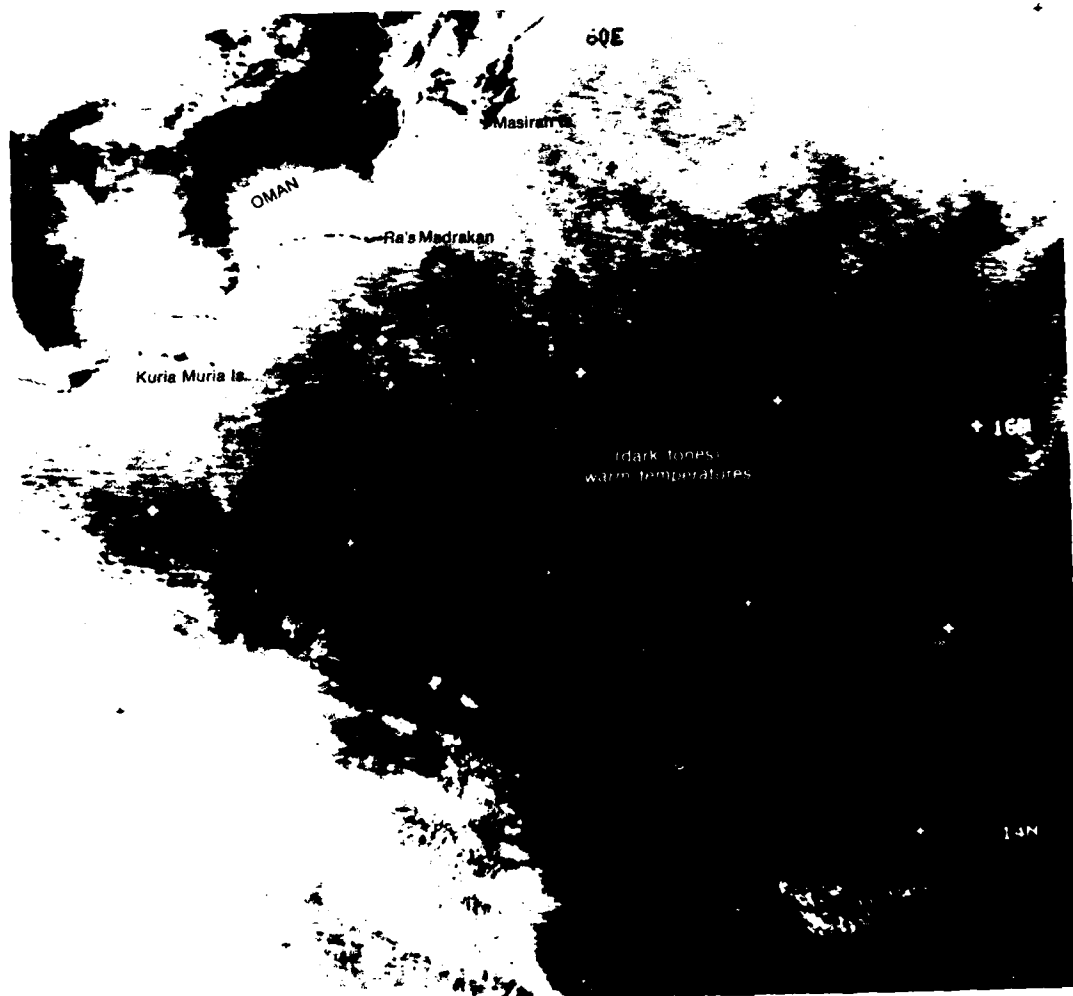




MICROCOPY RESOLUTION TEST CHART
 NATIONAL BUREAU OF STANDARDS-1963-A



4B-10a. Surface Analysis
1200 GMT 1 April 1980.



4B-10b NOAA-6 Channel 3 Mid-Infrared Image 1506 GMT 1 April 1980

*Surface Ridge Line
Arabian Sea
April 1980*

1 April

The NOAA-6 mid-infrared image from Channel 3 (3.55-3.93 μm) in the late afternoon (1506 GMT, 1906 LST; 4B-10b) displays a prominent elongated dark tone area (warm temperatures) between 16° to 18° N and 58° to 62° E. A surface analysis at 1200 GMT (4B-10a), about 3 hr prior to the satellite image, shows a ridge of high pressure that extends from the Gulf of Aden eastward over the Arabian Sea. Note that the central region of the high and the dark tone area on the satellite image coincide. The light surface winds in the vicinity of the high pressure ridge axis has allowed the afternoon insolation to heat the surface as much as 1° or 2° C and the satellite image clearly depicts this warming.

Also appearing are cool, thin, curled lines adding to the appearance of the surface signature. These curled lines are associated with surface slicks. Under light winds, areas of alternating slick and wavelets wrap and bend to conform to the dynamic flow of the upper layers of the sea. This signature coupled with surface warming will often obscure the normal sea surface temperature signature. Eddy location and sea surface temperature boundary analysis becomes more difficult under such conditions. In this example (4B-10b), numerous surface slicks are present, however, they do not mask the warm sea surface temperatures which denote the location of the surface ridge line.

During the spring of 1984, the crew of the U.S. Shuttle Flight STS-13 photographed a very complex oceanic surface slick pattern (4B-11a). The slicks appear as narrow dark streaks. The surface winds are light in this mid-ocean photograph. The lighter areas between the slicks are where the water is disturbed by wavelets. The surface slick pattern occurs in a region of sunglint, which is brightest in the upper-right portion of the image (slick pattern is obscured by sunglint); the sunglint decreases in brightness toward the lower-left portion where the slick detail is enhanced by the lighter areas between slicks due to sunglint from wavelets.

Important Conclusions

1. Surface ridge lines can be located in daytime infrared as well as in visible imagery, from warm temperature areas associated with calm or light wind areas along ridge lines.
2. Surface slicks which are most prominent in calm areas, if numerous in number, can mask the warm sea surface temperatures used to locate surface ridge lines.

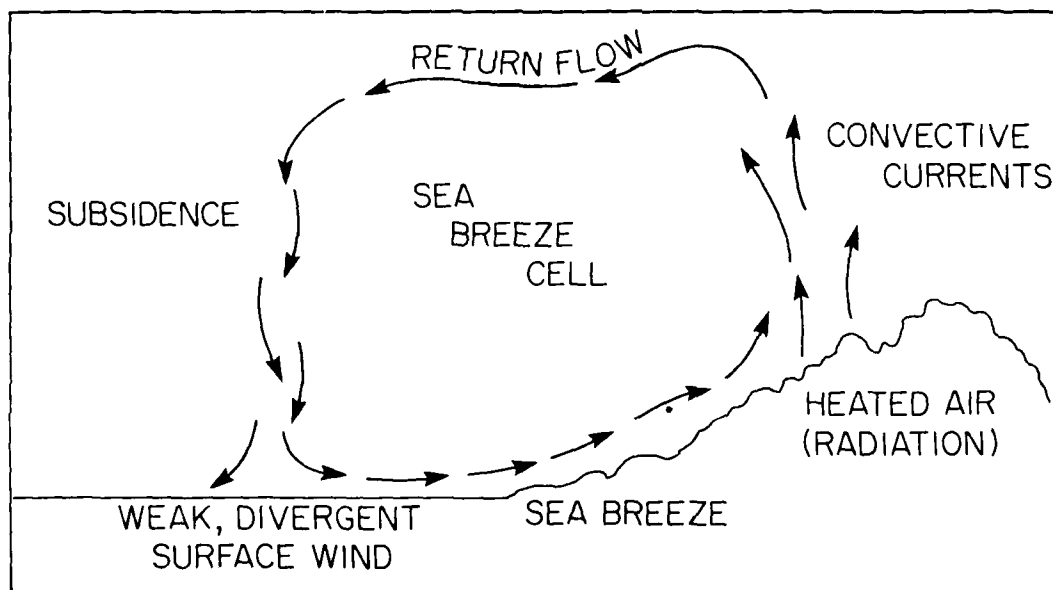
4B/0B



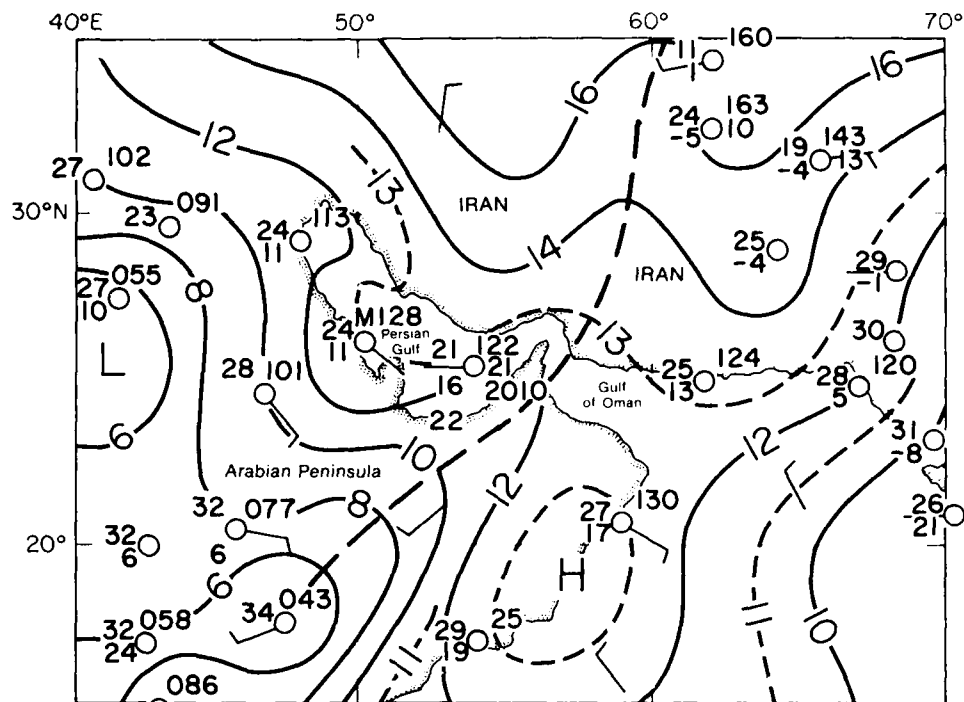
4B-11a. STS-13. Visible Photograph. (Location, time, and date: not available.)

*Case 1 Detection of Sea Breeze Offshore
Subsidence Regions in Daytime
Infrared Imagery*

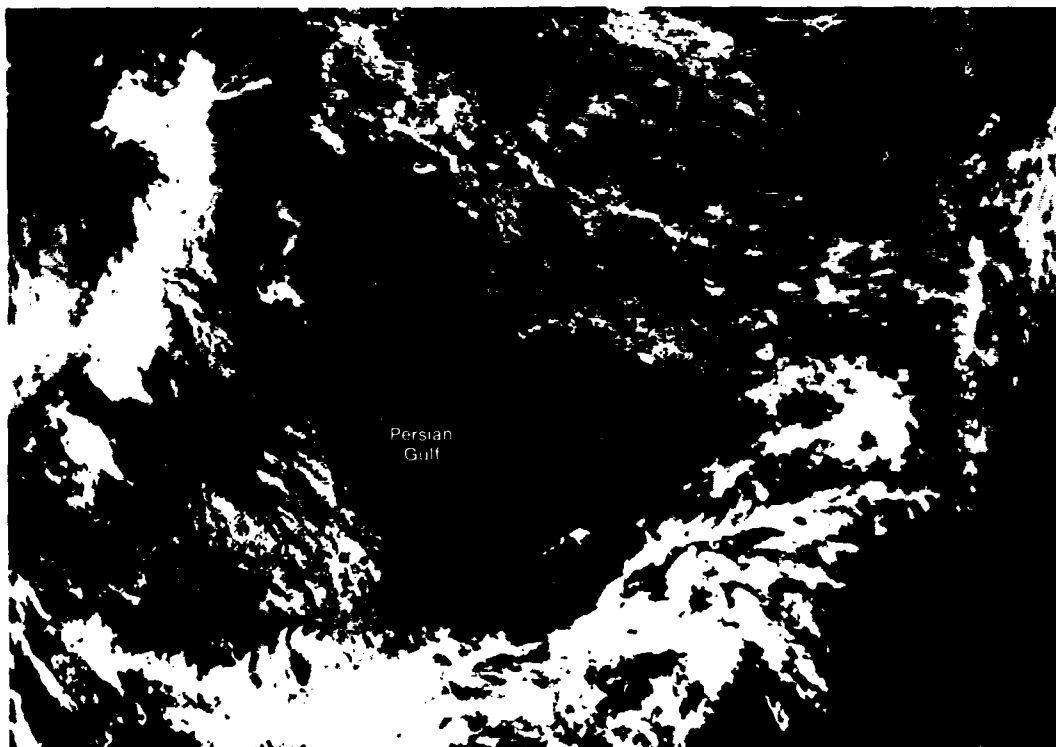
During the monsoon spring transition over the Persian Gulf, the land areas heat up more rapidly than the adjacent waters of the gulf. This discontinuity coupled with a weak pressure gradient is conducive for local afternoon sea breeze development along the coastal regions. The offshore subsidence areas associated with the sea breeze circulation (4C-1a) are often detectable in daytime infrared imagery by the appearance of a zone of warmer temperatures offshore.



4C-1a. Schematic of Sea Breeze Circulation System



4C-2a. Surface Analysis, 1200 GMT 29 March 1983.



4C-2b. NOAA-7. Channel 2 Visible Image, 1114 GMT 29 March 1983.

*Sea Breeze
Persian Gulf
March 1983*

29 March

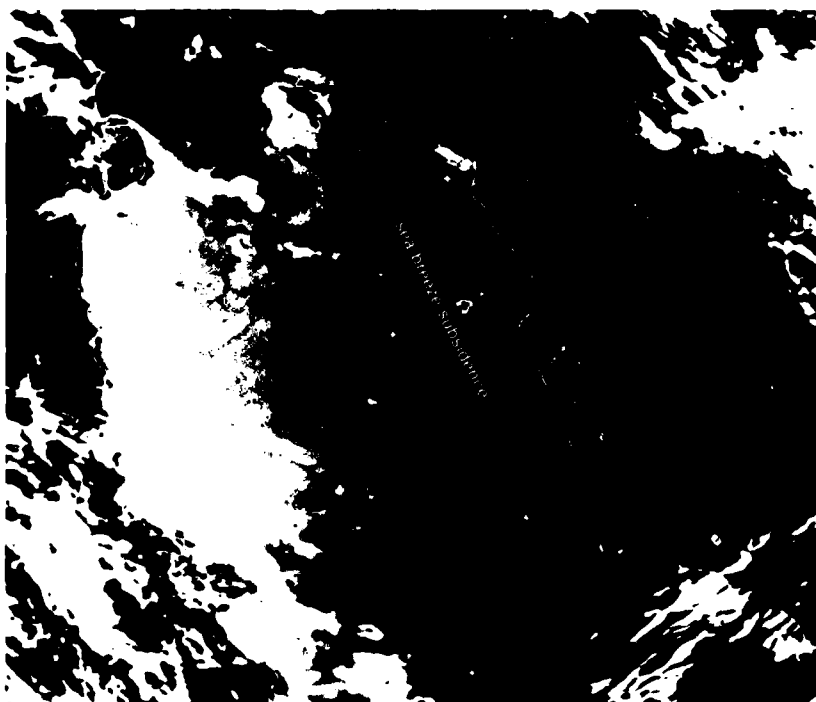
The surface analysis (4C-2a) shows a flat high-pressure system covering most of the desert regions of Iran, with weak ridging through the Persian Gulf into the eastern portions of the Arabian Peninsula. A weak surface trough extends from the southeast portions of the Arabian Peninsula across the Gulf of Oman and into Iran.

AVHRR imagery from the NOAA-7 spacecraft were collected in the afternoon. The large-scale unenhanced Channel 2 (0.725-1.10 μm) visible image (sampled only every four pixels; 4C-2b) shows what appears to be a cloud-free view of the northern Persian Gulf. However, an enlarged and enhanced full-resolution view of the area (Channel 2 visible; 4C-3a) shows aerosol and cloud details not apparent in the first image. Of particular interest are smoke plumes emanating from burning oil wells in the northern portion of the Gulf. The smoke originates in a light northwest surface wind as indicated by the smoke tracers. As the smoke approaches the eastern shore, the wind is light and variable, with a slight northward component, where a sea breeze circulation is occurring. Evidence of the sea breeze circulation is apparent on the corresponding infrared image (4C-3b). Solar insolation has heated the surface water 1 to 2 $^{\circ}\text{C}$ due to little or no wind, and the sea breeze subsidence zone parallels the coast.

4C-2B



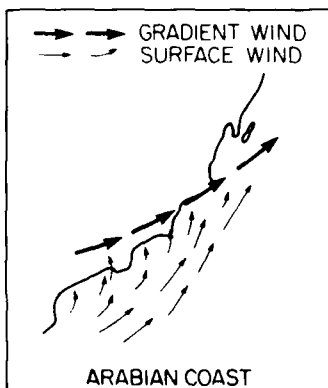
4C-3a Enlarged View, NOAA-7, Channel 2 Enhanced Full-Resolution Visible Image, 1114 GMT 29 March 1983.



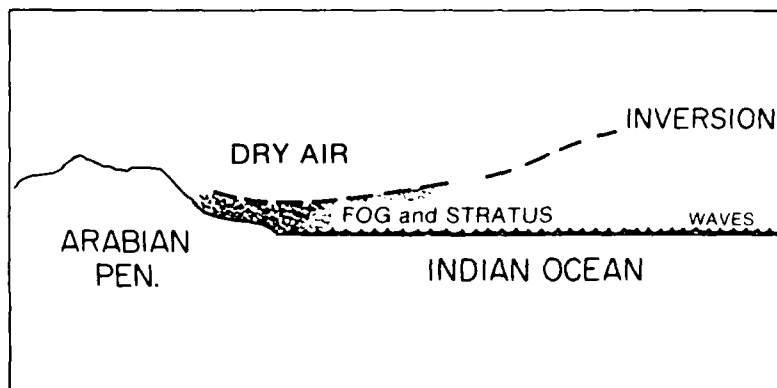
4C-3b Enlarged View, NOAA-7, Channel 4 Infrared Image, 1114 GMT 29 March 1983.

Case 2 *Fog Formation over Cold Upwelled Coastal Waters*

During the period from late May through the middle of September of each year, the southwest monsoonal flow is fully developed over the northern Indian Ocean. Upwelling occurs in several areas along the Arabian Peninsula, due to the prolonged southwest flow parallel to the coast. Fog, low stratus, and occasional drizzle formation in the warm, moist monsoon air are not an uncommon occurrence in the coastal region. Shallow, low-level convergence (4C-5a) can enhance fog formation over the cold coastal water, while warm, dry air aloft tends to cap the moisture under a strong low-level inversion (4C-5b). Once the fog and stratus have developed, they can persist in the same general area for an extended time period.



4C-5a. Coastal wind convergence pattern



4C-5b. Capping inversion over coastal fog region

4C-6a NIMBUS-7
 CZCS Channel 5
 Far Red Image
 0744 GMT 31 July 1981



4C-6b Enlarged View, NIMBUS-7, CZCS Channel 5 Far Red Image 0744 GMT 31 July 1981

*Coastal Fog
Arabian Peninsula Southern Coast
July and August 1981*

31 July and 2 August

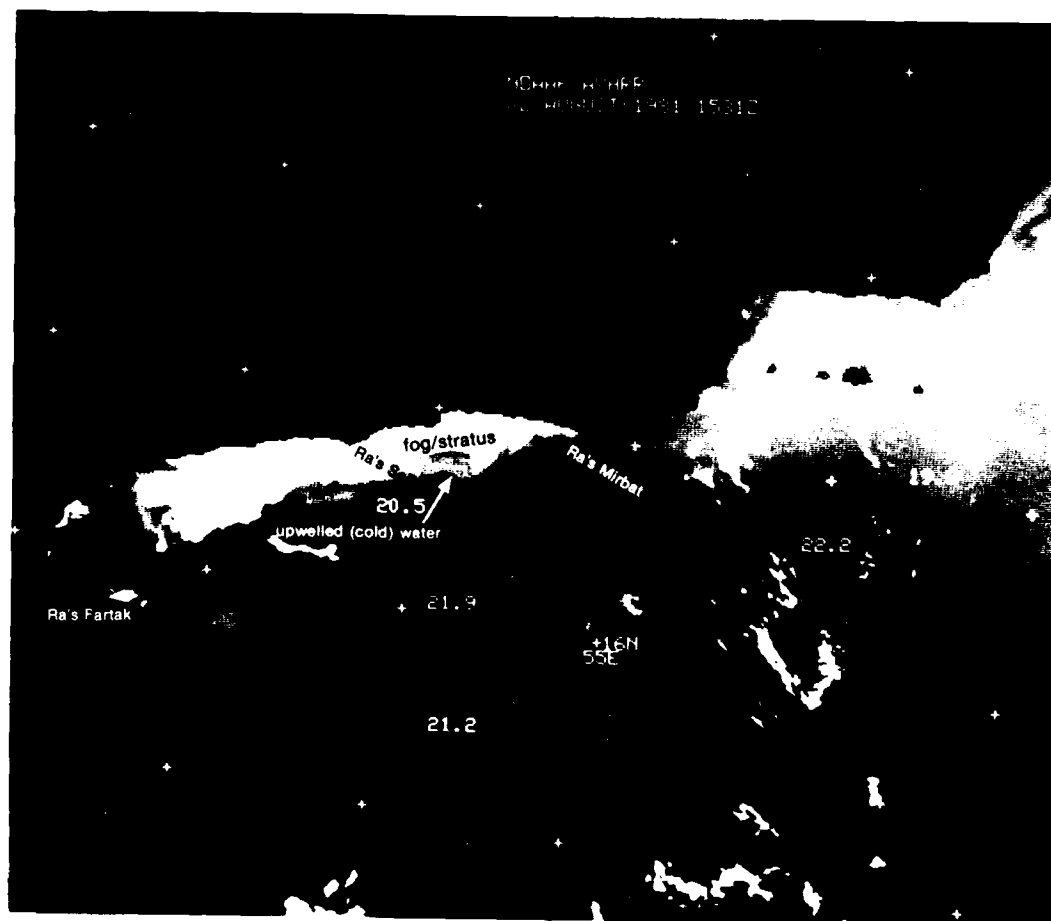
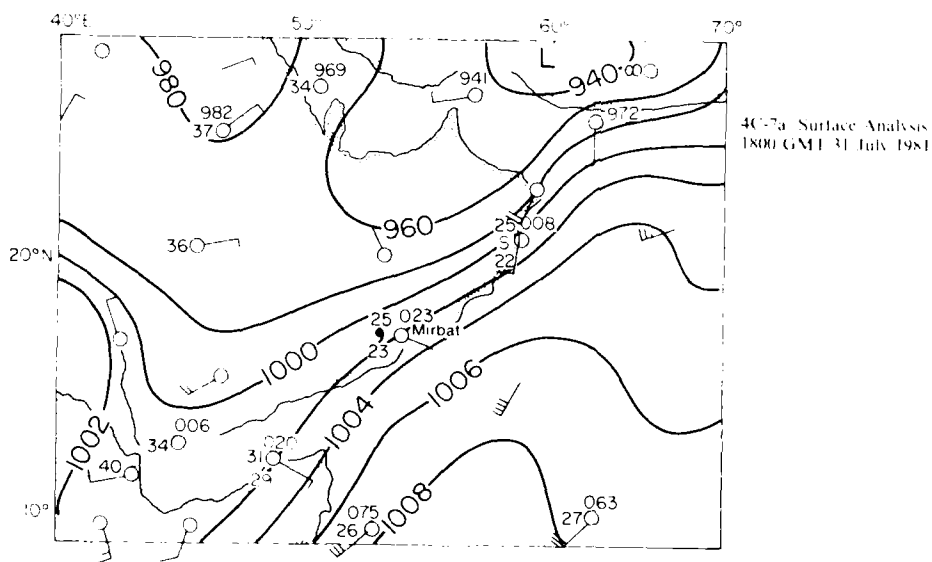
In the NIMBUS-7 CZCS Channel 5 (0.7-0.8 μm) far red image at 0744 GMT (4C-6a), an isolated layer of clouds is observed along the coastal region between Yemen and Oman. The enlarged view of this area (4C-6b) reveals that the cloudiness has the characteristic appearance of coastal fog and stratus. The surface analysis (4C-7a) shows strong, southwest monsoon wind flow (generally 25-40 kt) parallel to the Arabian Peninsula. Note that intermittent light drizzle is being reported at Mirbat. Gravity waves in the offshore stratus (4C-6b) indicate that there is a strong, low-level temperature inversion over the coastal region. The fog and low stratus appear below the inversion, where the air is warm and very moist.

The NOAA-6 Channel 4 (10.3-11.3 μm) infrared image two days later (4C-7b) indicates some fog and stratus in the same general area. The fog and stratus have persisted for two days and appear to overlie a region of cold upwelled water, partially visible on either side of the fog as a slightly darker gray shade tone.

Important Conclusions

1. During the southwest monsoon, cold water upwells near the capes which protrude from the Arabian coast line.
2. Fog and stratus that develop in the warm, moist tropical air advected over the cold coastal water can persist for several days.

4C5B



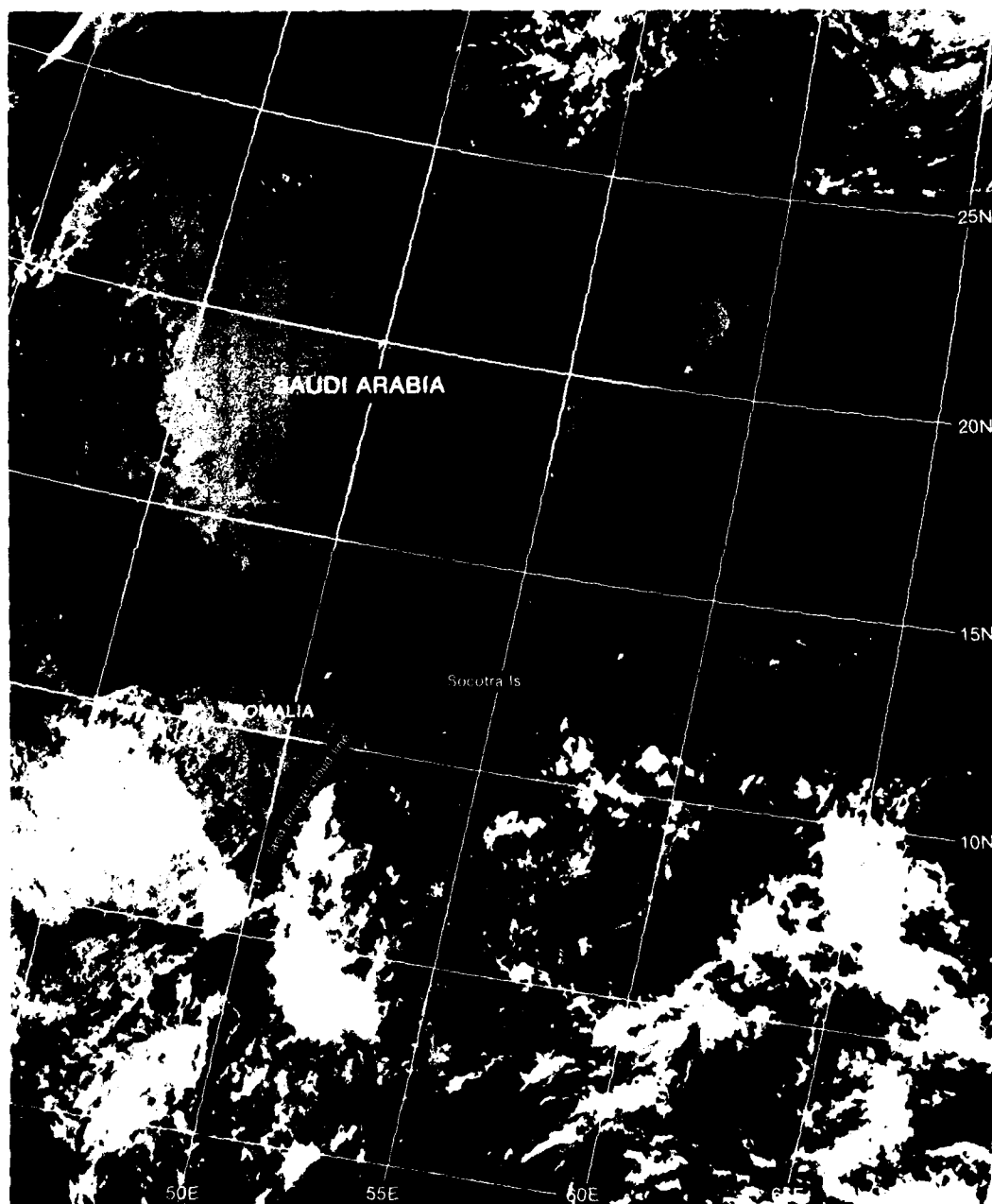
Case 3 Island Barrier Effects

For the interpreter of satellite imagery island barrier effects offer useful clues concerning inversion height, low-level wind direction, strength of flow, mesoscale changes in low-level humidity and changes in sea state (see NTAG, Vol. 1, Sec. 2C). Operational use can often be made of such information in mesoscale analysis and in positioning ships for an optimum operating environment.

4C Case 3

References

- Deardorff, J. W., 1976: Island wind shadows observed by satellite and radar. *Bull. Am. Meteorol. Soc.*, **57**(10), 1241-1242.
- Raynor, G. S., P. Michael, R. M. Brown, and S. Sethu Raman, 1974: A research program on atmospheric diffusion from an oceanic site. *Preprints, Symposium on Atmospheric Diffusion and Air Pollution* (Santa Barbara, CA). Am. Meteorol. Soc., Boston, 289-295.



4C-10a F-1 DMSP LF Low Enhancement, 0721 GMT 4 June 1979.

*Island Barrier Effects Revealed by Sunlint Patterns
Socotra Island, Eastern Arabian Sea
June 1979 and June 1983*

4 June 1979

The southwest monsoon started late in 1979, with onset occurring around 11 June. The DMSP visible image (4C-10a), a week earlier, was acquired during conditions of light southwesterly winds over Somalia, Socotra Island, and the southern coast of Saudi Arabia. Land breeze effects are revealed by the cloud line with convective build-ups off the Somalia coast. This cloud line, developing here under generally weak mid-morning synoptic flow (1021 LST), does not occur once the southwest monsoon becomes established.

An enlargement of the Socotra Island region (4C-11a) shows that Socotra is on the west edge of a sunlint pattern and is exhibiting lee effects on the north side indicating southerly low-level flow past the island. A dark pattern **C** on the edge of sunlint indicates calm seas while a brighter pattern **R** indicates rougher seas. It can be seen that calmer regions extend from sections of the north coast of Socotra northward toward a mesoscale cloud eddy, apparently formed due to turbulent effects of flow past the island.

A map of Socotra (4C-11c) shows high terrain features which could cause such blocking effects. In the DMSP visible image (4C-11a), note that the bay area (Ghubbat Kharmah) has a lighter gray shade tone and therefore rougher seas than the surrounding areas. The map (4C-11c) shows a valley leading from the south side of the island to this bay which could afford a channel for slightly stronger winds to exit into the bay and cause the noted rougher effects.

The DMSP infrared image (4C-11b), acquired simultaneously with the visible image, is especially interesting in that it reveals warmer temperatures (dark tone) downstream in a swath conforming to the exact dimensions of the island's width. The IR sensor for Flight Test Vehicle, F-1, which acquired these data, was responsive to radiation in a broad band extending from 8 to 13 μm . This bandwidth is very susceptible to water vapor absorption. In a typical tropical atmosphere, over 50% of the outgoing radiation is absorbed by water vapor in the atmosphere and retransmitted at a cooler temperature. Under low-level inversion conditions, with clear skies above, most of the water vapor in the atmosphere is trapped below the inversion. Air flowing over an island barrier, in such conditions, is heated by the island and mixed in a turbulent fashion by bringing warmer air from above the inversion down into the boundary layer. Under such circumstances water vapor in the lee of the island would re-radiate at a much warmer temperature than the surrounding unmixed and unheated air. It is suggested that this is the cause for the lee pattern observed.

13 June 1983

A different perspective of barrier effects in the lee of Socotra is provided by Coastal Zone Color Scanner (CZCS) data. The NIMBUS-7 CZCS Channel 5 (0.7-0.8 μm) far red image (4C-12a) shows an unenhanced large-scale view of the region. Note that Socotra in this view is on the east side of a sunlint

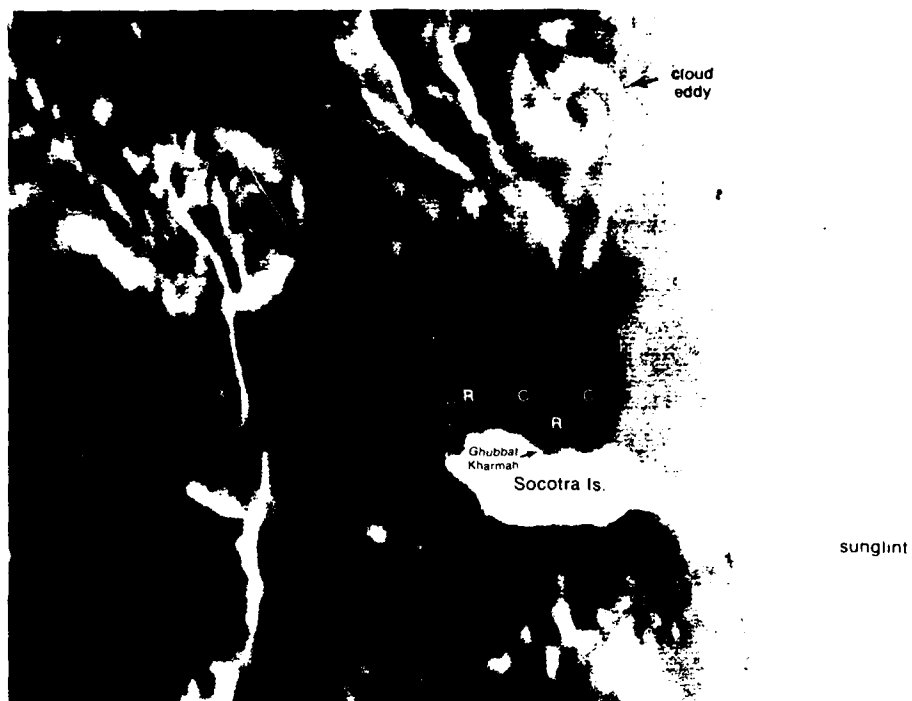
pattern. Lee effects past Socotra are faintly discernable in this image.

An enlargement of the Socotra Island region from the CZCS Channel 1 (0.433-0.453 μm) blue-spectrum image (4C-12b) shows detailed effects which should be compared to the DMSP visible depiction (4C-11a). In this CZCS image, sun angles have changed so that rough ocean areas appear dark (in sunlint) while calm areas appear bright. Note that the image still consistently indicates a rougher area (dark tones) in the bay of Ghubbat Kharmah and calm seas (light tones) bounding this region and extending well down stream. The surface analysis (4C-13a) indicates strong southwesterly flow across Socotra Island. Arc clouds or aerosols appearing upwind of the Brothers Islands and Socotra Island (4C-12b) indicate a strong, island blocking effect due to a very low inversion on this date. Unfortunately no nearby RAOBs are available to verify this condition.

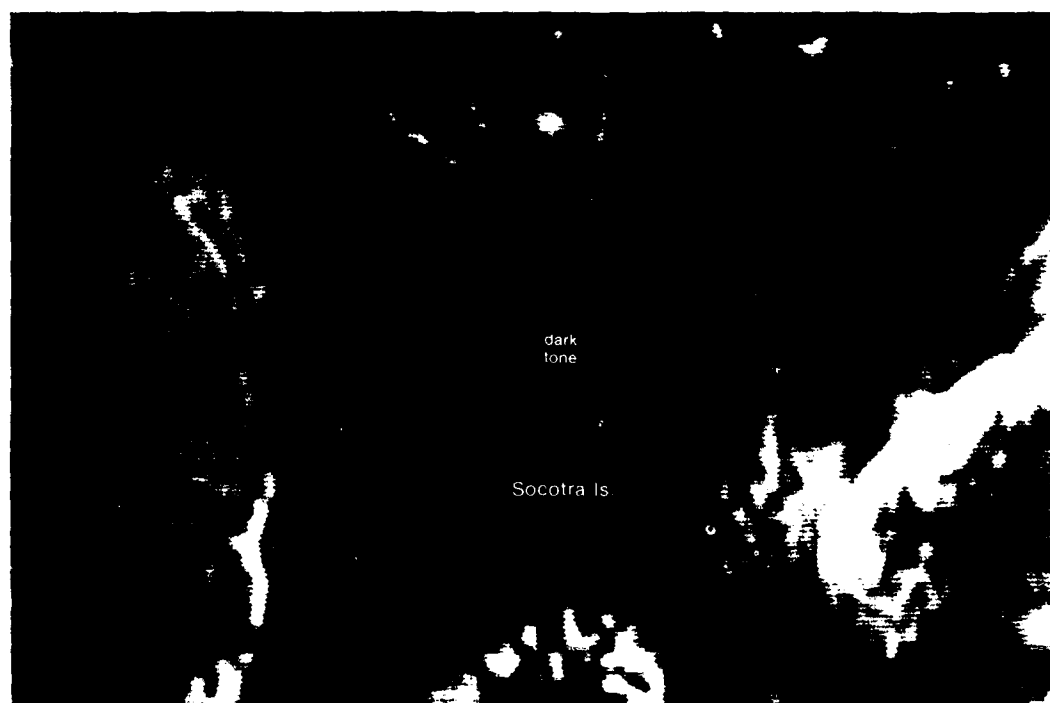
The NIMBUS-7 CZCS Channel 6 (10.5-12.5 μm) infrared image (4C-13b) displays some very subtle but important effects. Note the faint tendency for warmer temperatures in the lee of each of the islands. This is not as decisive as in the similar DMSP infrared image (4C-11b), since the CZCS channel is less susceptible to water vapor absorption.

On Socotra Island, two thin warm (dark tone) streaks extend from the north coast of the island. The easternmost streak appears almost aligned with a 5,021 ft mountain and the westernmost streak extends from a 1,470 ft mountain on the northwest coast (4C-11c). Note that the infrared streaks coincide with highest reflectivity bands emanating along the north coast in the visible image (4C-11a), indicating especially calm seas. It is believed that the added turbulent effect or heated effect of air flowing down and in the lee of these mountains results in especially warm air that stabilizes the lapse rate in a narrow line extending from these features. The added stability prevents strong winds from aloft in reaching the surface and insures calm seas confined to the narrow lines in the infrared image.

Deardorff (1976) first discussed this possible explanation for island wind shadows referring to them as "thermal-stability" patterns. He referred to diffusion studies by Raynor *et al.* (1974), who showed that a smoke plume "showed virtually no lateral spread (over 4 km) when the air was 1-2 K warmer than the sea." As indicated by Deardorff, "the great persistence of the wind shadow seems due to the associated stable stratification that both protects the plume from significant lateral mixing and micrometeorologically causes weak winds at small heights."



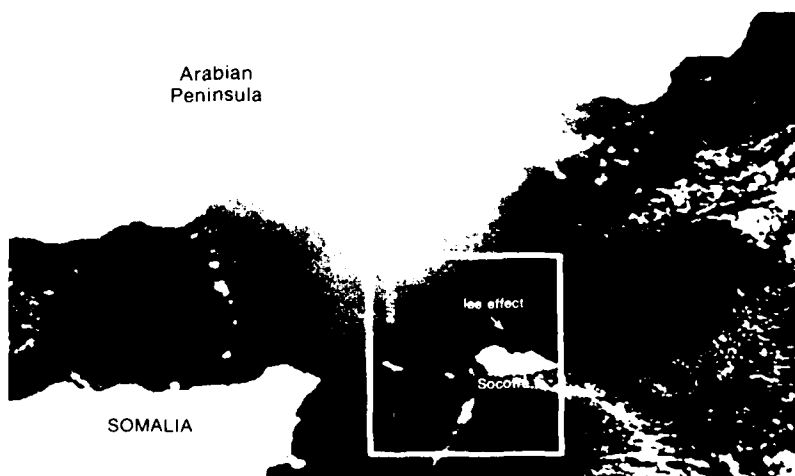
4C-11a. Enlarged View. F-I. DMSP LF Low Enhancement. 0721 GMT 4 June 1979.



4C-11b. Enlarged View. F-I. DMSP TS Normal Enhancement. 0721 GMT 4 June 1979.

4C-12a. NIMBUS-7.
CZCS Channel 5
Far Red Image.
0817 GMT 13 June 1983.

Arabian
Peninsula



SOMALIA

lee effect

Socotra

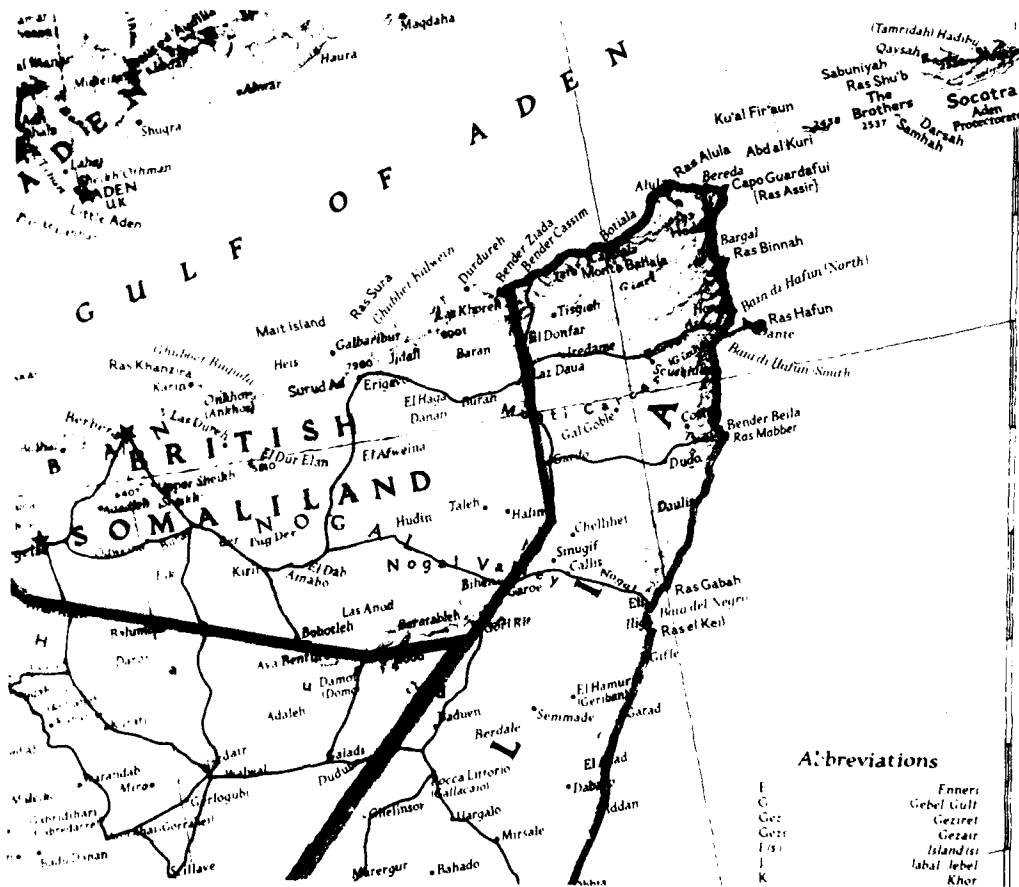
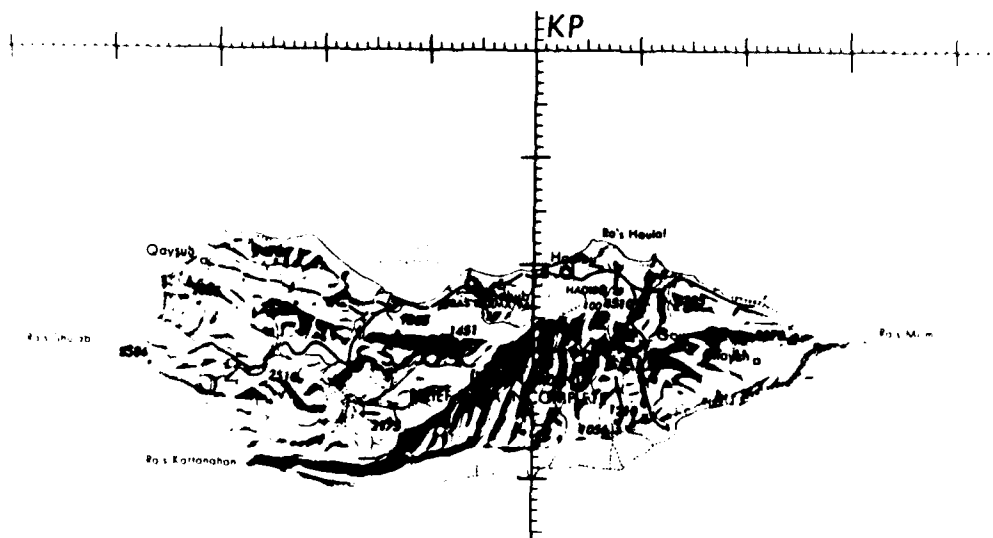


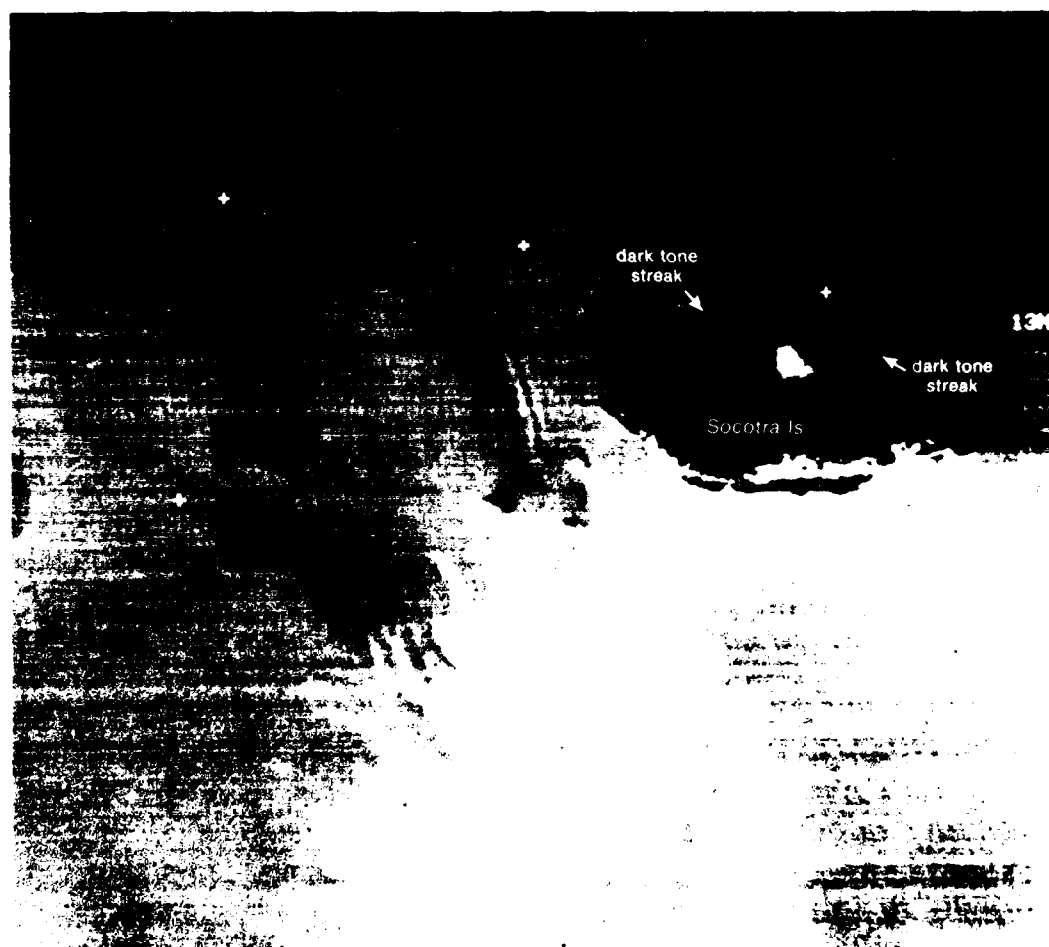
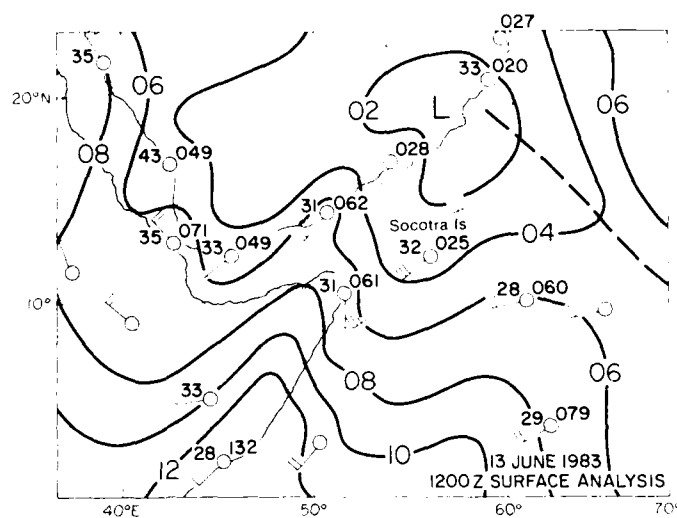
Ghubbet
Kharmah

SOKOTRA IS.

The Brothers

4C-12b. Enlarged View. NIMBUS-7. CZCS Channel 1 Blue-spectrum Image. 0817 GMT 13 June 1983.





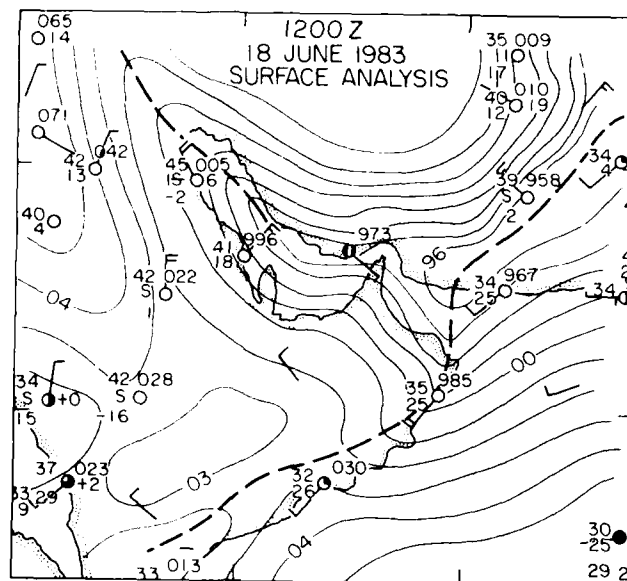
Case 4 Detection of Oil Spills in Sunglint

The areal extent of oil spills from damaged offshore oil fields can be detected and tracked in satellite imagery when sunglint is present. The reason for this is that surface tension effects of oil act to significantly dampen sea state structure. Under such conditions sunglint will be reflected strongly from the oil slick pattern and appear as either bright or dark streaks or patches in satellite visible imagery, depending upon satellite versus sun angle perspective.

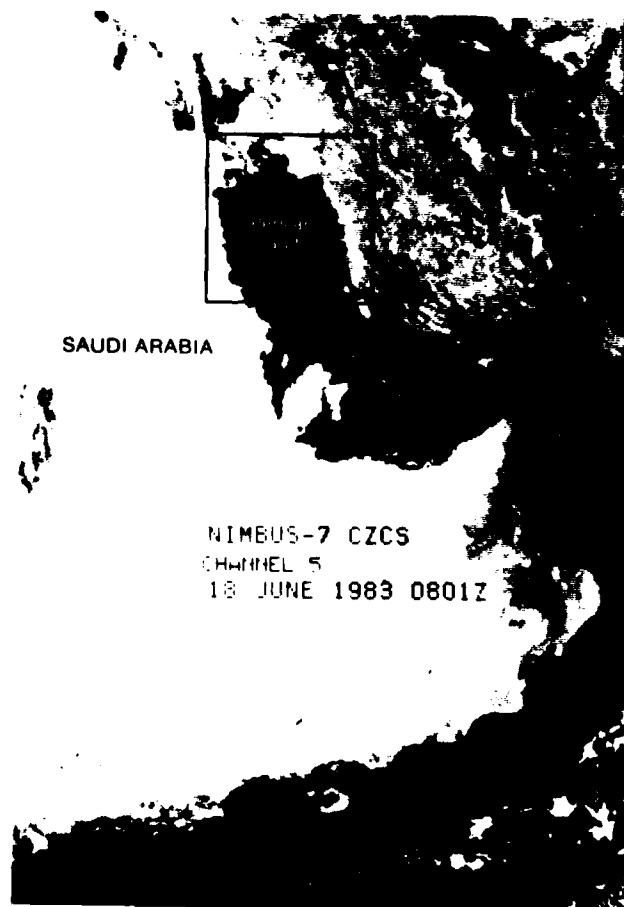
Attempts to detect oil slicks in satellite infrared imagery have largely failed despite laboratory experiments which indicate that oil slicks are warmed as much as 10°-18° C more than the surrounding water, under clear sky, daylight conditions (see NTAG, Vol. 2, Sec. 3E, Case 5). The reason for this appears to be that the much lower emissivity of oil, as compared to water, acts to diminish the oil-water temperature difference as sensed by satellite infrared sensors, which inhibits the detection of oil slicks in infrared imagery.

4C Case 4

4C-16a Surface Analysis
1200 GMT 18 June 1983



4C-16b NIMBUS-7
CZCS Channel 5
Far Red Image
0801 GMT 18 June 1983



*Damaged Oil Fields
Persian Gulf
June 1983*

19 June

Damaged oil fields were reported in the northern Persian Gulf. The NIMBUS-7 CZCS Channel 5 (0.7-0.8 μm) far red image (4C-16b) does not show any trace of the oil spills from the damaged oil fields. A sunglint envelope appears along the northeastern coastal waters and the east-central Persian Gulf. The surface analysis (4C-16a) indicates that a moderate northwesterly surface wind pattern prevails over most of the Persian Gulf, with light and variable winds near the northeast coast in the vicinity of the trough which lies along the Iranian coastline.

In the NIMBUS-7 CZCS Channel 1 (0.433-0.453 μm) blue-spectrum image (4C-17a), the alternating dark and bright patterns are located in the sunglint along the northeast coastal waters of the Persian Gulf. The bright squiggly lines in the outlined area are oil slicks which have propagated from the damaged oil well area. Dark tones near the Iranian coast indicate calm sea regions, some of which may also be due to oil slick effects. The oil is made discernable by reflection of the sun's rays from the slicks--the water surface is very smooth in the slicks. Wind waves in the water between the oil slicks results in the diffused reflection. The dark V-shaped streak west of the oil slick pattern is smoke from a damaged oil well that widens and dissipates as it spreads in the divergent surface winds. Oil visible near the edge of the smoke curls under the smoke (4C-17a and 17b).

Pictures taken from the space shuttle show the smoke to appear black when photographed in the visible spectrum. The variability in surface Persian Gulf waters coupled with the variability in the surface winds have created the complex downstream signature in the oil that remains at the surface. As the oil is dispersed and sinks, the more or less continuous concentrations of oil become less obvious and more detached downstream.

Important Conclusion

The surface environment (wind and stability) and the presence of sunglint determine whether oil on the surface of a body of water can be detected in satellite imagery.

4C 16 a



4C-17a NIMBUS 7
CZCS Channel 1
Blue-spectrum Image
0801 GMT 18 June 1983



4C-17b Enlarged View
NIMBUS 7 CZCS Channel 1
Blue-spectrum Image
0801 GMT 18 June 1983

*Case 5 Differentiation of Phenomena of
Atmospheric Origin from Oceanographic
Origin in Satellite Imagery*

In Landsat (formerly called ERTS) imagery, atmospheric phenomena can generally be differentiated from oceanographic phenomena due to their simultaneous appearance in all four channels in the spectrum from 0.5 to 1.1 μm . Oceanographic phenomena (underwater sediment and shallow water features) are best delineated by Channels 4 (0.5-0.6 μm) and 5 (0.6-0.7 μm) respectively.

4C Case 5

4C-20a LRTS-I
Channel 4 (0.5-0.6 μ m)
0743 GMT 30 June 1973



4C-20b LRTS-I
Channel 5 (0.6-0.7 μ m)
0743 GMT 30 June 1973



*Dust Storm
Red Sea
June 1973*

30 June

ERTS-I imagery in Channels 4, 5, 6, and 7 covering the Sinai Peninsula and the northern Red Sea, are shown in 4C-20a through 4C-21b, respectively. A most obvious difference between these various depictions is the indication of turbid and/or shallow water around the coastal island areas. They are most evident in the Channel 4 depiction (4C-20a), and almost totally lacking in the Channel 7 response (4C-21b). However, the light gray shade that covers the southwest sector of the Channel 4 image is also evident in Channel 7, although reduced in brightness and area. The light gray shade is, therefore, of atmospheric origin.

The DMSP visible image (4C-22a) was acquired about 2 hr after the ERTS-I imagery. A surface report at Port Sudan (4C-22a) shows an obscured ceiling in a plume of blowing sand and dust extending from Egypt over the Red Sea. A fainter plume of dust is also indicated over the northern Red Sea. On the enlargement of this area (4C-23a), a surface report (Aswan) in the interior of Egypt indicates dust or sand raised by wind at the time of observation. Note that this light tone gray shade (dust) was also viewed in the ERTS-I imagery (light tone areas in the southeast sectors of 4C-20a, 20b, 21a, and 21b).

A reasonable conclusion is, therefore, that the light gray shades in the ERTS-I imagery indicate blowing sand and dust extending over the northern Red Sea. Their extension eastward against northeasterly low-level flow (4C-23a) implies that the sand or dust extends to a higher level, where winds of necessity must have a westerly component. Such an extension is not unusual since strong dust storms have been reported by aircraft to have a vertical extent reaching 20,000 ft and higher. Verification for this example is shown in the NMC 500-mb analysis (4C-23b), which reveals the southward extension of an upper-level trough over the Red Sea.

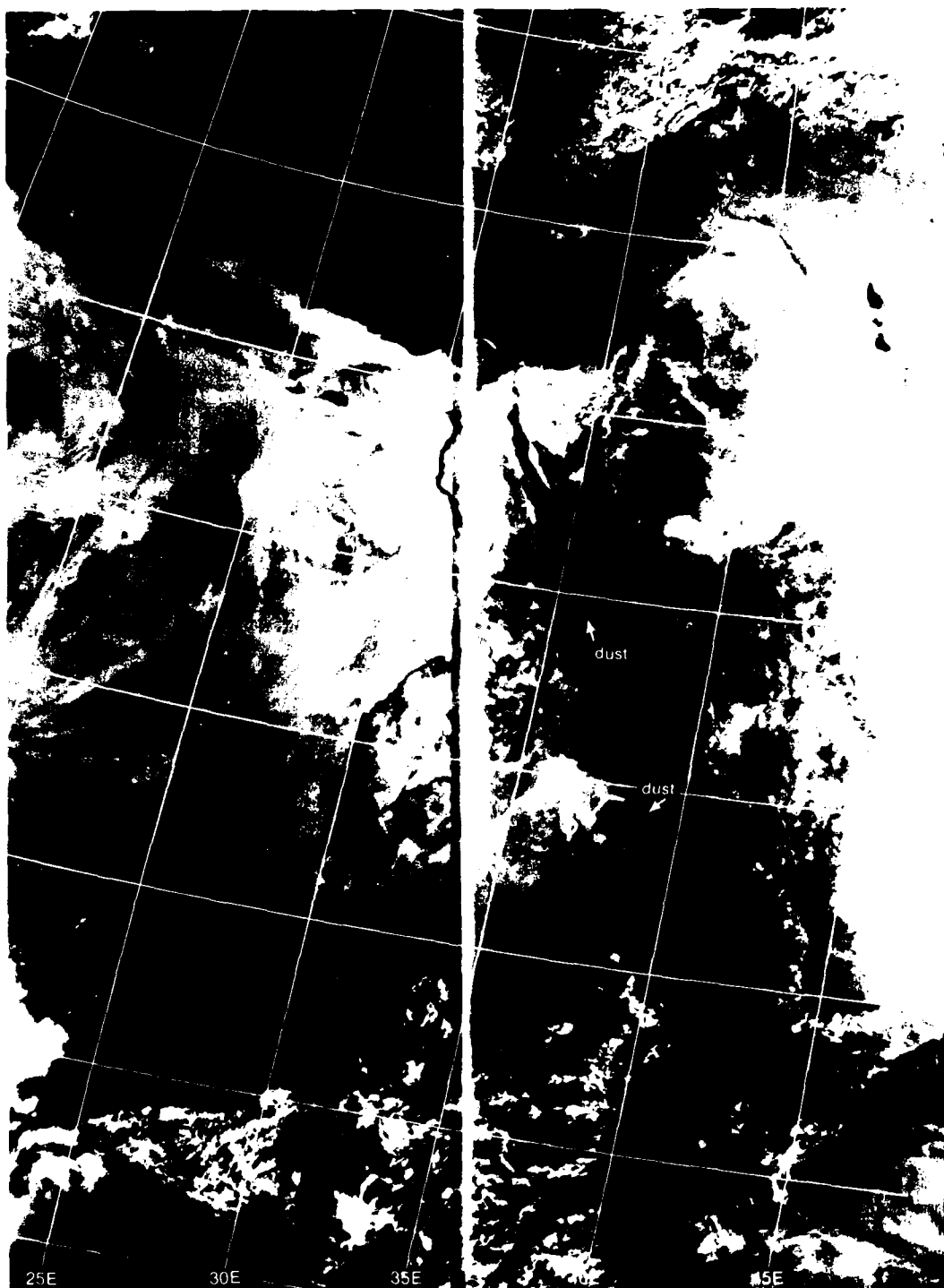


4C-21a ERTS-I
Channel 6 (0.7-0.8 um)
0743 GMT 30 June 1973



Sinai
Peninsula

4C-21b ERTS-I
Channel 7 (0.7-1.1 um)
0743 GMT 30 June 1973



4C-22a. FTV-28. DMSP LF Low Enhancement. 0959 GMT 30 June 1973



40-23b (Continued)
 11/1/73 (DISPATCH)
 11/1/73 (DISPATCH)
 0000 GMT 30 June 1973
 Surface Reports of 00 GMT



40-23b NMC 500-mb Analysis 1200 GMT 30 June 1973

40-23

DATA
FILM
9-8